Manuel Pirker, BSc.

Non-linear seismic analysis of a concrete gravity dam using a microplane material model

MASTER'S THESIS
to achieve the university degree of
Master of Science
Master's degree programme: Hydraulics and Geotechnical Engineering

submitted to

Graz University of Technology

Supervisor

Univ.-Prof. Dipl.-Ing. Dr.techn. Gerald Zenz

Co-supervisor

Dipl.-Ing. Edwin Josef Staudacher, BSc.

Institute of Hydraulic Engineering
and Water Resources Management

Graz, March 2020

Statutory Declaration

I declare that I have authored this thesis independently, that I have not used other than the declared sources / resources, and that I have explicitly marked all material which has been quoted either literally or by content from the used sources.

. . . .
             Date   Signature

Acknowledgement

I would first like to thank my thesis co-supervisor Edwin Staudacher. The door to his office was always open whenever I ran into a trouble spot or had a question about my research or writing. He consistently allowed this paper to be my own work, but steered me in the right the direction whenever he thought I needed it.

I would also like to acknowledge Professor Gerald Zenz' support as supervisor and guide to this thesis. He is one of the reasons why I choose this master program.

Finally, I must express my very profound gratitude to my family, especially to my Mam and my Dad for their unwavering trust, providing me with unfailing support and for covering my back throughout my years of study. Also, I must thank my friends for continuous encouragement and motivation through the process of writing this thesis. This accomplishment would not have been possible without any of them.

Thank you all.

Abstract

The formation of cracks is an intentional phenomenon in reinforced concrete structures because they are essential for the activation of the reinforcement. In unreinforced mass concrete this phenomenon is rather unwanted. Although small cracks are not a hazard for the dam safety, they still bear the potential of developing larger crack patterns. In concrete dams, extending crack patterns can then lead to seepage which influences the structural integrity and the serviceability of the dam. Various material models exist which are capable of the simulation of non-linear material behaviour caused by these crack patterns. However, there is few calibration data available regarding non-linear behaviour of concrete with large grain sizes, e.g. as used for the construction of dams.

The aim of this thesis is the application and evaluation of the available microplane models that are implemented in the commercial finite element software *Ansys Mechanical* as well as their applicability to represent non-linear material behaviour during seismic loading of concrete dams.

After a brief introduction, the following two chapters focus on the fundamentals of fracture mechanics and structural dynamics. They summarize the required knowledge and applied methodology for this thesis, Furthermore, they give an inside on the available alternatives for modelling certain aspects. Chapter four is designated to the development of an understanding for the applied material model by presenting performed numerical analyses on a small scale. The final chapter consists of linear and non-linear investigations on Pine Flat Dam followed by a comparison with an analysis done on this dam performed during an *ICOLD Benchmark Workshop*. Finally, an alternative, analytical way to investigate partial dam safety by a *Newmark* deformation analysis is presented.

Kurzfassung

Die Bildung von Rissen ist eine gewollt auftretende Erscheinung bei bewehrten Konstruktionen in Beton, da es die Voraussetzung für die Tragwirkung der Bewehrungsstäbe ist. In unbewehrten Massebetonbauwerken ist dieses Phänomen jedoch unerwünscht. Obwohl kleine Risse keine Gefahr für die Sicherheit der Staumauer darstellen, können sich daraus größere Rissmuster entwickeln. Bei Betonmauern können diese sich ausdehnenden Rissmuster dann zu unerwünschten Wassereintritten führen. Dadurch werden die Standsicherheit und Gebrauchstauglichkeit der Staumauer nachteilig beeinflusst. Es stehen verschiedene Materialmodelle zur Verfügung welche das, durch diese Rissmuster verursachte, nichtlineare Materialverhalten abbilden können. Es sind jedoch nur wenige Daten für die Kalibrierung solcher Modelle verfügbar welche sich auf das nichtlineare Verhalten der Betone mit großen Korndurchmessern beziehen, wie sie zum Beispiel beim Bau von Staumauern Verwendung finden.

Ziel dieser Arbeit ist die Anwendung und Bewerten der verfügbaren Microplane-Modelle, die in der kommerziellen Finite-Elemente-Software *Ansys Mechanical* implementiert sind. Weiters wird deren Anwendbarkeit zur Darstellung des nichtlinearen Materialverhaltens während der seismischen Belastung von Staumauern betrachtet werden.

Nach einer kurzen Einführung konzentrieren sich die folgenden beiden Kapitel auf die Grundlagen der Bruchmechanik und der Strukturdynamik. Sie fassen das erforderliche Wissen und die angewandte Methodik für diese Arbeit zusammen. Darüber hinaus geben sie einen Einblick in die verfügbaren Alternativen zu bestimmten Themen. Das vierte Kapitel dient dem Ausbau des Verständnisses für das angewandte Materialmodell, indem es durchgeführte numerische Analysen in kleinem Maßstab beschreibt. Das letzte Kapitel besteht aus linearen und nichtlinearen Untersuchungen der *Pine-Flat*-Talsperre. Darauf folgend, werden die erhaltenen Ergebnisse mit denen einer Analyse dieser Staumauer im Zuge eines *ICOLD Benchmark Workshops* verglichen. Abschließend wird eine alternative, analytische Methode zur Untersuchung der Teilsicherheit von Staumauern mit einem *Newmark*-Verschiebeverfahren vorgestellt.

Contents

1 Introduction

Finite Element Analysis of massive concrete structures - such as dams - is a challenging task, especially for earthquake excitation or seismic events. This arises not only from the complex behaviour of involved materials like concrete, water, rock and their interaction, as well as discontinuities need to be considered [1]. For example, the opening and closing of a discrete joint between the dam's base and the foundation rock due to variation of loading. Or the change of the structure's natural frequencies depending on the water level in the reservoir due to the principle of fluid structure interaction (FSI) respecting the compressibility of water together with hydrodynamic forces acting onto the structure during a seismic event. Furthermore, their interaction at the reservoir boundaries due to reflection needs to be considered.

Another aspect is the temperature loading on the dam that are part of high head hydro power schemes. There, dams are situated in mountainous regions to maximize their potential energy capacity [2]. Another example is presented from the *14th ICOLD Benchmark Workshop* in Sweden [3], where the response of a very slender concrete dam to very low temperature is investigated. The dam's surface temperature can significantly vary based on daily or seasonal impacts. This can lead to major crack patterns which may locally influence the structural integrity. Therefore, special attention must be given to material behaviour of concrete considering structural attributes as well as the performance due to thermal loading.

The most common form of numerical modelling the material behaviour are continuum models. These models formulate a high-order tensorial relationship between an input (i.e. strain) and the response (i.e. stress) of the material. Although these models work perfectly for linear-elastic materials, their non-linear capabilities are limited. In contrary to continuum models the so-called microplane model uses a different approach. This is, that the constitutive material laws are applied on various oriented planes forming a unit-sphere instead on a definite cube.

The aim of this thesis is the application and evaluation of the available microplane models that are implemented in the commercial finite element software *Ansys Mechanical* as well as their applicability to represent non-linear material behaviour during seismic loading of concrete dams. The performed analyses use the massless rock approach in order to limit the scope of this work.

After a brief introduction, the following two chapters focus on the fundamentals of fracture mechanics and structural dynamics. They summarize the required knowledge and applied methodology for this thesis, Furthermore, they give an inside on the available alternatives for modelling certain aspects. Chapter four is designated to the development of an understanding for the applied material model by presenting performed numerical analyses on a small scale. The final chapter consists of linear and non-linear investigations on Pine Flat Dam followed by a comparison with an analysis done on this dam performed during an *ICOLD Benchmark Workshop*. Finally, an alternative, analytical way to investigate partial dam safety by *Newmark's sliding block* is presented.

2 Fracture Mechanics

2.1 Fundamentals

Initially, the theory of fracture mechanics was developed to describe the ductile response of steel bars during tensile failure. Simply using these already developed procedures was not suitable for describing the fracturing of concrete. First, concrete undergoes strain softening during its post-peak behaviour in contrary to the hardening observed on steel bars (2.2). Second, in aggregate materials like concrete the zone involved in the cracking process is much larger than in brittle (e.g. glass) or ductile materials (e.g. steel), see figure 2.1.
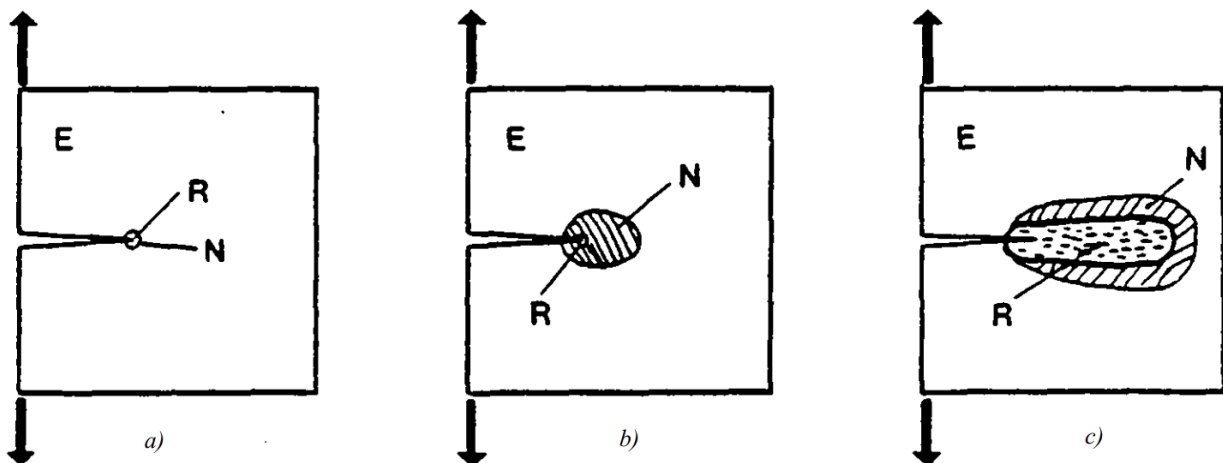
Fig. 2.1: Material behaviour close to crack tip: **E**...linear elastic behaviour, **N**...non-linear behaviour and **R**...Fracture Process Zone for *(a)* brittle materials, *(b)* ductile materials and *(c)* quasi-brittle materials [4]

The main parameter describing the concrete's resistance against forming of crack is its tensile strength. The resulting crack pattern displayed in figure 2.2, obtained from uni-axial test done on cubic specimens, show that even under uni-axial compressive loading the resulting stress perpendicular to the loading direction leads to tensional cracking parallel to the specimen's axis.

This part is following Shah's description of crack forming [5]: If the tensional strength is exceeded locally, micro cracks are forming within the concrete structure. Due to the heterogeneity of the material itself, these cracks can form with any orientation inside the so-called fracture process zone (FPZ). Further increase of loading leads to the connection of these micro cracks and the forming of a macroscopic crack feature. However, this newly formed crack can still transfer stresses due to friction or connecting aggregates (see figure 2.3) until the complete separation of the material.
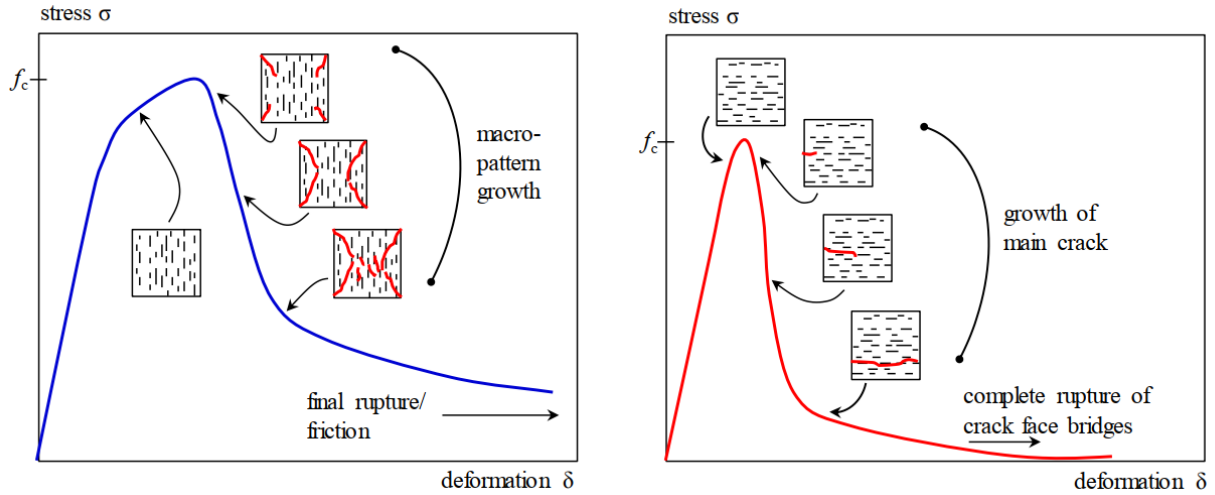
Fig. 2.2: Macroscopic failure modes acc. to [6] for uni-axial compression (*left*) and uni-axial tension (*right*)

Some of the lasting stress inside the fracture process zone (FPZ) gets redistributed within the fracture zone (FZ) in the intact material (see figure 2.4a). Is a crack loaded in normal to the crack plane - i.e. plane where the material separates, the tensional strength forms the boundary between the intact material and the softening happening in the FPZ.
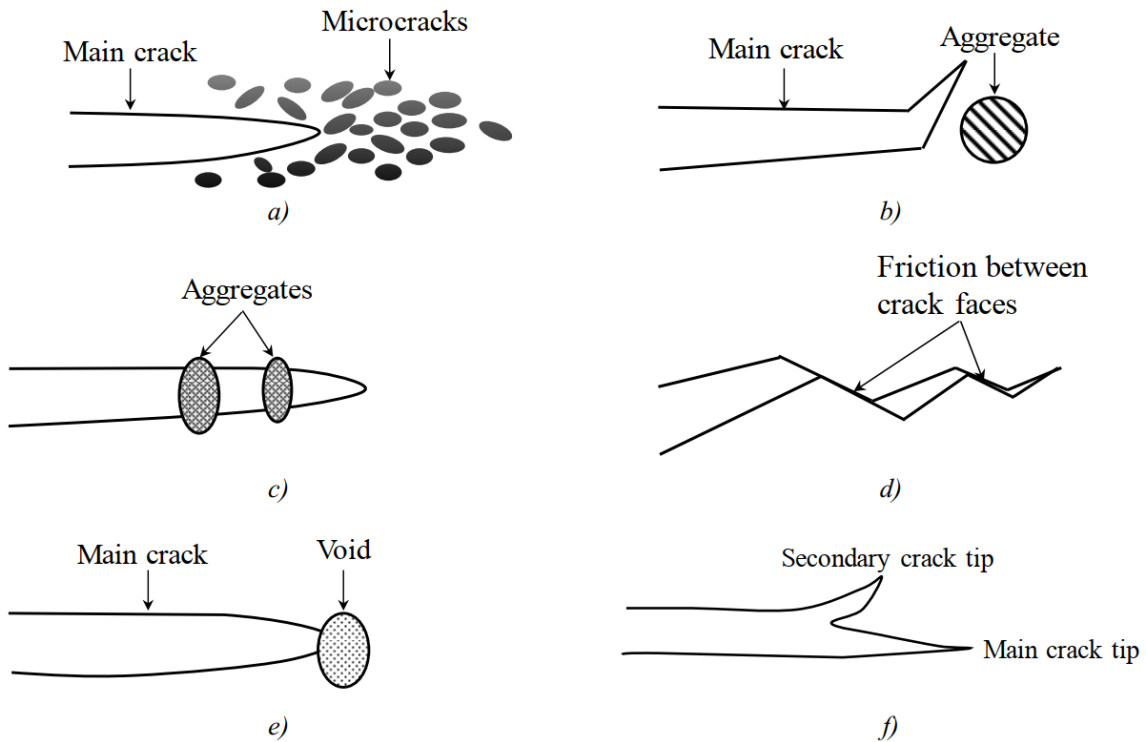
Fig. 2.3: Toughening mechanics in the Fracture Process Zone: *(a)* crack shielding, *(b)* crack deflection, *(c)* aggregate bridging, *(d)* crack surface roughness-induced closure, *(e)* crack tip blunted by void and *(f)* crack branching [5]
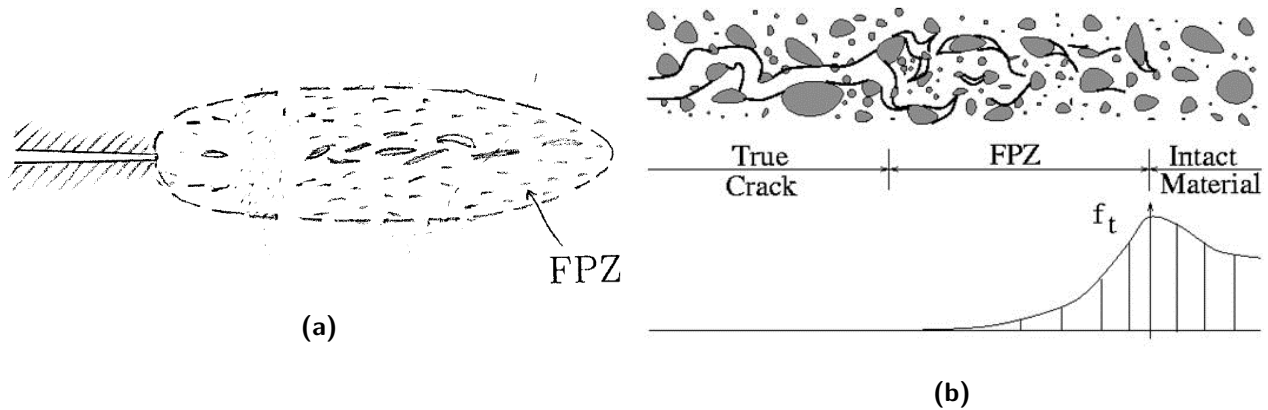
Fig. 2.4: (a) Fracture Process Zone (FPZ) ahead of macro crack, **(b)** stress distribution normal to the crack within the Fracture Zone [6, 5]

2.1.1 Size Effects

The size effect of concrete can be described as the dependence of material properties on the specimen size. How it was shown in various studies [8, 9, 7], material properties like strength or fracture energy obtained from testing geometrically similar specimens of different sizes, vary significantly.

Bažant showed, that this behaviour follows a so-called size-effect law. A detailed description and explanation can be found in [10]. Furthermore, he names 6 reasons for the size effect on structural strength:

- *Boundary layer effect:* It is also known as Wall Effect. Three different types exist involving the strength differences arising from the smaller relative content of larger aggregate pieces and a larger relative content of cement and mortar in the layer adjacent to the wall than in the interior of the member. The second arises from transverse stresses in the interior during normal stress parallel to the surface, while the stress on the surface is zero. The third one arises from the Poisson effect or lateral expansion, which causes the surface layer nearly to be in plane stress while the interior is nearly in plane strain.

- *Diffusion phenomena:* Diffusion processes like heat conduction or pore water transfer changes the material properties and lead to residual stress producing inelastic strains and cracking.

- *Hydration:* Hydration heat during concrete curing leads to an increase in volume of the structural member. As a result a non-uniform temperature distribution along the cross section can lead to thermal cracking and even alter the material properties.

- *Statistical size effect:* It is caused by the randomness of material strength. This is believed to be the cause of most size effects in concrete structures.

- *Fracture mechanics size effect:* It arises from the stored energy released into the fracture front. As shown in figure 2.5 for a constant ratio of specimen size D and crack length a_0, the energy released due a crack extension of Δa - represented through the area of the densely cross-hatched strip - rises as the specimen size increases. Furthermore, h_f represents the constant crack band width and the cross-hatched area marks the area where the strain energy density is reduced to zero.
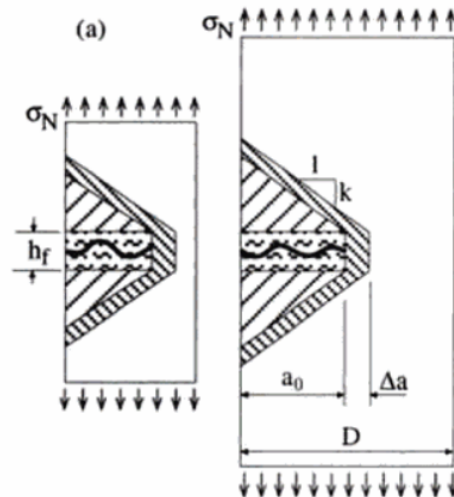
Fig. 2.5: Sketch of geometrical size effect for a blunt crack band [10]

- *Fractal nature of crack surfaces:* As it is for the measurement of the length of coastlines, closer observation enlarge the observed length of the coastline until it becomes infinite (see *Coastline Paradox*). Bažant points out that this kind of effect may be hypothetical.

2.1.2 Fracture Energy

The softening behaviour of concrete is governed by multiple factors. Its heterogeneous composition, characterized by aggregates, mortar mix, pores, voids and flaws, as well as the pre-existence of micro cracks play a major role. These micro cracks form during the hardening process due to the differences in stiffness of the various components. Furthermore, the differences in stiffness lead to unequally distributed stress fields.

If the concrete locally exceeds its tensional strength, damage starts to grow and available deformation energy is dissipated by the fracture process. However, development of a single crack is hindered by the concrete's heterogeneity. Instead, pre-existing micro cracks are extended until they connect each other forming a macroscopic crack. The energy which is dissipated during this process is called fracture energy. It is defined as energy dissipated within the Fracture Zone per unit area in units $[J/m^2]$ or $[N/m]$. The Fracture Zone covers the material involved in the exchange of deformation energy and its release due crack formation inside the Fracture Process Zone. The Fracture Process Zone is situated ahead of the tip of a macro crack. In this zone, microcracking leads to the growth of this macro crack.

The easiest way for determination of Mode-I fracture energy is directly from an uni-axial tension test. There, the fracture energy equals the area below the load-deformation curve (see figure 2.7). However, discussion about the boundary conditions and the minimum specimen size are still ongoing.

Alternatively, if special equipment for uni-axial testing is unavailable, fracture energy can be determined indirectly through three-point-bending test or Brazilian tests. Although some things should kept in mind if using these testing methods: (i) energy dissipation outside the fracture zones should be negligible and (ii) concrete compressive strength should be much larger than tensile strength to avoid energy dissipation in the compressive zone of the specimen.
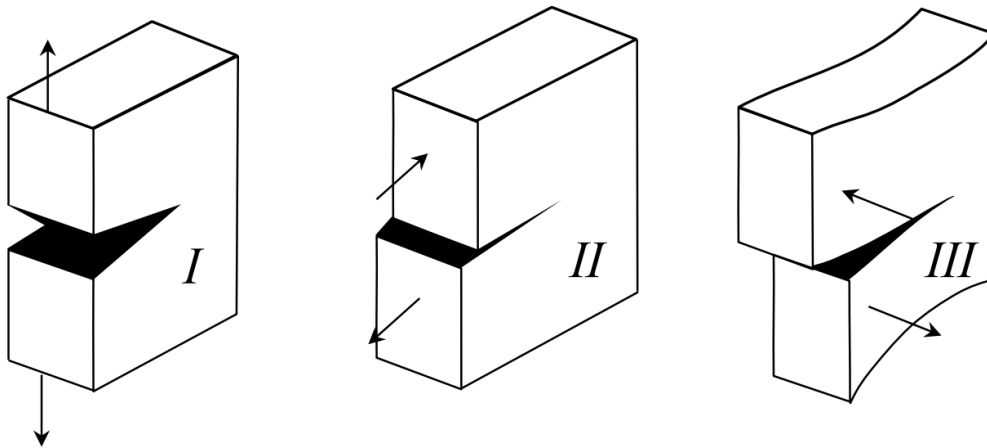
Fig. 2.6: The three opening modes of cracks, **Mode I:** due normal stress perpendicular to the fracture plane, **Mode II:** due shear stresses on the fracture plane and **Mode III:** due stresses resulting from a tearing load [10]

For normal concrete, the typical value lies between 50 and 200 [N/m], for dam concrete values up to 500 [N/m] are possible. This results mainly from the much larger aggregate sizes used for dam concrete, which is up to 150 mm according to *The Concrete Society*. In contrary, normal concrete mostly contains maximum aggregate sizes of 20 or 32 mm.

Fracture Energy from Uni-Axial Tensile Testing

Mode-I fracture energy can be obtained in different ways from uni-axial tension tests. Three of them will be described here. They differ due to the measured quantities and may be more suitable for experiments or numerical material models.

The data used is taken from the same modelled tensile test described in chapter 4.2.1.

From Force-Displacement-Curve: Commonly used in laboratory experiments. The specimen - usually in cylindrical form - is attached with epoxy attached to the machine ring. This ring is displacement controlled and feasible to record the applied tensile force. Therefore, a force displacement curve is obtained. The area below this curve represents the work done by the applied force until complete fracture of the specimen (see U_s at figure 2.7). This work divided by the fractured area (ligament area A_0) results into the fracture energy as an energy dissipated per unit area - G_F. The ligament area is the cross section area normal to the main stress axes.

$$A_0 = 0.49 \ [m^2] \tag{2.1}$$

$$U_s = \int F \mathrm{d}u = 122.04 \ [J] \tag{2.2}$$

$$G_F^{fdc} = \frac{U_s}{A_0} = 249.05 \ [N/m] \tag{2.3}$$
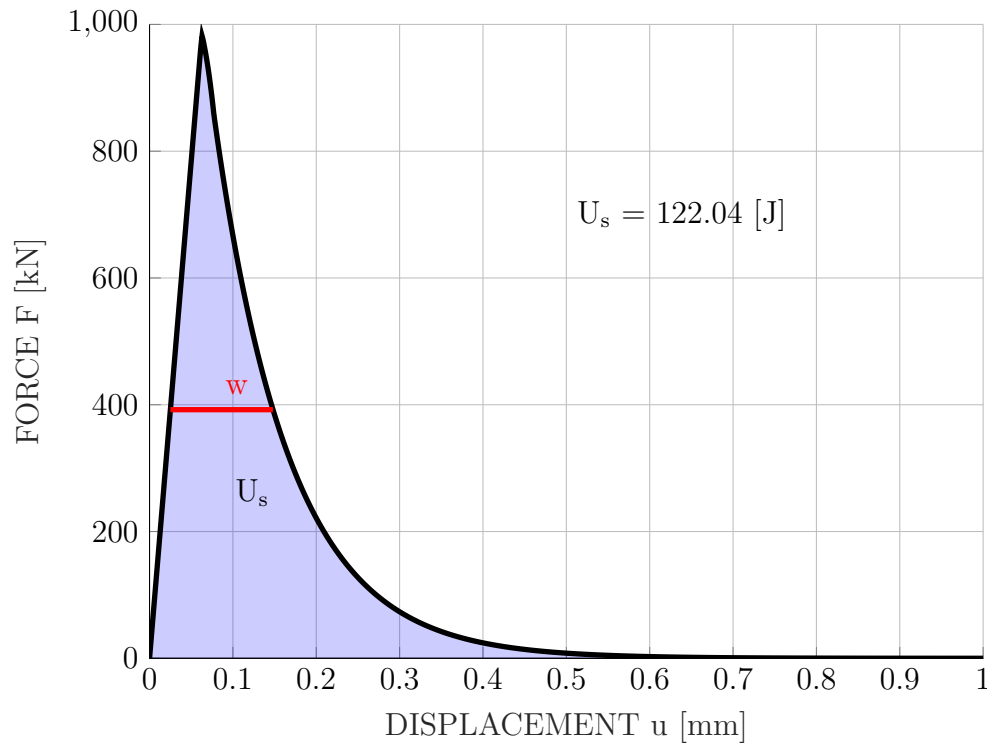
Fig. 2.7: Example of force displacement curve, blue coloured area represents work done by the applied force

From Fictitious Crack Opening: This method introduced by *Hillerborg* in 1978 [11] is based on a force-displacement-curve. From this curve a fictitious crack opening width (see w at figure 2.7) is calculated. The axial stress is then plot over this width. The fracture energy equals then the area under the obtained curve (see figure 2.8).
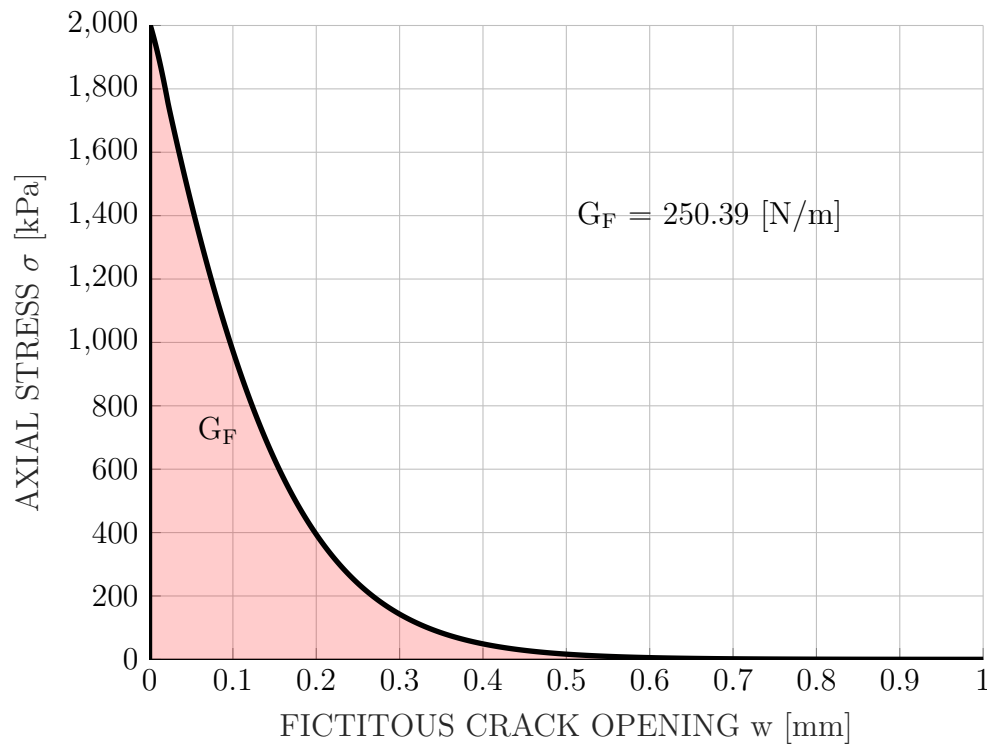
Fig. 2.8: Example of stress crack opening curve, red area represents fracture energy per unit area

Advantage of this representation is its independence from the specimen size, therefore experimental results can be easily compared. Fundamental equations are:

$$w = u - \frac{F \cdot l}{E \cdot A} \tag{2.4}$$

$$G_F^{fcw} = \frac{1}{A} \int F \mathrm{d}w = \int \sigma \mathrm{d}w = 250.39 \ [N/m] \tag{2.5}$$

Where E is the Young's modulus, A is the cross section area and l the length of the specimen.

Stress-Strain-Curve: In case of an uniformly distributed strain field, the fracture energy can also be determined from a stress strain curve. At normal tensile test, the epoxy attachment from the specimen to the machinery results in hindered radial deformation in this region. In order to avoid this fixation, glued and spaced rods can be used for this attachment - as described by Bažant in [12].

The area under this stress-strain curve represents the energy dissipated during the fracture process per unit volume (see W_s at figure 2.9). The relation between this fracture energy per unit volume to the desired fracture energy per unit area is given by the characteristic length l_{ch}. For a non-notched specimen this characteristic length equals its dimension.

$$G_F^{ssc} = W_s \cdot l_{ch} = 249.05 \ [N/m] \tag{2.6}$$
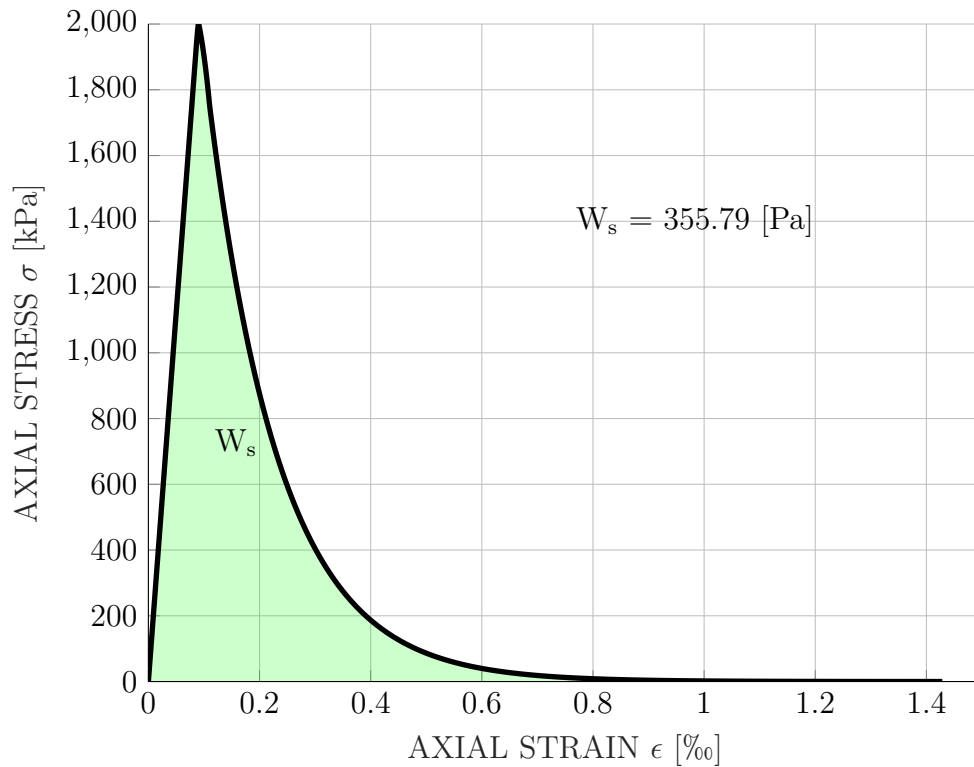
Fig. 2.9: Example of stress strain curve, green area represents fracture energy per unit volume

Fracture Energy from Three-Point-Bending Test

Determining fracture energy that way is more suitable for laboratory testing. First, support areas have less influence to the result, i.e. no fixed support is needed as in tensile tests. Second, no special manipulation of the specimen and machinery is necessary, e.g. epoxy attachments. Furthermore, much larger specimens can be tested as in uni-axial tensile tests [13]. On the downside, the self-weight plays has to be reconsidered while evaluating the results. *Perersson* [14] shows two ways to compensate self-weight during the testin procedure itself by enlarging the specimen beyond the supports or due applying additional weight at the outcrops (see figure 2.10).
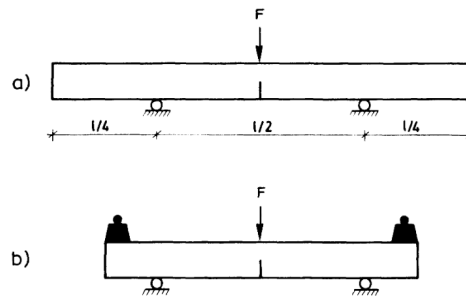
Fig. 2.10: Self-weight compensation due **(a)** enlargement of specimen and **(b)** additional weight on outcrops

Alternatively, he shows a way to reconsider self-weight directly in the formula where the fracture energy is obtained:

$$G_F = \frac{W + M \cdot g \cdot \delta_0}{b(d - a)} \tag{2.7}$$

Where W is the area below the load-deflection curve ($=$ total work done by force applied to the beam), M is the weight of the specimen between the supports, δ_0 is the final deflection of the beam, b is the beam width, $(d - a)$ is the ligament length above the notch.

For numerical modelling, self-weight is usually not reconsidered. Therefore, fracture energy can be calculated by:

$$G_F = \frac{W}{b(d - a)} \tag{2.8}$$

Because measurement of deflection is highly dependent on the test set-up, spurious deflections are sometimes obtained. In order to avoid these erroneous measurements, the crack mouth opening displacement (CMOD) can be used. CMOD is measured horizontally at the start of the notch. Fracture energy can be obtained from the area below the force-CMOD W^{CMOD} curve by:

$$G_F^{CMOD} = \frac{W^{CMOD}}{b(d - a)} \tag{2.9}$$

Fracture Energy from Brazilian Test

A Brazilian test is indirect testing method for tensional strength and is also capable of recording post-peak softening effects. It is mostly used when large specimen sizes are required

for testing and ordinary direct tension test are not feasible. The required specimen size to obtain representative results are depending on the concretes grain size. Larger aggregate sizes (like it is the case for dam concrete) require larger size of the specimen to be tested. As a rule of thump, the minimum dimension of the specimen should be at least three times the maximum aggregate size [8].

The most commune variants a cylindrical specimen which is compressed in radial direction (see figure 2.11a). The material's uni-axial tensile strength is then obtained by:

$$f_{ut} = \frac{2 \cdot P}{\pi d \cdot t} \tag{2.10}$$

Where P is the maximum compressive force applied, d is the diameter and t the depth of the specimen. Alternatively, this kind of test can be transferred to a notched block (see figure 2.11b).

Fracture energy related parameters can be obtained from both procedures. The fracture energy related to a unit volume G_V and to a unit area G_F are given by:

$$G_V = \frac{W}{V_f} \tag{2.11}$$

$$G_F = \frac{W}{A_f} \tag{2.12}$$

Where W is the are below the load deflection curve or load crack-widening curve respectively, V_f is the volume involved in the fracture process and A_f is the ligament area. This alignment area is given by notch length a the specimen thickness t:

$$A_f = H_f \cdot t = (H - a) \cdot t \tag{2.13}$$

The involved volume is related to the width of the fracture process zone h:

$$V_f = \int_0^{H_f} h^{FPZ}(z)\mathrm{d}z \tag{2.14}$$

Size Effect on Fracture Energy

Fracture energy - although it is widely seen as a material constant - also undergoes a size effect due to the same reasons as mentioned in section 2.1.1.

2.1.3 Modelling of Cracks

In order model fracture process or crack stability different models can be used. Roughly, they can be distinguished either they are following the *discrete crack approach*, where the crack is modelled as a gap between two bodies or the *smeared crack approach*, where the cracks are not modelled explicitly but, as a reduction of material strength inside an inflicted range.

Depending on the problem to be modelled - either a stationary crack problem or a crack growth simulation - both approaches have their advantages and disadvantages:

Discrete crack approach: One disadvantage of some available models (e.g. Linear Elastic Fracture Mechanics) is, that the location and propagation direction of the crack need to be known in advance. On the contrary, extended finite element models are capable of modelling crack propagation by formulating a crack criterion (e.g. in *Abaqus* a form of the J-integral)
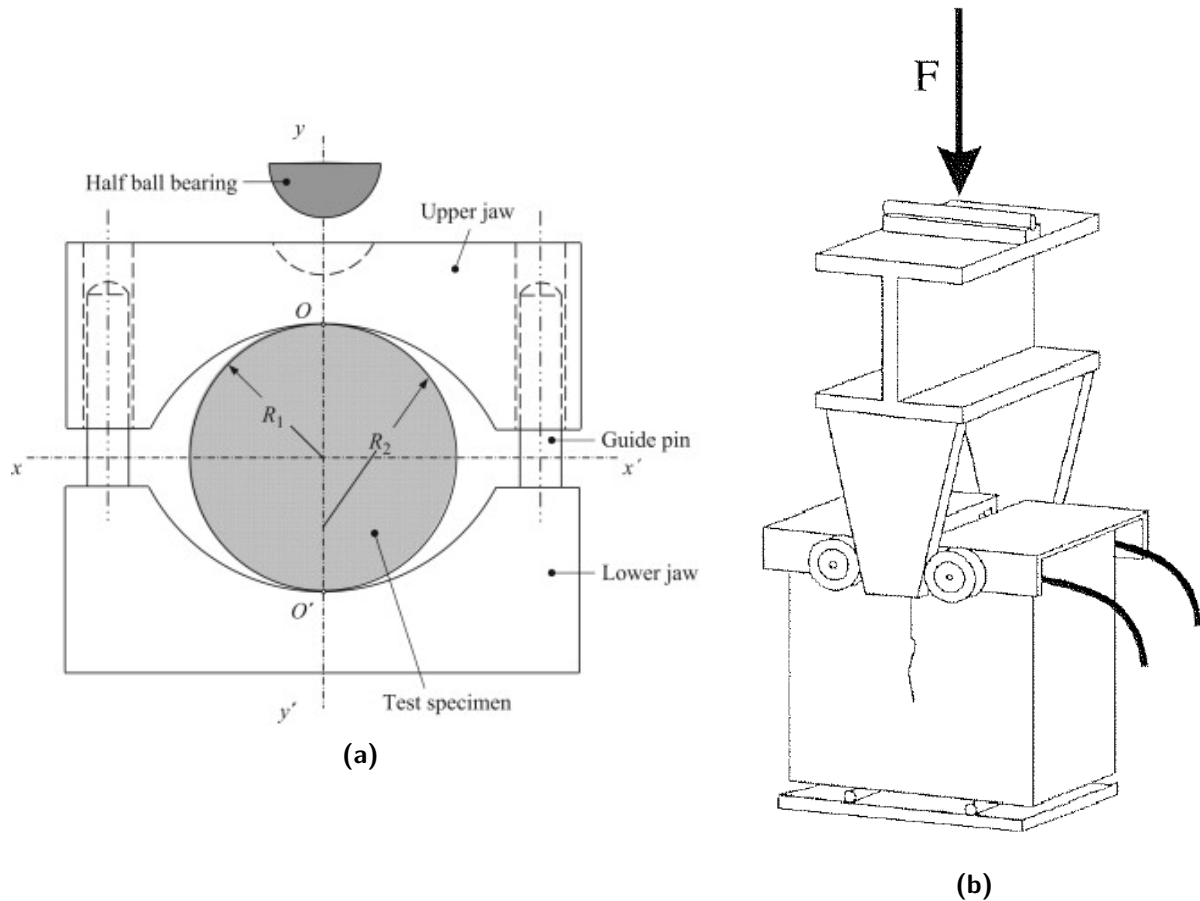
Fig. 2.11: Experimental setups for a Brazilian test for **(a)** cylindrical specimen and **(b)** block designed for dam concrete [8]

which leads to a partition of mesh elements. This means, the modelled area needs to be re-meshed every time the crack criterion is reached, leading to a high computational demand. Furthermore, contact formulations need to be defined if closured of the crack is considered.

Smeared crack approach: One advantage of this approach is its simplicity and its effectiveness in terms of computational demands, because topology of the mesh remains unaltered. On the other hand, these kinds of models posses a high dependency on the used mesh.

The following sections should provide a short overview on the various model types and links to available literature.

Linear Elastic Fracture Mechanics [10]

Linear elastic fracture mechanics (LEFM) is used to determine the stability of a single discrete crack. Its origin lies in the modelling of cracks in metals and other ductile materials. However, it can also be used to describe fracture in quasi-brittle materials like concrete, if the FPZ in relation to the structure size is small. LEFM is used by *Linsbauer* for evaluating stationary crack problems. E.g. he used it to determine damage potential of a crack in an gravity dam subjected to impact loading [15]. Furthermore, he used it to determine stability of cracks on the downstream side of *Kölnbrein* arch dam in Austria [16]. There he could verify that these cracks could have been formed only to dead load and grouting of the block joints. Also, he

found that these downstream cracks were formed during construction process and that filling of the reservoir will lead to the closure of the cracks.
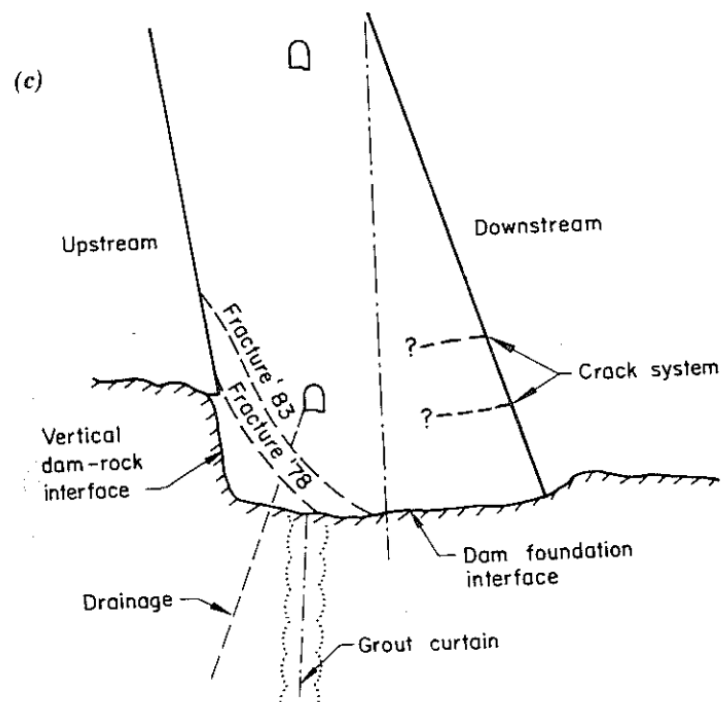
Fig. 2.12: Cross section with found cracks at the Kölnbrein arch dam [16]

However, the linear elastic approach does not represent perfectly the behaviour close to the crack tip. For a crack width tend to be zero, the stress at crack tip becomes infinite, which results into an unrealistic stress distribution inside the fracture zone (see figure 2.13(a)). Therefore, linear plastic fracture mechanics (LPFM) additionally takes into account the stress degradation in the fracture zone (see figure 2.13(b)).
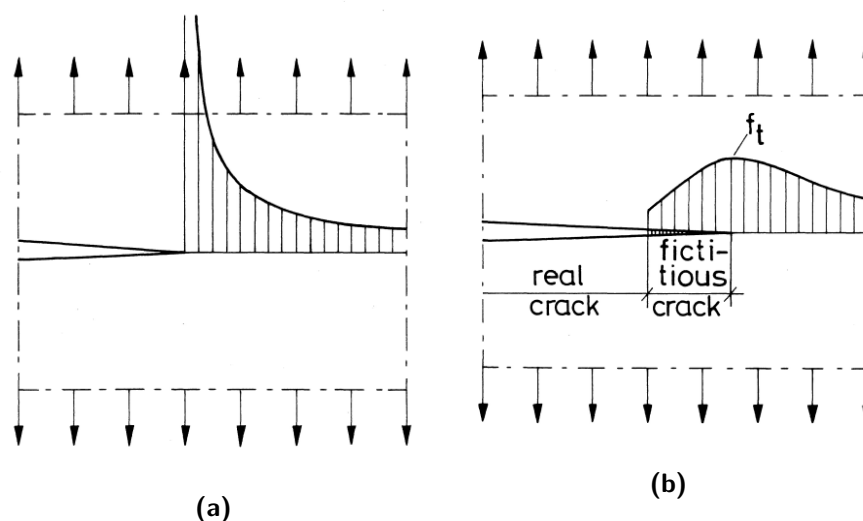
Fig. 2.13: Stress distribution at crack tip according to linear elastic and linear plastic fracture mechanics [10]

Rice's J-Integral [17] is derived from the general energy balance of the fracture process

(for a plane structure):

$$\underbrace{\delta W}_{\text{External work}} = \underbrace{\delta U}_{\text{Elastic energy}} + \underbrace{G \cdot b \cdot \delta a}_{\text{Energy release due fracture}} \qquad (2.15)$$

Where δW is the external work in its infinitesimal form, δU is the stored elastic energy and G is the energy release rate. Furthermore, b is the width of the plane structure and δa is the indefinite distance at which the crack advances. The J-integral is then given as:

$$\underbrace{J = G}_{\text{Energy released}} = \int_{\Gamma} \left(\underbrace{\overline{U} \cdot n_1}_{\text{Elastic energy}} - \underbrace{t_i \cdot \frac{\mathrm{d}u_i}{\mathrm{d}x_1}}_{\text{External work}} \right) \mathrm{d}s \qquad (2.16)$$

Where $\overline{U}$ is the elastic energy density (=energy per unit volume), n_1 is the normal vector to the contour Γ, $\mathrm{d}s$ is the differential arc-length along the contour, t_i components of the surface traction vector (=resultant of stress acting) and u_i are the components of the displacement vector.

The J-integral is an expression for the energy released due variation of stored elastic energy due to crack propagation (see figure 2.14). However, this is also true for non-elastic situations if the non-elastic zone reduces to a point inside the contour and the body is subjected to monotonic loading. This is used e.g. to determine the stress intensity factor at crack tip for determination of crack stability.
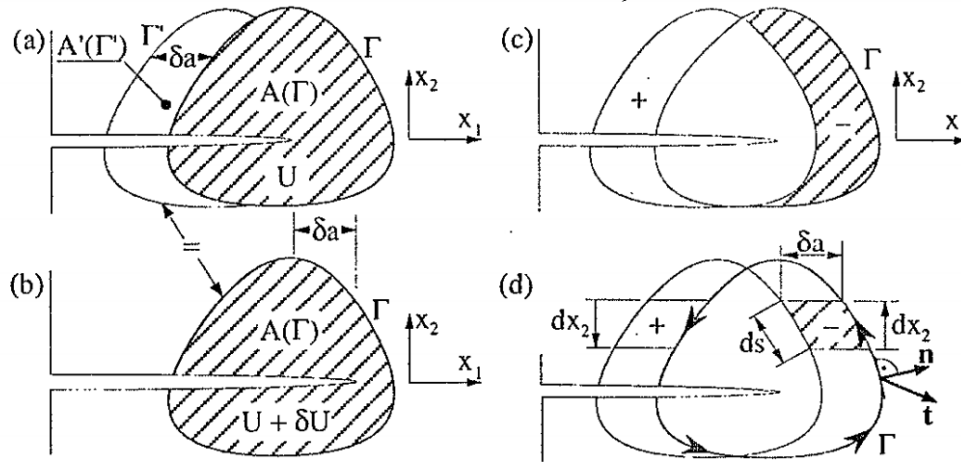
Fig. 2.14: Determination of the variation of elastic energy by the J-integral [10]

Stress intensity factors K_I, K_{II}, K_{III} close to the crack tip are used to determine whether the crack will propagate or not. This factors can be derived from the J-integral for the three known crack modes - normal (I), shear (II) and tearing shear (III) (see figure 2.6). **The fracture toughness** or critical stress intensies K_{Ic}, K_{IIc}, K_{IIIc} are used as an local fracture criterion.

Following pure mode I fracture, the critical stress intensity can be obtained from the Young's modulus E and the mode I fracture energy G_I:

$$K_{Ic} = \sqrt{E \cdot G_I} \qquad (2.17)$$

With this definition, it is possible to formulate the so-called *index fracture criterion in local approach*:

- if $K_I < K_{Ic}$: No crack growth (stable)

- if $K_I = K_{Ic}$: quasi-static crack growth

- if $K_I > K_{Ic}$: dynamic crack growth (unstable)

The same is true for the other two crack modes. Following relationship is given in order to connect mode dependent fracture energy release rates and therefore the stress intensity to Rice's J-integral:

$$J = G = G_I + G_{II} + G_{III} \tag{2.18}$$

Crack Band Model

The crack band model introduced by *Bažant* in 1973 can be seen as a less general concept of a non-local continuum model. The basic concept of this model is that the constitutive stress-strain relation is coupled with a certain crack band width. This width is stated to be a material property.
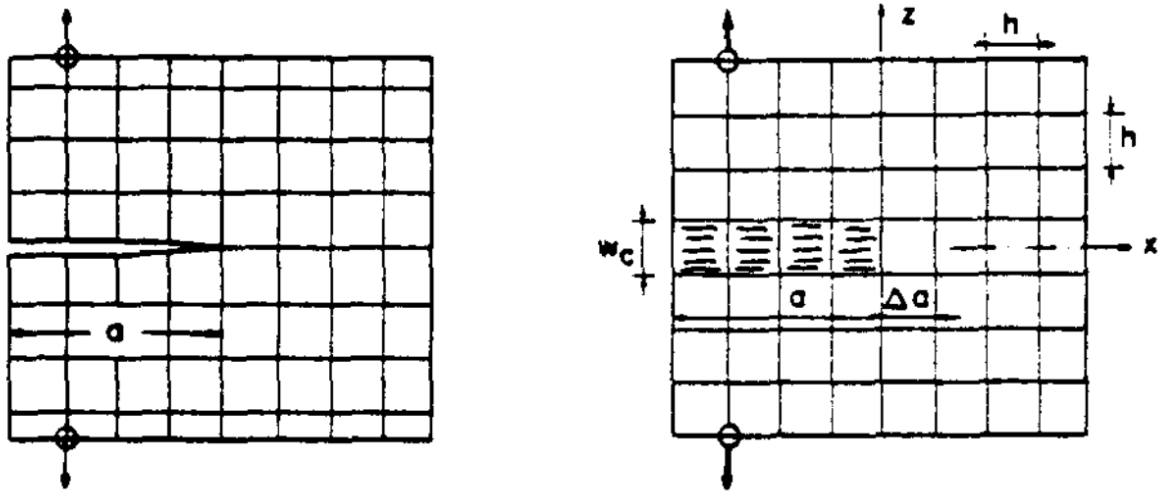
Fig. 2.15: Comparison between a linear crack model and the crack band theory [18]

Fictitious Crack Model
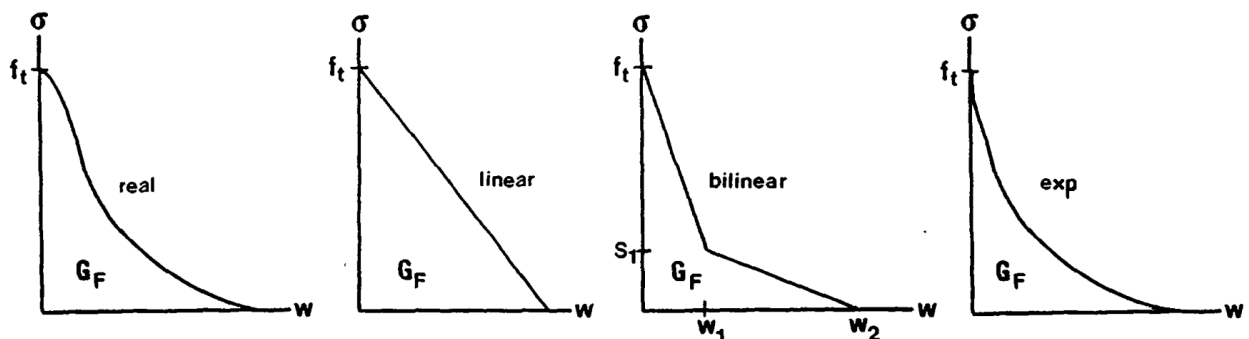
Fig. 2.16: Comparison between actual stress-strain degradation and linear, bilinear and exponential models (taken from [4] and modified)

Based on *Hillerborg*'s idea to introduce a fictitious crack width in order to obtain a fracture energy from a (tensile) stress-strain curve (see 2.1.2). He also introduced a characteristic

length l_{ch} by combining the material properties tensional strength, fracture energy and Young's modulus. This length is a material constant without physical meaning, but it enables the possibility to compare between different concrete mixtures.

$$l_{ch} = \frac{E \cdot G_F}{f_t^2} \tag{2.19}$$
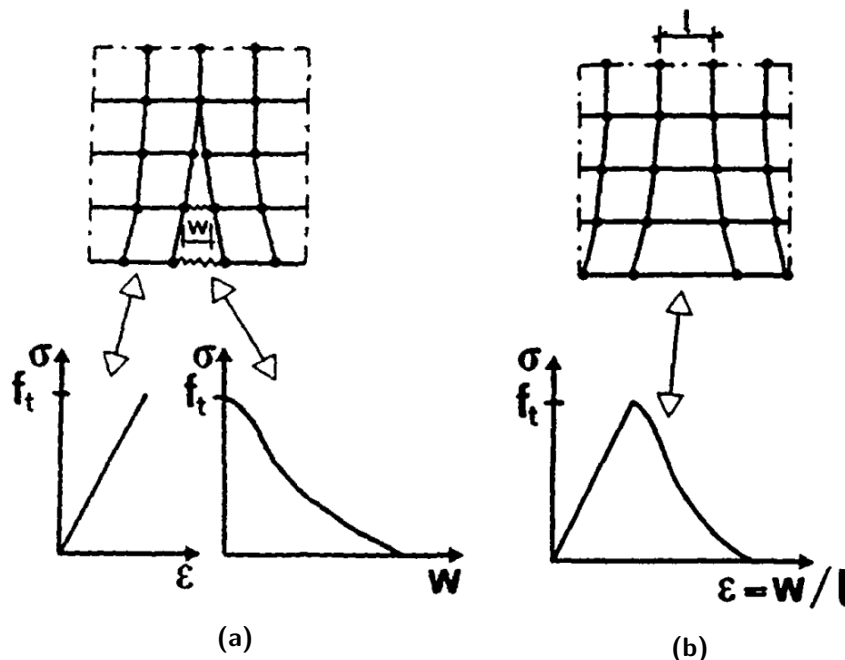
Fig. 2.17: Comparison between **(a)** fictitious crack model and **(b)** crack band theory [4]

Extended Finite Element Method

The extended finite element method is capable of modelling crack-growth due to feasible change of mesh topology. Therefore, it defines a crack criterion - most likely a form of J-integral. Elements which reach this criterion undergo a partition depending on the resulting crack plane. When quasi-brittle materials are to be modelled, some stresses can still be transferred after crack initiation. There the fictitious crack approach can be used after the partition took place.

A short introduction to the Extended Finite Element Method and links to in-depth literature can be found in [19].

Damage

In continuum mechanics damage represent the reduction of the internal integrity of the material due to formulation of cracks or similar defects. Various damage models are available using a so-called damage value. However, the definition of this value depends on the used model and general description of the damage value is difficult. Most commonly, the damage value is used as a linear stiffness reduction of the in the cracking process afflicted elements. As a simple example, the resulting stress of a damaged element may be formulated as (see also figure 2.18):

$$E^{damaged} = (1 - d) \cdot E \tag{2.20}$$

Usually damage is defined as a positive value between zero - representing undamaged state - and one - representing fully damaged state.

However, all models need a damage initiation or yield criterion. This criterion may be strain or stress depending. Commonly used are invariant based criterion like the Drucker-Prager or the Mises-Hencky-Huber criterion. Then, a damage evolution law has to be defined to receive the damage value. This is usually an exponential law with a tangent at one in order to avoid negative values. Finally, the resulting stress can be calculated.

Softening Plasticity

Plasticity models do not reduce the element stiffness but decrease the lasting elastic strains. Simply show, the total strain is a combination of its elastic and plastic part:

$$\varepsilon = \varepsilon^{el} + \varepsilon^{pl} \tag{2.21}$$

The resulting stress is only evaluated based on the elastic strain:

$$\sigma = E \cdot \varepsilon^{el} \tag{2.22}$$

Therefore, softening can be modelled by decreasing the share of elastic strain on the total strain afflicted to the element (see figure 2.18).

Furthermore, plasticity and damage models can be coupled. This is the case for the microplane model provided by *Ansys Mechanical* and is described in chapter 2.2.3.
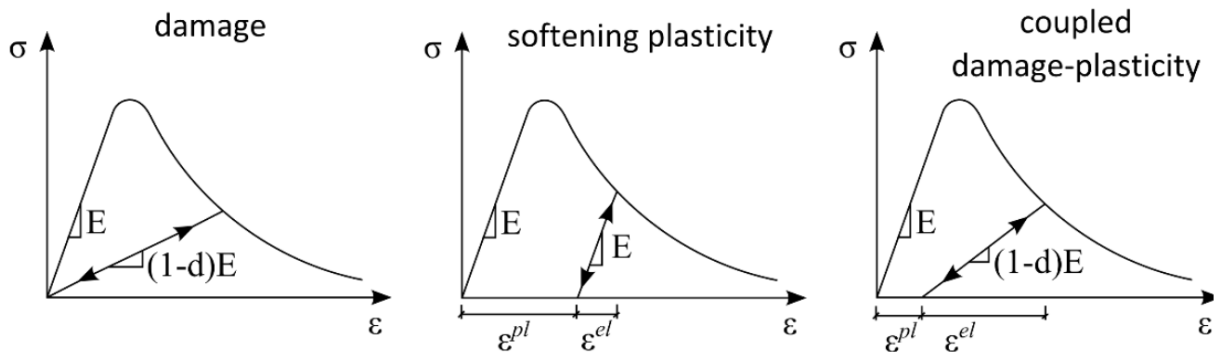
Fig. 2.18: Comparison of the stress-strain relationship of damage and plasticity models in a one dimensional case [20]

2.2 Microplane Material Model

2.2.1 Development

The microplane model has a long history. It was first proposed in 1983 by Bažant [21]. The aim was to describe the elastic and non-elastic behaviour of heterogeneous aggregate materials. For example concrete, rock or sea ice, which can exhibit strain-softening, i.e. declining stress at increasing strain, resulting from a progressive micro-cracking. The model is based on an idea of Taylor [22] from 1938, who described the material behaviour independently on planes with various orientations - the so-called *microplanes*. Since then, the model was enhanced multiple times in order to adapt new features or to overcome numerical problems. On top of that, the enormous increase of available computational power since the 1980s, overcame the performance problems in comparison with the classical tensorial models.
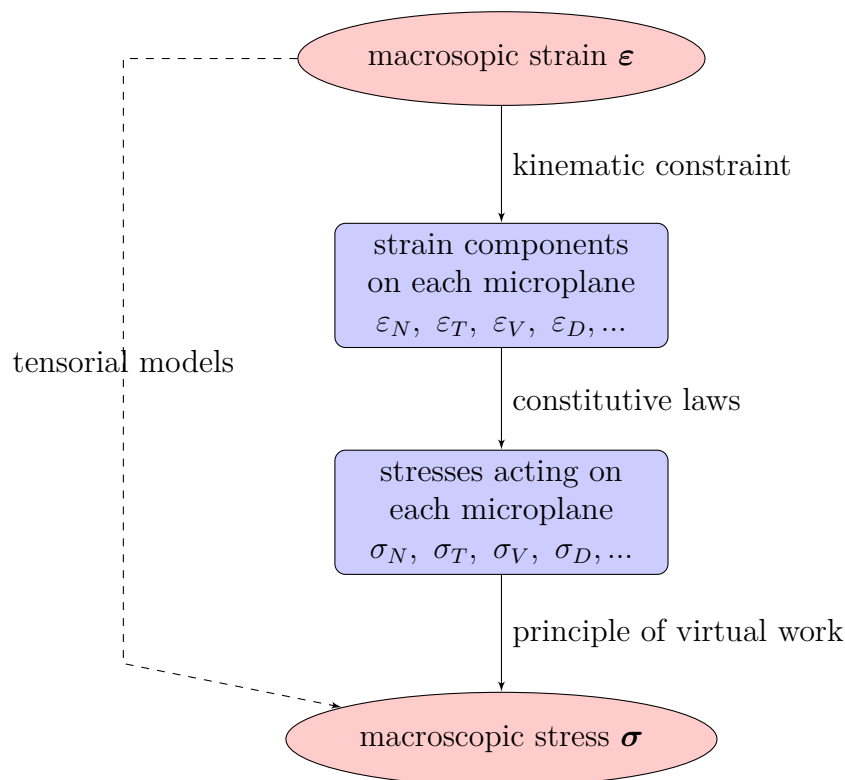
Fig. 2.19: Initial concept of the microplane model

At the beginning the model only considered tensile failure on the microplanes, this concept experienced further improvements over the years. Due to this, various different model types can be distinguished. In the following part, a short overview of the development and different approaches of this model.

The microplane model M1 [23] was only able to represent multi-directional tensile cracking and the post-peak tensile softening of concrete. Acting micro strains are separated into their normal and tangential parts (N-T-split). Next the uni-axial behaviour of the tensile failure is described by using the scalar relation between normal stress and strain. In combination with the crack band model [24] this model was able to simulate size effect on notched concrete specimens.

The model M2 [25] included compressive failure by introducing a volumetric-deviatoric split of the normal strain component acting on the microplanes. This V-D-T-split was necessary due

to the triaxial phenomenon of a compression failure, which is triggered by lateral expansion as well as by slip on inclined planes. However, it lead to a bunch of other problems. Especially, excessive lateral expansion and stress locking in far post-peak uni-axial tension as well as unrealistic unloading and reloading.

The model M3 [26, 27] introduced the concept of stress-strain boundaries (or softening strain-dependent yield limits) in order to avoid difficulties by the modelling of cyclic loading and the handling of the transition from reloading to virgin inelastic loading.

Model M4 [28, 29] improved formulations of boundary surfaces, frictional yield limits and damage, sequential identification of material parameters by data fitting, and a capability to control various response features by material parameters. Furthermore, a work-conjugate definition of the volumetric-deviatoric split was applied. A modified model M4 was introduced which removed the tensile volumetric boundary and the V-D-split of the normal component for dominant tensile failure. This neutralized the difficulties resulting from lateral expansion and stress locking, which were present since model M3.

The latest modification of Baẑant's model, model M7, appended the V-D-split of the normal component for bearing tensile failure, however, it remains in case of compression still using the concept of strain-stress boundaries. A detailed description of this model can be found in [30].

In 2018 Zreid and Kaliske [31] formulated another variant for applying the constitutive laws onto the microplanes. They used a coupled plasticity and damage model with a smooth cap yield function, i.e. a microplane version of the Drucker-Prager yield function. Furthermore, an implicit gradient enhancement eliminated mesh sensitivity and numerical instabilities. This approach also seems to be very rewarding due to the reduced number of material depended parameters, from 29 for model M7 to 12 for the coupled one, a reduced number of history variables per microplane, from 6 to 2.

The microplane model and their variants were based on 3 hypotheses formulated by Baẑant. First the macroscopic stress is sum of a purely elastic macrostress, untouched by inelastic processes on the microplanes, and an inelastic macrostress which represents the stress relaxations from these microplanes. Second the macroscopic strain tensor can be decomposed into normal and tangential microstrain vectors acting on any microplanes, i.e. kinematic constraint. This is the opposite of Taylor's Slip Theory of Plasticity, where microstresses are resolved compounds of the macrostress tensor, i.e. static constraint. Using a kinematic constraint gives the advantage that, in case of strain-softening, only one stress corresponds to a given strain. For a static constraint, on the other hand, two possible strains result from a given stress. The final hypothesis was the existence of an unrelated strain-stress relation on each microplane. These hypotheses lead to multiple advantages. It was now possible to formulate the material constitutive laws for each microplane independently. Hence, there was only a scalar strain-stress relationship rather than the tensorial one from a macroscopic continuum. Furthermore, this approach is capable of describing the fracture formation during rotating principal stress, e.g., during seismic events. Additionally, this gave the possibility to represent multi-surface plasticity with several vectorial limit surfaces. This captured the vortex effect, i.e. the existence of inelastic strain increments by loading to the side (for a more detailed explication of the vertex effect see [32]).

The principle of virtual work is finally used to obtain the acting macroscopic stresses in the continuum. Then as now, this is accomplished by using numerical integration on the surface of a (hemi-)sphere, where the used Gauss points and their weights represent the microplanes.

Because it is already implemented in the *Ansys Mechanical* software, this master thesis will focus on Zreid and Kaliske' coupled model which seems to be the most advanced with significant enhancements compared to its predecessors.

(a)
(b)
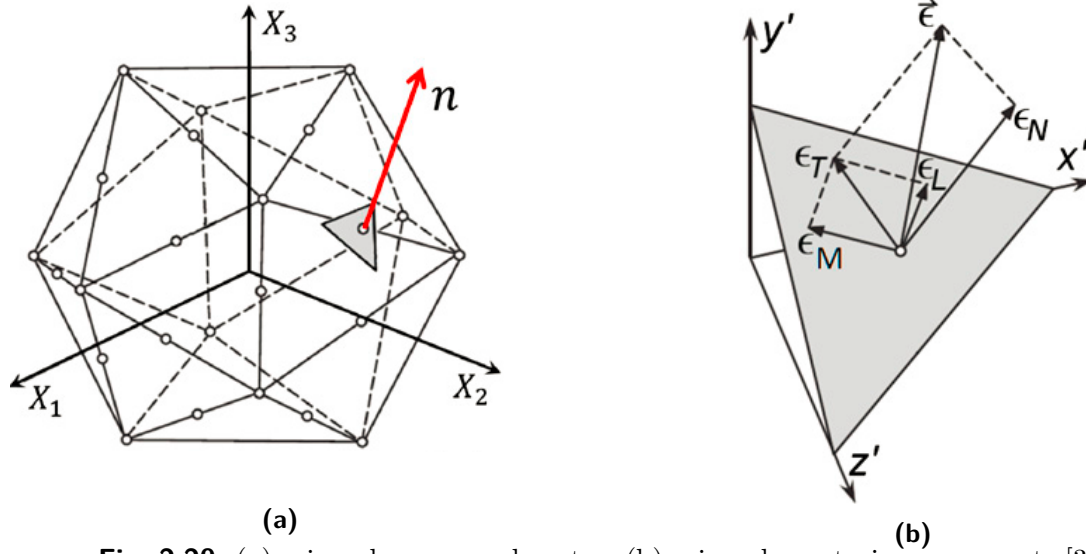
Fig. 2.20: (a) microplane normal vector; (b) microplane strain components [30]

2.2.2 Mechanical Background

Kinematic Constraint

The kinematic constraint - in relation to the microplane model - means that the imaginary microplanes experience the same strain as the material point on a macroscopic level. For the purpose of this work, these material points are chosen to be equal to the integration points of the finite element. Then, an evaluated strain tensor $\boldsymbol{\varepsilon}$ is projected onto a microplane. For this, it is necessary, to introduce the unit normal vector **n** of the microplane. Now it is possible to generate the normal strain vector ε_N.

$$\varepsilon_N = N_{ij}\varepsilon_{ij} \tag{2.23}$$

with

$$N_{ij} = n_i n_j \tag{2.24}$$

The subscript i refers to the global Cartesian coordinates x_i ($i = 1,\ 2\ and\ 3$). Furthermore, the volumetric-deviatoric split of the normal component for the damage softening model under compression need to be computed:

$$\varepsilon_V = \varepsilon_{kk}/3 \tag{2.25}$$
$$\boldsymbol{\varepsilon}_D = \boldsymbol{\varepsilon} - \mathbf{1} \cdot \varepsilon_V \tag{2.26}$$

Where ε_V as the scalar volumetric strain is the same for all microplanes generated from one integration point. The deviatoric strain tensor $\boldsymbol{\varepsilon}_D$ is unique for each microplane is subordinated on the microplane normal vector. Repeating subscripts kk implies summation over $i = 1,\ 2\ and\ 3$.

Constitutive Laws

Constitutive laws describe the material behaviour by giving a relationship between stress and strain. The simplest form would be a purely elastic relations given by Hook's law $\sigma = E \cdot \varepsilon$,

which is used in linear FEM simulations. For concrete this linear relationship exists only within a small range of strain, as it can be seen in Fig. 2.21. Outside this range other phenomenons have to be considered. First, the occurrence of plastic, irreversible deformation (plasticity) by passing the materials yield limit. Second, the reduction of the material's strength after reaching its ultimate stress limits (damage). Additionally, under compression, concrete undergoes a strain-hardening effect (or work hardening), where it deforms plastically with an increase of strength. Under Tension, concrete experience damage as soon it passes its ultimate tensile limit. Furthermore, after the material reaches its ultimate stress limits, the responding stress reduces. This behaviour is called strain-softening (or work softening).

This non-linear material behaviour needs now to be computed into (non-linear) FEM simulation. This happens either through multi-dimensional tensorial models on the macroscopic level, or, a way simpler, by formulating the constitutive laws directly onto microplanes.

Direct Stress-Strain Relationship

If only a uni-axial tension failure on the microplane is reconsidered, a direct stress-strain relationship can be formulated.

Stress-Strain Boundaries

Bažant introduced the concept of stress-strain boundaries into a microplane material model in his model M4 [28]. The underlying idea is, that a stress-strain state either lies inside the boundaries and in the elastic area, or it will be returned onto the stress-strain boundary. Following Fig. 2.22 shows the current strain on a microplane as ϵ^0_{mic} and its resulting stress σ^0_{mic}. If now the strain is further increased with $\Delta\epsilon_{mic}$, the corresponding elastic strain σ^{el}_{mic} would lie outside the boundaries. This stress is now reduced by the value $\Delta\sigma"_{mic}$ onto the boundary. In the model M4 a total of 5 stress-strain boundaries were formulated - normal, deviatoric, volumetric tension, volumetric compression and plastic-frictional. In the model M7, the volumetric and deviatoric boundaries were only applied in compression. Therefore, 4 stress-strain boundaries are remaining.

The calibration of a model using this kind of boundary bears difficulties. In total a number

(a)

(b)
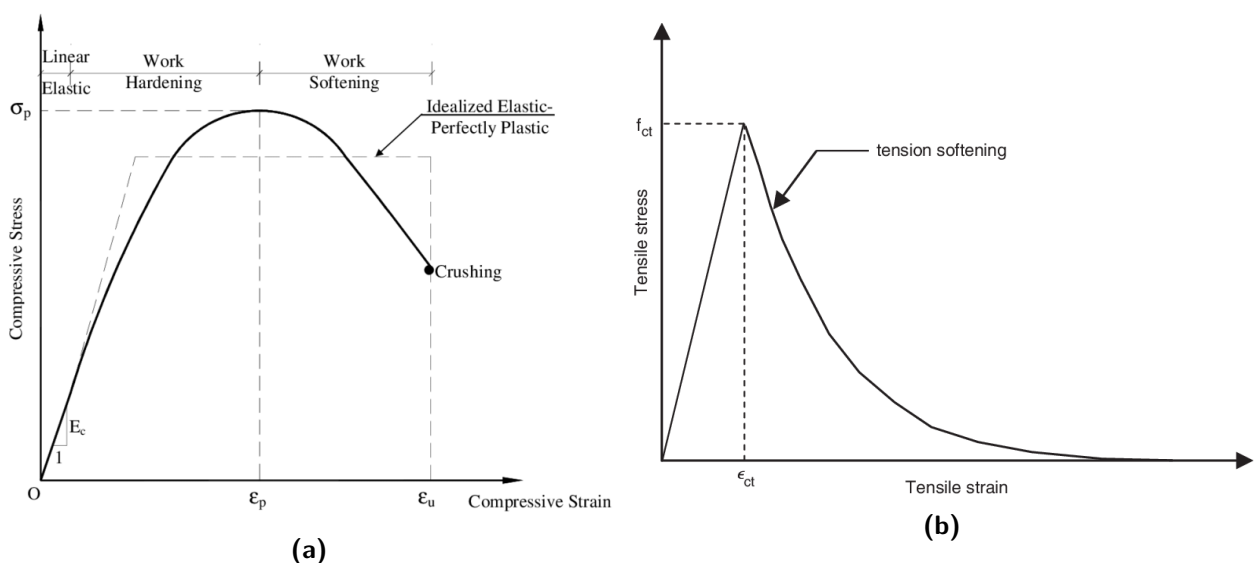
Fig. 2.21: typical behaviour of concrete under (a) uni-axial compression and (b) uni-axial tension
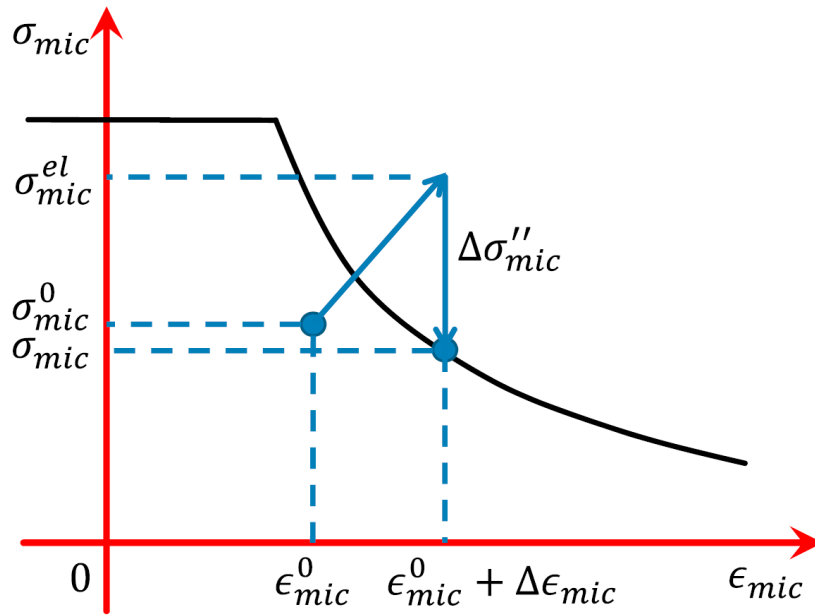
Fig. 2.22: 2-D case of the vertical return to the stress-strain boundary in the case of its exceedance [28]
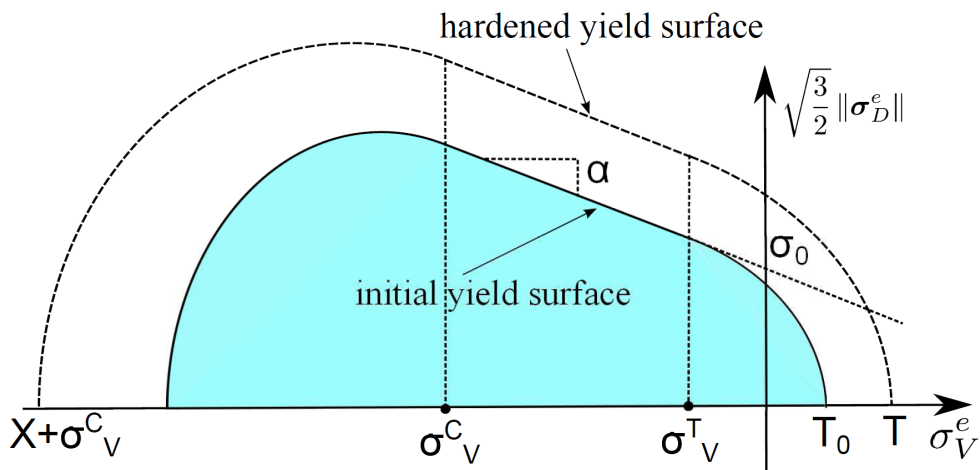
Fig. 2.23: Smooth three-surfaced Drucker-Prager cap yield function [31]

of 29 numerical constants needed to be found. Although Baẑant gives 22 constant as fixed in case of concrete, various test data needs to be fitted in order to obtain satisfying results.

Smooth Drucker-Prager Cap Yield Function

The *initial yield surface* (see Fig. 2.23) limits the elastic behaviour of the material. If the current stress state crosses this limit the hardening process begins. This means plastic deformations occur but the area of elastic behaviour is expanded until it equals the *hardened yield surface*. This new limit shall not be passed by a further increased stress state. It represents the maximum bearable stress state of the material. In a model without damage, the returned stress state would follow the yield surface. With damage on the other hand, the material strength reduces and softening begins.

The Drucker-Prager yield function in terms of microplane stresses defines as follows

$$f^{mic} = \sqrt{\frac{3}{2}\boldsymbol{\sigma}_D \cdot \boldsymbol{\sigma}_D} + \alpha\sigma_V - \left(\sigma_0 + H\kappa^{mic}\right). \tag{2.27}$$

Where H is the hardening stiffness and κ^{mic} the hardening variable. Furthermore, α represents the friction coefficient and σ_0 the initial yield stress.

Thermodynamic Consistency

Two main principles can be used in order to determine equilibrium conditions within the connection of the micro- and macroscopic level. The aim of both is to formulate the overall macroscopic stress in terms of the microscopic strains or stress components onto the microplanes. However, the principle of virtual work was shown to be more costly due to the handling of fourth-order tensors. This is why nowadays the approach with Helmholtz' free energy is used.

Principle of Virtual Work

The virtual work caused by a virtual strain tensor $\delta\boldsymbol{\varepsilon}$ is given by

$$\delta W = \frac{4}{3}\pi\boldsymbol{\sigma}^{mac}\delta\boldsymbol{\varepsilon} = \int_\Omega \boldsymbol{\sigma}^{mic}\delta\boldsymbol{\varepsilon}\,\mathrm{d}\Omega. \tag{2.28}$$

Where $\boldsymbol{\sigma}^{mac}$ is the overall macrostress and $\boldsymbol{\sigma}^{mic}$ are the microscopic stresses onto the microplanes, σ represents the surface of the sphere. Following [33], further computing leads to a fourth order tensor, the so-called tangent stiffness. Although this tensor only has 6 independent values, a numerical integration over the surface of a sphere has to be carried out 6 times in order to obtain them. It seems obvious why this approach was dropped for the formulation through the free energy.

Helmholtz' Free Energy

Helmholtz' free energy Ψ (also F or A is used) is defined from the internal energy of the system U, its absolute temperature T and its entropy S.

$$\Psi = U - TS \tag{2.29}$$

It measures the obtainable work from a closed thermodynamic system at constant volume. In order to obtain a thermodynamically consistent model, the macroscopic free energy needs to be computed as an integral of microplane free energies over the surface of a sphere. Due to the constant temperature on micro- and macroscopic level the entropy terms cancels out and only the inner energy remains:

$$\Psi^{mac} = \frac{3}{4\pi} \int_\Omega \Psi^{mic}\mathrm{d}\Omega \tag{2.30}$$

where, the free energy at each microplane including plasticity (see [34]) is

$$\Psi^{mic} = \frac{1}{2}K^{mic}\left(\varepsilon_V - \varepsilon_V^{pl}\right)^2 + G^{mic}\left(\boldsymbol{\varepsilon}_D - \boldsymbol{\varepsilon}_D^{pl}\right) \cdot \left(\boldsymbol{\varepsilon}_D - \boldsymbol{\varepsilon}_D^{pl}\right) \tag{2.31}$$

with

$$K^{mic} = 3K = \frac{E}{(1 - 2\nu)} \tag{2.32}$$

$$G^{mic} = G = \frac{E}{2(1 + \nu)} \tag{2.33}$$

Where $\boldsymbol{\varepsilon}_D$ is the deviatoric strain tensor, ε_V the volumetric strain within the elastic range and, with the superscript ^{pl}, their plastic counterparts. The elastic microplane material constants are related to the macroscopic bulk and shear moduli K and G (as shown in [31]). Furthermore, they can be expressed through Poisson's ratio ν and Young's modulus E.

The stress components on the microplane derivatives from this expression for the free energy as follows

$$\sigma_V = \frac{\partial \Psi^{mic}}{\partial \varepsilon_V} \tag{2.34}$$

$$\boldsymbol{\sigma}_D = \frac{\partial \Psi^{mic}}{\partial \boldsymbol{\varepsilon}_D} \tag{2.35}$$

Then integration of the stresses over all microplanes leads to the homogenized stress as

$$\boldsymbol{\sigma} = \frac{3}{4\pi} \int_\Omega \left[K^{mic} \boldsymbol{V} \left(\varepsilon_V - \varepsilon_V^{pl} \right) + 2G^{mic} \boldsymbol{Dev}^T \cdot \left(\boldsymbol{\varepsilon}_D - \boldsymbol{\varepsilon}_D^{pl} \right) \right] \mathrm{d}\Omega \tag{2.36}$$

Integration of a (Hemi-)Sphere

Numerical integration of microscopic stresses σ^{mic} over the surface of a unit sphere Ω leads to the macroscopic quantity σ^{mac} times its unit volume through:

$$\underbrace{\frac{4\pi}{3}}_{\text{unit volume}} \sigma^{mac} = \int_\Omega (\sigma^{mic}) \mathrm{d}\Omega \tag{2.37}$$

Because an analytical solution is not available, a numerical integration scheme has to be used:

$$\frac{3}{4\pi} \int_\Omega (\bullet) \mathrm{d}\Omega = \sum_{mic=1}^n (\bullet) w^{mic} \tag{2.38}$$

where n is the number of microplanes and w^{mic} their numeric weight respectively. Needless to say that this integration has to be very efficient, because this process must be done for every integration point in the macroscopic model. Bažant published a study regarding efficiency of numerical integration schemes [35]. The study compared resulting stress response for uni-axial stress applied in various directions using different integration schemes. As a result stress-strain curves are plotted and compared. Bažant recommended the usage of the 21-integration point set fully symmetric (representing a total of 42 microplanes due symmetry). However, another recommendation of [30] favoured the usage of the 37-integration point set fully symmetric (equals 74 microplanes) due to the better accuracy in far post peak softening. Both point sets were derived from Taylor expansion of the analytical sphere integral until the 9th grade. The results from Bažant's study is shown in figure 2.24

(a)

(b)
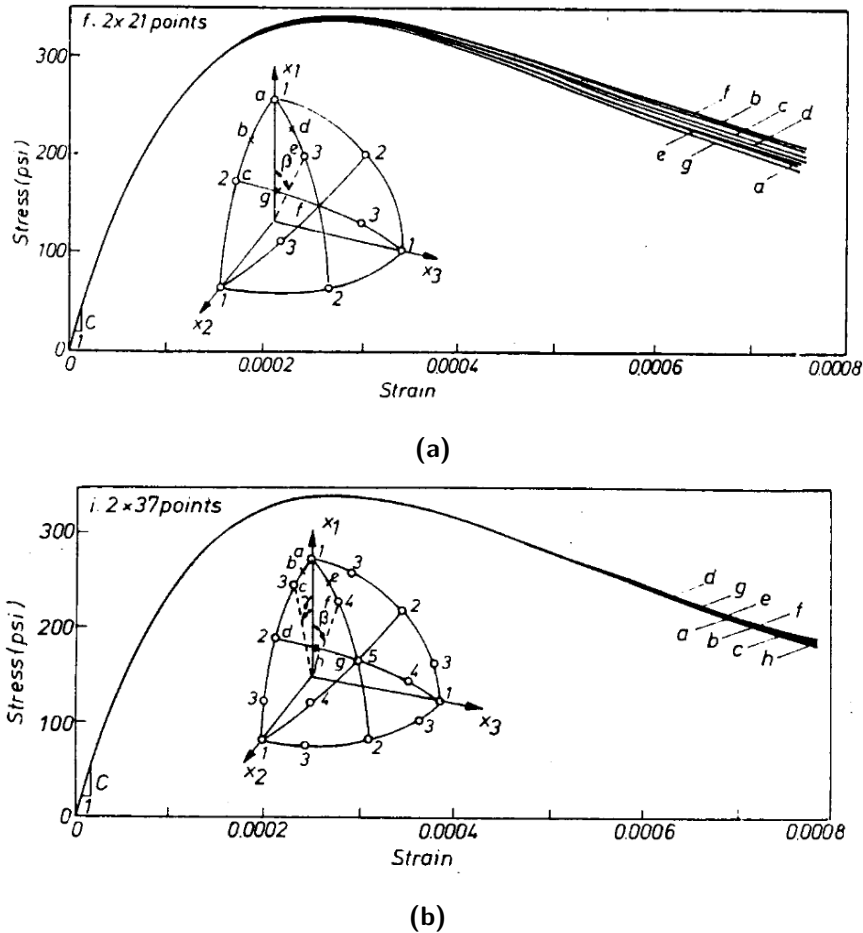
Fig. 2.24: Resulting stress-strain curves obtained by different integration schemes of a hemisphere. The scheme uses the **(a)** 42-point set and **(b)** 72-point set with symmetric formula [35]

2.2.3 Microplane Models in *Ansys Mechanical*

Two different microplane models are avaiable in *Ansys Mechanical*. However, both are only accessible through console commands and don't show up in the graphical user interface. Also, solution quantities like damage variables are not available in the GUI, although they can be accessed via APDL scripting.

This part should give an overview on the input parameters needed. Calibration attempts are presented in detail in chapter 4.3.

Elastic Microplane Model considering Damage

This model is available for elements of type: three-dimensional *SOLID65, SOLID185, SOLID186* and *SOLID187* as well for two-dimensional *PLANE182, PLANE183* and *PLANE185*.

A simplified work-flow is displayed in figure 2.25. A transformation matrix (kinematic constraint) links the macroscopic strain in a point with the microscopic strains on each microplane. Onto each plane the strain is split into its volumetric and deviatoric part. For this variant, the yield criteria is formulated in terms of the first and second invariant of the obtained strains. This yield criteria defines the elastic range and when damage initiates.

The exponential damage law itself is controlled by the equivalent strain energy obtained from the strain invariants. In combination with Hook's law, the microplane stress is calculated.

Finally, integration of all microplane stresses over the unit sphere leads to macroscopic stress, where the reaction force for the Newton-Raphson solver can be obtained.
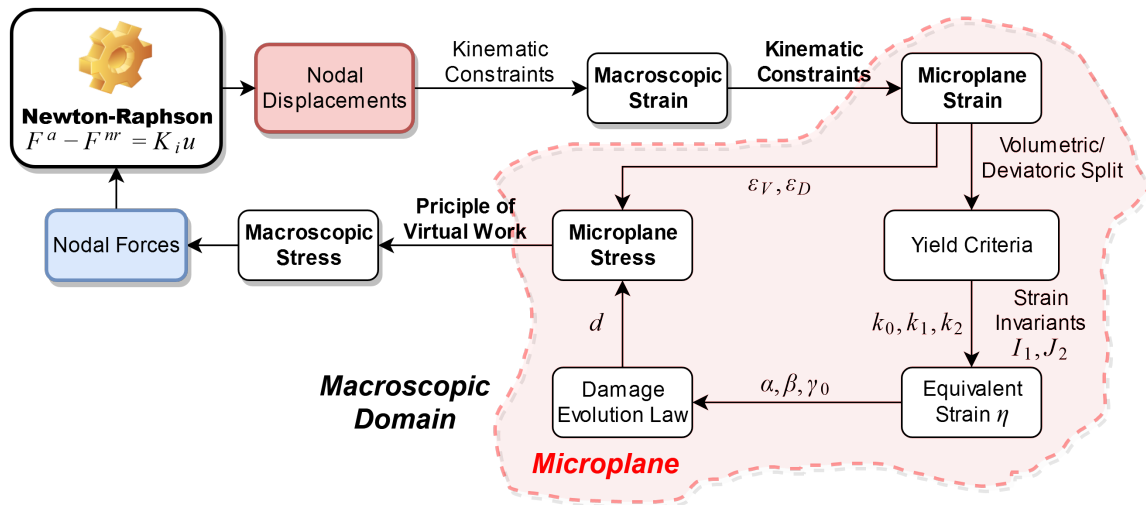
Fig. 2.25: Simplified work-flow of the elastic microplane based on the description in *Ansys Help System* under *Microplane Model formulation*

Parameter Subtype	Parameter	Description
Elasticity		
	E	Modulus of elasticity
	ν	Poisson's ration
Damage		
	k_0	Damage function constant
	k_1	Damage function constant
	k_2	Damage function constant
	γ^{mic}	Critical equivalent strain
	α^{mic}	Maximum damage parameter
	β^{mic}	Scale for rate of damage

Tab. 2.1: Elastic microplane model parameters

The elasticity material parameters can be obtained from uniaxial test. The Drucker-Prager criterion defines the form of the damage function by giving values for $k_0 > 0$, $k_1 = 0$ and $k_2 = 1$. Alternatively, the Mises-Hencky-Huber criterion for brittle materials can be used with $k_0 = k_1 = 0$ and $k_2 = 1$.

Coupled Damage-Plasticity Microplane Model

This variant was developed from *Zreid* in cooperation with *Ansys Corporation*. A detail description of the model can be obtained from [31]. Aim was the introduction of a non-local interaction in order to gain mesh independent results.

The model is only available with coupled pore-temperature elements like: three-dimensional *CPT214, CPT215, CPT216* as well for two-dimensional *CPT211, CPT212* and *CPT213*.

However, downside of the two-dimensional elements is that they are only capable of modelling in plane strain.

As for the simple elastic model before, figure 2.26 gives an overview from the model's work-flow. Again a transformation matrix is used to determine the volumetric and deviatoric parts of the macroscopic strain lasting onto each microplane. As the yield criteria, a Drucker-Prager function is implemented. Because for this model it is formulated in terms of stress, a stress return algorithm is necessary. However, a detailed description of this algorithm can be obtained in the model's paper [31].

The volumetric plastic strain rate is calculated from the strain of the previous step. These rates are used to obtain an equivalent strain, one representing compressive loading during the step and the other one tensile loading. From these equivalent strains the mean over all microplanes is calculated. This mean serves as an input for the implicit gradient regularization. From this regularization the non-local counterpart of the equivalent strains is obtained.

Linear combination of the equivalent strain's local and non-local part leads to the modified equivalent strains. These modified versions then control the exponential damage laws - still split into compressive and tensile fragments.

In order to represent crack closure during compressive loading, a weighting factor calculated from the principle microplane strains is introduced. This factor governs the intensity of the tensile damage.

The overall damage leads then in combination with Hook's law to the microplane stresses. Finally, integration of all microplane stresses over the unit sphere leads to macroscopic stress, where the reaction force for the Newton-Raphson solver can be obtained.
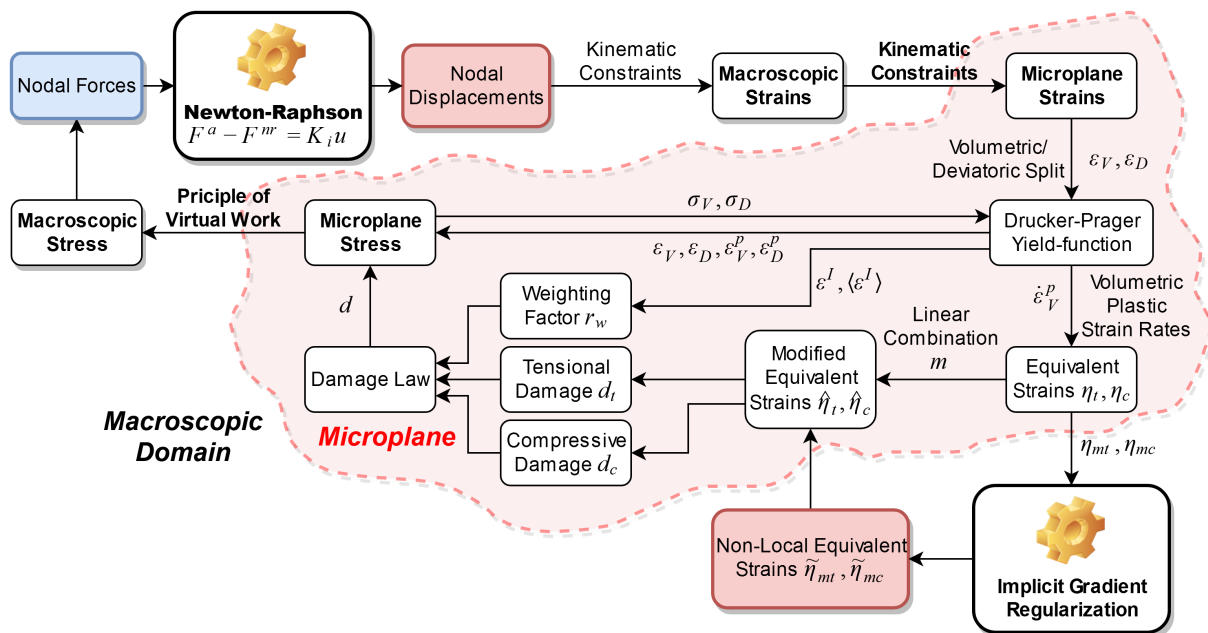
Fig. 2.26: Simplified work-flow of the coupled damage-plasticity microplane based on the description in *Ansys Help System* under *Microplane Model formulation*

Parameter Subtype	Parameter	Description
Elasticity		
	E	Modulus of elasticity
	ν	Poisson's ration
Plasticity		
Drucker-Prager yield function	f_{uc}	Uniaxial compressive strength
	f_{bc}	Biaxial compressive strength
	f_{ut}	Uniaxial tensile strength
Compression cap	σ_V^C	Intersection point abscissa between compression cap and Drucker-Prager yield function
	R	Ratio between the major and minor axes of the cap
Hardening	D	Hardening material constant
	R_T	Tension cap hardening constant
Damage		
	γ_{t0}, γ_{c0}	Tension and compression damage thresholds
	β_t, β_c	Tension and compression damage evolution constants
Nonlocal		
	c	Nonlocal interaction range parameter
	m	Over-nonlocal averaging parameter

Tab. 2.2: Coupled damage-plasticity model parameters

Elastic parameters, *Poission' ratio* and *Young's modulus*, define the linear elastic behaviour of the model. They can be obtained from common test performed on concrete, e.g. uni-axial compressive or uni-axial tension test. They can also be obtained from literature. **Plastic parameters** define the used Drucker-Prager yield function onto the microplanes. Although it is recommended to obtain parameters for *uni-axial compression strength*, *uni-axial tension strength* and *bi-axial compression strength* directly from testing, some relationships can be shown for concrete :

$$f_{bc} = 1.15 f_{uc} \tag{2.39}$$

$$f_{ut} = 1.4(f_{uc}/10)^{2/3} \tag{2.40}$$

Due to the linear range of the Drucker-Prager function is only defined by the compressive entities f_{uc} and f_{bc}, dilation angle and cohesion can be obtained by:

$$\alpha = \frac{\sqrt{3}(f_{bc} - f_{uc})}{2f_{bc} - f_{uc}} \tag{2.41}$$

$$\sigma_0 = \left(1/\sqrt{3} - \alpha/3\right) f_{uc} \tag{2.42}$$

The *intersection point* between the compression cap and the Drucker-Prager function can be obtained from triaxial testing. If this test is unavailable, the point can be set directly after the bi-axial strength point:

$$\sigma_V^C = \frac{2}{3} f_{bc} \tag{2.43}$$

Although a well described procedure exists for the calibration of this model variant, obtaining the necessary data to represent dam concrete is difficult. Firstly, the minimum required data for a fit, i.e. uni-axial tension and uni-axial compression test data, could not be obtained from literature. This kind of data exists very sparely for large aggregate concrete. One reason for this may be that the required specimen size for a representative test should be at least 10 times the maximum grain size. The maximum grain size for dam concrete is up to 150 mm (acc. to *The Concrete Society*) which results in a minimum specimen size of 1.5 m. It may not be difficult to imagine that the performance a test on such a large specimen longs for special machinery which inflicts high costs. Another problem is the determination of the non-linear interaction range parameter. This parameter results from the effective width of the fracture process zone, which, according to Bažant [12], can be approximated as:

$$l \approx 2.7 \cdot D_{max} \tag{2.44}$$

This formulation depends only on the maximum grain size D_{max} and was only obtained from tests performed on normal sized concrete. However, it still lacks the validation for large grain sizes. **Damage Evolution Law** The damage in this model is split into compressive and tensile damage. The total damage d^{mic} on each microplane is then given by:

$$(1 - d^{mic}) = (1 - d_c^{mic}) \cdot (1 - r_w d_t^{mic}) \tag{2.45}$$

$$\tag{2.46}$$

Where d_c, d_t are the damage variables and r_w is the split weight factor. The exponential damage evolution law is then given separately as:

$$\mathrm{d}_t^{mic} = 1 - \exp(-\beta_t \gamma_t^{mic}) \tag{2.47}$$

$$\mathrm{d}_c^{mic} = 1 - \exp(-\beta_c \gamma_c^{mic}) \tag{2.48}$$

Where β_t, β_c are the damage evolution parameters and γ_{t0}, γ_{c0} are equivalent strains controlling the damage development. The splitting factor r_w is given from the positive part of the strain tensor principle values $\langle \varepsilon^I \rangle$ and the absolute principle strain $|\varepsilon^I|$:

$$r_w = \frac{\sum_{I=1}^{3} \langle \varepsilon^I \rangle}{\sum_{I=1}^{3} |\varepsilon^I|} \tag{2.49}$$

Figure 2.27 shows a complete hysteresis loop starting with tensile loading obtained from the microplane model. Figure 2.28 follows the total damage evolution during this loop. It can be seen that the weighting factor r_w needs time to reach its maximum during uni-axial tensile loading. It stays fully active until compressive loading initiates leading to a harsh degradation below 40% although it never becomes zero. After the compressive peak, the factor starts growing again until it reaches again its maximum when tensile loading begins.
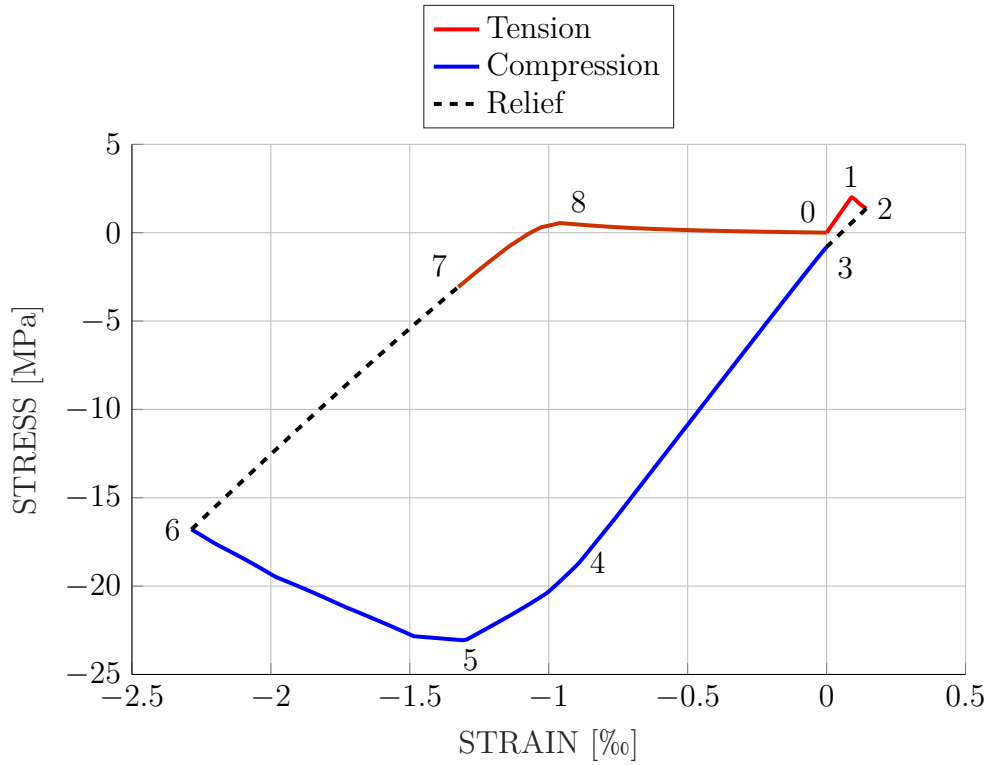
Fig. 2.27: Hysteresis loop obtained by the coupled damage-plasticity microplane model
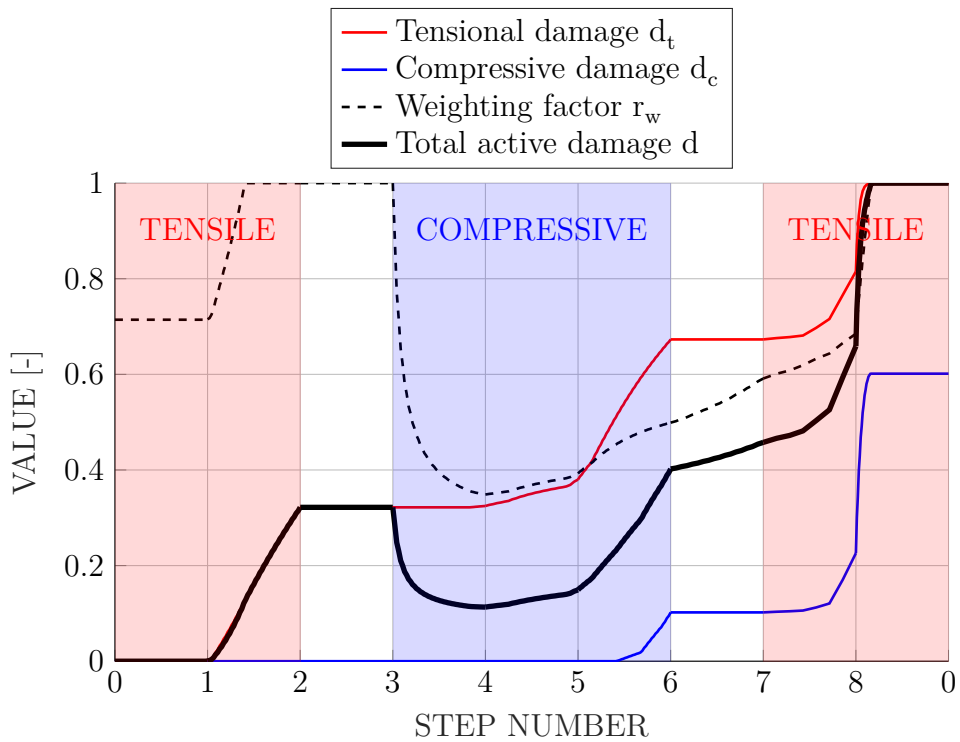
Fig. 2.28: Damage evolution while undergoing a cyclic deformation

Non-Local Gradient Enhancement The used non-local gradient enhancement modifies the equivalent strains which control the damage evolution. The resulting strains are then the weighted sum of the non-local strains $\overline{\eta}$ and the local one η. The non-local strains are obtained

from the Helmholtz equation with Neumann boundary conditions:

$$\bar{\eta} - c\nabla^2\bar{\eta} = \eta \tag{2.50}$$

$$\nabla\bar{\eta} \cdot \mathbf{n}_b = 0 \tag{2.51}$$

The local strain, obtained at every integration point i given by the integral over a unit sphere:

$$\eta = \frac{1}{4\pi}\int_{\Omega}\eta^{mic}\mathrm{d}\Omega \tag{2.52}$$

Then the modified strain $\hat{\eta}$ at any microplane is given by:

$$\hat{\eta}^{mic} = m \cdot \bar{\eta} + (1 - m) \cdot \eta^{mic} \tag{2.53}$$

Where m is a numerical parameter which controls the influence of the non-local interaction (normally $m = 2.5$). Finally, the equivalent strain, which serves as an input to the damage evolution law, is:

$$\gamma^{mic} = \left\{ \begin{array}{ll} \hat{\eta}^{mic} - \gamma_0 & \hat{\eta}^{mic} > \gamma_0 \\ 0 & \hat{\eta}^{mic} \leq \gamma_0 \end{array} \right. \tag{2.54}$$

This procedure is applied to the compressive and tensile behaviour. Therefore, two additional degrees of freedom are needed to be provided. These two DoFs are the non-local enhanced strain for tension and compression $\bar{\eta}_t$ and $\bar{\eta}_c$. The results for these DoFs are accessible in *Ansys Mechanical* via the non-local-field values (GFV).

3 Structural Dynamics

The following chapter is based on *Fundamentals of structural dynamics* [36] by *R. R. Craig* and *Dynamics of structures: theory and applications to earthquake engineering* [37] by *A. K. Chopra.*
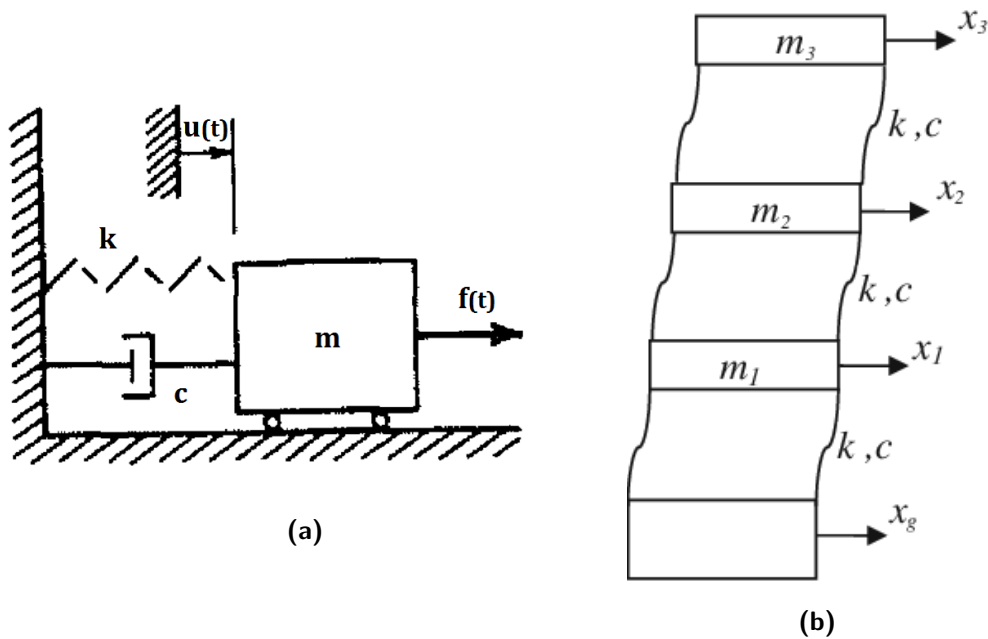
Fig. 3.1: Example of **(a)** single degree and **(b)** multiple degree of freedom system [36]

3.1 Single Degree of Freedom Systems (SDoF)

The governing differential equation for a damped single degree of freedom system is given by:

$$m\ddot{u} + c\dot{u} + ku = f(t) \tag{3.1}$$

3.1.1 Physical properties of the System

▷ **Mass**
It represents the mass of the system. It can be discrete or continuous.
▷ **Stiffness**
It represents the resistance of the system against deformation. It can be discrete (e.g. springs) or continuous (e.g. bending beam).
▷ **Undamped natural frequency**
Undamped natural frequency or fundamental frequency is one of the two key parameters for dynamic analysis of a system.

$$\omega_n = \sqrt{\frac{k}{m}} \ \ [\text{rad/s}] \qquad f_n = \frac{\omega_n}{2\pi} \ \ [\text{Hz}] \tag{3.2}$$

▷ **Viscous damping factor**

The viscous damping factor is the second key parameter. It is defined as the ratio between the system's damping factor c and the critical damping factor c_r

$$\zeta = \frac{c}{c_r} \;\; [\text{-}] \tag{3.3}$$

where:

$$c_r = 2m\omega_n = 2\sqrt{km} \tag{3.4}$$

The magnitude of the damping factor can be distinguished in three cases: *underdamped* $(0 < \zeta < 1)$, *critically damped* $(\zeta = 1)$ or *overdamped* $(\zeta > 1)$. The final two cases lead to an extinction without oscillation. Structural analysis normally only deals with underdamped systems.

▷ **Damped natural frequency**

For damping factors smaller than 5% - like it is the case for most structures - it can be seen as equal to the undamped natural frequency. Otherwise, it is determined through:

$$\omega_d = \omega_n\sqrt{1 - \zeta^2} \;\; [\text{rad/s}] \tag{3.5}$$

▷ **Natural period**

The natural period can either be undamped or damped. Can be determined directly from the natural frequency.

$$T_n = \frac{1}{f_n} \;\; [\text{s}] \tag{3.6}$$

$$\tag{3.7}$$

They represent the physical properties of the system and are determined at the beginning of the calculation. For linear systems, mass and stiffness are constant over time. For non-linear systems, stiffness and/or mass changes with time.

3.2 Multiple Degrees of Freedom Systems (MDoF)

MDoF systems cover multiple lateral and rotational movements of the discretized system. In FE-analysis, the number of degree of freedoms depend on the number of nodes and the individual freedom of the nodes. E.g. a discretized system consisting of n nodes which allows only horizontal and vertical movement, has a total of $2 \cdot n$ degrees of freedom. The governing differential equation for a damped multiple degree of freedom system is given by:

$$\boldsymbol{M}\ddot{\mathbf{u}} + \boldsymbol{C}\dot{\mathbf{u}} + \boldsymbol{K}\mathbf{u} = \mathbf{f}(t) \tag{3.8}$$

Where $u, \dot{u}, \ddot{u}$ are the displacement vector and its time derivatives of size $m \times 1$ with m is the number of degree of freedoms. The mass matrix $\boldsymbol{M}$ is usually a diagonal matrix of size $m \times m$ The stiffness matrix $\boldsymbol{K}$ is usually a spares matrix with entries close to its main diagonal. Because the damping matrix $\boldsymbol{C}$ cannot be derived directly from the physical and geometrical properties of a system, different approaches have to be taken. Some of them are presented in the following section. On the right hand side, the force vector $\mathbf{f}$ describes the external loading.

3.2.1 Damping of MDoFS
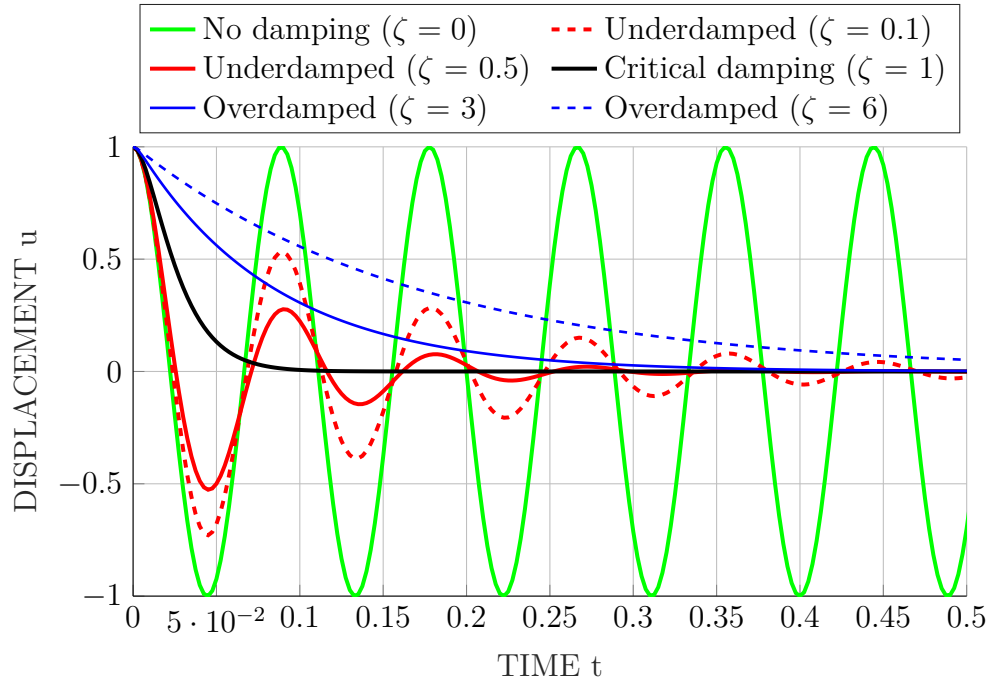
Fig. 3.2: Response of a SDoF system to an initial displacement with different damping ratios

There are various ways to determine a damping matrix. If it is formulated in the physical domain, it is called physical damping matrix. To obtain it in the domain of principal coordinates, this physical damping matrix must be transformed into the generalized one using system's modal matrix.

3.2.2 Modal Damping

Modal damping is only applicable on linear systems using modal superposition. The damping ratio is defined for every decoupled system separately so that:

$$\mathbf{C} = \mathbf{\Phi}^T \mathbf{C} \mathbf{\Phi} = diag(c_j) = diag(2\zeta_j \omega_j m_j) \tag{3.9}$$

Where j is the index for the decoupled degree of freedom.

3.2.3 Non-proportional Damping

Non-proportional damping is also only applicable on linear systems using modal superposition. It couples the undamped normal modes leading to the generalized damping matrix will not become diagonal. It appears e.g. as shock absorbers in automotive vehicles. It usually not occurs in structural analysis.

3.2.4 Proportional Damping

Proportional damping is the simplest way to assume damping matrix $\boldsymbol{C}$. It is stated to be directly proportional either to the mass matrix or the stiffness matrix.

$$\boldsymbol{C} = a_0 \boldsymbol{K} \qquad \boldsymbol{C} = a_1 \boldsymbol{M} \tag{3.10}$$

The mass-proportional variant leads to very high damping in the lower frequency range and almost zero damping at higher frequencies. The stiffness-proportional variant leads to a linear increasing damping ratio (see Fig. 3.3a).

3.2.5 Rayleigh Damping
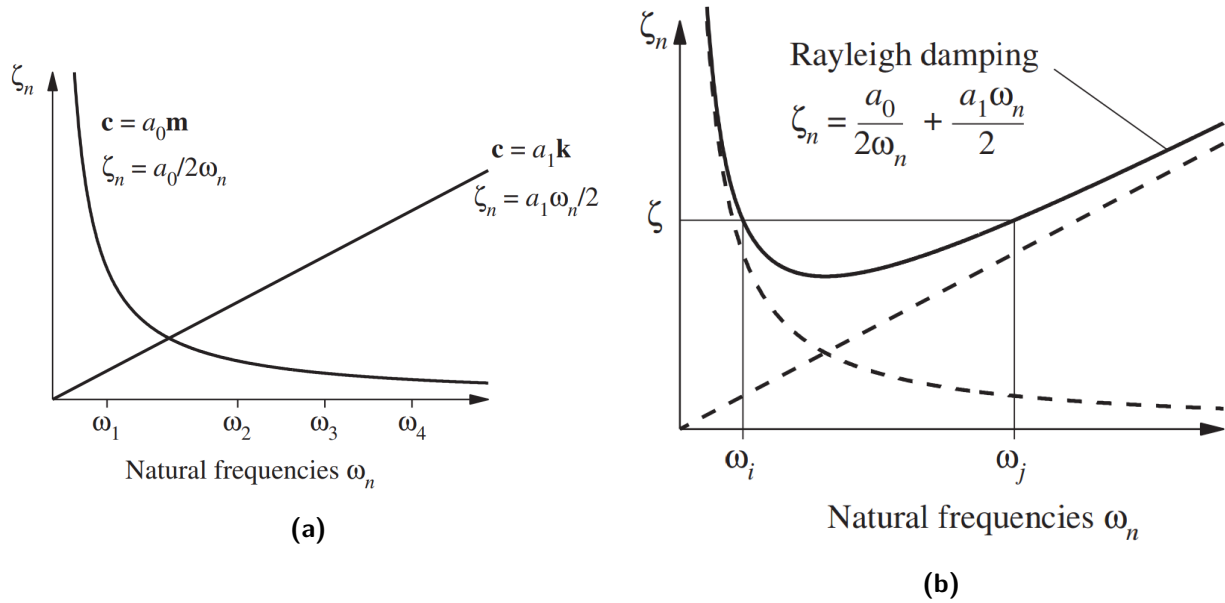
Fig. 3.3: Determination of Rayleigh damping constants [37]

Rayleigh damping is a combination of mass-proportional and stiffness-proportional damping.

$$\boldsymbol{C} = a_0\boldsymbol{K} + a_1\boldsymbol{M} \tag{3.11}$$

The underlying idea is the definition of the damping ratio on two different natural frequencies of the system. The dependency on mass and stiffness matrices leads the damping ratio for frequencies lower than ω_i to follow nearly mass proportional damping and for frequencies higher than ω_j stiffness damping respectively. Frequencies in between undergo damping lower than the chosen damping ratio ζ.

$$\zeta = \frac{1}{2}\left(\frac{a_0}{\omega_n} + a_1\omega_n\right) \tag{3.12}$$

$$a_0 = \zeta\frac{2\omega_i\omega_j}{\omega_i + \omega_j} \qquad a_1 = \zeta\frac{2}{\omega_i + \omega_j} \tag{3.13}$$

Due its simplicity and the applicability in mode superposition it is the most common way to assume a damping matrix.

3.2.6 Caughy Damping
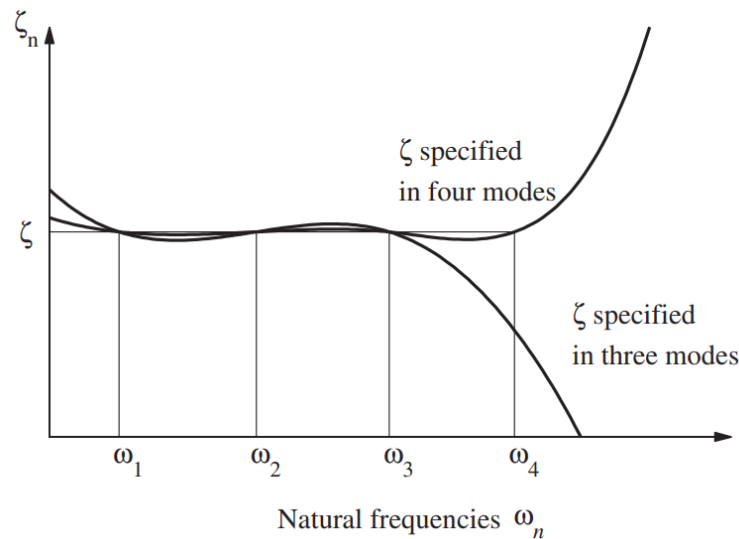
Fig. 3.4: Determination of Caughy damping constants [37]

Caughy damping is a modification of the Rayleigh damping so that the damping ratio can be defined in more than two modes.

$$\boldsymbol{C} = \boldsymbol{M} \sum_{k=0}^{n-1} a_k \left(\boldsymbol{m}^{-1} \boldsymbol{K} \right)^k \qquad \zeta_n = \frac{1}{2} \sum_{k=0}^{n-1} a_k \omega_n^{2k-1} \tag{3.14}$$

where n specifies the number of selected modes and ζ is the modal damping ratio.

3.3 Excitations

The most common form of excitations are either forces, movement or acceleration. Depending on their type, different solution options are available. They can then separated into following types:

Free vibration: If no excitation is given in any form, the system enters the state of free vibration. Its response only depends on the given initial conditions, e.g. displacement.

Harmonic excitation: Main type of excitation for simple models, it is always the goal to transform more complex types of excitation into a harmonic ones. Excitation follows a sinusoidal path. Resonance occurs when excitation frequency equals the natural frequency of the system.

Periodic excitation: Excitation repeats itself after a defined time period. Because there is no restriction to the length of the period, even a whole time-history record of an earthquake can be seen as one period.

Non-periodic excitation: Excitation which does not repeat after a certain amount of time (e.g. impulses, earthquakes).

For seismic analysis of dam structures mainly non-periodic excitations are used. Depending on the problem to be modelled, they should be representative for the site's seismic conditions and in tone with local regulations. Also, it is common to expose a model to specific recorded or artificial signals in order to compare results obtained by different models (so the case in 15th ICOLD benchmark workshop on numerical analysis of dams in Milan 2019 [38]).

3.3.1 Recorded Signals

One type of excitation used for seismic analysis is a recorded signal of an actual earthquake. However, these signals vary drastically in their duration, maximum excitation and distribution in the frequency domain. For a first comparison between systems, the system's response to one of those signals can be used. As an example, the response of a single degree of freedom system to two famous earthquakes - *El Centro 1940*, which is the first recorded earthquake in history and *Friuli 1976*, which is close to the Austrian border - with various damping ratios are shown in the figures below.
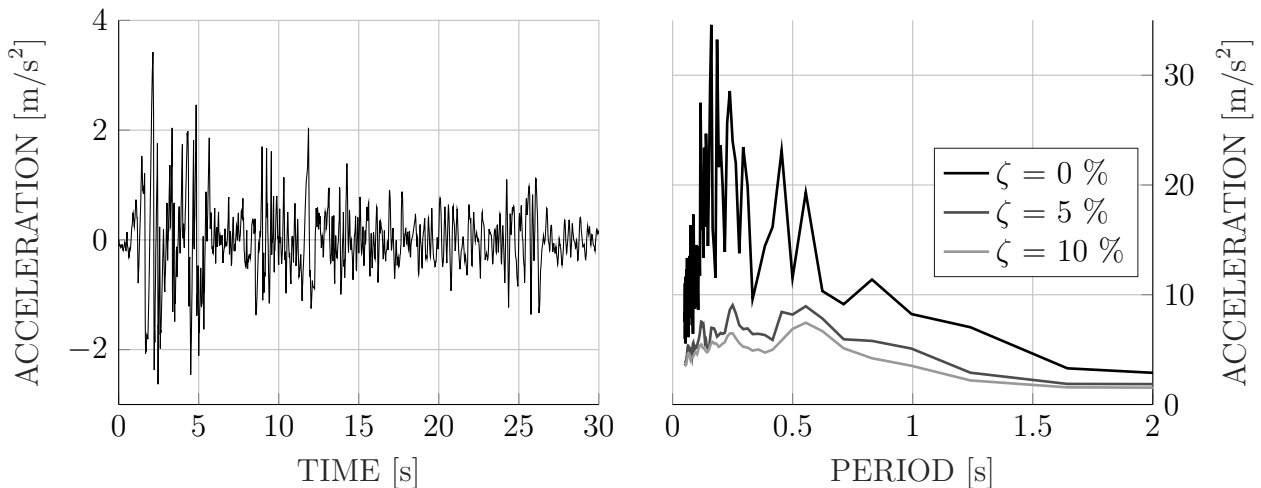
Fig. 3.5: Recorded acceleration time history a response spectra for various damping ratios of El Centro earthquake in Central Valley (Mexico, USA) of May 18, 1940
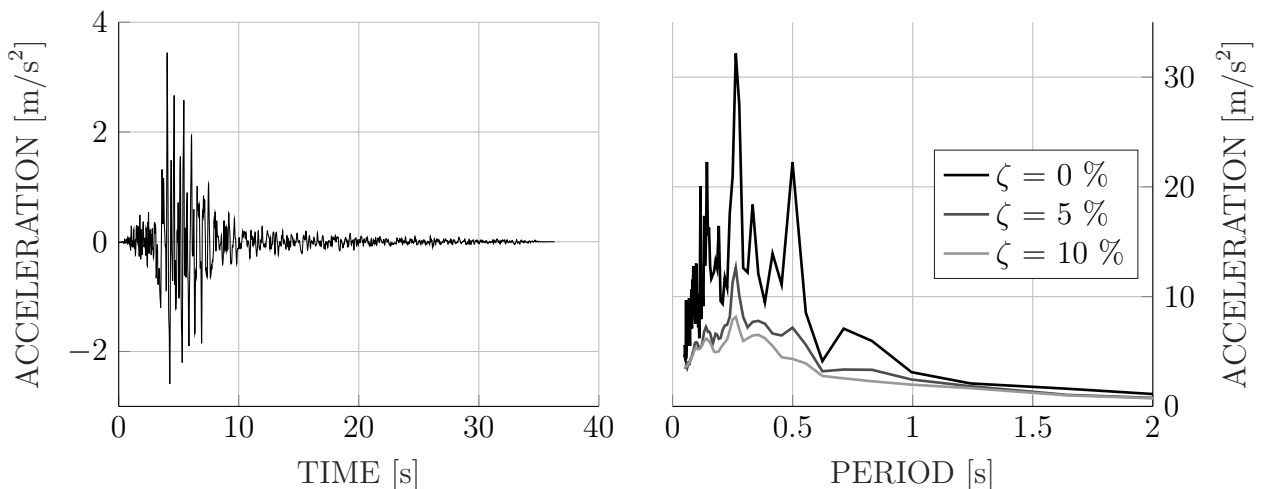
Fig. 3.6: Recorded acceleration time history spectra for various damping ratios of earthquake in Friuli (Italy) of May 06, 1976

3.3.2 Design Response Spectrum

The *American Society of Civil Engineers* (ASCE) and the *Structural Engineer Institute* (SEI) defines in their standard to the minimum design loads for buildings and other structures ASCE/SEI 7-10 [39] a so-called design spectra, depending on seismic design category of the building and site class (see figure 3.7). The peak ground acceleration for pseudo static analysis - corresponding to the natural frequency of the system - are obtained from this design spectra. Furthermore, artificial earthquakes can be generated and serve as an input for a time history analysis.
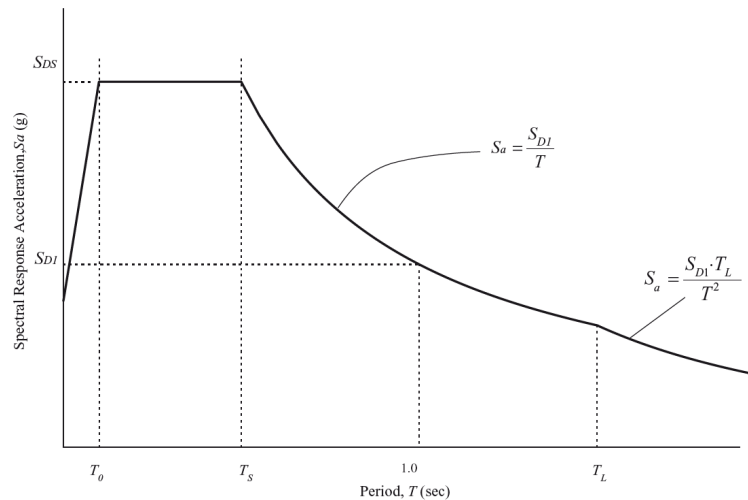
Fig. 3.7: Design spectrum according to ASCE/SEI 7-10 [39]

The earthquake produced from ASCE's design spectra represents the **Maximum Credible Earthquake (MCE)**. However, there are more types of design earthquakes based on probability of occurrence to be considered:

Safety Evaluation Earthquake (SEE): Maximum level of ground motion the structure should be designed for and no uncontrolled water loss takes place. The corresponding return period is 10,000 years.

Operation Basic Earthquake (OBE): Level of ground motion at which dam and appurtenant structures retain their functionality. The corresponding return period is 145 years (equals a 50% probability of occurrence during lifespan of 100 years).

Reservoir Triggered Earthquake (RTE): Maximum level of ground motion triggered due filling and draw-down of the reservoir.

3.3.3 Endurance Time Record

Endurance Time Analysis (ETA) is a dynamic pushover procedure which estimates the seismic performance of the dam when subjected to a pre-designed intensifying excitation. A detailed explanation and a numerical study done on arch dams can be found here [40].
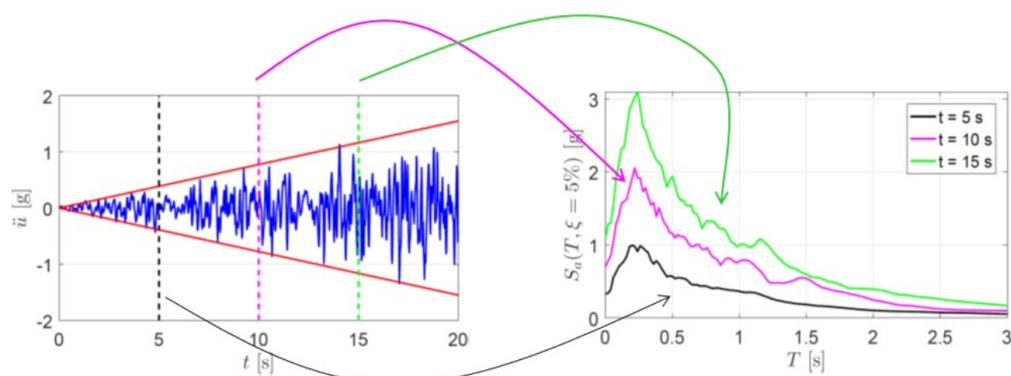
Fig. 3.8: Endurance time acceleration function (ETAF) as time acceleration history and corresponding response spectra for various sample length [38]

3.4 Solving an Equation of Motion

It follows a short overview on different solution techniques for single and multiple DoF-systems. Although there are many ways to theoretical solve an equation of motion, FE-analyses almost exclusively use numerical methods.

3.4.1 Theoretical Solution
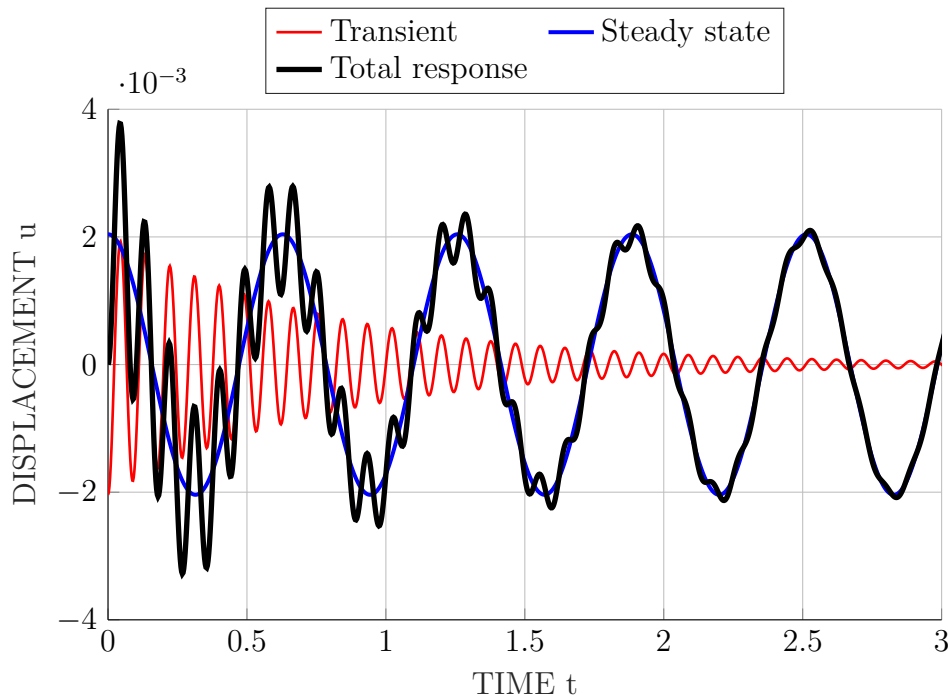
Fig. 3.9: Steady state and transient response of a damped SDoF system with initial displacement and harmonic excitation

Theoretical solutions are only applicable on SDoF systems undergoing free vibration. By adding a steady state term this can be extended to harmonic excited systems - i.e. excitations with a fixed amplitude U following a sinusoidal path with a frequency of Ω and a phase shift α. The total response is then a combination of an expiring transient and a steady state response.

$$u(t) = \underbrace{U\cos(\Omega t - \alpha)}_{\text{steady state respone}} + \underbrace{e^{-\zeta\omega_n t}(A\cos\omega_d t + B\cos\omega_d t)}_{\text{transient response}} \tag{3.15}$$

where constants A and B have to be determined from the initial conditions. A visualization of this Combination is given by figure 3.9.

3.4.2 Convolution Integral Method (Duhamel Integral Method)

The Duhamel Integral is derived from the system response to a unit impulse function, where the duration of the impulse is smaller than the system's natural period:

$$h(t) = \frac{1}{m\omega_d}e^{-\zeta\omega_n t}\sin\omega_d t \tag{3.16}$$

The underlying idea is now to see the excitation function as assembled from finite number of responses to unit impulses:

$$u_p(t) = \int_0^t f(\tau)h(t-\tau)\mathrm{d}\tau \tag{3.17}$$

For a viscous underdamped system the solution is then given by:

$$u(t) = \frac{1}{m\omega_d} \int_0^t f(\tau)e^{-\zeta\omega_n(t-\tau)}\sin\omega_d(t-\tau)\mathrm{d}\tau + e^{-\zeta\omega_n t}\left(A\cos\omega_d t + B\sin\omega_d t\right) \tag{3.18}$$

where constants A and B have to be determined from the initial conditions.

3.4.3 Mode Superposition

Mode superposition or modal analysis is a method for solving the response of linear system undergoing forced excitation. After gathering the physical properties of the system - stiffness and mass - its natural frequencies ω_r and their natural modes (Eigenvectors $\phi_\mathbf{r}$) are determined. The assembly of these Eigenvectors form the so-called modal matrix $\boldsymbol{\Phi}$.

$$\{\phi_\mathbf{1}, \phi_\mathbf{2}, .., \phi_\mathbf{r}\} = \boldsymbol{\Phi} \tag{3.19}$$

This matrix is then used to diagonalize (= decouple) stiffness and mass matrix leading to the equation of motion in principal coordinates η:

$$\mathbf{M}\ddot{\eta} + \mathbf{C}\dot{\eta} + \mathbf{K}\eta = \boldsymbol{\Phi}^T\mathbf{p}(t) \tag{3.20}$$

where

$$\mathbf{K} = \boldsymbol{\Phi}^T K \boldsymbol{\Phi} = \text{diagonal modal stiffness matrix}$$
$$\mathbf{C} = \text{generalized damping matrix}$$
$$\mathbf{M} = \boldsymbol{\Phi}^T M \boldsymbol{\Phi} = \text{diagonal modal mass matrix}$$

As a result N-number of independent SDoFs equations of motions are obtained which can then be solved separately. Where N is the number of natural frequencies - or respectively DoFs of the whole system. The final solution is then obtained by superposition:

$$\mathbf{u} = \sum_{r=1}^N \phi_r\eta_r = \boldsymbol{\Phi}\eta \tag{3.21}$$

Due to this decoupling, the generalized damping matrix $\mathbf{K}$ also has to be diagonal. Modal damping or Rayleigh damping full-fills this necessity. Therefore, only damping methods can be used which relate to mass and/or stiffness matrix e.g. modal damping or Rayleigh damping.

3.4.4 State Space

Another possibility for solving linear system is transforming the given equation of motion into state space. This is done by introducing a state vector consisting of the displacement and velocity variable of the original system. The aim is to reduce the given second order differential equation to a first order one, where further solutions techniques exist.

3.4.5 Direct Time Integration

If non-linearities are present in the system, the only way to solve is due direct time integration. The basic idea is to extrapolate known quantities from a time t_i to a time t_{i+1}. For an exact solution, the underlying equilibrium equation if full-filled at both time steps. Since a numerical solution always introduces a slight error, this equilibrium can only be formulated either at the present time step t_i or the following one t_{i+1}. If the elected method formulates the equilibrium at the present time step it is called *implicit*. On the other hand, if it is formulated at the following time step it is called *explicit*. Explicit methods are used for systems where high shifts at accelerations are present, e.g. simulation of an impact or a detonation. Implicit methods are commonly used for structural dynamics.

Figure 3.10 shows a comparison of different time integration method with and without numerical damping. Approximated problem is the response of a damped SDoF system to an initial displacement undergoing free vibration. The following section points out the different performances of the applied methods.

Central Difference Method

The central difference method was introduced by the English mathematician *Brook Taylor* in 1715. Till today, it is the most widely used integration scheme from the explicit methods. Although it was initially meant as an approximation method for derivatives of continuous functions.

The fundamental idea is to proximate the derivative of the desired, discrete function value by their discrete neighbours and their interval (in the time domain this interval equals the time step Δt). The accuracy can be enhanced by increasing the number of neighbours involved or by reducing the interval length. Furthermore, if only values related to t_{i-j}, $j = 1, 2, 3 \cdots$ are used, the formulation is called **Backward Differences**. If only values related to t_{i+j}, $j = 1, 2, 3 \cdots$ are used, it is called **Forward Differences**. If both values are used, it is called **Central Differences** .

One simple way to derive this approximation is by Taylor series expansion:

$$T_1: \quad u_{i-1} = u_i - \Delta t \left(\frac{\partial u}{\partial t}\right) + \frac{\Delta t^2}{2}\left(\frac{\partial^2 u}{\partial t^2}\right) - \frac{\Delta t^3}{6}\left(\frac{\partial^3 u}{\partial t^3}\right) + \cdots \tag{3.22}$$

$$T_2: \quad u_{i+1} = u_i + \Delta t \left(\frac{\partial u}{\partial t}\right) + \frac{\Delta t^2}{2}\left(\frac{\partial^2 u}{\partial t^2}\right) + \frac{\Delta t^3}{6}\left(\frac{\partial^3 u}{\partial t^3}\right) + \cdots \tag{3.23}$$

Subtraction and addition of these two series lead to the approximated first and second derivatives of u_i:

$$T_2 - T_1: \quad \dot{u}_i = \frac{u_{i+1} - u_{i-1}}{2\Delta t} + O(\Delta t)^2 \tag{3.24}$$

$$T_1 + T_2: \quad \ddot{u}_i = \frac{u_{i+1} - 2\cdot u_i + u_{i-1}}{\Delta t^2} + O(\Delta t)^2 \tag{3.25}$$

The caused truncation error is represented by the order of the excluded terms from the Taylor series. Furthermore, this method is conditionally stable. This requires that the selected time step must full-fill the following criterion:

$$\frac{\Delta t}{T_n} < \frac{1}{\pi} \tag{3.26}$$

Where T_n is the period of the highest natural frequency of the discretized system which is not directly involved in the system's response.

Newmark-β Method

The Newmark method was developed in 1959 from the US-American civil engineer *Nathan M. Newmark*. Based on the known displacement u_i, velocity $\dot{u}_i$ and acceleration $\ddot{u}_i$ at time t, it computes their unknown quantities at time $t + \Delta t$. It is a one step method due to only quantities at one time step are used to solve the following one. This *implicit* method is based on the following equations:

$$\dot{u}_{i+1} = \dot{u}_i + \underbrace{\left[(1 - \gamma)\,\ddot{u}_i + \gamma\ddot{u}_{i+1}\right]}_{\text{weighted average}}\Delta t \tag{3.27}$$

$$u_{i+1} = u_i + \dot{u}_i\Delta t + \underbrace{\left[\left(\frac{1}{2} - \beta\right)\ddot{u}_i + \beta\ddot{u}_{i+1}\right]}_{\text{weighted average}}\Delta t^2 \tag{3.28}$$

Depending on the selected values for *beta* and γ, this method equals to the average or linear acceleration method. The difference between these methods lies within their stability criterion. While for the linear acceleration method ($\beta = \frac{1}{6}$ and $\gamma = \frac{1}{2}$) is conditionally stable depending on the system's natural period T_n for $\frac{\Delta t}{T_n} \le 0.551$, the averaged acceleration method ($\beta = \frac{1}{4}$ and $\gamma = \frac{1}{2}$) is unconditionally stable and therefore independent of the selected time step Δt. As can be seen in figure 3.10, both methods undergo slight numerical damping and an enlargement of the responding period. An example to implement the algorithm to solve the response of a SDoF system can be seen at [37].

Wilson-θ Method

The underlying idea of the Wilson-θ Method is that each component of the acceleration vector $\ddot{\mathbf{u}}$ varies linearly with time over the extended time step $s = \theta\Delta t$. It is an *implicit* method. An example is given by [36]. As can be observed in figure 3.10, this method performs slightly worse - at same time step size - than its counterparts. Therefore, its usage in numerical analysis is limited.

Hilber-Hughes-Taylor-α Method (HHT-α-Method)

Hilber-Hughes-Taylor Method is based on the Newmark-β Method from 3.4.5, but it adds numerical damping to the processed equilibrium equation. This damping is controlled by the parameter α defined between $\left[-\frac{1}{3},\, 0\right]$. The smaller this value, the larger is the introduced numerical damping. Note that if alpha is set to zero, this methods equals Newmark's averaged acceleration method. A step-for-step implementation can be seen at [41]. The outcome of numerical damping can be observed in figure 3.10.

Due to the formulation of equilibrium at time $t + 1$, this method is *explicit*. This is the standard method for time integration in transient analysis in FEM software like *Ansys Mechanical* or *Abaqus*.
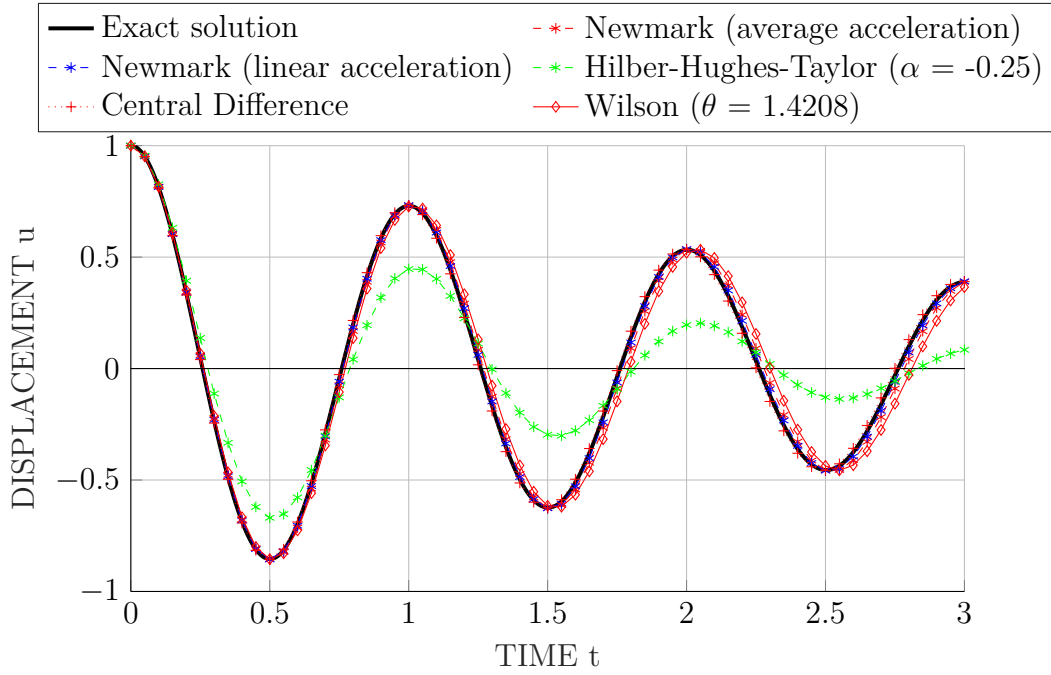
Fig. 3.10: Response of a damped SDoF system to initial displacement solved through various integration schemes with and without numerical damping

3.4.6 Effective Modal Mass

The compression of effective modal masses between modes, can be seen as method for judging the mode's significance. The more effective mass results at a mode, the more the system excite by excitation at this frequency. Furthermore, as a rule of thumb of how many modes should be extracted during modal analysis: The sum of effective modal masses of the extracted modes should be at least 90% of the system's total mass.

The effective modal mass is obtained for any mode i and any degree of freedom j as follows:

$$m_{i,j}^{eff} = \frac{L_{ij}^2}{M_{ii}} \tag{3.29}$$

where

$$\mathbf{M} = \mathbf{\Phi}^T \boldsymbol{M} \mathbf{\Phi} \tag{3.30}$$

$$\mathbf{L} = \mathbf{\Phi}^T \boldsymbol{M} \boldsymbol{r} \tag{3.31}$$

$$\boldsymbol{r} = \text{static influence matrix} \tag{3.32}$$

The influence matrix $\boldsymbol{r}$ represents the displacements of masses resulting from static application of unit displacements and rotations. The sum over all modes of one degree of freedom results in the system's total mass involved:

$$m^{total} = \sum_{n=1}^{max} m_{n,j}^{eff} \tag{3.33}$$

Effective mass can be used to find appropriable modes for determination of Rayleigh damping factors.

3.5 Seismic Analysis of Concrete Dams

This section should provide a brief overview on the current praxis of seismic modelling of dams. Furthermore, it lists the common assumptions taken during these analyses. This part is oriented on the guideline *Evaluation of non-linear material models in concrete dam finite element Analysis* [1] by the *U.S. Bureau of Reclamation* and the guideline provided by *R. Malm* which summarizing the most import aspects for FE-analyses of dams [42].
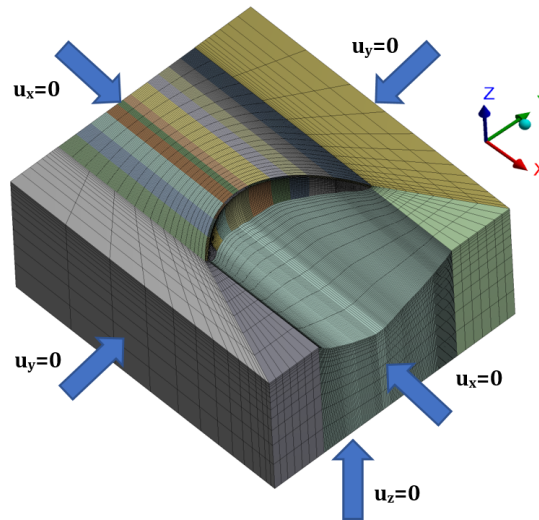
Fig. 3.11: Boundary conditions applied on foundation model

Two and three-dimensional models are both common for FE-analyses of concrete das. Two dimensional models with plane strain conditions are in most cases sufficient for modelling of gravity dams with straight axes. For arch dams on the other hand, only three-dimensional analyses are representative. A Modal analysis can be performed to obtain Eigenfrequencies and mode shapes if using linear material models and linear contact formulations. Furthermore, mode superposition or time history analysis can be used to obtain the model's response to a specific excitation. If using non-linear material models or if non-linear contacts are present, time history analysis can be performed.

3.5.1 Model Boundary Condition

The boundary condition are usually applied only onto the foundation's outer boundaries. Their displacement is constrained in the normal direction to the faces of the foundation block.

3.5.2 Massless Foundation Approach

Representative modelling of the foundation behaviour while subjected to an earthquake is difficult. This mainly arises from the complexity of the foundation and its influence on the dynamic behaviour - e.g. orientation and spacing joint sets, position of failure zones. Also, modelling these kinds of structures is very computational costly and does not always lead to satisfying results when using commercial codes. Furthermore, determining the damping coefficient of the foundation is difficult because of the described features. Therefore, the massless foundation approach is chosen to reduce influence of the foundation on the dam model.

3.5.3 Maximum Element Sizes

The maximum edge size L of the used mesh depends on the largest frequency of interest f_{max} to be obtained by the model. According to the guideline, as a rule of thumb the following criterion should be fulfilled:

$$L < \frac{c}{n_{min} \cdot f_{max}} \tag{3.34}$$

Where n_{min} is the minimum number of points to approximate a sinus wave (usually taken as 10) and c is the shear wave velocity of the modelled material. Furthermore, in relation the used time step Δt the *Courant-Friedrichs–Lewy Condition* must be fulfilled:

$$C = \frac{u \cdot \Delta t}{L} \leq 1 \tag{3.35}$$

Where u is the wave velocity in the material. The expression on the left hand side equals the so-called *Courant number C*. Also, when non-linear material models are used, the following criterion should be fulfilled:

$$L < \frac{E \cdot G_f}{f_t^2} \tag{3.36}$$

Where E is the Young's modulus, G_f the fracture energy and f_t the materials tensile strength. This criterion relates from the approximated length of the fracture process zone.

4 Numerical Analyses

4.1 Getting started with Ansys Mechanical

This chapter provides an overview of the essential processes and parts of the finite element software *Ansys Mechanical.*

4.1.1 Solution Procedure

For solving structural and transient problems, *Ansys Mechanical* provides two different solution procedures. The most common is the Newton-Raphson procedure, which is capable of solving geometrical and material non-linear problems until a certain extant. Depending on the type of convergence (displacement or force) it is also capable of solving problems including material softening behaviour. However, more complex problems, e.g. highly non-linear geometries, are longing for a more powerful solver. One example is the arc-length method, which is also described here.

(a) One iteration   **(b)** Next iteration
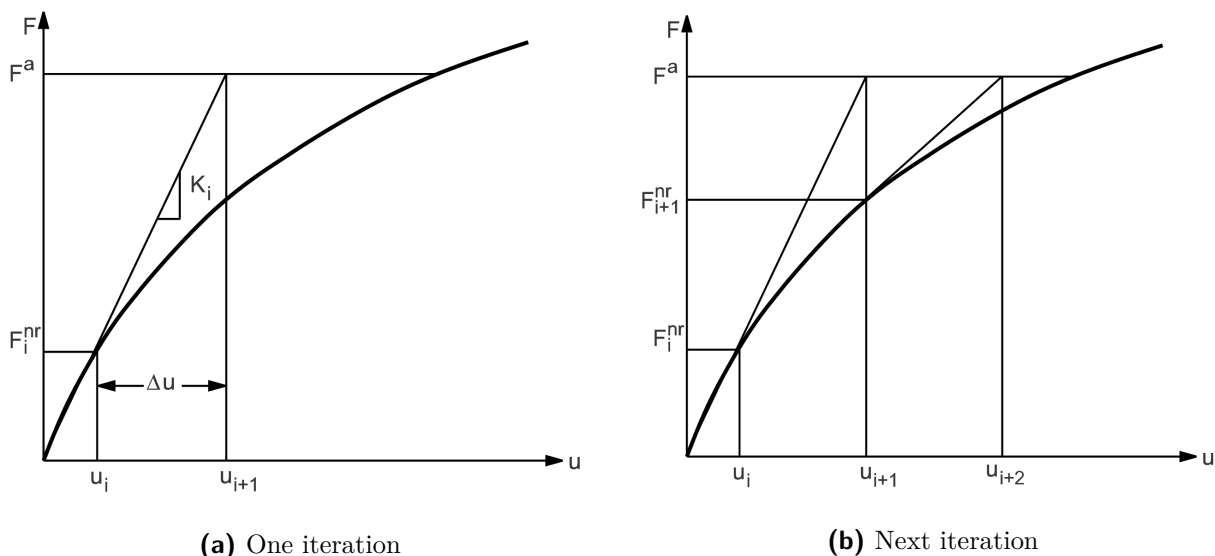
Fig. 4.1: Iteration procedure of the Newton-Raphson Method [43]

Newton-Raphson Procedure

The Newton-Raphson Procedure is an iterative process of solving non-linear equilibrium equations. It was initially developed in the 17th century by the English mathematicians *Sir Isaac Newton* and *Joseph Raphson* to find an approximation to the roots of a given function. The procedure itself did not change over the years: in the one-dimensional case, it starts with an initial guess for the location of the roots x_0 (this guess can also be the value from a previous iteration step). Knowing the function value and its first derivative in this point, it is then

possible to approximate one desired root. As shown in 4.1, this process can be repeated until a certain accuracy is reached.

$$x_1 = x_0 - \frac{f(x_0)}{f'(x_0)} \tag{4.1}$$

$$x_{n+1} = x_n - \frac{f(x_n)}{f'(x_n)} \tag{4.2}$$

In structural analysis, this procedure can be applied on non-linear systems of equilibrium equations. There the stiffness matrix $\boldsymbol{K}$ is a function of the unknown displacement values u and its derivatives. A non-linear stiffness matrix may result from non-linear material laws or non-linear geometry effects of the structure.

$$\boldsymbol{K}\mathbf{u} = \mathbf{F^a} \tag{4.3}$$

$$\tag{4.4}$$

where

$$\boldsymbol{K} = \text{stiffness matrix} \tag{4.5}$$
$$\mathbf{u} = \text{displacement vector} \tag{4.6}$$
$$\mathbf{F^a} = \text{vector of applied loads} \tag{4.7}$$

The iterative Newton-Raphson process applied on the equation above, can be written as:

$$\boldsymbol{K}_i \Delta\mathbf{u} = \mathbf{F^a} - \mathbf{F}_i^{nr} \tag{4.8}$$
$$\mathbf{u}_{i+1} = \mathbf{u}_i + \Delta\mathbf{u}_i \tag{4.9}$$

where

$$\boldsymbol{K} = \text{tangent stiffness matrix (Jacobian matrix)} \tag{4.10}$$
$$\mathbf{F}^{nr} = \text{force vector calculated from the element stresses} \tag{4.11}$$
$$i = \text{subscript of the current iteration step} \tag{4.12}$$

The solution procedure itself can be either load or displacement driven. This means, a load or displacement increment is defined by the user and the other entity is iteratively solved by the procedure from above. This procedure is repeated until convergence is reached. As a convergence criterion serves the difference of outer and inner forces of the structure, called residual force. The value of the residual can be increased to achieve faster convergence but on the costs of accuracy. Additionally, a displacement criteria can be chosen as a convergence indicator. This eases the achieving of convergence for non-linear material behaviour.

Although this procedure is a fast and accurate way to solve non-linear problems on systems with reducing stiffness, it has its limits. For the load driven procedure (see Fig. 4.2a), the stiffness matrix become singular in **B** and **L**, meaning that the solution in this point is not unique. Furthermore, it is clear that softening behaviour cannot be simulated with this setup. The displacement driven procedure (see Fig. 4.2b) on the other hand doesn't allow negative displacement increments, as from point **T** to point **T**.

(a) load driven procedure   **(b)** displacement driven procedure
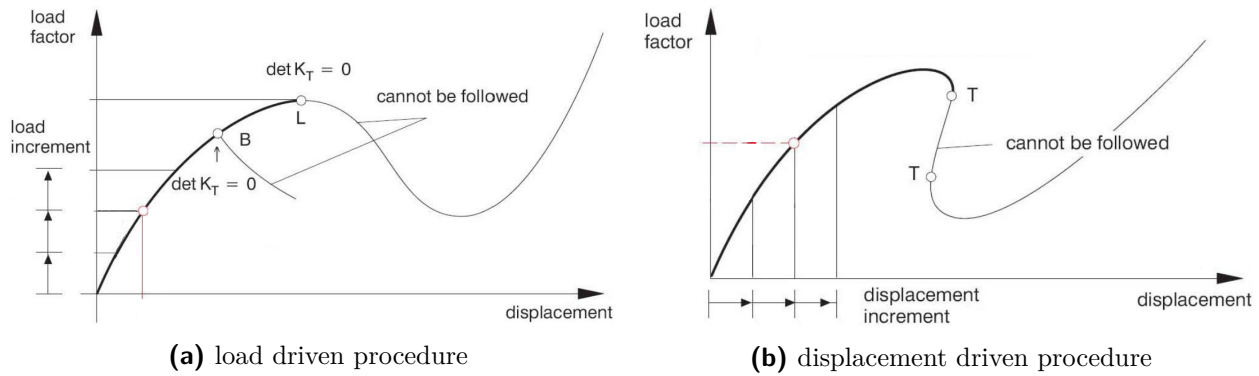
Fig. 4.2: Limits for Newton-Raphson procedure for solving non-linear equilibrium equations [43]

Arc-length Method

The arc-length method is a modification of the Newton-Raphson procedure. It causes the Newton-Raphson equilibrium iterations to converge along an arc, which often helps to prevent divergence, even when the slope of the load becomes zero or negative (see points **L** and **T** in figure 4.3). Therefore, both, displacement and load increments, are modified each iteration. The arc length itself depends on the applied load and displacement increments and remain constant while they are varied to obtain equilibrium.
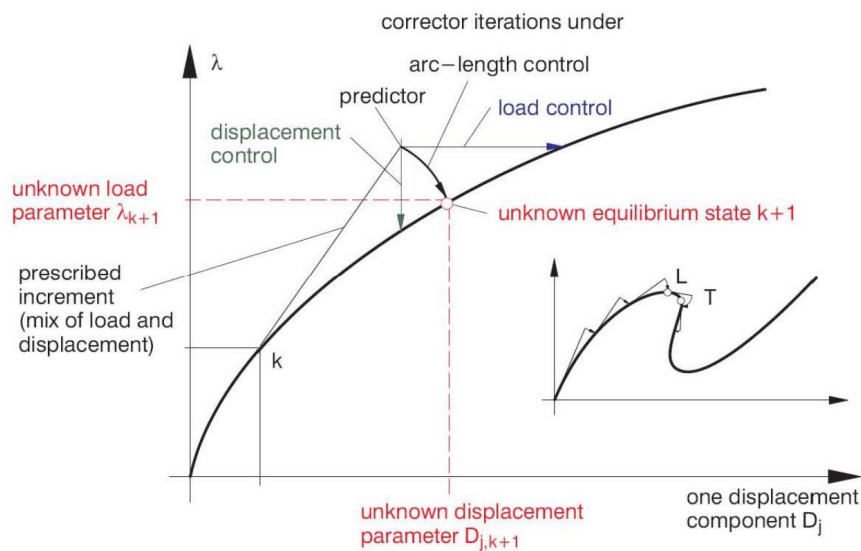
Fig. 4.3: Graphical interpretation of the arc-length method [43]

Although there are different variants of arc-length or continuation methods, they all consist of two phases. In the first phase - prediction phase -, an estimation for the next equilibrium point is established starting from a known converged solution point. In the second phase - correction phase -, Newton-iterations are employed to find a new point on the equilibrium curve.

4.1.2 Element Types

Structural Elements

They are the most basic element type for structural elements. They are available as one dimensional *BEAM* elements, two-dimensional *PLANE* elements and thee dimensional *SOLID* elements. Various material models are available which are able to represent elastic or inelastic, isotopic or anisotropic as well as linear or non-linear behaviours. Available degree of freedom depend on the element type. Basically, elements have three displacement and three rotational DoFs per node. Additionally, some types are capable of modelling a temperature DoFs and pressure DoFs, e.g. coupled pore-pressure and temperature elements (*CPT*). Furthermore, user-defined DoFs (Generic Field Variables *GFV*) can be applied to the elements. Material properties can be defined depending on the material model used, e.g. for linear elastic behaviour, Young's modulus and Poisson ratio are sufficient. Other material properties may be shear and bulk modulus, temperature expansion coefficient or density.

All element types are available with linear and quadratic order. If changing the element type - e.g. how it is required for the microplane model - the element order of the pre-defined mesh and the element type must be the same. For static structural analysis, the governing differential equation is given from the balance of internal and external forces:

$$\mathbf{F^{int}}(t) = \mathbf{F^{ext}}(t) \tag{4.13}$$

For transient structural analysis, the governing differential equation is given by the equation of motion:

$$\boldsymbol{M}\ddot{\mathbf{u}}(t) + \boldsymbol{C}\dot{\mathbf{u}}(t) + \mathbf{F^{int}}(t) = \mathbf{F^{ext}}(t) \tag{4.14}$$

Acoustic Elements

In *Ansys Mechanical*, acoustic elements are available in linear and quadratic order (*FLUID30* and *FLUID220*). They pose two formulations of degree of freedoms. The first considers pressure DoF and three displacement DoFs and the second one only considers pressure DoF. The first formulation is used to model fully reflective surfaces or fluid structure interactions (FSI). The second one is used to model fluid elements inside the domain, where no BCs are present. Required material properties to be defined are fluid density and sonic speed in media. The governing differential equation is the acoustic wave equation given by:

$$\nabla \cdot \left(\frac{1}{\rho_0} \nabla \mathbf{p} \right) + \frac{1}{\rho_0 \cdot c^2} \frac{\partial^2 \mathbf{p}}{\partial t^2} = 0 \qquad c = \sqrt{\frac{K}{\rho_0}} \tag{4.15}$$

where ρ_0 is the mean density, $\mathbf{p}$ the fluid pressure and c the sound velocity in the media obtained from the Bulk modulus. However, the acoustic wave equation is derived from the linearized Navier-Stokes equation and the linearized continuity equation for a fluid, under the following assumptions:

  ⋄ the fluid is compressible
  ⋄ the fluid is irrotational
  ⋄ no body forces are acting
  ⋄ small pressure distribution of the fluid
  ⋄ no mean flow

Additionally, following assumptions are taken in order to model dynamic behaviour of water:

  ○ no mass source is present
  ○ dynamic viscosity of water is neglected

Miscellaneous Elements

Ansys Mechanical uses automatically generated elements in order to define boundary conditions like forces, contacts or interaction surfaces (e.g. FSI). If using the GUI-workbench these elements are created before user-defined APDL-scripts are run. Redefining element types via APDL using geometrical defined instances (*CMSEL*), may also redefine these elements which then lead to a major error. This should be kept in mind if the selection algorithm is created.

4.1.3 Contact Modelling
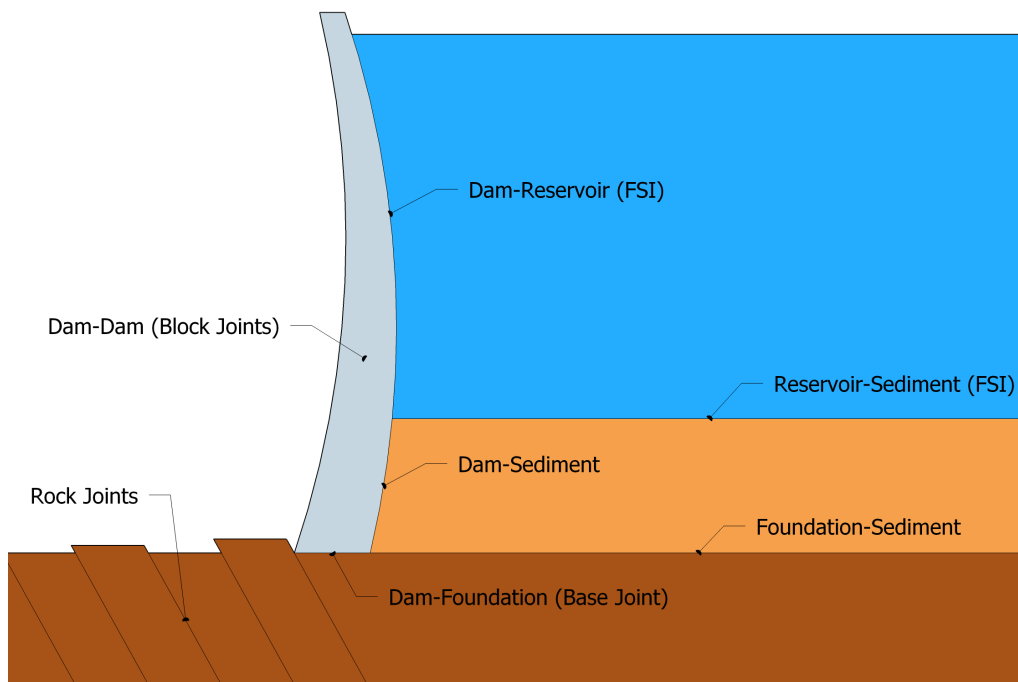
Fig. 4.4: Schematic examples for contacts to be encountered when modelling an arch dam

This chapter should give an overview on how to model contact behaviour between two bodies. Although it is oriented on available option in *Ansys Mechanical* [44], the principles shall be the same for all commercial finite element software.

Contact vs. Target
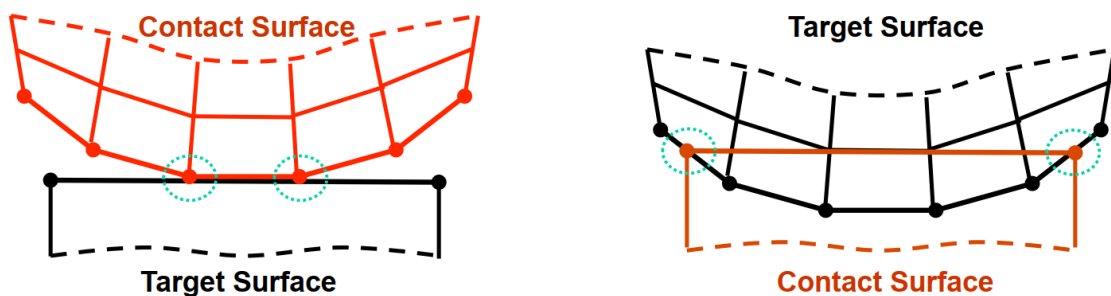
Fig. 4.5: Increasing penetration when changing contact with target surfaces for asymmetric behaviour type [45]

To model contact, two additional element types have to be added. One type is applied to the contact surface (a.k.a. master) and the other one on the targeted surface (a.k.a. slave). In *Ansys Mechanical*, target surfaces are modelled with either TARGE169 (line) or TARGE170 (surface) elements. Available contact surface elements are CONTA171 (linear line), CONTA172 (quadratic line), CONTA173 (linear surface) or CONTA174 (quadratic surface). Also, contact between linear and surface elements is possible by using CONTA175 elements. Furthermore, node-to-node contact is possible, although it is not recommended due bad convergence performance in 2D- or 3D-contacts.

Selecting the correct surfaces as contact and target can be highly important for asymmetric behaviour types (see figure 4.5). **Symmetric Behaviour** Contact and target geometries are constrained from penetrating each other. It is the default behaviour. However, it is more computational costly than the asymmetric behaviour. Also interpreting results can be more difficult because they are reported in both, contact and target geometries. **Asymmetric Behaviour** Only contact geometry is constrained from penetrating target geometry. As mentioned above, it is important which geometry to be selected as target or as contact. This may influence the results tremendously. Also, results are only reported on contact geometry.

Contact Behaviour Types

Various behaviour types exist to model different problems like sliding and separation including and excluding friction. Table 4.1 lists the available behaviour types in *Ansys Mechanical*.
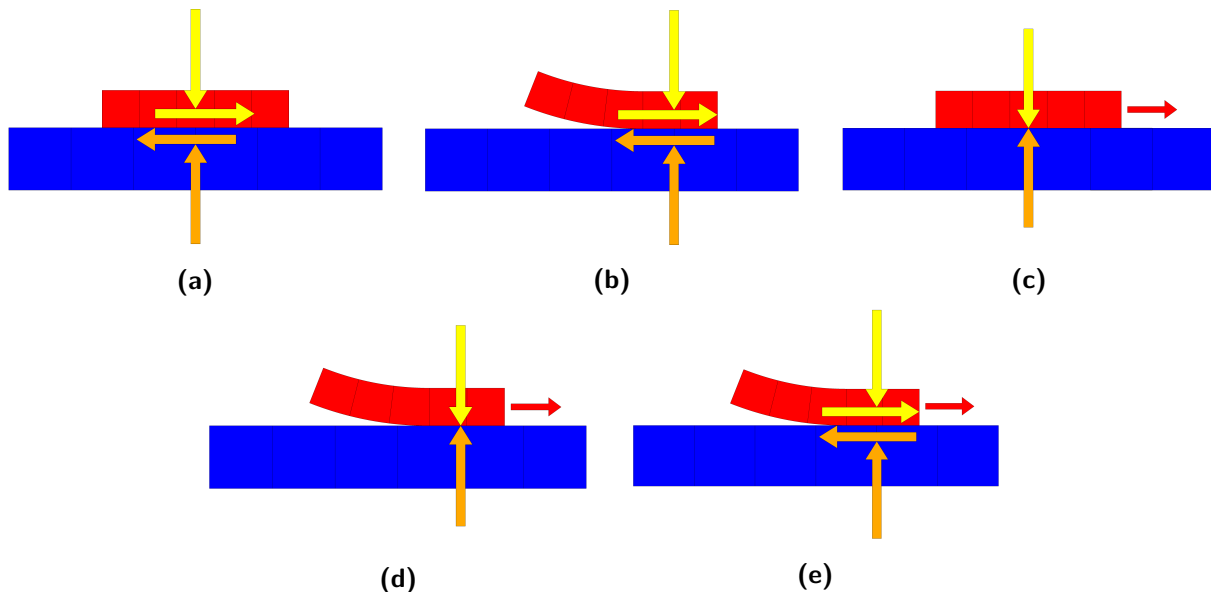
Fig. 4.6: Overview of available contact behaviour types showing submitted forces and movement: **(a)** bounded, **(b)** rough, **(c)** no separation, **(d)** frictionless and **(e)** frictional

The displayed behaviour types are additionally described below:

(a) Bounded: This type of behaviour allows for linear solution, gaps are closed and initial penetration is ignored. This type leads to the same results as due to a node merge inside the contact region.

(b) Rough: This type doesn't allow sliding and corresponds to a joint with an infinite friction coefficient. However, gaps openings and closing can take place. In case of separation the normal pressure is reduced to zero. This type leads to a non-linear solution.

(c) No Separation: Here the separation of the geometries is not allowed, although frictionless sliding is enabled.

(d) Frictionless: Geometries can open and close gaps. In case of separation the normal pressure is reduced to zero. Sliding happens frictionless. This type leads to a non-linear solution.

(e) Frictional: Geometries can open and close gaps. In case of separation, the normal pressure is reduced to zero. The contact can submit shear stresses up to a certain magnitude defined by the friction coefficient and the contact pressure. After exceeding this shear stress limit, geometries begin to slide relative to each other. This type leads to a non-linear solution.

Name	Gap can open/close	Sliding allowed
Bounded	NO	NO
Rough	YES	NO, $\mu_s = \infty$
No Separation	NO	YES, $\mu_s = 0$
Frictionless	YES	YES, $\mu_s = 0$
Frictional	YES	YES, $\mu_s \neq 0$

Tab. 4.1: Overview on the contact behaviour types available in *Ansys Mechanical*

Contact Formulations

Choosing the right contact formulation for the right problem can save a lot of computational power and may lead to faster convergence. Following, the different types are briefly described and application examples are given. Furthermore, the table in figure 4.8 shows pros and cons of the different formulation types.

- **Pure Penalty**

$$F_{normal} = k_{normal} \cdot x_{penetration} \tag{4.16}$$

This method uses the *concept of contact stiffness* where the finite contact force F_{normal} and the reaction force resulting from the geometrical penetration of the two bodies. It is valid for all behaviour types. It has a good convergence behaviour, although it is sensitive to the selected contact stiffness. Furthermore, penetration is always present even if the contact stiffness is very high. Therefore, results should be checked carefully.

- **Augmented Lagrange**
This method is an iterative series of pure penalty methods where the contact pressure and frictional stress are increased during the equilibrium iteration until the final penetration is smaller than the allowed tolerance. Although this method requires additional iterations, it tends to be less sensitive to the selected normal stiffness.

- **Normal Lagrange or Pure Lagrange**

$$F_{normal} = DoF \tag{4.17}$$

This method adds contact traction (pressure and frictional stress) as an additional degree of freedom. It is valid for all types of contact behaviours. If the contact is closed, it enforces zero penetration and during sticking it enforces zero slip. This often leads to the so-called chattering. If no penetration is allowed the contact statues is represented through a step function (see

figure 4.7 left) which cause convergence difficulties. Slight penetration, on the other hand, may help the solution to converge faster (see figure 4.7 left). Furthermore, it should be noted that only direct solver can handle normal or pure Lagrange formulations and only asymmetric penetration behaviour is allowed.
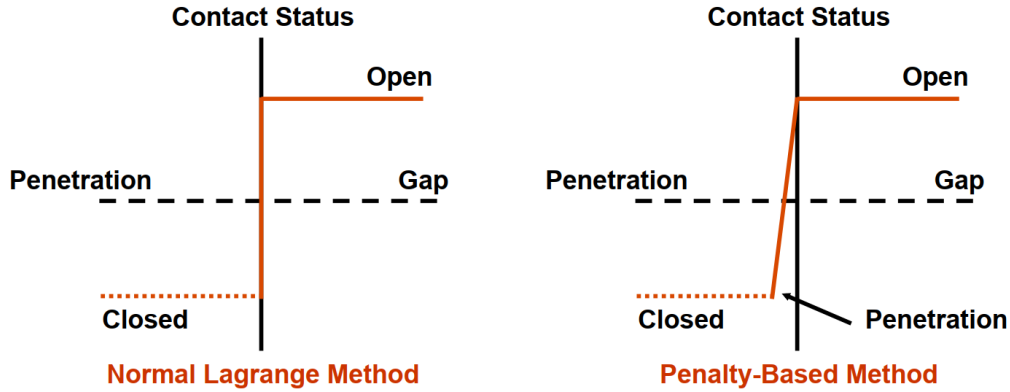
Fig. 4.7: Chattering effect [44]

- **Multi-Point Constraint (MPC)**

This method uses kinematic constraint equations, defined on contact pairs. For small deformation problems, this results into linear contact behaviour. If large deformation is present, constraint equations are updated during every iteration. This method doesn't need normal stiffness as an input and lead to zero penetration. But it is only valid for bounded and no separation behaviour types. Furthermore, it only supports asymmetric penetration behaviour.

	Pure Penalty		Augmented Lagrange		Normal Lagrange		MPC
+	Good convergence behavior (few equilibrium iterations)	-	May require additional equilibrium iterations if penetration is too large	-	May require additional equilibrium iterations if chattering is present	+	Good convergence behavior (few equilibrium iterations)
-	Sensitive to selection of normal contact stiffness		Less sensitive to selection of normal contact stiffness	+	No normal contact stiffness is required	+	No normal contact stiffness is required
-	Contact penetration is present and uncontrolled		Contact penetration is present but controlled to some degree	+	Usually, penetration is near-zero	+	No penetration
+	Useful for any type of contact behavior	+	Useful for any type of contact behavior	+	Useful for any type of contact behavior	-	Only Bonded & No Separation behaviors
+	Either Iterative or Direct Solvers can be used	+	Either Iterative or Direct Solvers can be used	-	Only Direct Solver can be used	+	Either Iterative or Direct Solvers can be used
+	Symmetric or asymmetric contact available	+	Symmetric or asymmetric contact available		Asymmetric contact only		Asymmetric contact only
+	Contact detection at integration points	+	Contact detection at integration points		Contact detection at nodes		Contact detection at nodes

Fig. 4.8: Pros and cons of various contact formulation types [44]

Contact Detection

There are two ways to detect of contact between geometries depending on the used formulation. Pure Penalty and Augmented Lagrange use integration point detection. This leads to more detected points resulting in less unaccounted penetration at a full body contact. Normal

Lagrange and MPC uses nodal point detection. This leads to less detected points but may handle contact on edges slightly better.

Concept of Normal Stiffness

Aim is to establish an equilibrium between the finite contact force F_{normal} and the reaction force resulting from the geometrical penetration of the two bodies times the contact normal stiffness k_{normal}. Regarding *Ansys Mechanical*, the normal stiffness is calculated automatically but can be adjusted by the normal stiffness factor (FKN). This factor simply multiplies the calculated normal stiffness. Depending on the problem to be solved, following inputs for the factor are recommended: for bounded and no separation behaviours $FKN = 10$, for bulk-dominated problems $FKN = 1$ and for bending dominated problems $FKN = 0.01$ to 0.1.

However, there are certain things to be considered by the use of contact stiffness. First of all, higher contact stiffness lead to more accurate results, but also the problem become more difficult to converge. This means there will be more iterations needed to reach convergence or it won't even be reached at all. Furthermore, too high contact stiffness may cause the contact surfaces to bounce off each other, they may start oscillating.

Tangential Stiffness

$$F_{tangential} = k_{tangential} \cdot x_{slip} \tag{4.18}$$

If the contact behaviour type is bounded, rough or frictional, an additional friction force has to be balanced with a finite tangential force $F_{tangential}$. The friction force or tangential force is the product of tangential stiffness and geometrical slip. Tangential stiffness $k_{tangential}$ is calculated depending on the contact normal stiffness and friction coefficient. As an alternative, tangential stiffness can be calculated due contact normal pressure, friction coefficient and a maximum allowable elastic slip.

4.2 Studies – Microplane Model Parameters

Aim of this chapter is to get a better understanding of the microplane model's input parameter. Therefore, the following analyses were performed:

- **Cube**

Tension and compression failure was simulated on a simple cube while varying different input parameters. It shows that the uni-axial compressive strength has no influence one the macroscopic tensile behaviour while the tensile damage evolution parameter influences the macroscopic compressive behaviour quite strong. The Variation of the Poisson ratio also seems to have little influence during uni-axial deformation. Furthermore, the non-local range has no influence due to the equally distributed strain field of the cube. Finally, both - compressive and tensile - uni-axial strength defined for each microplane were not reached on a macroscopic level. Also, the macroscopic strength is influenced by the damage evolution parameter.

- **Cylinder**

Cylinders with various diameters were exposed to uni-axial tension. They were fixed on both ends and all possessed the same height. Then, the radial stress distribution was investigated. Furthermore, fracture energy was calculated from the resulting stress-strain curves. Although the material parameters remained unaltered, calculated fracture energy is found to depend on the cross-section area. This may be explained due to the used non-local regularization and the unequally distributed strain field due to the fixed ends.

- **Vertex**

First curve fitting attempted in order to calibrate material model parameters. Aim was the replication of the so-called vertex effect, i.e. rotation of principal stress axis leading to a too stiff response when using ordinary FEM methods compared to experimental data. The experiment was set-up in two steps. First, a cylinder is undergoing uni-axial compression until softening initiates. Second, compressive displacement is kept and the cylinder is rotated around its main axes. The microplane parameters were calibrated to fit only the compressive stress-strain curve. The obtained initial stiffness response from the rotational step fits closely the experimental data. Additionally, the parameter influence on the stress-strain and torque-rotation curves were investigated. However, radial stress distribution shows uniform distribution in the elastic range and increased stress at the edges in the post-peak softening range - like it was expected from theoretical descriptions.

- **L-Shaped Plate**

A simple L-shaped geometry was meshed with different element sizes and orientation. Then, the unsupported side was displaced and the damage growth at the inner corner was observed. This process was carried out with two models: one with a non-local regularization and the second one without. For the non-regularized model, results clearly show an influence of element size and element orientation on the resulting damage pattern as well as on the overall performance in the force-displacement curve. On the other hand, an active non-local regularization delivers almost identical results independent of mesh size and orientation.

4.2.1 Cube

A parameter study was performed to receive a better understanding of the influence of the input parameters on the material behaviour. Therefore, two cubes with an edge length of 0.1 m, consisting of 100 linear hexahedral CPT215 elements was modelled. Displacement boundary conditions were applied on three adjacent faces, each locking a different spatial direction. A displacement controlled setup was used. Therefore, the displacement was applied on of the free faces. One of the cubes was then exposed uni-axial compression and the other one uni-axial tension. The resulting force was recorded at the same nodes where the displacement was applied. Then, microplane model input parameters were varied and the resulting stress strain curves were plotted. From analysing these results, the following could be shown: First, non-local range parameter has an overall influence on the non-linear behaviour – in tension as well as in compressive regime. Second, linear elastic range remain uninfluenced by Drucker-Prager and non-local parameters. In contrary, Poisson' ratio show little to no influence on non-linear range. Furthermore, tension damage parameters have a significant influence on compressive behaviour. Vice versa compressive damage parameter show no influence on tensional behaviour. Last, defined uni-axial compressive and tensional strength were not reached in the model (deviation of about 5%).
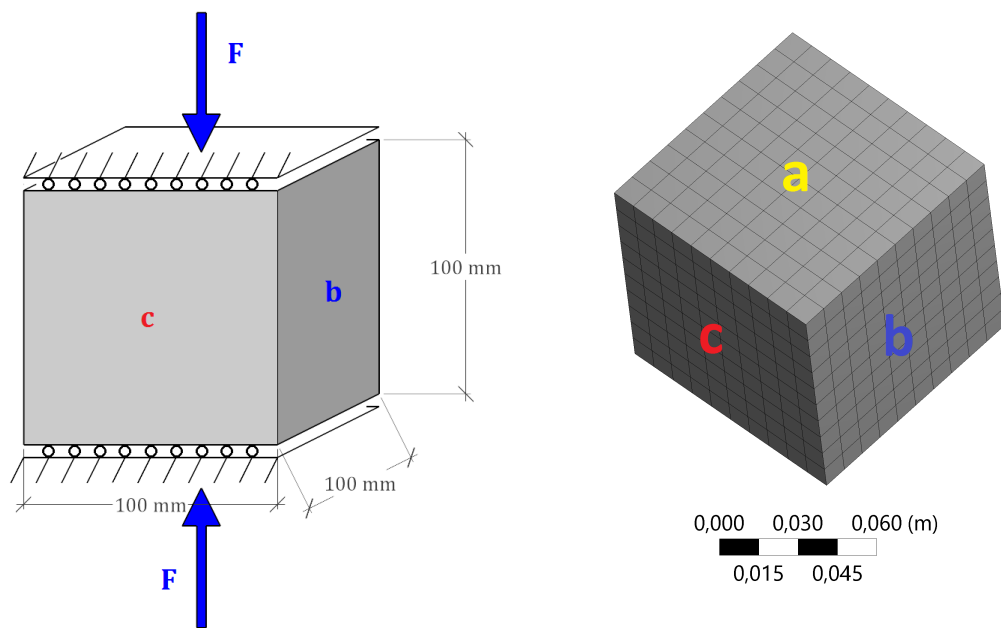
Fig. 4.9: Model setup and cube mesh

Input parameters for the microplane model were varied one after another and the results were plotted in respect to the ones obtained by the parameters in table 4.3.

Geometry and Mesh

The mesh consists of 1000 linear hexahedral CPT215 elements with an edge length of 0.01 m. The same mesh was used for compressive and tensional testing.

Mesh properties		
Form	Cube	
Edge length	100	mm
Area	0.01	m²
Nodes	1331	
Elements	1000	
Element length	0.01	m

Tab. 4.2: Mesh properties

Parameters		
E	25000	MPa
ν	0.2	
f_{uc}	40	MPa
f_{ut}	3.53	MPa
c	0.0004	
γ_{t0}	0	
β_t	6000	
γ_{c0}	0.003	
β_c	2500	

Tab. 4.3: Material model input parameters

The faces of the cube were locked in one direction each, see figure 4.9. Namely, face (a) was locked in X-direction, face (b) in Y-direction and face (c) in Z-direction. Compressive and tensional displacement was applied in Z-direction on the opposite face of (c). Displacement was applied ramped to a maximum value of 0.0002 m for tension and -0.001 m for compression.

Results

Normal reaction force was recorded on face (c) and displacement was recorded on the other opposite face. Then, stress-strain curves were plotted.
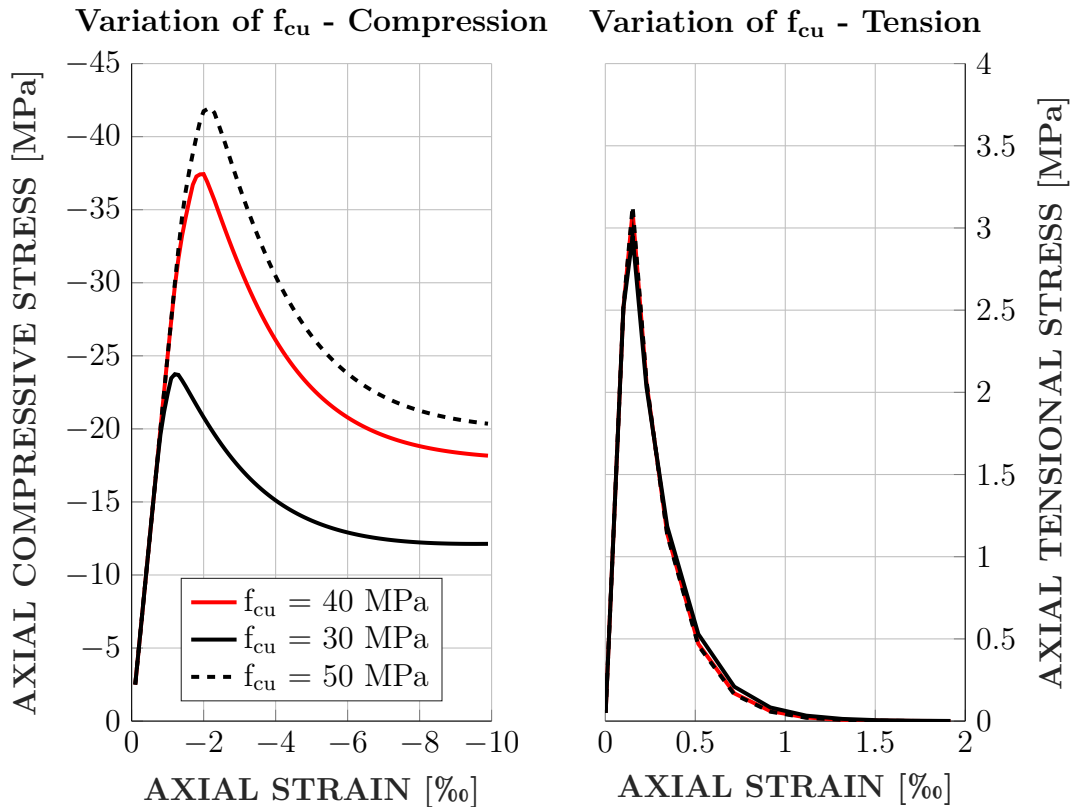
Fig. 4.10: Cube: parameter variation of uni-axial compressive strength

Variation of β_t - Compression

Variation of β_t - Tension
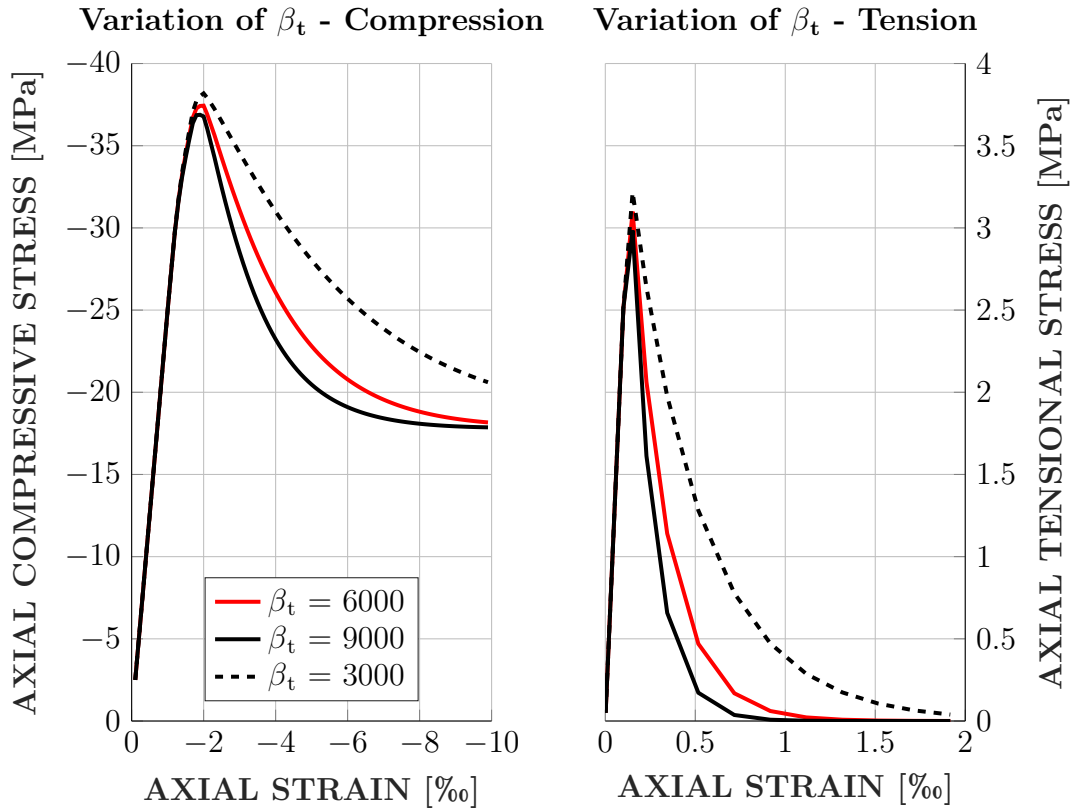
Fig. 4.11: Cube: variation of tensional damage evolution parameter

Variation of E - Compression

Variation of E - Tension
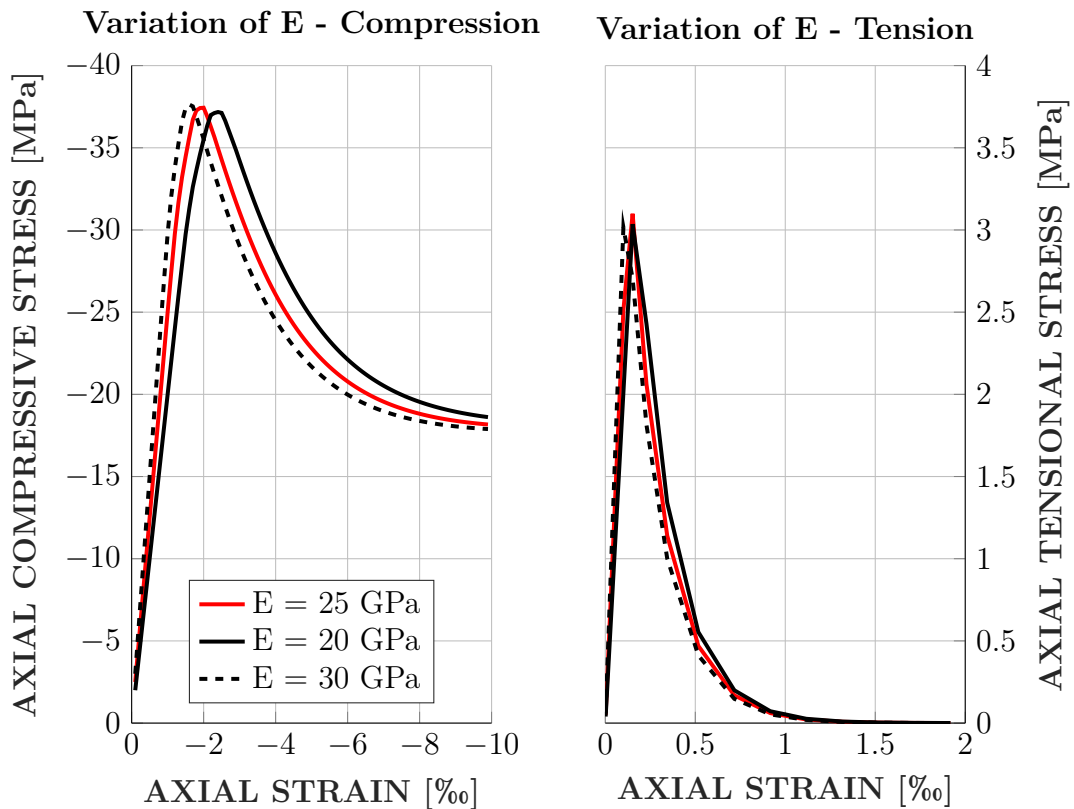
Fig. 4.12: Cube: parameter variation of Young's modulus

Variation of ν - Compression   **Variation of ν - Tension**
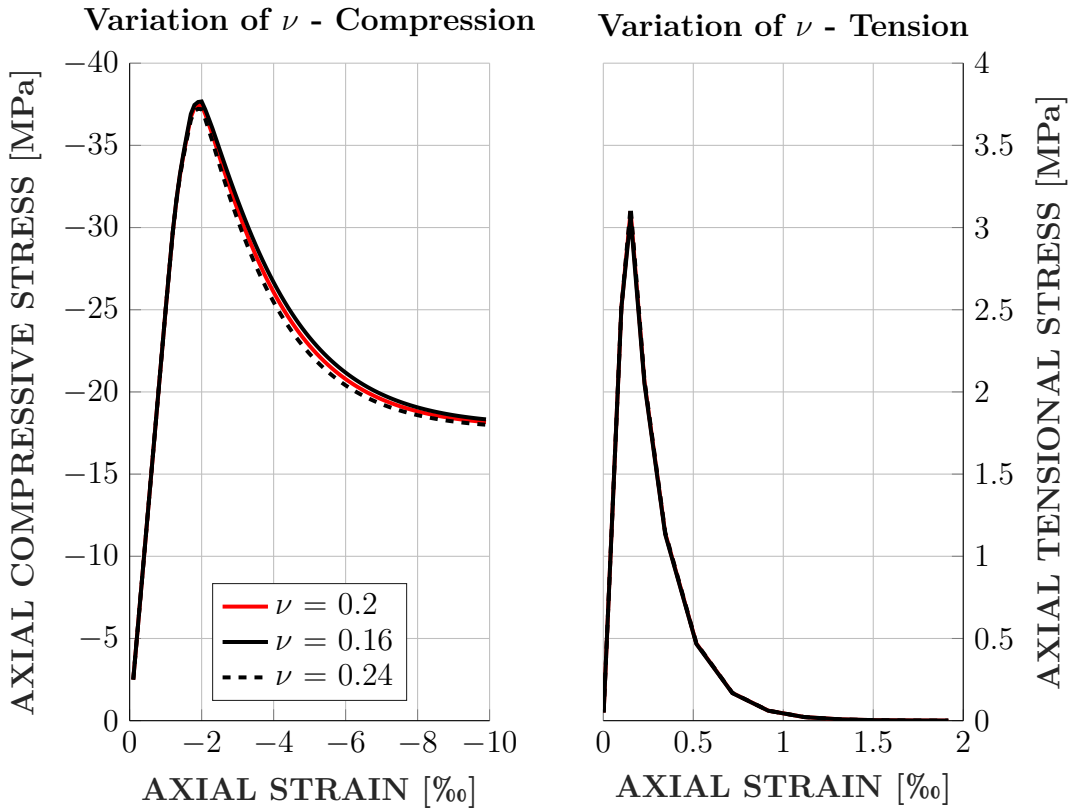
Fig. 4.13: Cube: parameter variation of Poisson ratio

Variation of c - Compression   **Variation of c - Tension**
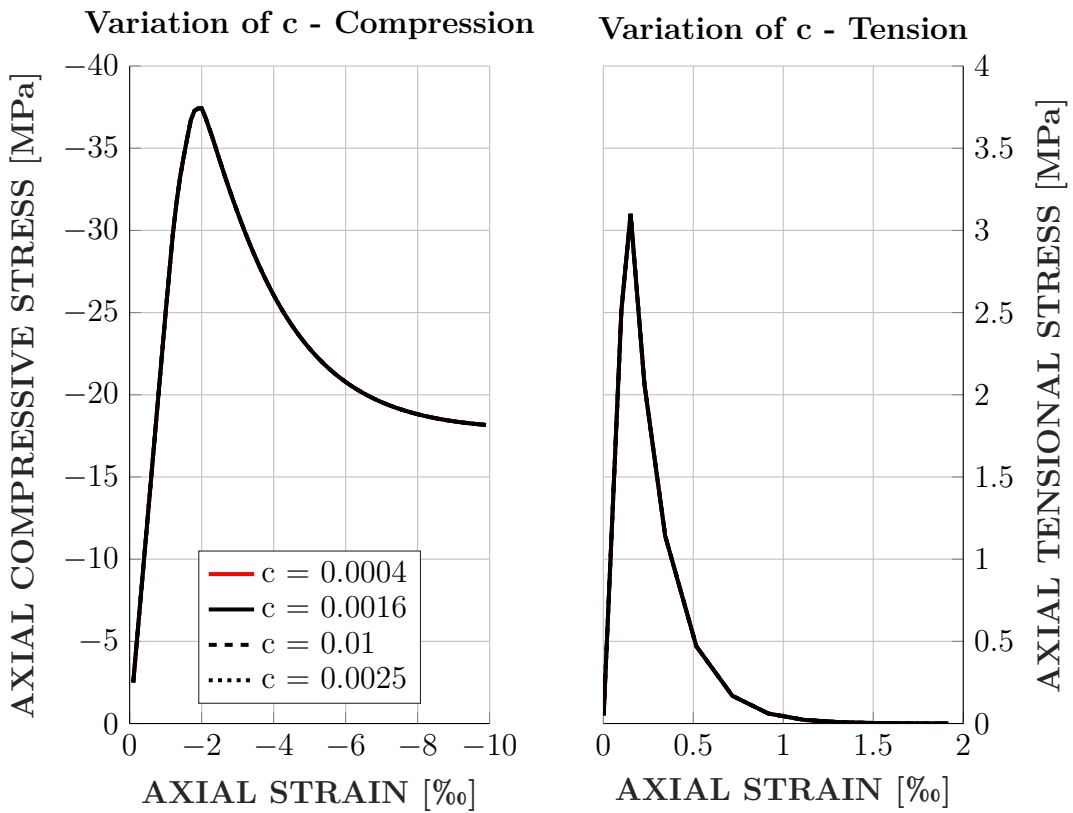
Fig. 4.14: Cube: variation of non-local interaction parameter

4.2.2 Cylinder

Aim of this analysis was to find a convergence value of the determined fracture energy by only varying a cylinder's diameter. As can be seen in figure 4.16, although the length of the cylinder remain unaltered, the softening evolution decreases with larger cross sections. Also, the responding stress value at the maximum displacement seems to increase with larger diameter sizes. Although the fracture energy seems to approach a certain value in figure 4.17, these values need to be corrected due to the previously described stress value at the maximum displacement. This correction was done with an exponential fit due through the post-peak softening curve and the determination of the inflected area.
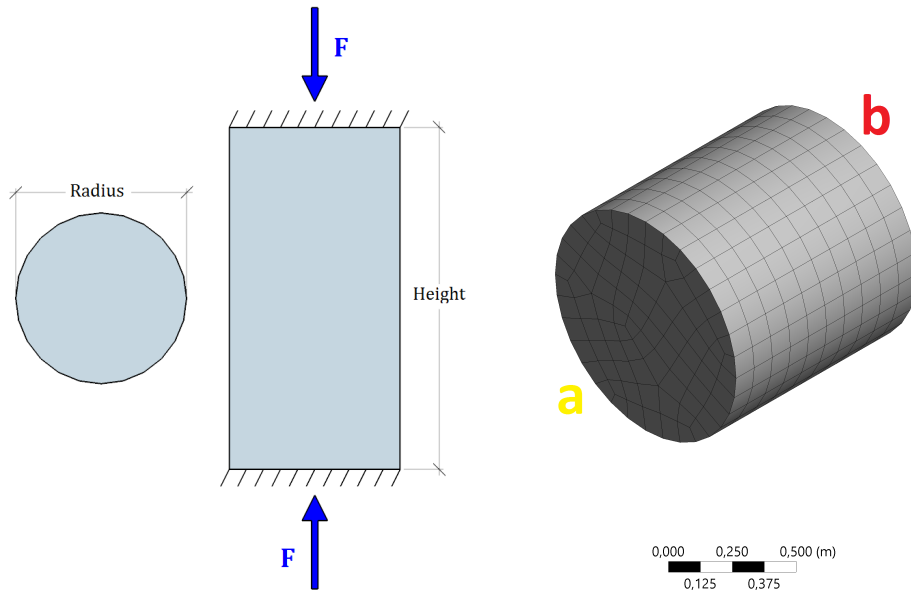
Fig. 4.15: Model setup and mesh for cylindrical specimen

Additionally, the stress distribution along the cylinders cross-section was obtained. Figures 4.18 and 4.19 shows a quadratic stress distribution with higher stresses at the boundaries during the post-peak regime and a linear stress distribution in the elastic one. These two observation fit the theoretical expectations. Input parameters for the microplane model are listed in table 4.5.

Geometry and Mesh

The mesh consists of linear hexahedral CPT215 elements with an edge length of 0.1 m.

Mesh properties	Cylinder 1	Cylinder 2	Cylinder 3	Cylinder 4	Cylinder 5	
Radius	100	200	500	750	1000	mm
Height	1000	1000	1000	1000	1000	mm
Area	0.031	0.126	0.785	1.76	3.14	m^2
Area Elements	0.028	0.122	0.780	1.76	3.14	m^2
Nodes	121	418	1155	2519	4312	
Elements	60	290	880	2040	3590	

Tab. 4.4: Mesh properties

Face (a) was fixed in all three spacial directions. A ramped displacement of 0.0005 m was applied on face (b) in axial direction. Meanwhile, the displacements on face (b) in the normal directions kept zero.

Input Parameters			
Young's modulus	E	28300	MPa
Poisson ratio	ν	0.18	
Uni-axial compressive strength	f_{uc}	44.7	MPa
Uni-axial tensional strength	f_{ut}	2.10	MPa
Tension cap parameter	R_t	1	
Hardening parameter	D	10000	
Compression cap parameter	R	2	
Non-local range	c	0.01	
Non-local interaction parameter	m	2.5	
Tensional damage threshold	γ_{t0}	0	
Tensional damage evolution parameter	β_t	8000	
Compressive damage threshold	γ_{c0}	0.001	
Compressive damage evolution parameter	β_c	1000	

Tab. 4.5: Material model input parameters

Results

An APDL-script was created to obtain the fracture energy using a fictitious crack width w. Therefore, the axial reaction force F on one the fixed end of the cylinder (a) and the displacement u on face (b) were recorded on 50 equally spaced time points. The fictitious crack width w was calculated by:

$$w = u - F \cdot \left(\frac{h}{EA} \right) \tag{4.19}$$

where

$$
\begin{array}{lll}
w & \dots & \text{fictonal crack width} \\
u & \dots & \text{displacement} \\
F & \dots & \text{axial force} \\
A & \dots & \text{cross section area} \\
h & \dots & \text{cylinder height} \\
E & \dots & \text{Youngs modulus}
\end{array}
$$

Then fracture energy was calculated as integral of the axial force over the crack width:

$$G_F = \frac{1}{A} \int F \mathrm{d}w \approx \frac{1}{A} \sum_{n=1}^{50} \frac{F_{n-1} + F_n}{2} \cdot (w_{n-1} - w_n) \tag{4.20}$$

Finally, the obtained fracture energy was plotted over radius of the cylinder.
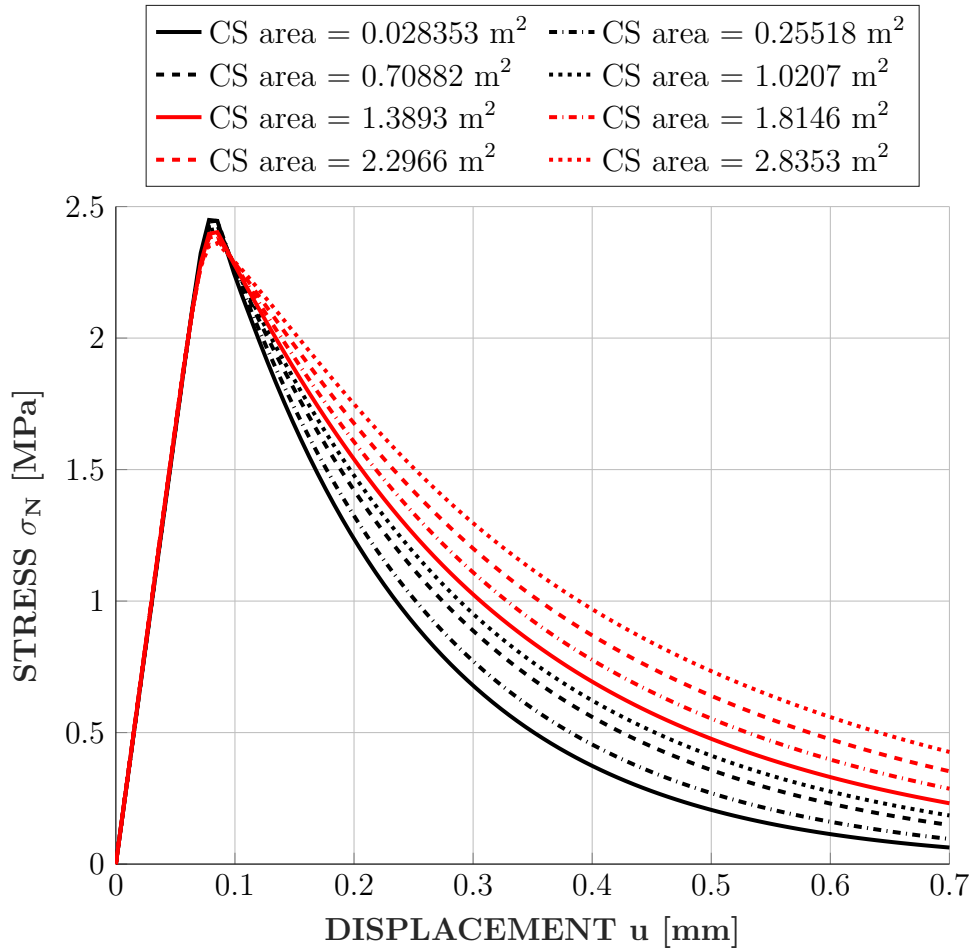
Fig. 4.16: Variation of diameter: influence on post-peak softening behaviour
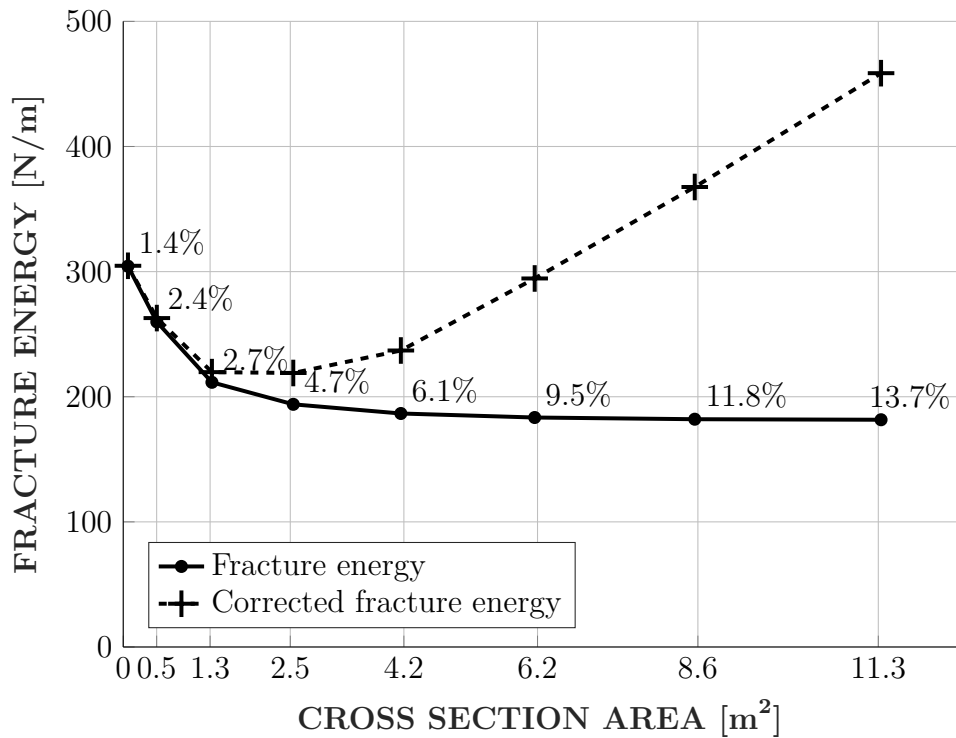
Fig. 4.17: Variation of diameter: influence on fracture energy
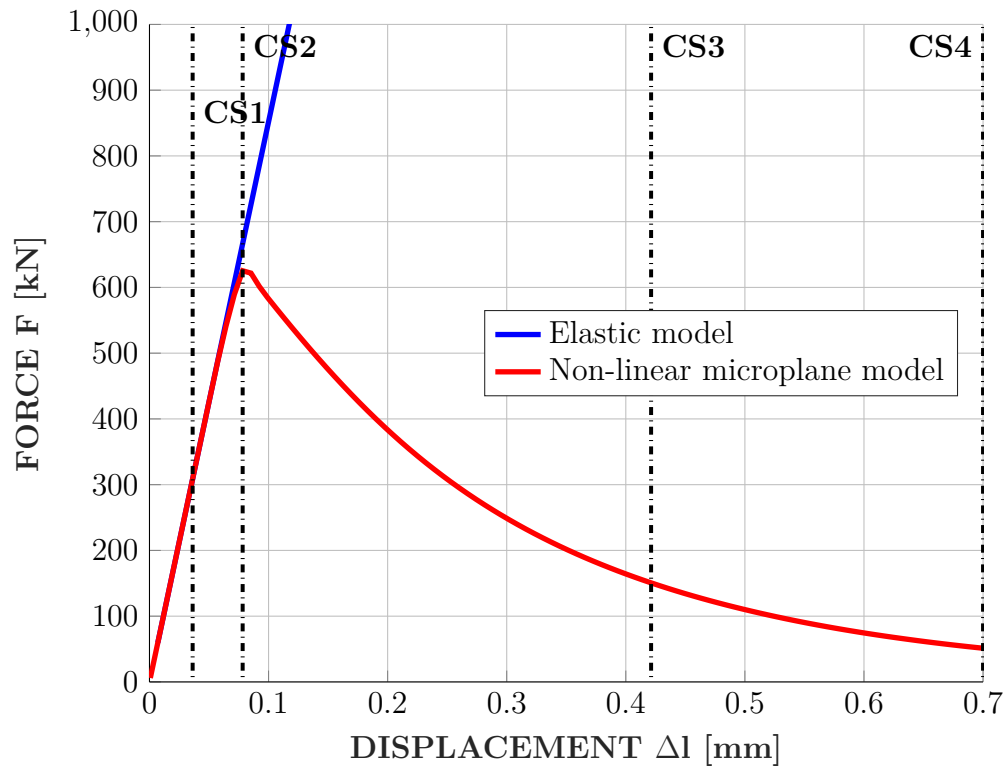
Fig. 4.18: Force displacement curve of linear and non-linear material model
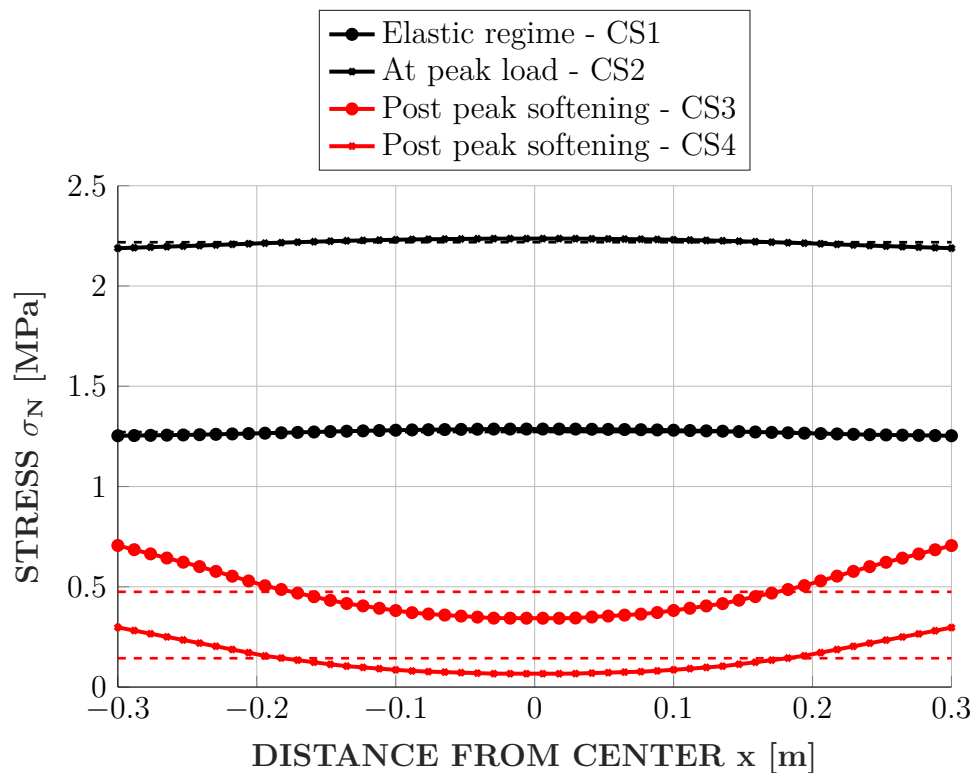
Fig. 4.19: Stress distribution in cross section for non-linear material models

4.2.3 Vertex Test

One of the advantages of the microplane model is its capability to reproduce effects hardly covered by invariant models, where constitutive laws are described by invariants of the stress and strain tensor. An example for such effects is presented by Bažant and Caner in 2002 [32], the so-called vertex effect. The consequence of this effect can be shown by an simple experiment: a compressive deformation is applied on a cylindrical specimen until the stress response shows softening behaviour. Then the axial deformations is stopped and an additional rotational deformation is started. The axial deformation, the rotational angle and the required force and torque for the deformations are recorded and plotted in charts. From these charts the initial stiffness for both, axial deformation and rotation, are determined. If the results from the experiment are then compared to the numerical ones, it is shown that the initial rotational stiffness for post peak rotation is lower than the one resulting invariant based material models. On the other hand the microplane material model is able to reproduce the degradation of the initial stiffness quite well.
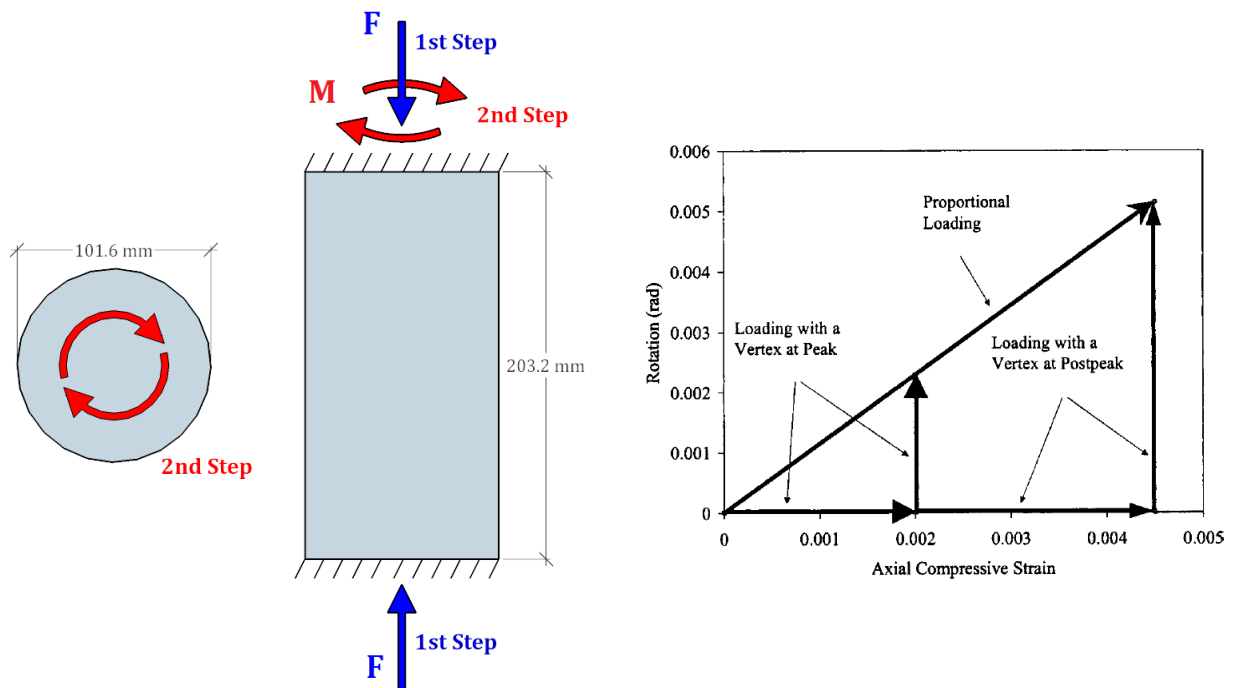
Fig. 4.20: Model setup and load application for the vertex test [32]

The idea was now to use the coupled damage-plasticity microplane model from *Ansys Mechanical* to replicate these results. Therefore, the cylindrical specimen was modelled using 784 linear, hexagonal element mesh with a fixed support on bottom. On the top, the deformations were applied in two loadsteps, i.e. an axial deformation up to -9.144×10^{-4} mm followed by an axial rotation up to $-0.2865°(= 5$ rad) (see figure 4.20). Resulting torque and force were obtained at the bottom of the specimen. Deformation and rotation were obtained at the top of it. Only the loading change at post-peak were modelled, because then the vertex effect is at its high.

The necessary input parameters for the new model were obtained from the input for the invariant model (grain size, Young's modulus, Poisson's ratio, uni-axial strengths) and by fitting the stress-strain curve of the experiment. The parameters of the microplane model M4 from the paper could not be reused due to the different constitutive laws on used on the

microplane level, i.e. stress-strain boundaries in model M4 and a Drucker-Prager yield function in the coupled *Ansys Mechanical* model.

Input parameters for the microplane model as well as element size were varied one after another and the results were plotted in respect to the ones obtained by the parameters in table 4.6.

Input Parameters			
Young's modulus	E	36900	MPa
Poisson ratio	ν	0.18	
Uni-axial compressive strength	f_{uc}	38	MPa
Uni-axial tensional strength	f_{ut}	3.23	MPa
Tension cap parameter	R_t	1	
Hardening parameter	D	7800	
Compression cap parameter	R	2	
Non-local range	c	0.000812	
Non-local interaction parameter	m	2.5	
Tensional damage threshold	γ_{t0}	0	
Tensional damage evolution parameter	β_t	400	
Compressive damage threshold	γ_{c0}	0.000287	
Compressive damage evolution parameter	β_c	600	

Tab. 4.6: Material model input parameters

Geometry and Mesh

The mesh consists of 784 linear hexahedral CPT215 elements with an edge length of 0.015 m.
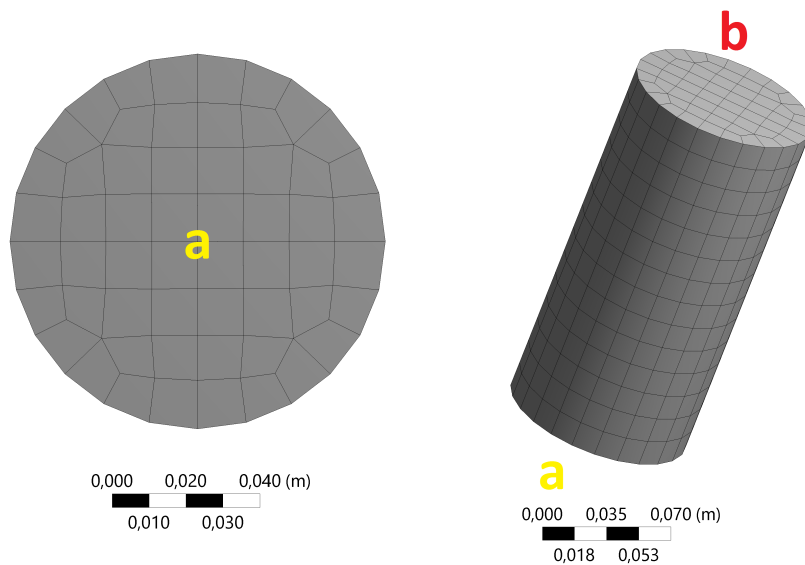
Fig. 4.21: Cylindrical mesh for vertex test

Mesh properties		
Form	Cylinder	
Diameter	101.6	mm
Height	203.2	mm
Area	0.032	m²
Nodes	1035	
Elements	784	
Element length	0.015	m

Tab. 4.7: Mesh properties

Face (a) was fixed in all three spacial directions. Displacement was applied in two loadsteps on face (b). The first loadstep consists of a ramped compressive displacement up to a maximum of -0.0009144 m in axial direction. Meanwhile, the displacements on face (b) in the normal directions kept zero. In the second loadstep, a ramped axial rotation of 0.2865 degrees (=0.005 radiant) was applied. Displacements on face (b) were kept the same as in the end of the first loadstep.
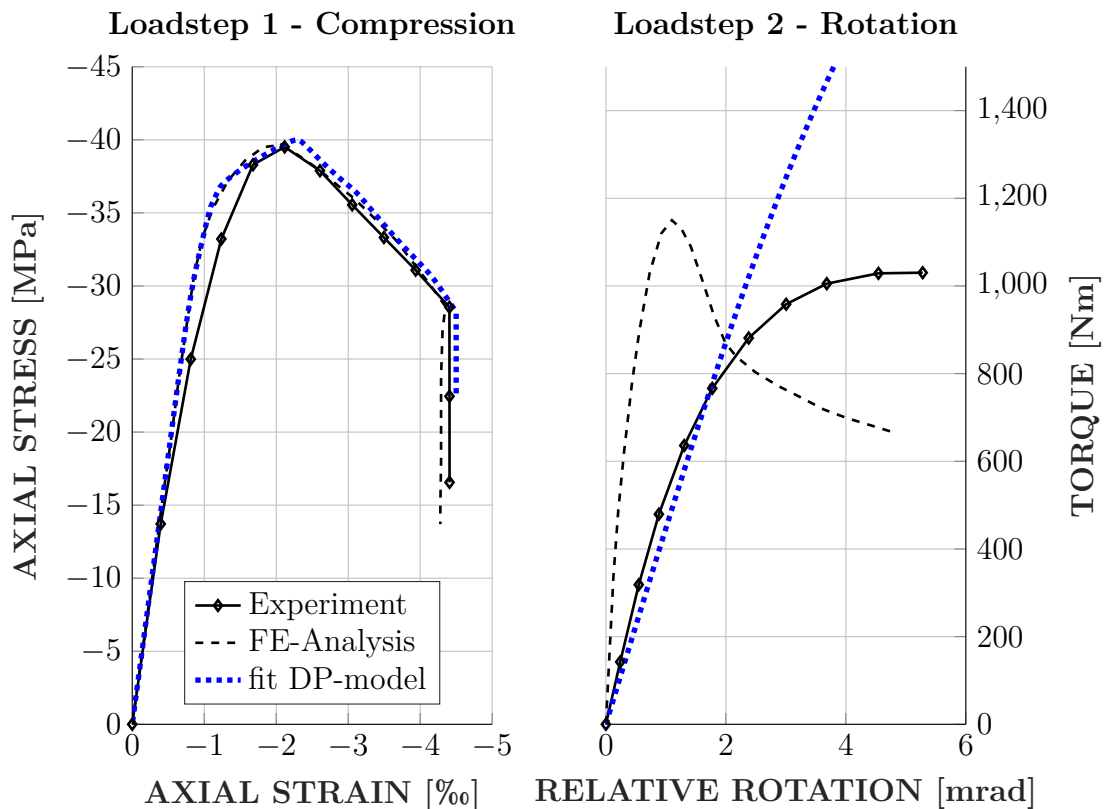
Fig. 4.22: Stress-strain and moment-rotation curves obtained from the experiment and numerical analysis

Results - Parameter Study

Two types of plots were created. One displays axial stress over axial strain and the other one shows reaction torque over rotation.

Variation of f_{ut} - Compression   **Variation of f_{ut} - Torque**
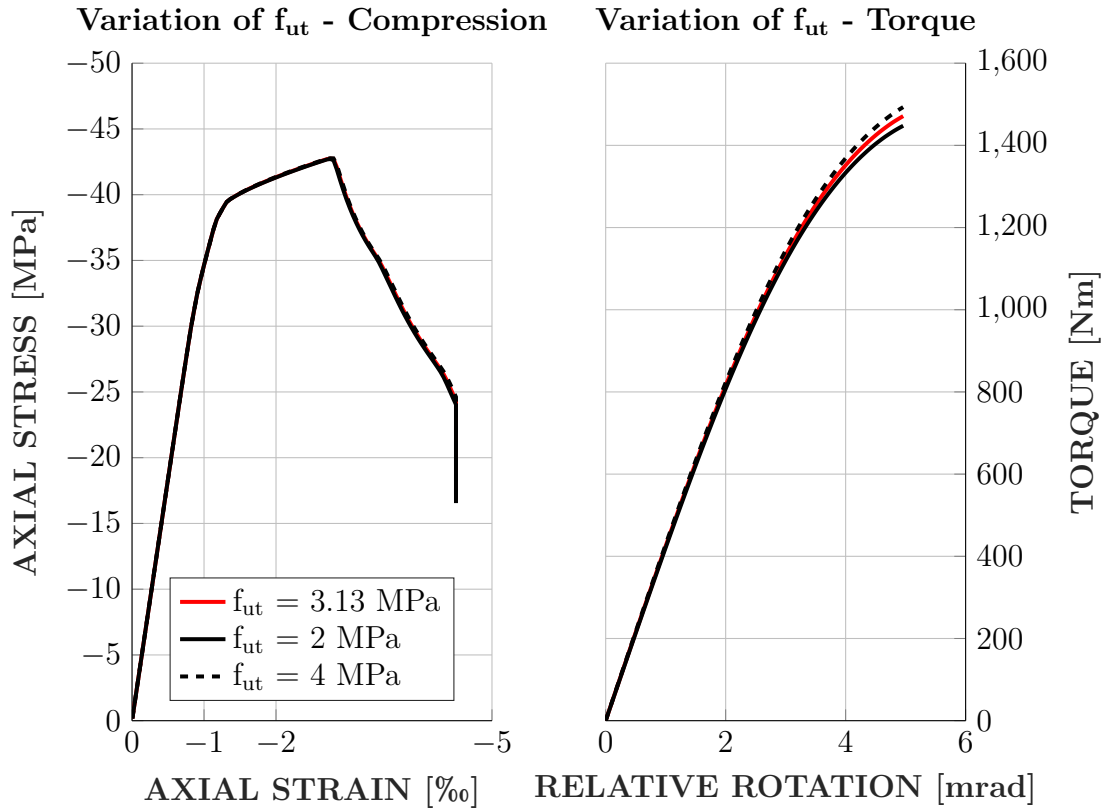
Fig. 4.23: Vertex-test: parameter variation of uni-axial tension strength

Variation of γ_{c0} - Compression   **Variation of γ_{c0} - Torque**
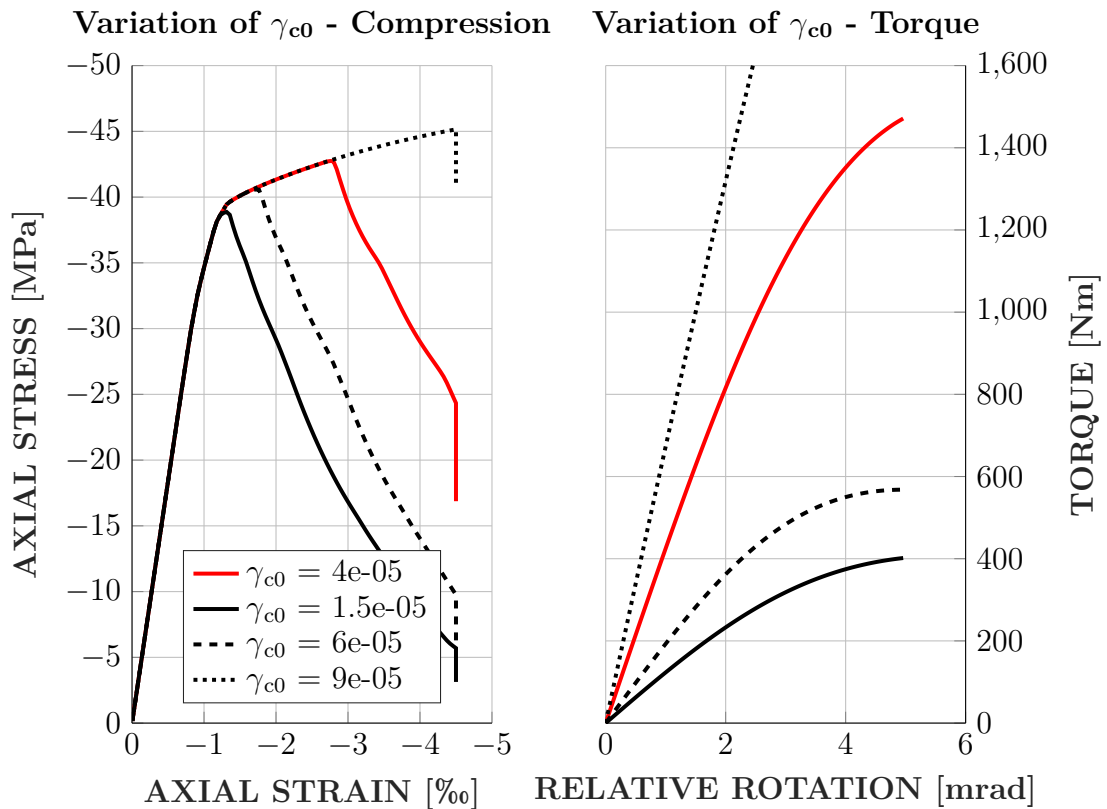
Fig. 4.24: Vertex-test: parameter variation of compression damage threshold

Variation of D - Compression

Variation of D - Torque
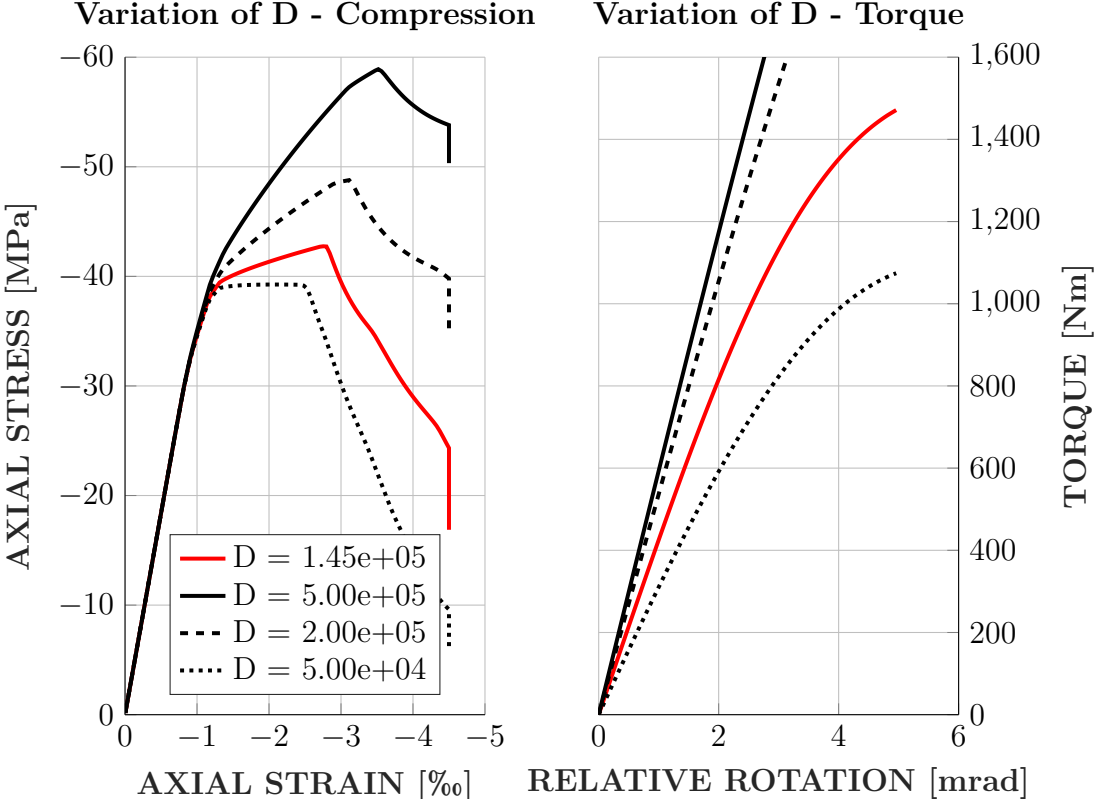
Fig. 4.25: Vertex-test: variation of hardening parameter

Variation of β_t - Compression

Variation of β_t - Torque
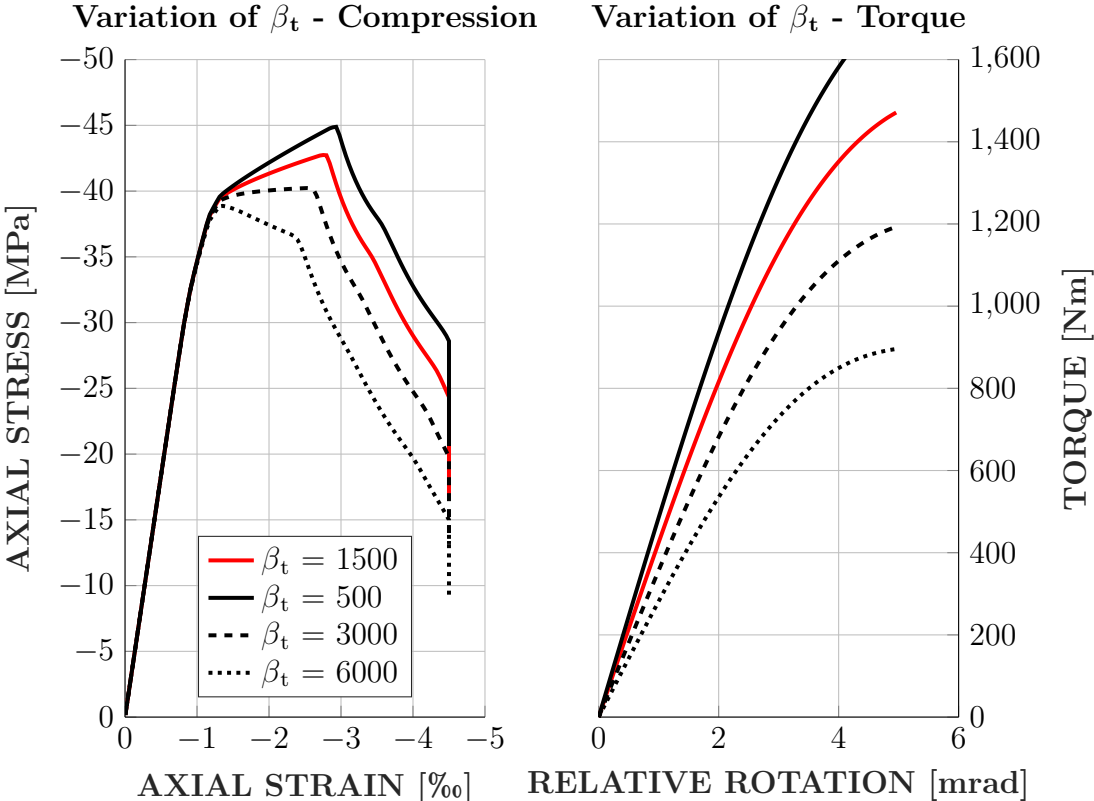
Fig. 4.26: Vertex-test: variation of tensional damage evolution parameter

Variation of β_c - Compression

Variation of β_c - Torque
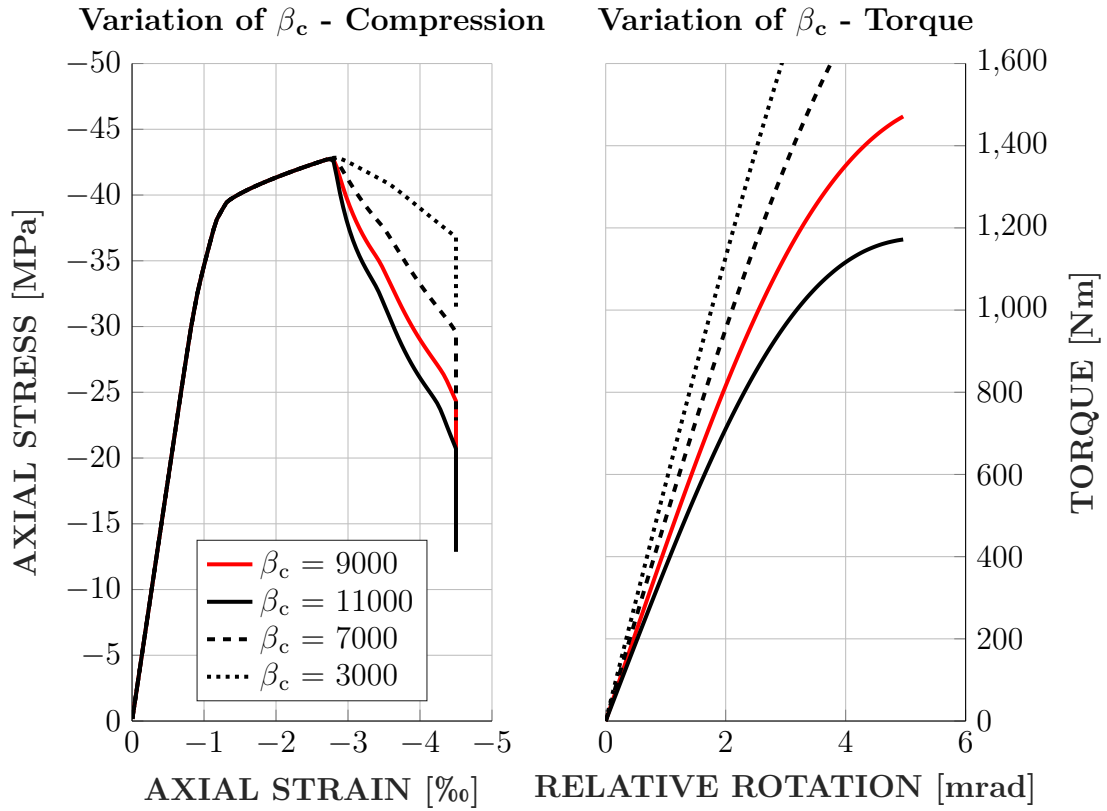
Fig. 4.27: Vertex-test: variation of compression damage evolution parameter

Variation of c - Compression

Variation of c - Torque
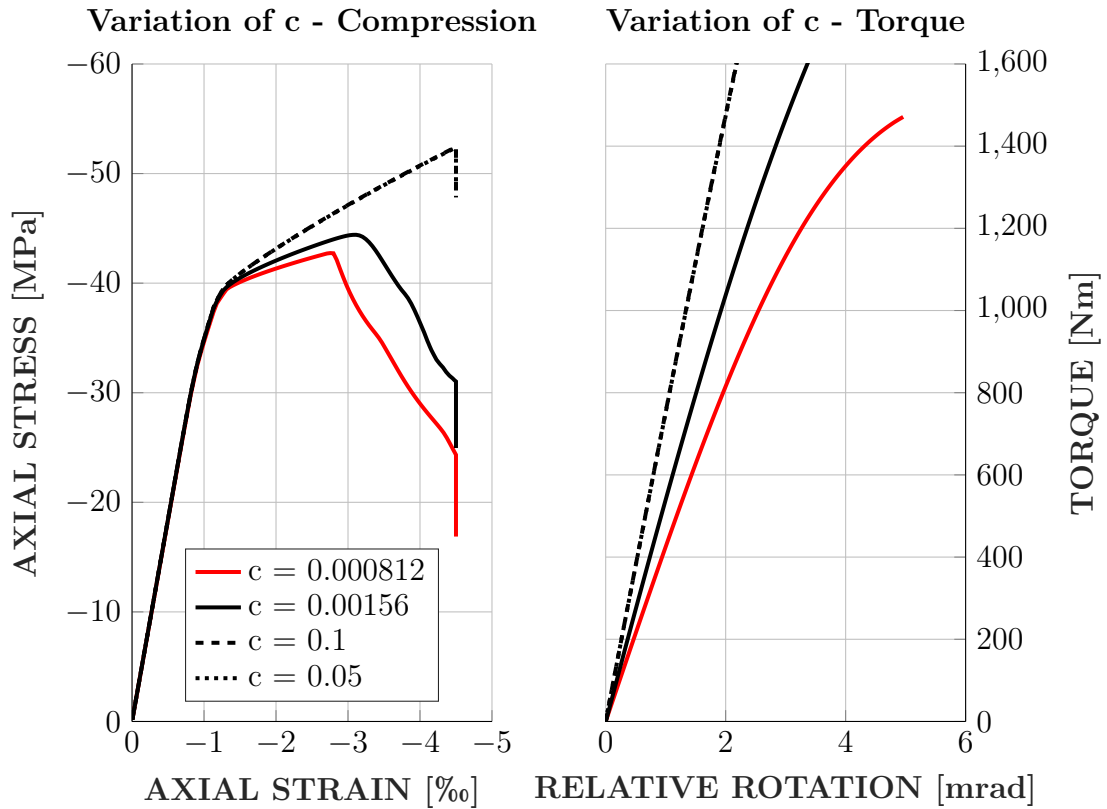
Fig. 4.28: Vertex-test: variation of non-local interaction parameter

4.2.4 Mesh Dependency (L-Shaped Plate)

Aim of this parametric study was to show the sensitivity of damage models the used element size and shape. Furthermore, the effects of non-local strain interaction should be presented. The test geometry is a L-shaped profile in plane strain. A skew and structured mesh in two different refinements were created. First the simulation was computed without non-local interaction. Afterwards it was repeated with an active non-local interaction. Both material models used the same input parameters.

The final damage distribution was compared (see figure 4.30 and 4.31) and a force displacement curve was created (see figure 4.2.4). It is clearly shown that the mesh size as well as the mesh skewness has a significant influence on the results obtained from a local model. The model with non-local regularization on the other hand remains untouched by the different mesh types.
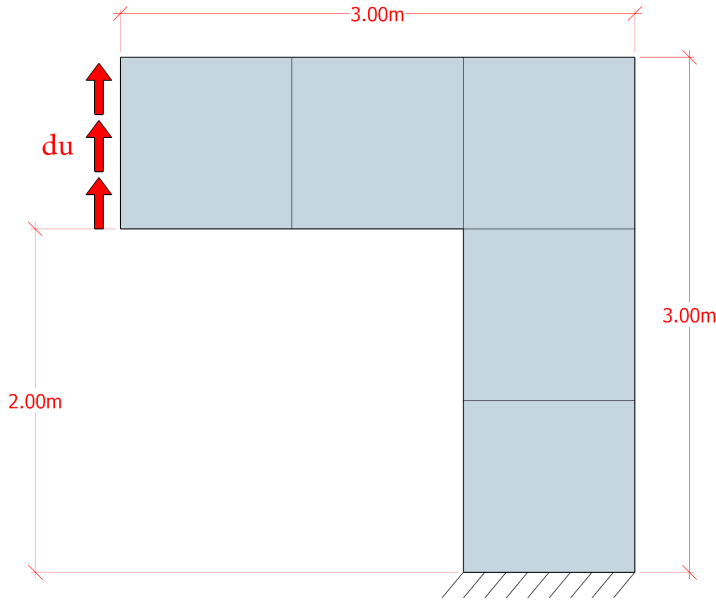
Fig. 4.29: L-shape geometry

Parameters

E	31600	MPa
ν	0.18	
f_{uc}	44.7	MPa
f_{ut}	2.10	MPa
R_t	1	
D	1	
R	2	
c	0.02	
m	2.5	
γ_{t0}	0	
β_t	5000	
γ_{c0}	0.0001	
β_c	1000	

Tab. 4.8: Material model input parameters

Geometry and Mesh

Four different meshes were created.A structured, orthogonal one with quadratic-shaped elements an edge length of 0.10 m and 0.05 m. The other one with skew elements with a diagonal of 0.10 m and 0.05 m. All meshes were created from two-dimensional, linear CPT213 elements.

The model was locked in vertical and horizontal direction on the bottom. A displacement of 0.001 m was applied in upwards direction on the left face of the model (see figure 4.29). Due to the used CPT elements, the model was computed in plane strain.

Input parameters for the microplane model are listed in table 4.8. The material model was applied on four different meshes with and without non-local interaction. This interaction was controlled with the parameter c. For $c = 0$ the non-local interaction is deactivated and only local strains are taken into account.

Results

Reactional force was computed at the support. Only the vertical part was used in the force displacement curves. Vertical displacement was obtained from the left face (see figure 4.29).

The plotted damage variable represent the maximum tensional damage from all microplanes

at the integration points. Due to the used CPT elements, values at integration points are written directly as nodal results (no extrapolation is computed).

Figures 4.30 and 4.31 show the damaged area at time of the maximum displacement. Size and shape of this area is quite similar for the model with non-local regularization independent of mesh element sizes or orientation. On the other hand, the model without regularization shows a clear dependency on the used mesh.

(a)   **(b)**

(c)   **(d)**
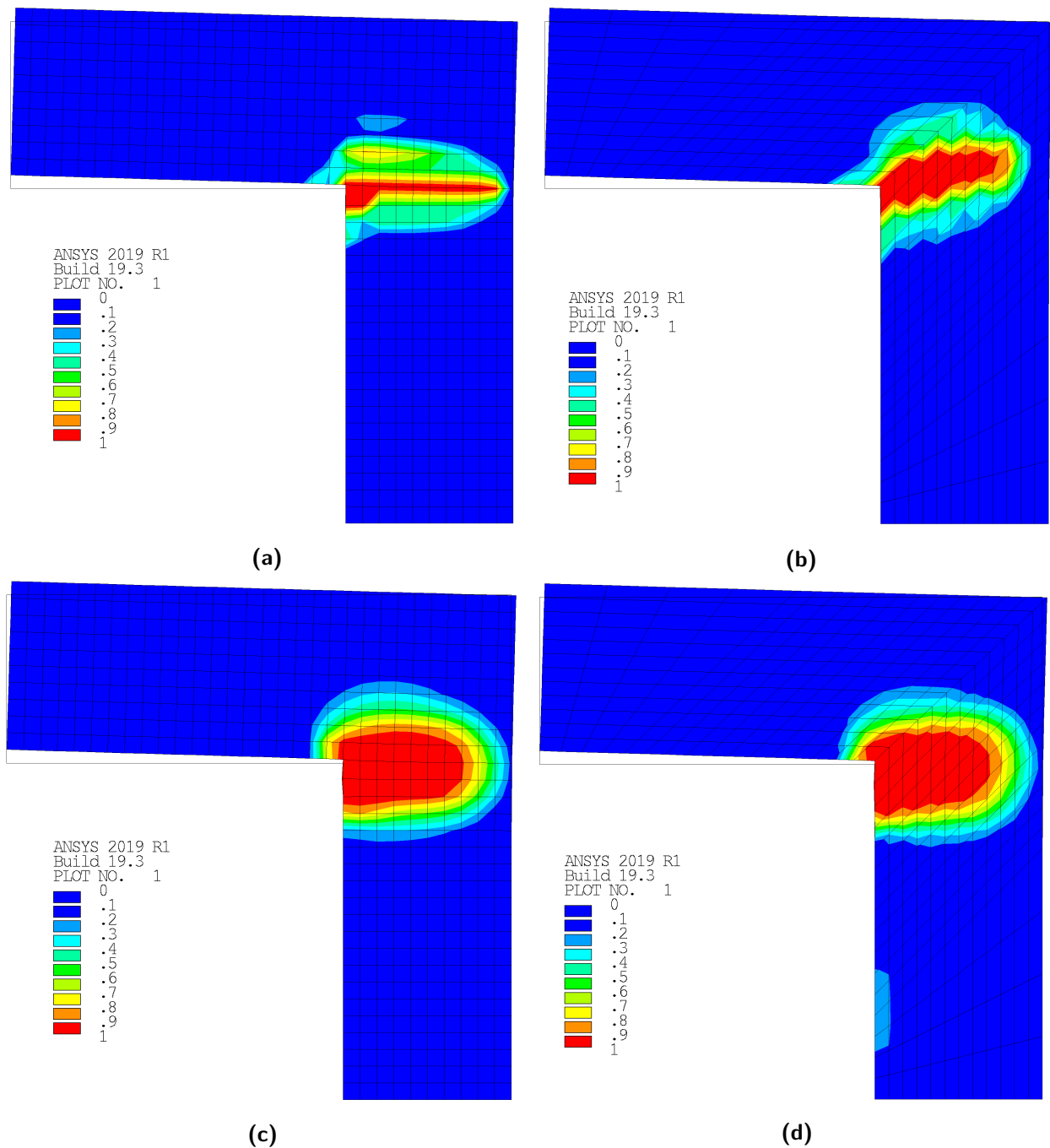
Fig. 4.30: Damage distribution for skewed and structured meshes with non-local interaction (see **(c)** and **(d)**) and without non-local interaction (see **(a)** and **(b)**)

(a)

(b)

(c)

(d)
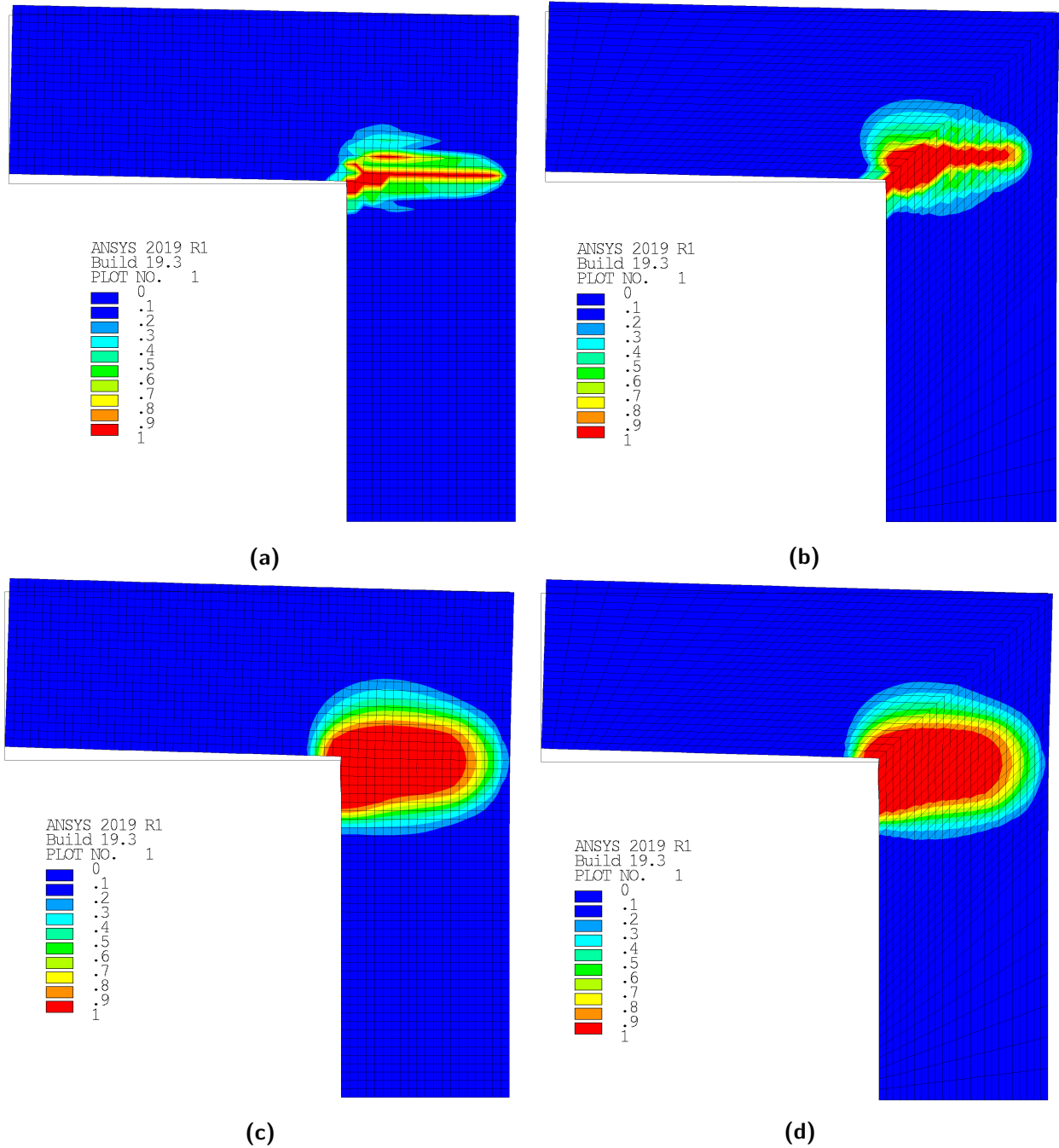
Fig. 4.31: Damage distribution for refined skewed and structured meshes with non-local interaction (see **(c)** and **(d)**) and without non-local interaction (see **(a)** and **(b)**)

Figure 4.2.4 shows the performance of the model as the reaction force versus the applied displacement. It can be seen that the model using non-local regularization delivers similar results independent of the used mesh. Also, it should be noticed that the reached peak value is larger than the one from the model without non-local regularization. This needs to be considered for the calibration of the non-local model.
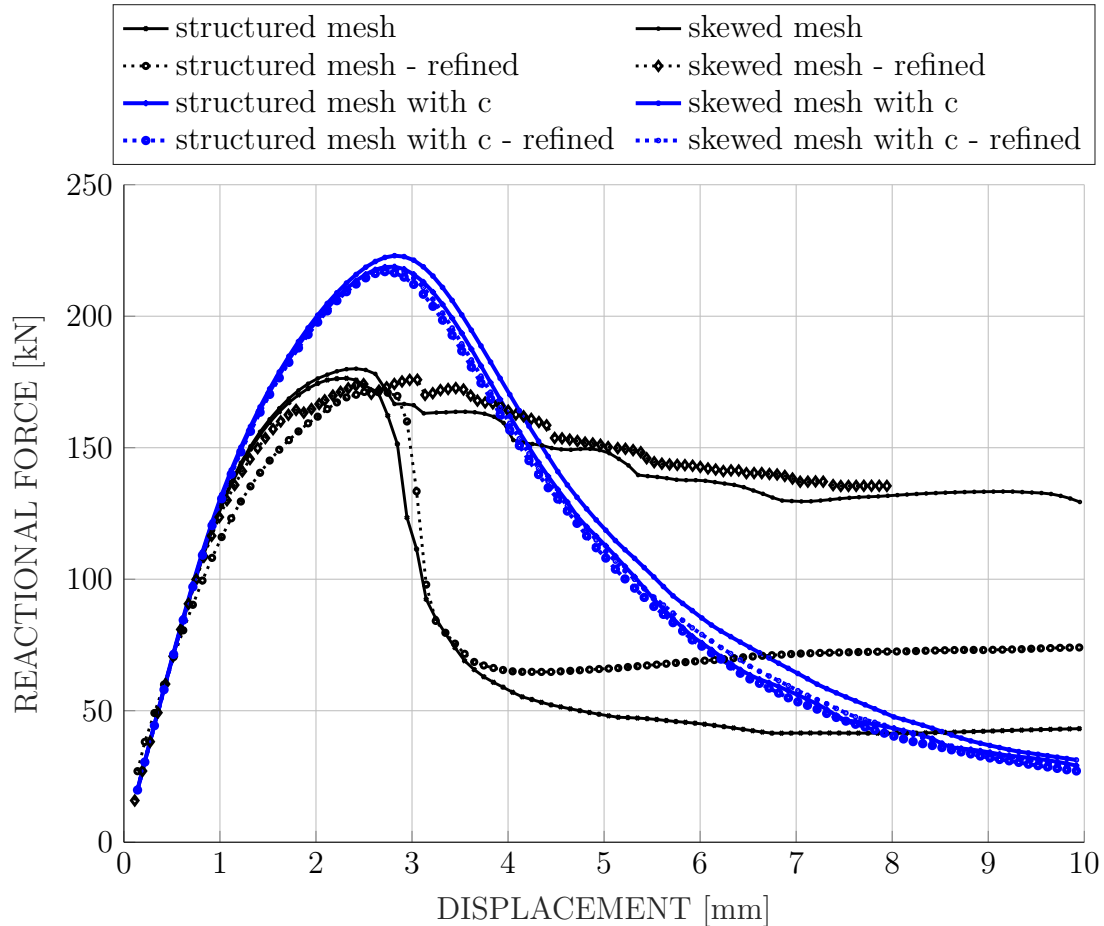
Fig. 4.32: L-shape: comparison of force displacement curves, in blue is shown the model with non-local regularization

4.3 Calibration of a Microplane Model

As mentioned in chapter 2.2.3, various ways are provided to calibrate the non-local range of the given microplane model, e.g. calibration on tensile test data [12], crack roughness [46] or due size effect [9]. However, due to the lack of specific test data on dam concrete, none of these calibration procedures seemed to be feasible. Another problem is the model size itself. In order to appropriately represent the interaction inside the fracture process zone the used element size is restricted to the selected non-local range. Although dam concrete possesses large grain sizes - which is according to Bažant [12] the main factor for estimation of the size of the FPZ - the ratio between FPZ' size and the model of the dam is quite small. This leads to very fine meshes consisting of a tremendous amount of elements.

The aim was to calibrate the material model on a small scale and verify it on a dam scaled model. Therefore, three calibration attempts are presented in this chapter. A first verification of these calibrations is a comparison of displacement and hydrodynamic pressure data from FE analyses of the Pine Flat Dam done by the *15th International Benchmark Workshop on Numerical Analysis of Dams*, 2019 in Milan. These results are then presented in chapter 5.5.

⬦ **Brazilian Test:** Force displacement curves of Brazilian test were encountered in a Doctoral thesis done by *Trunk* [8]. The curves were obtained from various specimen sizes and concrete types. Especially the tests done on dam concrete were from high interest.
Two different calibration attempts were performed. First, the influence of the non-local parameter was evaluated. The aim was to vary only the non-local range to fit the force-displacement curves from different sized specimens, while the other material parameters were kept constant. However, this was not even achieved for fitting the peak force only 4.35. Second, the non-local range was determined from the used maximum grain size. Then, the curve of the largest specimen was fitted. However, the model's response was much stiffer than expected 4.37. Therefore, the stress distribution along the crack line was examined and compared with a theoretical reference. From there it was concluded, that the singularity at the notch tip leads to a kind of stress looking. This may be the cause of the much stiffer response. However, these numerical difficulties weren't overcome during this master thesis.
Finally, it can be stated that the calibration of the tested model on Brazilian tests is not feasible due the substantial influence of the boundaries on the non-local regularization.

⬦ **On Single Element:** Because the damage evolution law is defined due plastic strains, a length scale is needed to derive a fracture energy. Therefore, a characteristic length was used. Initially, this length was determined by the theoretic length of the fracture process zone, thus this leads to very damage evolution parameters. In order to avoid convergence problems resulting from these high values, the width of the FPZ was used instead. Also, a formula for the direct determination of the tension damage evolution parameter β_t from fracture energy could be derived.
However, for coupled damage-plasticity model the influence of the non-local regularization couldn't be determined.

⬦ **Three-Point Bending Test:** This testing procedure was thought to consider the non-local influence on a mode-I crack. This seems to be the principle crack mode for gravity dams during seismic loading. There two calibration steps are involved. First, single elements are calibrated to represent the desired fracture energy. Then these elements were used in a crack band to model an oversized three point bending test. Second, the non-regularization model is calibrated to fit the force-displacement curve or simply the fracture energy obtained from the previously done model.

4.3.1 Brazilian Test

The Brazilian Test is a laboratory test for indirect measurement of tensile strength of rocks or rocks. Usually, it is performed on cylindrical specimens where their size depends on the maximum grain size of the concrete. Due to the large grain sizes used in dam concretes and the lack of the therefore required testing machinery, the test is performed on notched blocks (see figure 4.33).
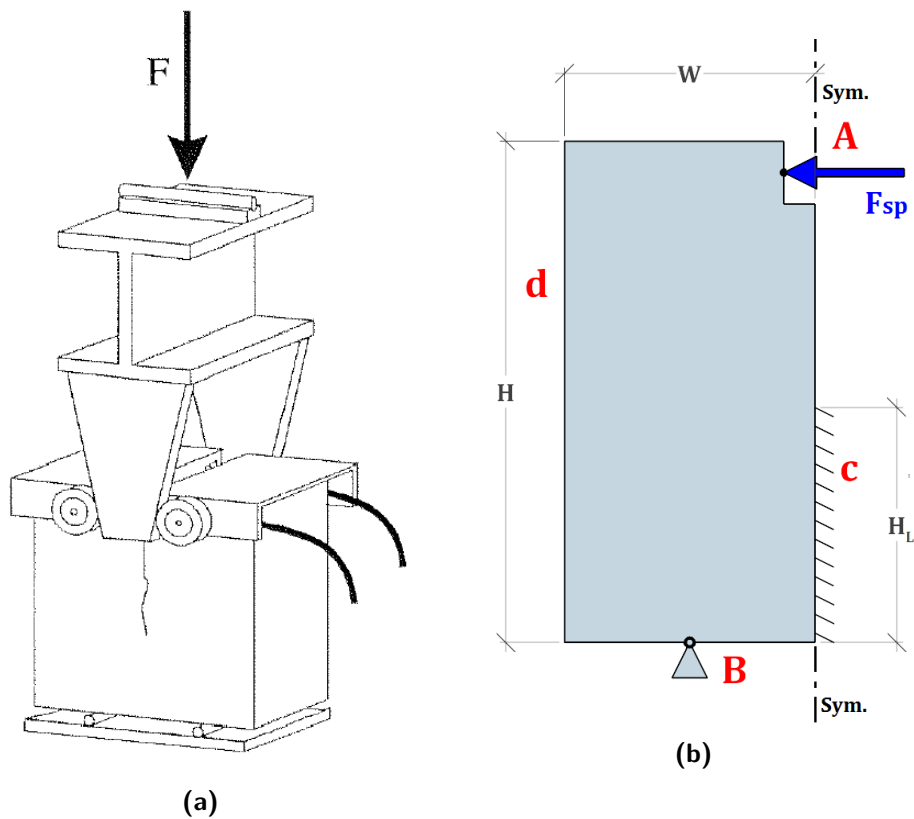
Fig. 4.33: Brazilian test: (a) experimental setup [8] and (b) model setup in *Ansys Mechanical*

Input parameters for the microplane model are listed in table 4.5.

Input Parameters			
Young's modulus	E	28300	MPa
Poisson ratio	ν	0.18	
Uni-axial compressive strength	f_{uc}	44.7	MPa
Uni-axial tensional strength	f_{ut}	2.10	MPa
Non-local range	c	0.01	
Non-local interaction parameter	m	2.5	
Tensional damage threshold	γ_{t0}	0	
Tensional damage evolution parameter	β_t	8000	
Compressive damage threshold	γ_{c0}	0.001	
Compressive damage evolution parameter	β_c	1000	

Tab. 4.9: Material model input parameters

Geometry and Mesh

The mesh consists of linear hexahedral CPT215 elements with an edge length of 0.05 m.
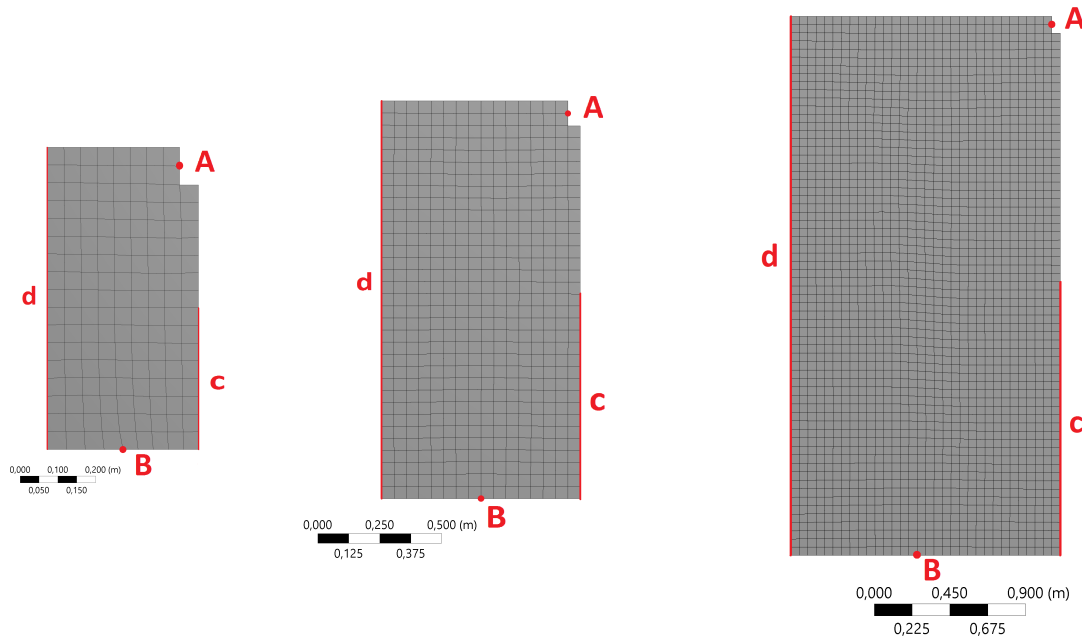
Fig. 4.34: Meshes for small, medium and large sized Brazilian test

In point (B), along the whole depth, the vertical displacement in Z-direction was fixed, rotation was permitted. Displacement in Y-direction was fixed along face (d) to ensure a sufficient constrained model. The alignment area (c) serves also as symmetry area to reduce specimens' dimensions. For loading, a horizontal displacement was applied in point (A).

Mesh properties					
Form		Small	Middle	Large	
Height	H	800	1600	3200	mm
Width		800	1600	3200	mm
Depth	t	400	400	400	mm
Notch	s	100	100	100	mm
	k	100	100	100	mm
Ligament	H_L	375	775	1575	mm
Area		0.15	0.31	0.63	m^2
Nodes		1602	5184	19584	
Elements		1208	4208	16624	
Element length		0.05	0.05	0.05	m

Tab. 4.10: Mesh properties

Results

Displacements and horizontal forces along (A) were recorded. A script was created to determine maximum diverting force, diverting force at maximum displacement and fracture energy. Fracture energy was calculated from fracture work divided by the crack area - idealized equal to alignment area (c). Fracture work is obtained by integration of the horizontal diverting force over its covered way. Due to symmetry, this way is equal to the double displacement obtained from point (A).

$$G_F = \frac{1}{A} \int F \mathrm{d}u \approx \frac{1}{A} \sum_{n=1}^{50} (F_{n-1} + F_n) \cdot (u_{n-1} - u_n) \tag{4.21}$$

Where

$$
\begin{array}{lll}
u & \ldots & \text{displacement in (A)} \\
F & \ldots & \text{diverting force} \\
A & \ldots & \text{alignment area}
\end{array}
$$
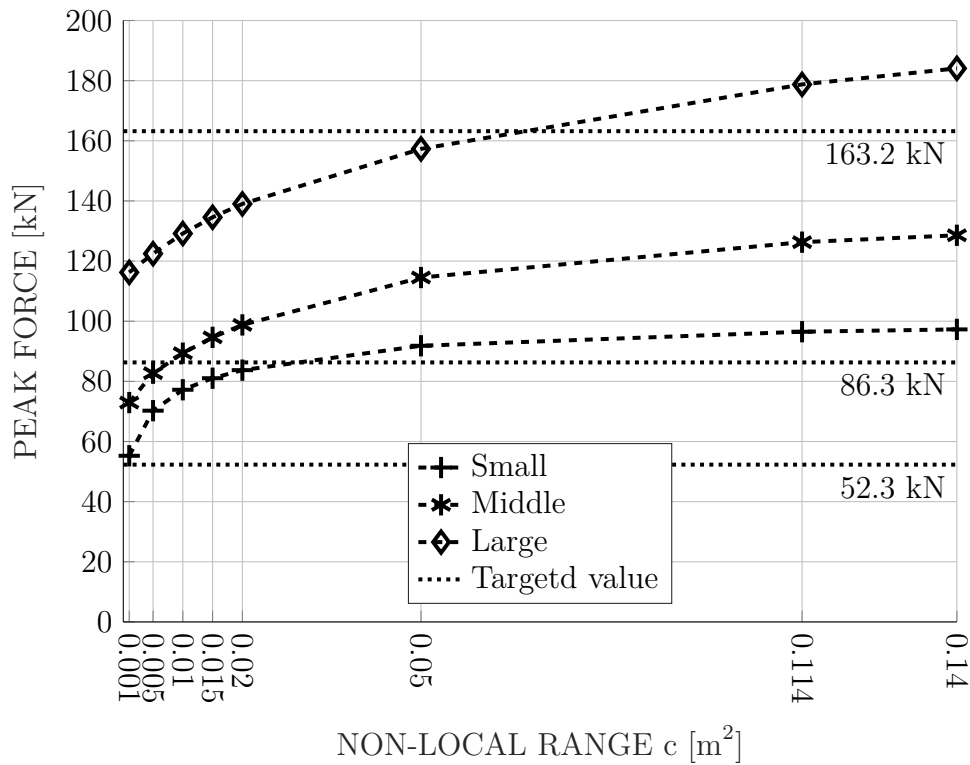
Fig. 4.35: Calibration attempt on peak force due varying of non-local range parameter

This calibration attempt is based on experimental data from Brazilian test carried out on dam concrete from [8]. There the splitting force and the crack opening width were measured. The fracture energy released during the process was calculated as the integral of the splitting force F over the crack opening width w divided by the ligament area A_L. This area represents the projection of the fractured surface into the ideal fracture plane.

$$G_F^{ref} = \frac{1}{A_L} \int F \mathrm{d}w \tag{4.22}$$

The first attempt to calibrate the parameters for the microplane model was to repeat the experiment numerically and fit the resulting force displacement curve to the one obtained from the experimental data. However, various parameters could be obtained directly from the data such as uni-axial compressive, Young's modulus and Poisson ratio as well as the maximum grain size of the concrete. Furthermore, compressive behaviour is assumed to remain linear during the whole process. This is proven due to no compressive damage resulted in any point (i.e. compressive strength limit is never reached) in the model test (see figure 4.37). Because of this assumption, parameters regarding post-peak compressive behaviour - compressive damage parameters, hardening parameter and compressive cap parameter - were taken from normal concrete given by the paper the model is based on [31]. The same applies for other parameters like non-local interaction range, bi-axial compressive strength and tensional damage threshold value. Those were calculated according to the presented paper. Finally, the only remaining parameters for the fit were the tensile damage progression parameter and uni-axial tensile strength. Although a uni-axial tensile strength was contained in the experimental data, a fit with this strength leads to a very high maximum fore and thus it was only considered as a reference. This is also reasonable because this strength was obtained from a direct tensile test and not from the experiment which was tried to be model.
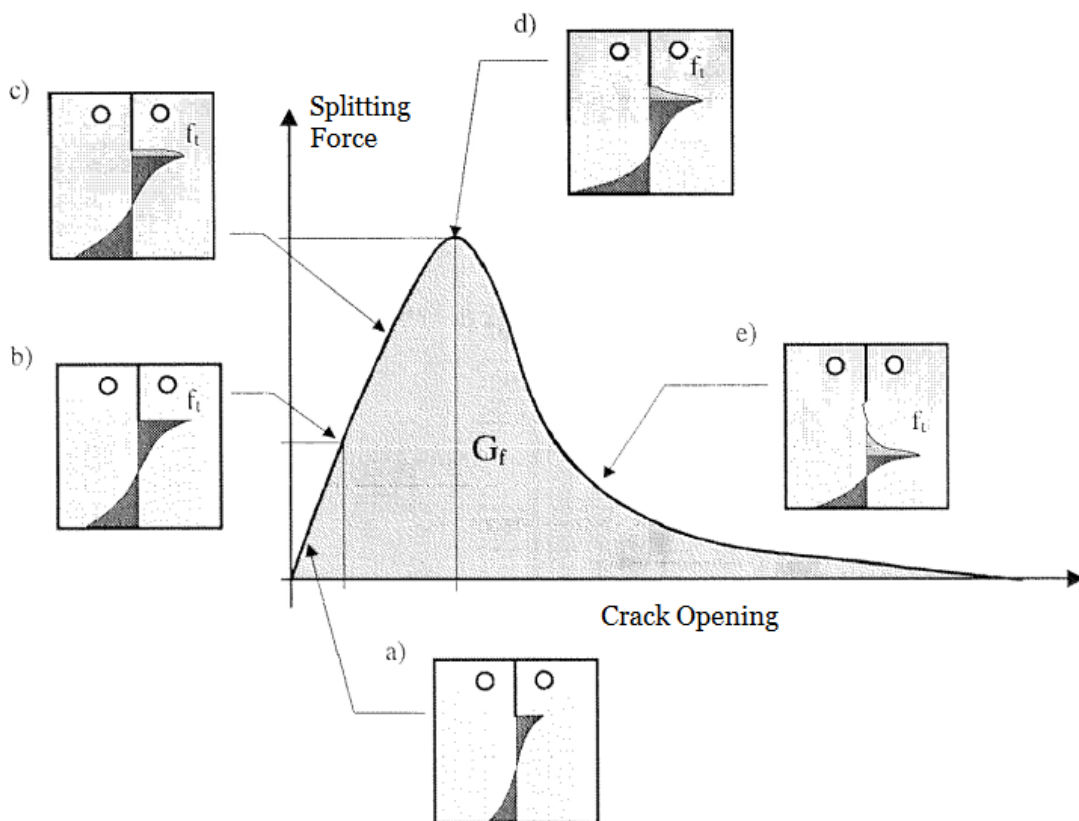
Fig. 4.36: Reference of the normal stress distribution along the crack line [8]

In the simulation, 3D and 2D models with and without symmetry were used. First, a complete three-dimensional one in order to verify results from a three-dimensional model with a symmetry plane (using linear or quadratic order elements). Second, two-dimensional model also using quadratic or linear elements. Horizontal force and horizontal displacement were obtained at attachment point of the applied force. This obtained displacement was then doubled to represent the crack opening width.

Fitting attempts - as the one in figure 4.37 - lead to very low tensile strength (lower than 30% of the reference value) and very high damage values. Besides the obtained fits were far from being satisfying, this high damage values also resulted into convergence problems. To overcome these problems the convergence criteria was altered from a combined force-displacement one to a pure displacement one. However, Instabilities in the softening area were not overcome. Following, the stress distribution normal to the fracture plane was obtained and compared with the reference from the experimental data set in figure 4.36.
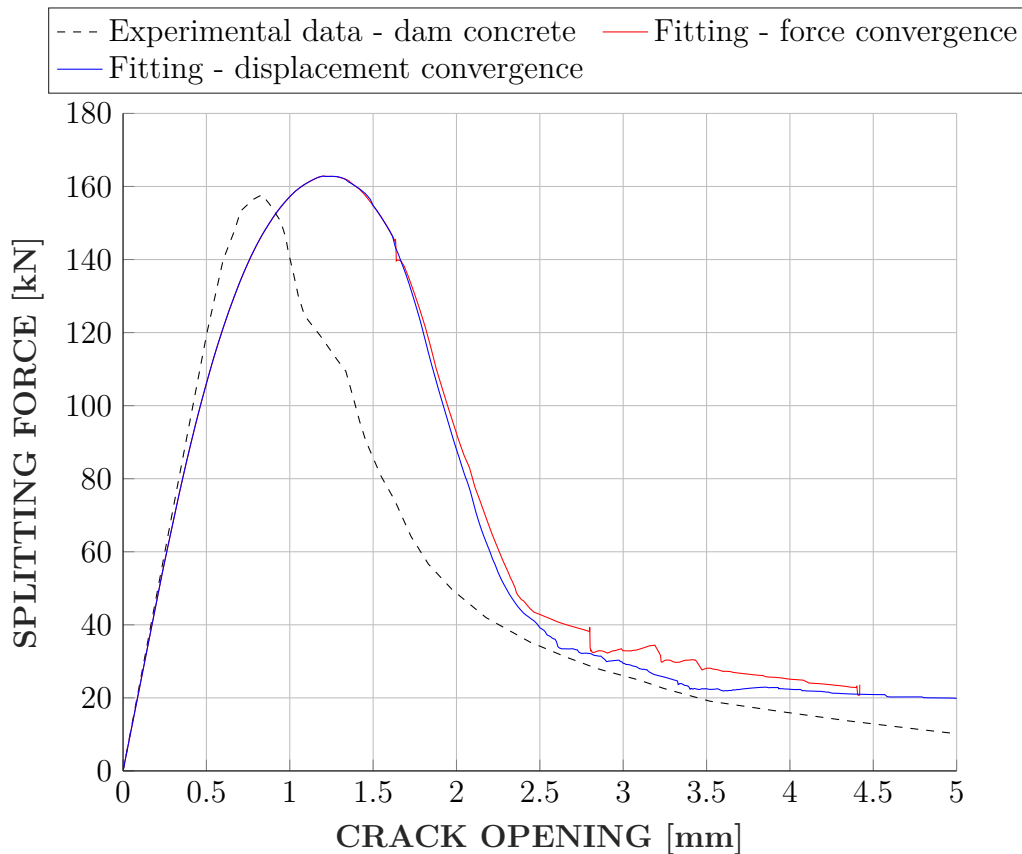
Fig. 4.37: Fitting attempts on the force displacement-curve

In figure 4.38, the normal stress distribution along the crack line depending on the crack opening width is plotted. Firstly, it can be stated that the shown distribution resemble the one from the reference (see figure 4.36). It overshoots the maximum tensile strength (given with 2 MPa) tremendously. Secondly, in close range to the crack tip, no softening behaviour happens at all. However, these results are obtained from various mesh sizes, 3D- and 2D-analysis.

Taken a closer look to the behaviour at the crack tip, figure 4.39 shows the directional stresses plotted over the crack opening width. Results are obtained from 2D-analysis. It can be seen, that the stress pointing outwards of the model plane (σ_Z) starts to decrease after the elastic yield limit was reached. This leads to high compressive stresses (forming horizontal tangent at nearly -10 MPa) acting. This results from the plane stress model configuration. The stress normal to the crack line ($\sigma_X = \sigma_N$) increase over the double of the actual tensile strength and forms a horizontal tangent. The stress in crack direction (σ_Y) reaches a maximum and then declines again until another horizontal tangent is reached. The shear stress (σ_{XY}) remains quasi zero, with small variation most likely depending on a numerical error. Furthermore, the damage variables can be seen. Both - tensional and compressive - remain zero. This, together with the clearly displayed reaching of the yield limit due stress behaviour, leads to following

conclusion: The equivalent strain, which controls the damage development and therefore the softening behaviour of the model, is the responsible factor for the obtained solution.
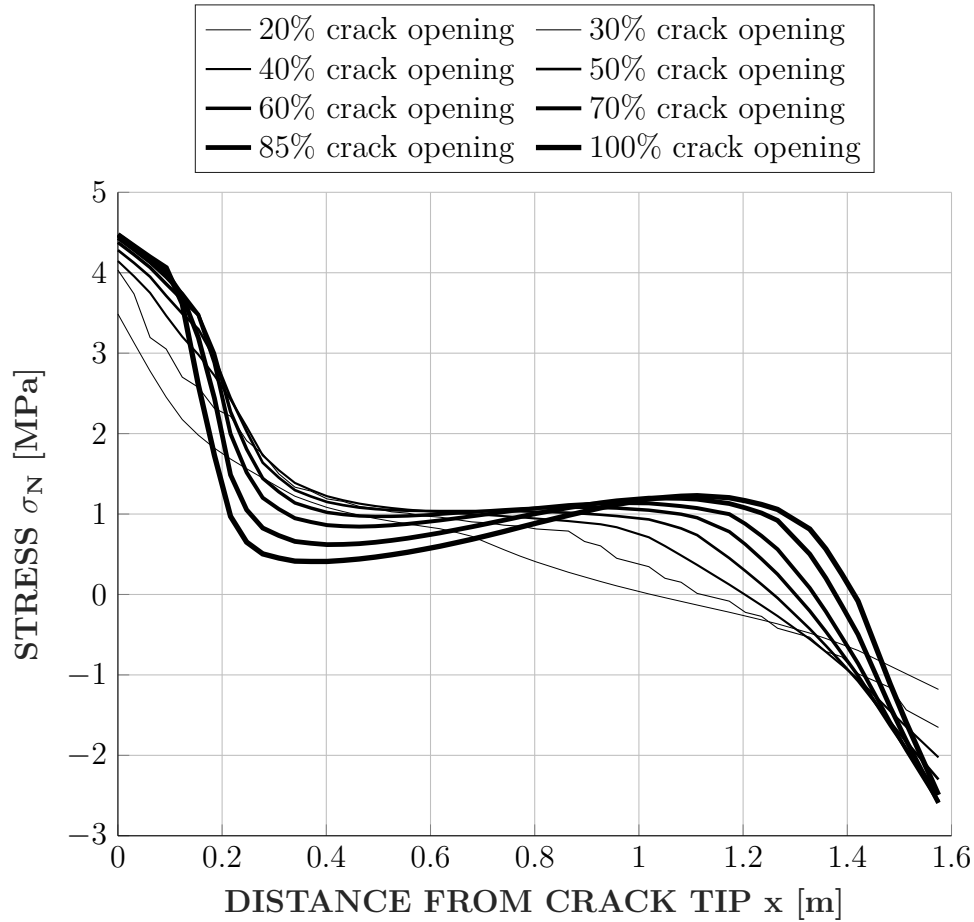
Fig. 4.38: Development of normal stress distribution along crack line with non-local interaction ($m = 2.5$ and $c = 0.1$)
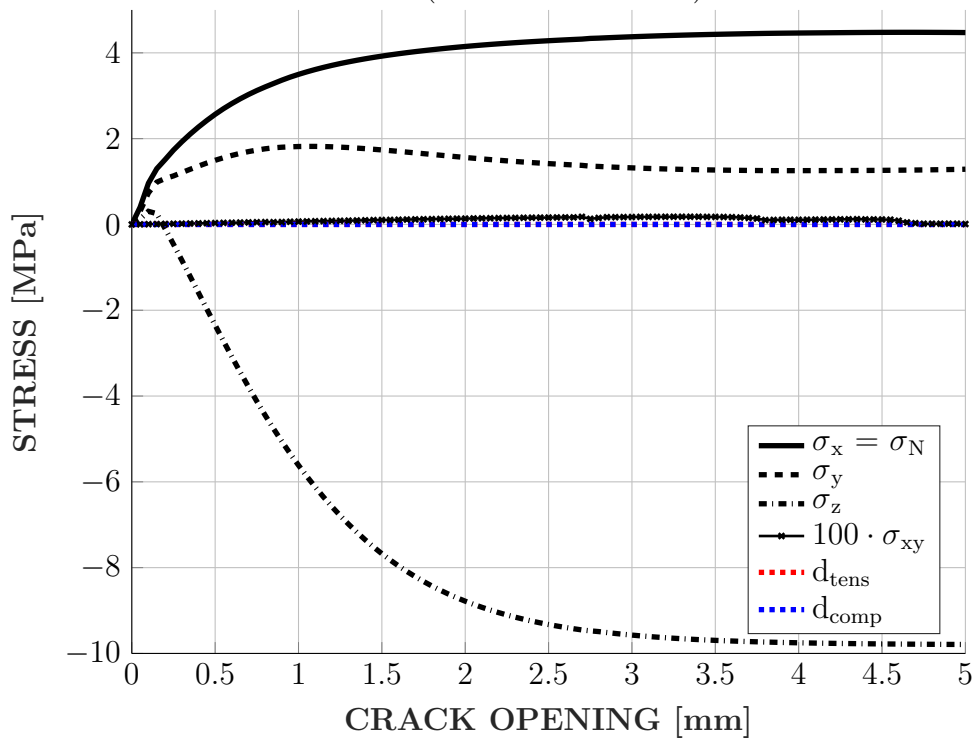
Fig. 4.39: Development of normal stress at crack tip with non-local interaction ($m = 2.5$ and $c = 0.1$)

4.3.2 Fracture Energy: Single Element

Material damage models - like the microplane coupled damage-plasticity model - often describe the growing damage variable in terms of an equivalent strain and a damage variable $\beta > 0$:

$$d(\eta) = 1 - e^{-\beta \cdot \eta} \tag{4.23}$$

This strain η results from the volumetric strain rate and a threshold value. In case of uniformly increased uni-axial tensional strains, this threshold value for concrete is zero and the equivalent strain η equals the volumetric strain ϵ reduced by the elastic yield limit ϵ^e. The resulting stress on a microplane is given by:

$$\boldsymbol{\sigma}^{mic} = (1 - d(\eta)) \cdot \left[K^{mic} \cdot (\varepsilon_V - \varepsilon_V^p) + 2G^{mic} \cdot (\boldsymbol{\varepsilon}_D - \boldsymbol{\varepsilon}_D^p) \right] \tag{4.24}$$

Because this formulation is a representation of *Hook's Law* it must reduce in the one dimensional case to:

$$\sigma_{elastic}^{mic} = E \cdot \epsilon \qquad\qquad \epsilon < \epsilon^e \tag{4.25}$$

$$\sigma_{post-peak}^{mic} = (1 - d(\epsilon - \epsilon^e)) \cdot \underbrace{E \cdot \epsilon^e}_{=f_{ut}} \qquad\qquad \epsilon \geqslant \epsilon^e \tag{4.26}$$

The volumetric fracture energy is then given as the integral of the resulting stress on the microplane over the strain. For a material model with damage-plasticity formulation where the elastic strains remain constant after the yield limit (= uni-axial tensile strength f_{ut}) is reached, this integral can be written as:

$$W_s^{mic} = \int_0^\infty \sigma \mathrm{d}\epsilon = \underbrace{\frac{f_{ut}^2}{2 \cdot E}}_{\text{elastic deformation}} + \underbrace{\int_0^\infty (1 - d(\eta)) f_{ut} \mathrm{d}\eta}_{\text{strain softening}} \tag{4.27}$$

This results for the given, exponential damage evolution law in:

$$W_s^{mic} = \frac{f_{ut}^2}{2 \cdot E} + \frac{f_{ut}}{\beta} \tag{4.28}$$

Though, the uni-axial tensile strength f_{ut}, the Young's modulus E and the damage variable β are direct input variables for the used microplane model, the volumetric fracture energy for each microplane can be calculated directly.

The relation to the fracture energy per unit area is then again given by the characteristic length. For the given case, the characteristic length equals the length of the specimen, therefore:

$$G_F^{mic} = W_s^{mic} \cdot l_{ch} \tag{4.29}$$

This G_F^{mic} now represents the fracture energy for each microplane. Howerever, substitution from eq. 4.29 in eq.4.28 and solving for β leads to:

$$\beta = \frac{2 \cdot E \cdot f_{ut} \cdot l_{ch}}{2 \cdot E \cdot G_F^{mic} - f_{ut}^2 \cdot l_{ch}} \tag{4.30}$$

From this expression the fracture energy can be calculated for any given damage variable, or more useful, if a certain fracture energy and element size are given, the necessary damage variable can be obtained.

For finite element modelling the actual fracture energy per element depends on the elements size. Therefore, unstructured and unequal sized meshed may produce areas where more or less energy is dissipated. This causes a strong dependency on the used mesh for these kind of models. In order to overcome such dependency, a non-local interaction is introduced.

Geometry and Mesh

The cubical mesh consists of 1 linear hexahedral CPT215 elements with an edge length of 0.3 m. The edge length was chosen to fit the characteristic element length representing the width of the fracture process zone. As a reference, a two-dimensional element linear square CPT213 element was used. The edge length remained unaltered.
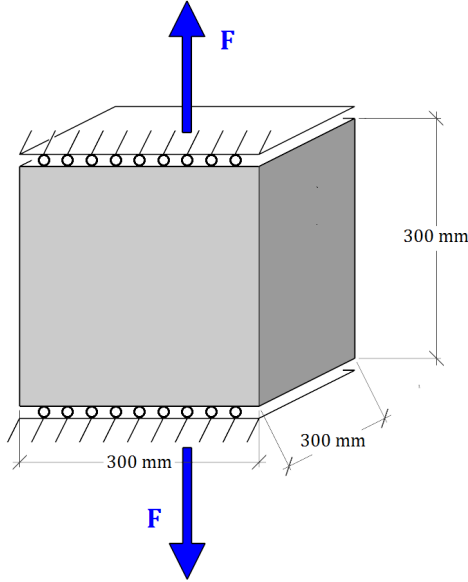
Fig. 4.40: Model setup and cube mesh

Mesh			
Form	Cube	Square	
Edge length	0.3	0.3	m
Nodes	8	4	
Elements	1	1	

Tab. 4.11: Mesh properties

Input Parameters			
Young's modulus	E	22.41	GPa
Poisson ratio	ν	0.2	
Uni-axial compressive strength	f_{uc}	28	MPa
Uni-axial tension strength	f_{ut}^{FIT}	2.15	MPa
Non-local interaction range	c	0	
Non-local averaging parameter	m	2.5	
Tension damage threshold	γ_{t0}	0	
Tension damage parameter	β_t^{FIT}	3200	
Compression damage threshold	γ_{c0}	0.0001	
Compression damage parameter	β_c	2133	

Tab. 4.12: Material model input parameters

Input parameters for the microplane model are given in table 4.11. Uni-axial tensional strength f_{ut}^{FIT} and tensional damage evolution parameter β_t^{FIT} were varied so element's fracture energy equals to $G_F = 250 \ [N/m]$.

Results
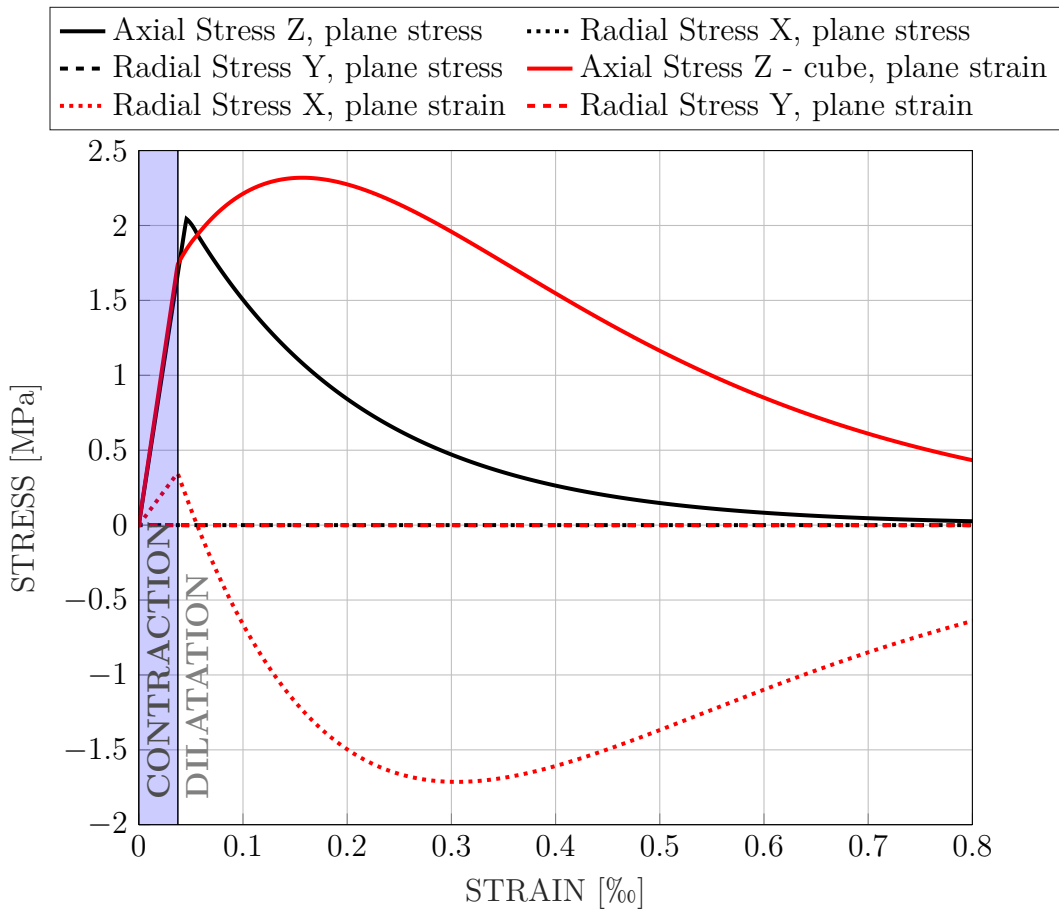
Fig. 4.41: Stress-strain curve from cube undergoing uni-axial tension in plane strain and plane stress
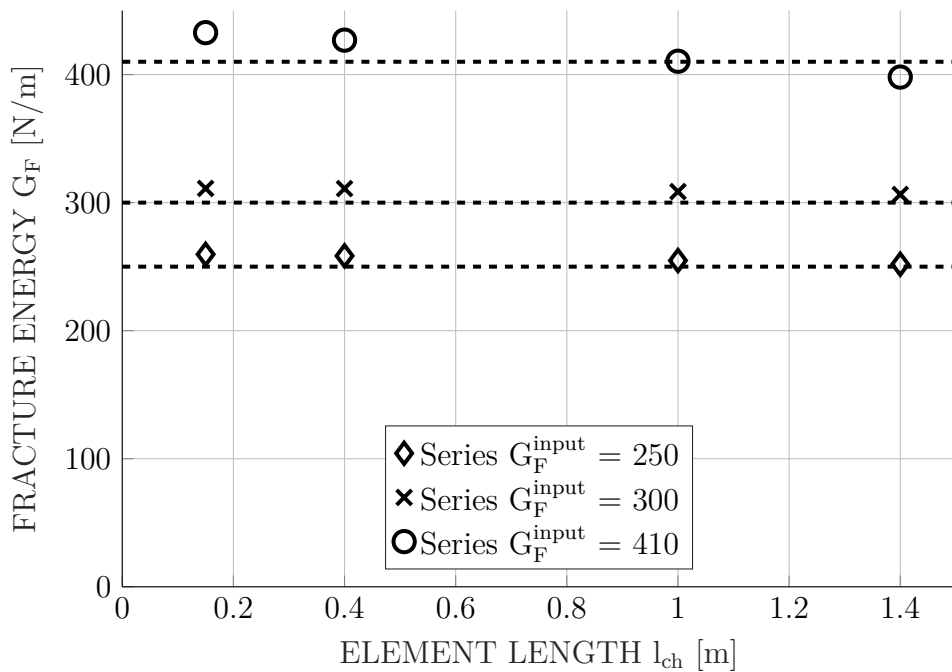
Fig. 4.42: Comparison between fracture energy as an input and the resulting from element

4.3.3 Fracture Energy: 3-Point-Bending Test
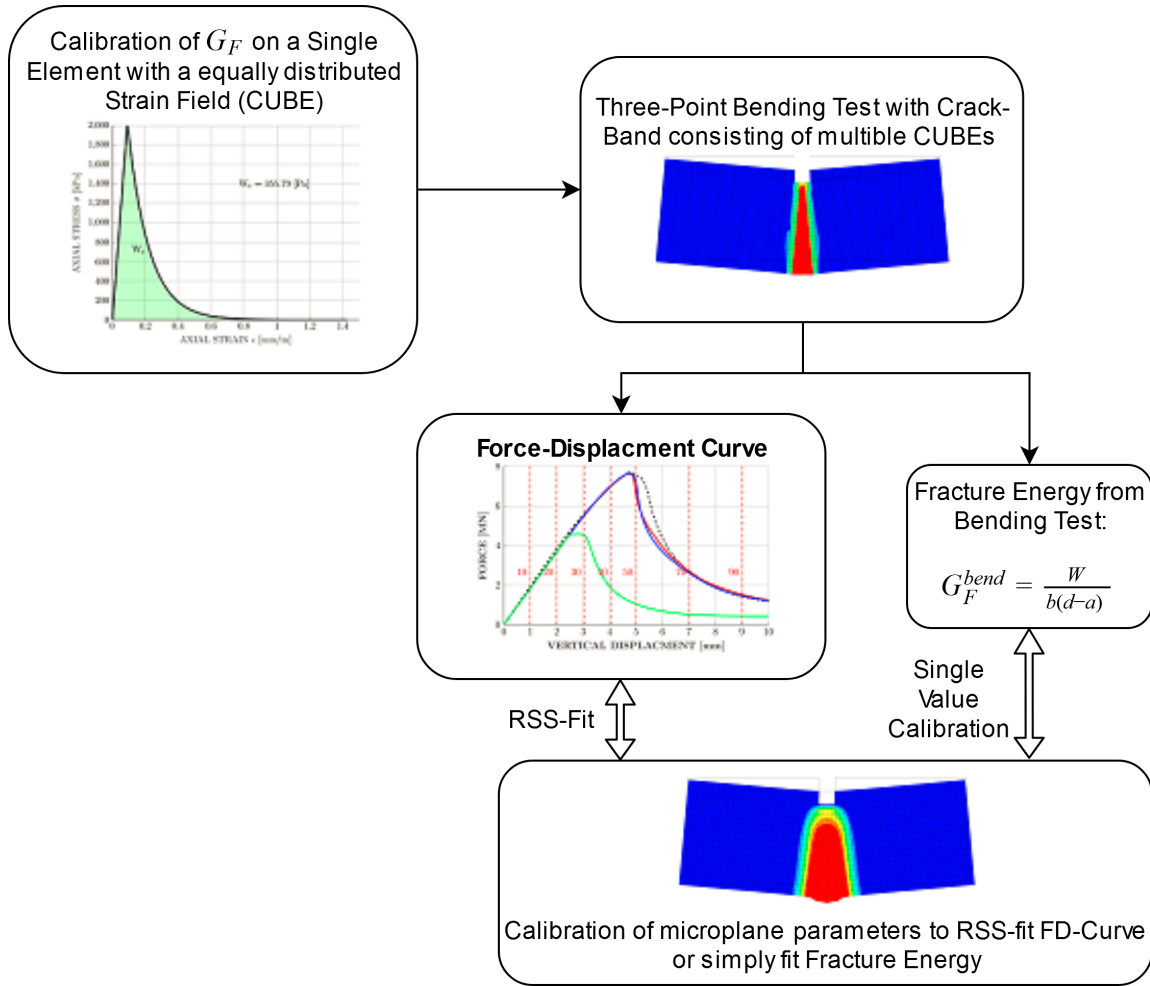
Fig. 4.43: Overview of the calibration procedure for the non-local range using three point bending test

As shown in chapter 4.3.2, it is possible to determine the dissipated energy from an element with a certain side length during the fracture process. Therefore, elements without non-local interaction are calibrated to represent the desired fracture energy - in this case $G_F = 250N/m$, taken from the Benchmark Workshop. Then a three-point-bending test is performed, using the calibrated elements in the fracture zone. The input parameters for the actual microplane model with non-local interaction will then be fitted to the resulting force-displacement curve from the three-point-bending test. In order to verify the obtained results, the stress distribution along the crack line was compared with a reference obtained from literature, see [14]. Model parameters for the model with active non-local interaction are then obtained by fitting the force-displacement curves or total fracture energy.

Input parameters for the three distinct fitting attempts are given in table 4.13. Where *REF* refers to the fitting of the fracture energy on a 3D cube under plane stress conditions. *FIT1* and *FIT2* refer to the fitting of force displacement curves in 2D plane strain conditions using the Root of Sum of Squares (RSS) as indicator. Uni-axial tensional strength f_{ut}^{FIT} and tensional damage evolution parameter β_t^{FIT} were adapted during fitting process. Other parameters are taken directly from the Benchmark example or assumed according to chapter 2.2.3.

Input Parameters		REF	FIT1	FIT2	
Young's modulus	E	22.41	22.41	22.41	GPa
Poisson ratio	ν	0.2	0.2	0.2	
Uni-axial compressive strength	f_{uc}	28	28	28	MPa
Uni-axial tensional strength	f_{ut}^{FIT}	2.00	2.00	2.15	MPa
Non-local range	c	0	0.05	0.10	
Non-local interaction parameter	m	2.5	2.5	2.5	
Tensional damage threshold	γ_{t0}	0	0	0	
Tensional damage evolution parameter	β_t^{FIT}	3200	4950	6100	
Compressive damage threshold	γ_{c0}	0.0001	0.0001	0.0001	
Compressive damage evolution parameter	β_c	2133	3300	4066	

Tab. 4.13: Material model input parameters

Parts of the model are using the simple linear-elastic material law if they are situated close to the supports and the applied displacement (as displayed in figure 4.44a). This is to avoid damage development due to high stresses caused by these singularity points.

(a)

(b)   **(c)**
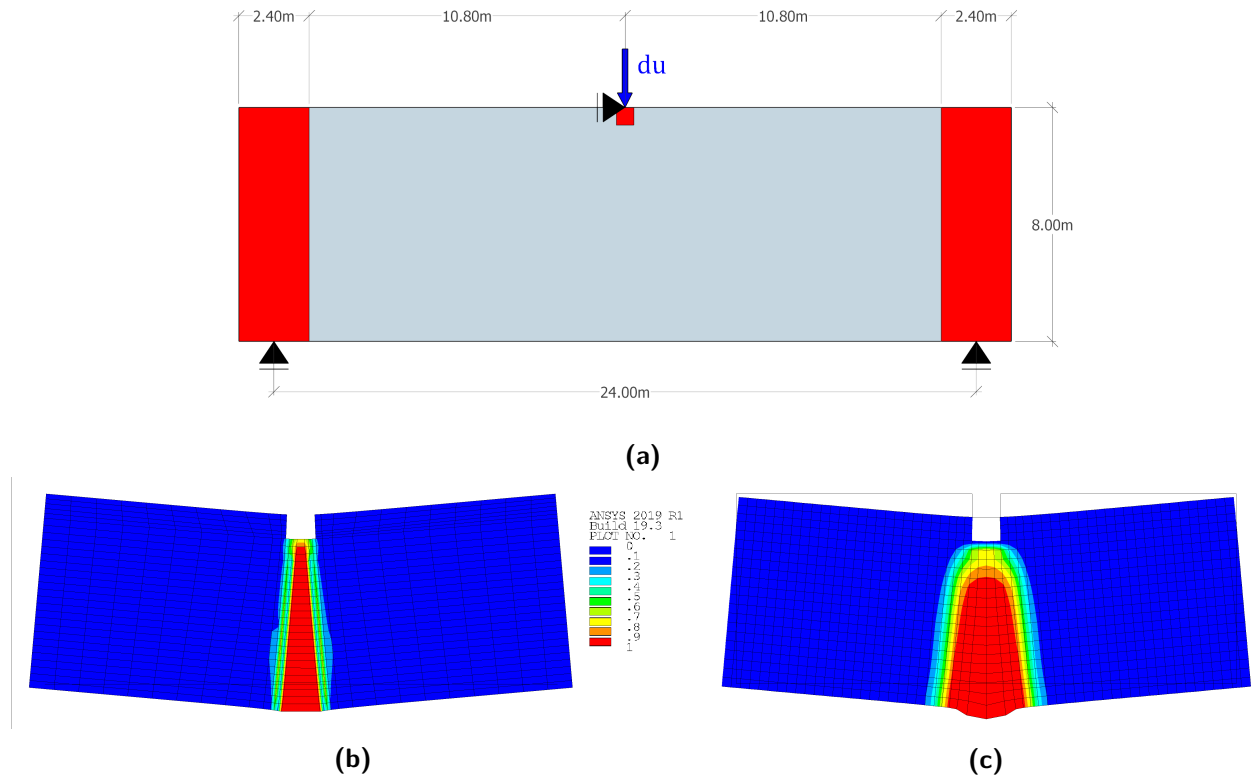
Fig. 4.44: (a) geometry of the 3-point-bending test model (red area with linear-elastic material model), **(b)** final damage state for model with crack band and **(c)** final damage state for fitted material model with non-local interaction

As can be seen in figure 4.45, the stress distribution represent quite well the theoretical one from literature. That the maximum normal stresses are higher than the uni-axial tensile strength, results from the model being in plane strain conditions.
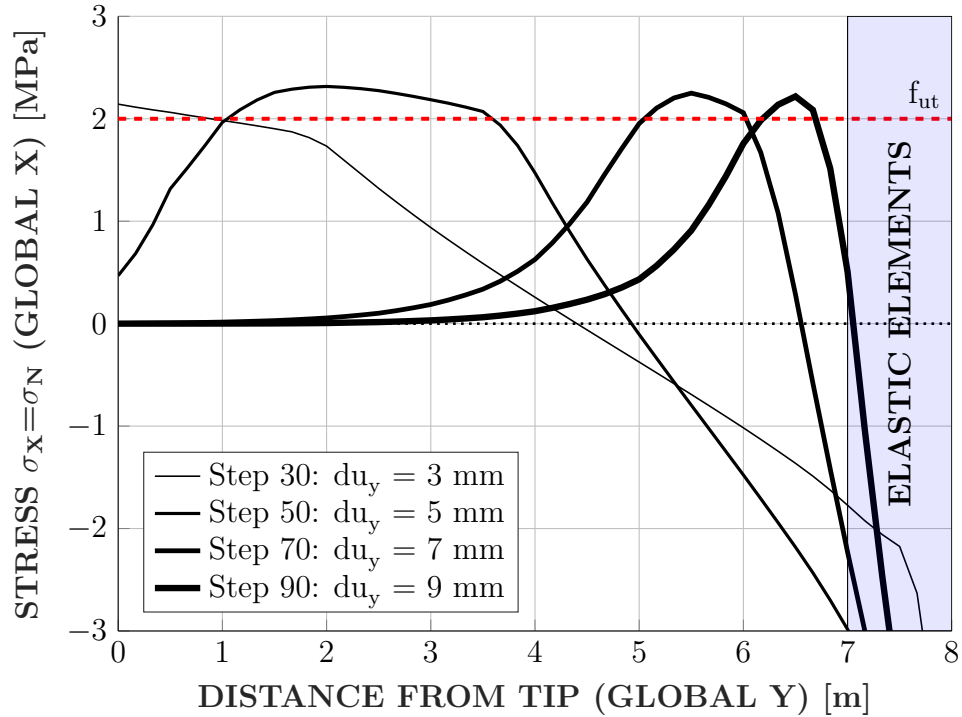
Fig. 4.45: Normal stress distribution along crack - Reference from Microplane model with c=0 for plane strain conditions

Figure 4.47 shows the resulting force displacement curve from the reference, two fits for different non-local ranges as well as the force displacement curve obtained under plane stress conditions.
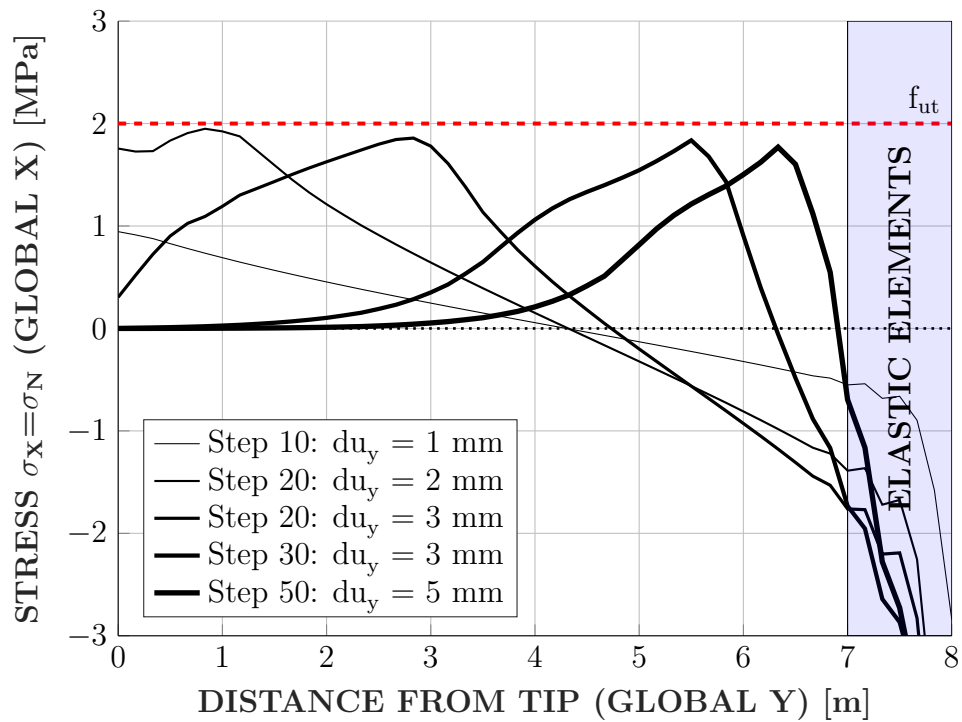
Fig. 4.46: Stress distribution along crack for plane stress conditions

The stress distribution given by plane stress conditions, is displayed in figure 4.46. It shows the initiation of softening close to the yield strength. Furthermore, the lines seems not so smooth than from the two-dimensional model test. This may be explained due the way *Ansys Mechanical* averages results onto paths in three-dimensional space.
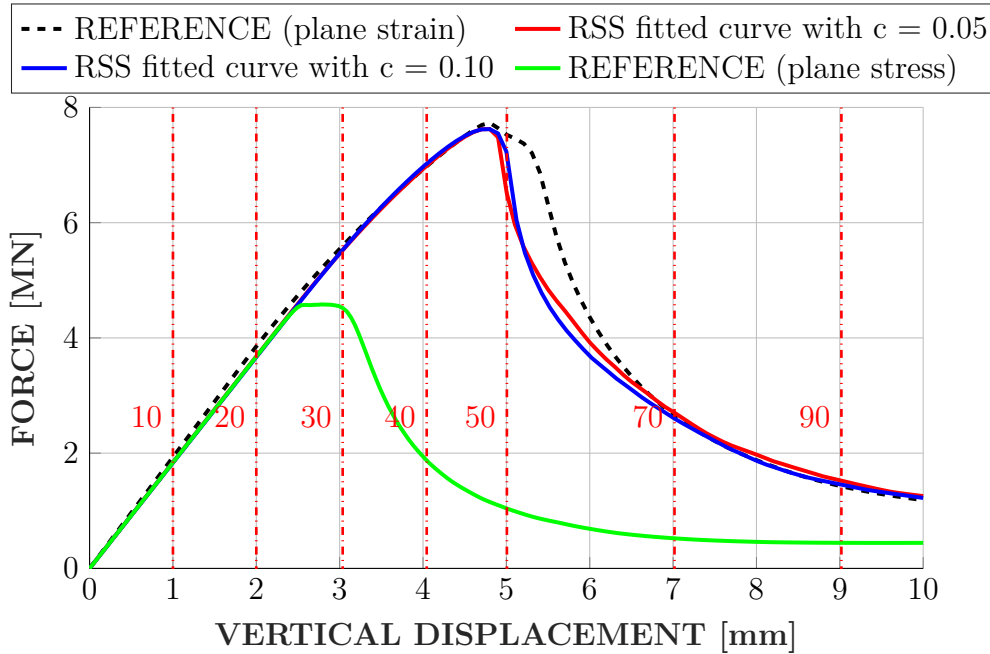
Fig. 4.47: Force displacement curves for three-point-bending beam

The following figures show the stress distribution for a non-local range of $c = 0.05$ (see 4.48) and $c = 0.10$ (see 4.49). Close to the boundaries of the model - i.e. distance from tip is zero - the stress distribution shows a residual value which declines slower than their neighbours. This may result from the way the non-local interaction is computed as shown in chapter 2.2.3.
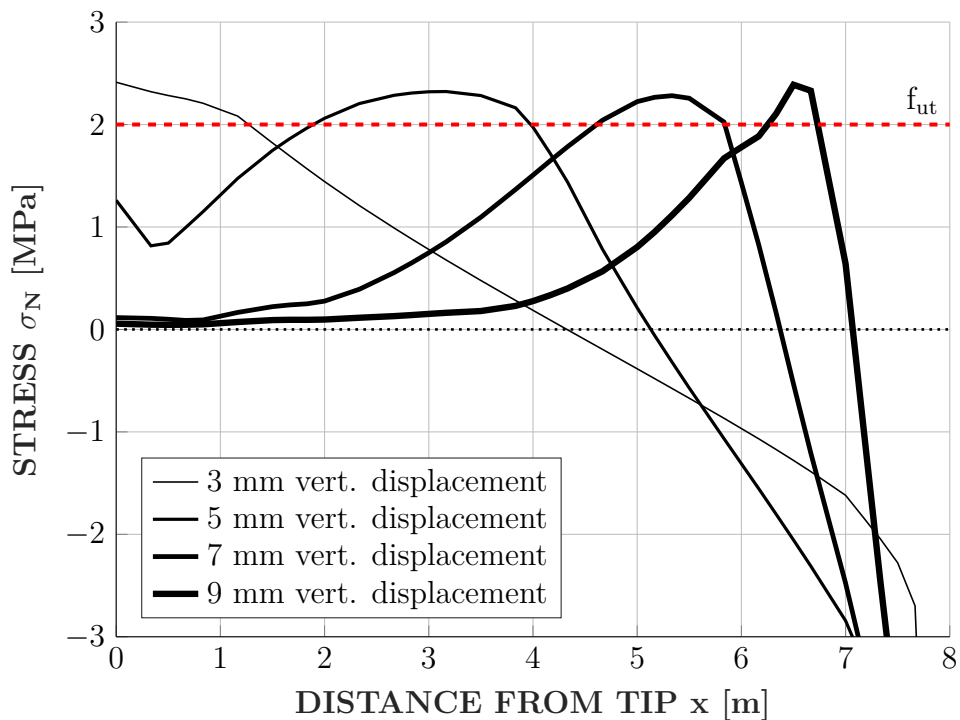
Fig. 4.48: Normal stress distribution along crack - Fitting Microplane model with c=0.05

However, these problems can be overcome by increasing the element size in the affected boundary areas (see figure 4.50).
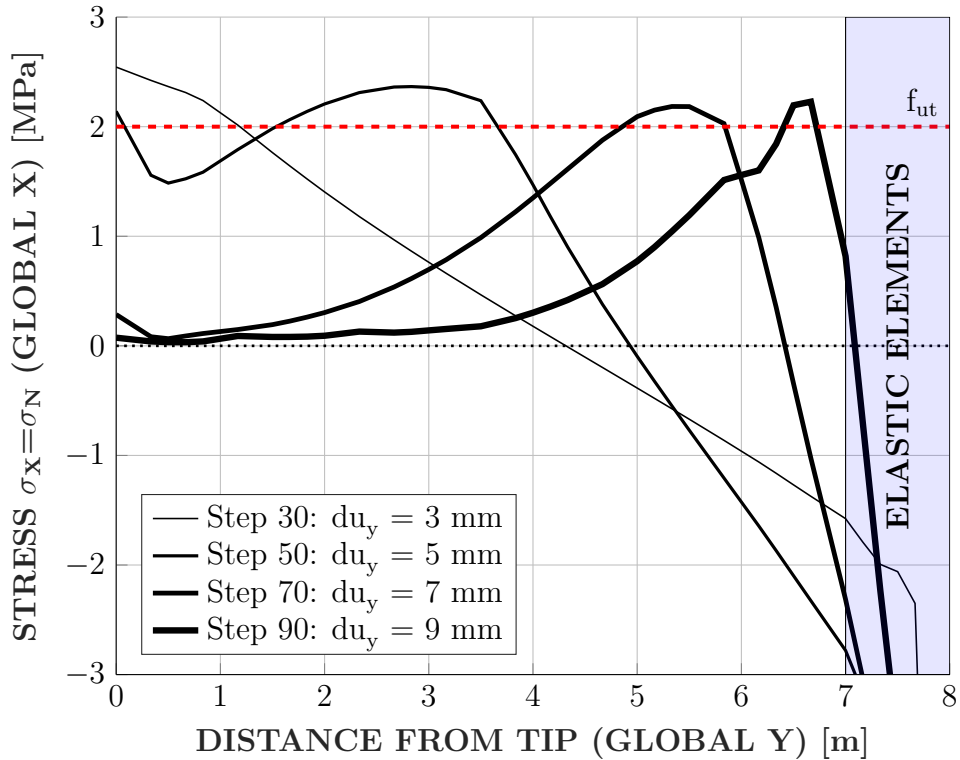
Fig. 4.49: Stress distribution along crack with a non-local range parameter *c* of 0.1 and an element length of 0.3 m
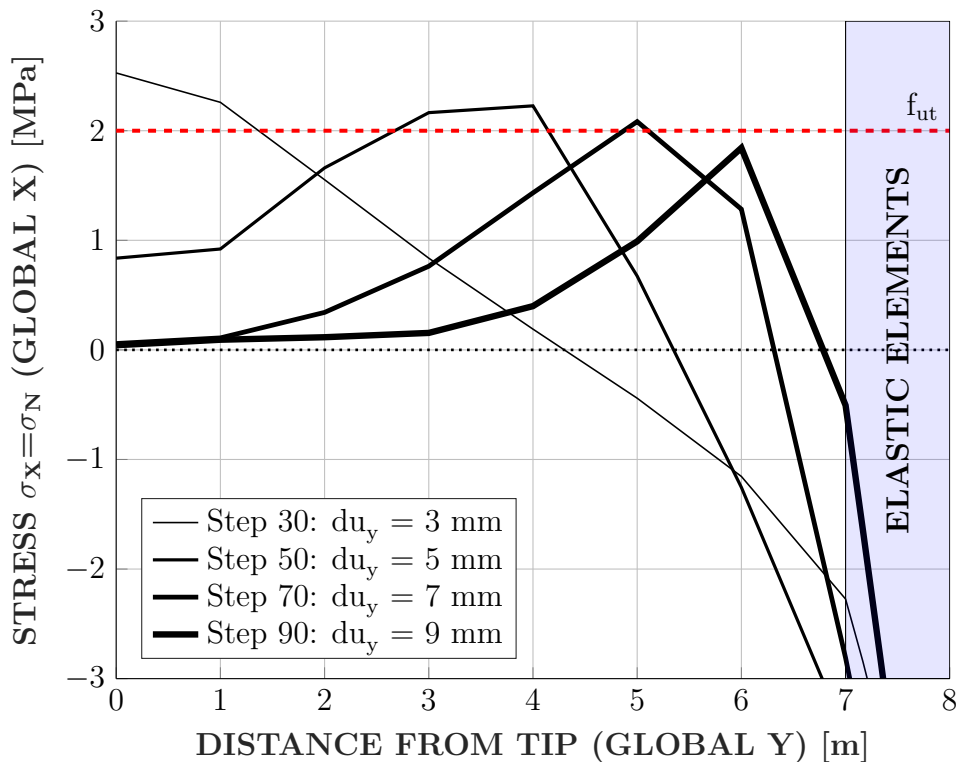
Fig. 4.50: Stress distribution along crack with a non-local range parameter *c* of 0.1 and an element length of 1.0 m

5 Investigations on Pine Flat Dam

(a) Downstream view on Pine Flat Dam from

(b) Pine Flat Lake overview

5.1 Pine Flat Dam

The Pine Flat Dam is a concrete gravity dam situated in Central Valley in California, USA. It impounds the Kings River and forms the Pine Flat Lake. It was built by the US Army Corps of Engineers between 1947 and 1954. First only sought for flood retention proposes, from 1984, three Francis turbines enabled electricity production with an annual generation of almost 390 GWh. The reservoir contains up to 55.9 million cubic metres of water and has a catchment are of about 4000 square kilometres. The dam itself is 130 meters in height and follows a straight axis crossing the river valley. Its spillway consists of six bays with a maximum capacity of 11,100 m^3/s. However, the maximum discharged yet to be released was 480 m^3/s in 1969 during an inflow from Kings River of 2,300 m^3/s. The maximum inflow in the reservoir reached so far was in 1955 with 3,200 m^3/s. During this flood event, the dam ensures a maximum discharge downstream of 135 m^3/s [47].

5.2 Pine Flat Dam Model

The given Pine Flat Dam is designed as a gravity dam with an inclined upstream face and a flat base abutment. The upstream side is inclined with ratio of 1 : 0.05 and the downstream side with ratio 1 : 0.77. Due to the block width of 15.24 m, plane strain condition are assumed.
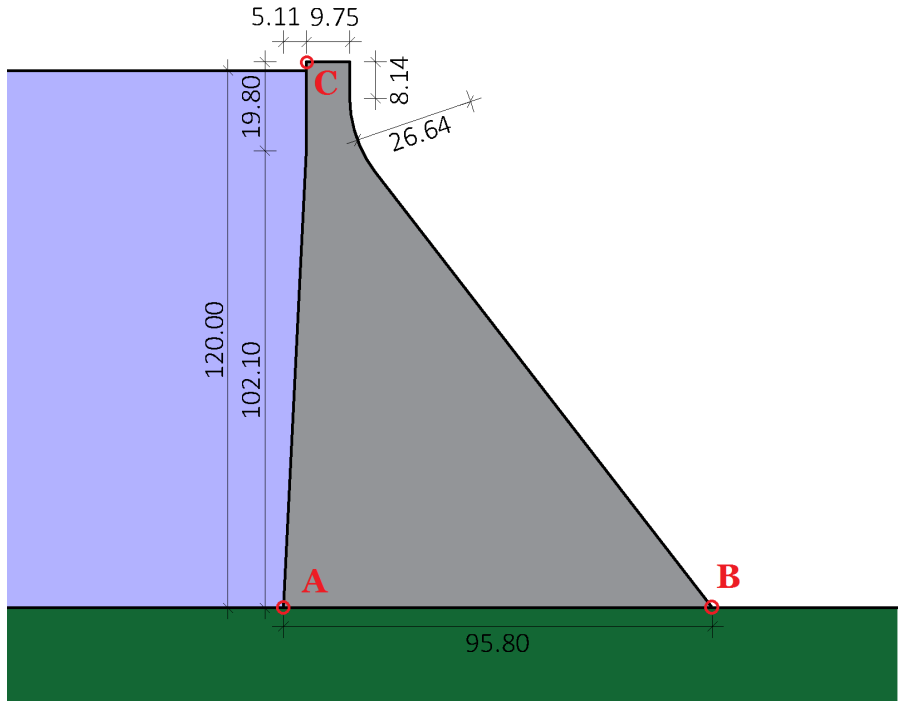
Fig. 5.2: Geometry of the Pine Flat Dam (units in [m])

The model extends upstream and downstream about 300 m each, which is roughly three times the base width (95.80 m). This is to reduce the influence of reflections from the reservoir's backside onto the dam body. The height of the rock foundations is 122 m and water level varies depending on the performed analysis. The displacement in horizontal direction is locked at the u/s and d/s side of the foundation. At the lower side of the foundation displacement in vertical direction is locked. At the backside of the reservoir an impedance boundary condition is applied representing full absorption of arriving pressure waves. Furthermore, a zero pressure condition is applied at the top of the reservoir.
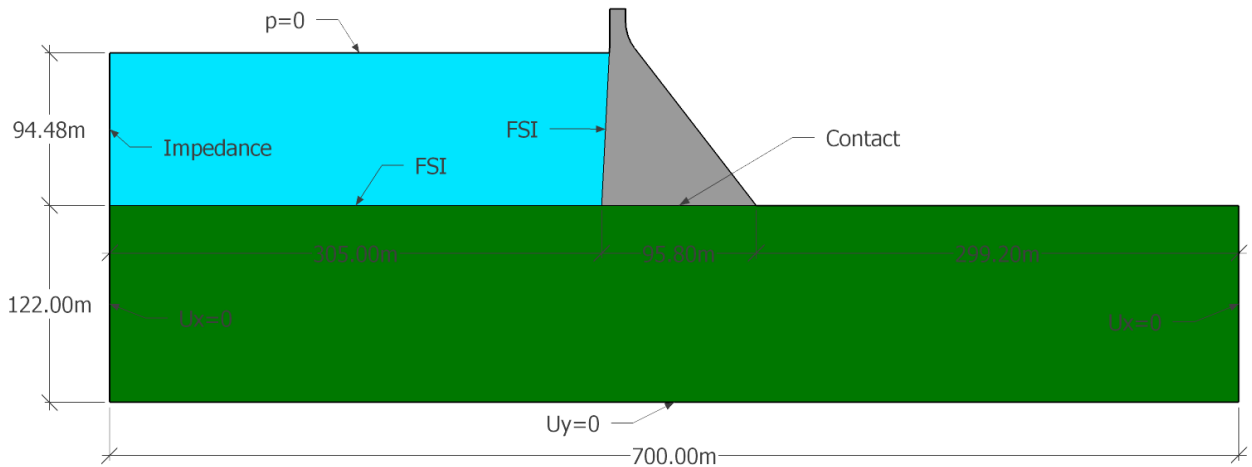
Fig. 5.3: Boundary conditions for Pine dam model

5.3 Linear Analysis: Determination of Damping

A modal analysis was performed to determine the first 10 natural frequencies. Then Rayleigh damping values were calculated using 1st and 5th mode with a supposed damping ratio of 10%. Relevant modes were determined by the effective mass involved in the motion in direction of the valley (X-direction).

Mesh

The model consists of 13556 elements with 33827 nodes. The reservoir is modelled by linear fluid elements. Dam body and foundation consist of quadratic elements under plane strain conditions. The same mesh is also used for non-linear analysis regarding the influence of the non-local range.
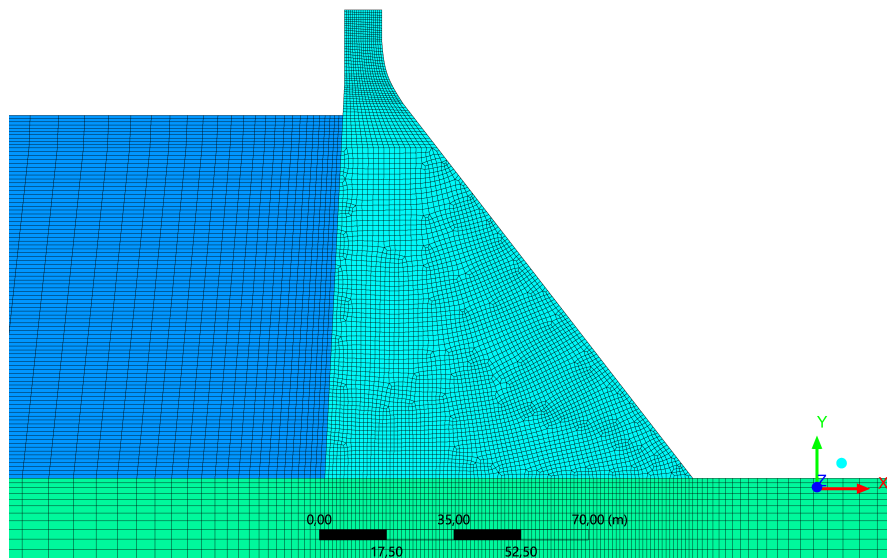
Fig. 5.4: Pine dam mesh for linear analysis

Material Parameters

The table below 5.1 lists the material parameters used for the linear modal analysis.

Results

From the modal analysis, the first 20 natural frequencies and the effective mass in respected to the degree of freedom of movement were obtained. Figure 5.5 shows the resulting damping from the Rayleigh approach and the effective mass involved. Here the effective mass is normalized due to the mass of the dam body only. It can be seen that the additional mass punned onto the dam from the fluid elements is about 55% of the dam's total mass. Furthermore, at about 10 Hz, over 99% total effective mass is reached. This means that higher frequencies have nearly no influence on the dam movement.

The Rayleigh damping values results 0.788 for the mass proportional damping and 0.00302 for the stiffness proportional damping. These damping values are then applied on the system for the following non-linear analysis.

Material	Parameter		Unit
Dam body			
Density	ϱ_c	2400	kg/m³
Dynamic Young's modulus	$E_{c,dyn}$	31.6	GPa
Poisson ratio	ν_c	0.18	
Foundation			
Density	ϱ_f	$1 \cdot 10^{-10}$	kg/m³
Dynamic Young's modulus	$E_{f,dyn}$	20.0	GPa
Poisson ratio	ν_f	0.25	
Reservoir			
Density	ϱ_w	1000	kg/m³
Sonic celerity	c_{sonic}	1440	m/s

Tab. 5.1: Material parameters for elastic and plastic (microplane) material models for dam body and massless foundation, as well as input parameters for reservoir (fluid elements) - Pine dam model
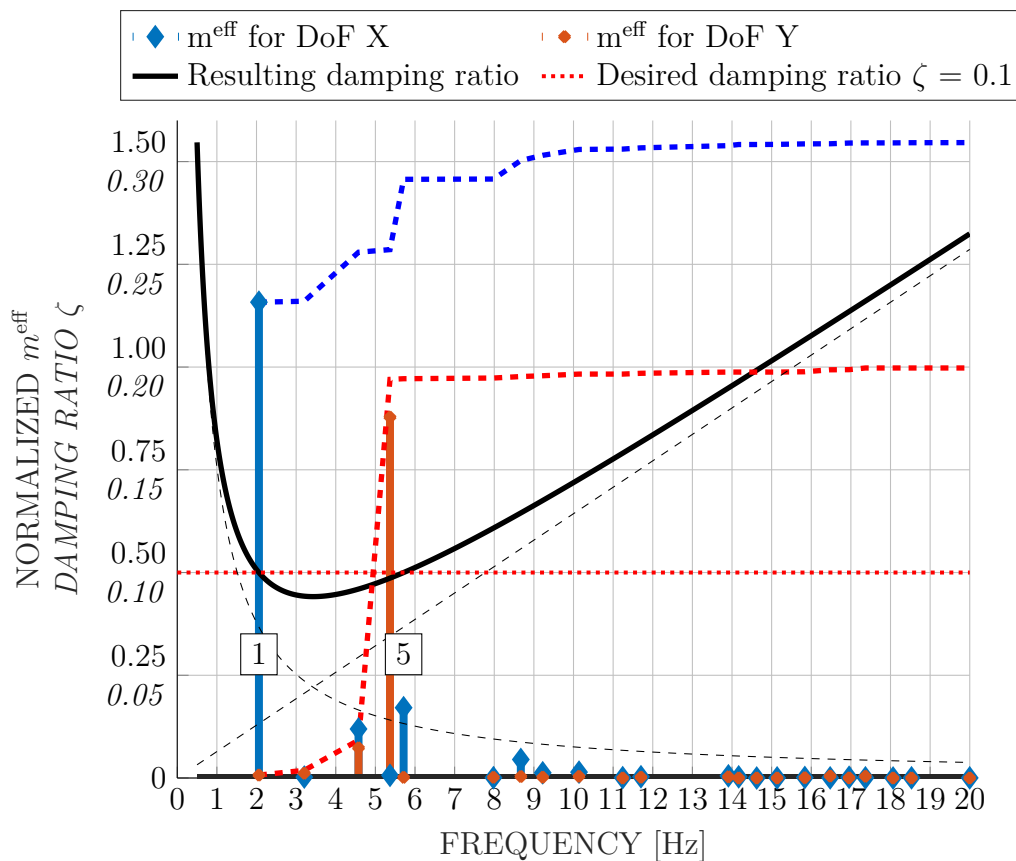
Fig. 5.5: Effective mass distribution normalized with the mass of the dam body over extracted modes for and horizontal (X) and vertical (Y) degree of freedom (DoF) - linear Pine Dam model (2D) with reservoir filled

5.4 Non-Linear Analysis: Parametric Non-Local Range Variation

In order to test the influence of the non-local regularization of the used microplane material model on a bigger scale, a non-linear analysis was carried out involving three non-local ranges. There the relative displacement of the dam crest and the resulting damage pattern were compared. Furthermore, the relative displacement and relative acceleration at the dam crest were compared for different contact types at the base joint. Results from a linear elastic model serves as reference.

It was found that the size of the non-local range has a significant influence on the dam performance. First, by setting the non-local range to zero, a mesh depending crack propagation could be observed. Second, smaller non-local ranges lead to failure of convergence below half of the time of the simulated earthquake. Third, for non-linear material model, maximum relative acceleration for a frictional contact are higher than the one obtained from the bounded one. Although, a higher damping behaviour can be observed.

Excitation

The excitation was the NS-acceleration time history from the 1940 El Centro Earthquake at the Imperial Valley in Southern California. It was applied in downstream direction onto the whole model (*Ansys Mechanical* specific).

A performed Fast Fourier Transformation shows the major acceleration peaks below a frequency of 6 Hz. This is in the range of the first five natural frequencies of the dam and should lead to amplifications causing a maximum amount damage to the model.
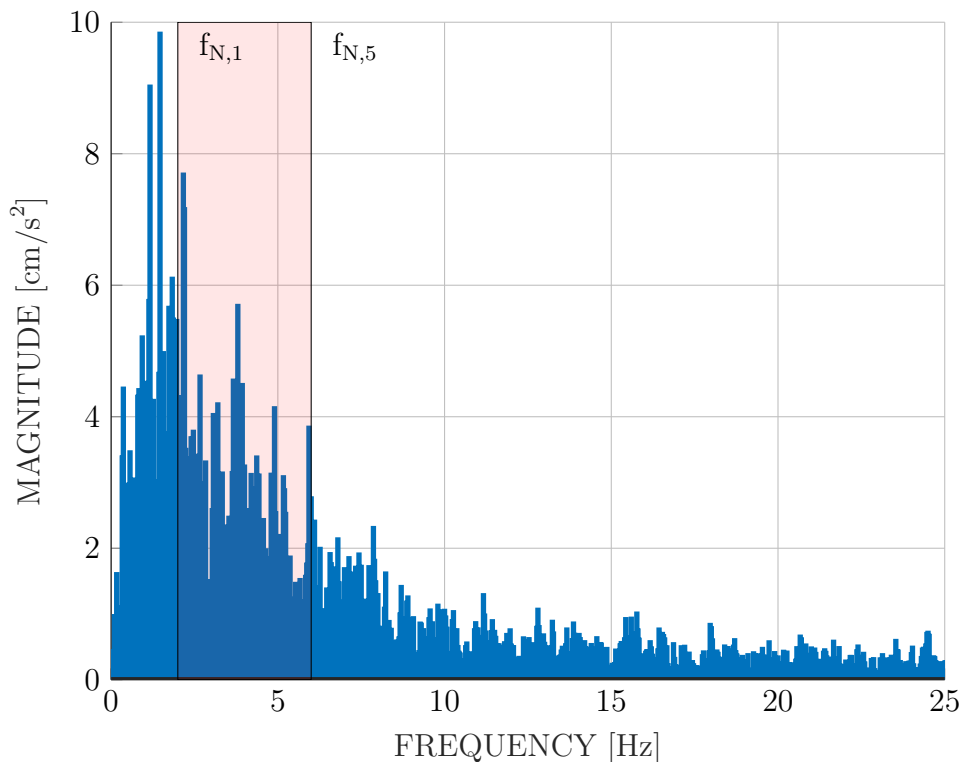
Fig. 5.6: Magnitude resulting from Fast Fourier Transformation on applied excitation - *El Centro* North-South acceleration with a sample rate of 50 [Hz]

Material Parameters

Material	Parameter		Unit
Dam body (non-linear)			
Density	ϱ_c	2400	kg/m^3
Dynamic Young's modulus	$E_{c,dyn}$	31.6	GPa
Poisson ratio	ν_c	0.18	
Uni-axial tensile strength	f_{ut}	2.1	MPa
Uni-axial compressive strength	f_{uc}	44.7	MPa
Bi-axial compressive strength	f_{bc}	51.4	MPa
Compressive cap parameter	σ_V^C	-34.3	MPa
Tensile damage threshold	γ_{t0}	0	
Compressive damage threshold	γ_{c0}	0.001	
Tensile damage evolution parameter	β_t	5000	
compressive damage evolution parameter	β_c	1000	
Tensile cap parameter	R_T	1	
Compressive cap parameter	R	2	
Hardening parameter	D	1000	
Non-local range	c	0	0.10	0.33	m^2
Non-local averaging parameter	m	2.5	
Foundation (linear)			
Density	ϱ_f	$1 \cdot 10^{-10}$	kg/m^3
Dynamic Young's modulus	$E_{f,dyn}$	20.0	GPa
Poisson ratio	ν_f	0.25	
Reservoir			
Density	ϱ_w	1000	kg/m^3
Sonic celerity	c_{sonic}	1440	m/s
Damping			
Mass proportional damping	α_{mass}	0.788	
Stiffness proportional damping	$\beta_{stiffness}$	0.00302	

Tab. 5.2: Material parameters for elastic and plastic (microplane) material models for dam body and massless foundation, as well as input parameters for reservoir (fluid elements) - Pine dam model

Mesh

The same mesh as in the linear analysis was used.

Results

The relative displacement at the dam crest is computed as the difference between absolute displacement at the crest and at the heel of the model:

$$u^{rel} = u_{crest}^{abs} - u_{heel}^{abs} \tag{5.1}$$

For the relative acceleration, the difference between absolute acceleration at the crest and the excitation was computed:

$$a^{rel} = a^{abs}_{crest} - a_{ELCentro} \tag{5.2}$$

The analysis performed with a non-local range lost convergence after 2.62 s. The on with a non-local range of 0.1 only performed little better and reached 3.59 s. The analysis with a non-local range of 0.33 completed the whole 10 s of excitation's duration.
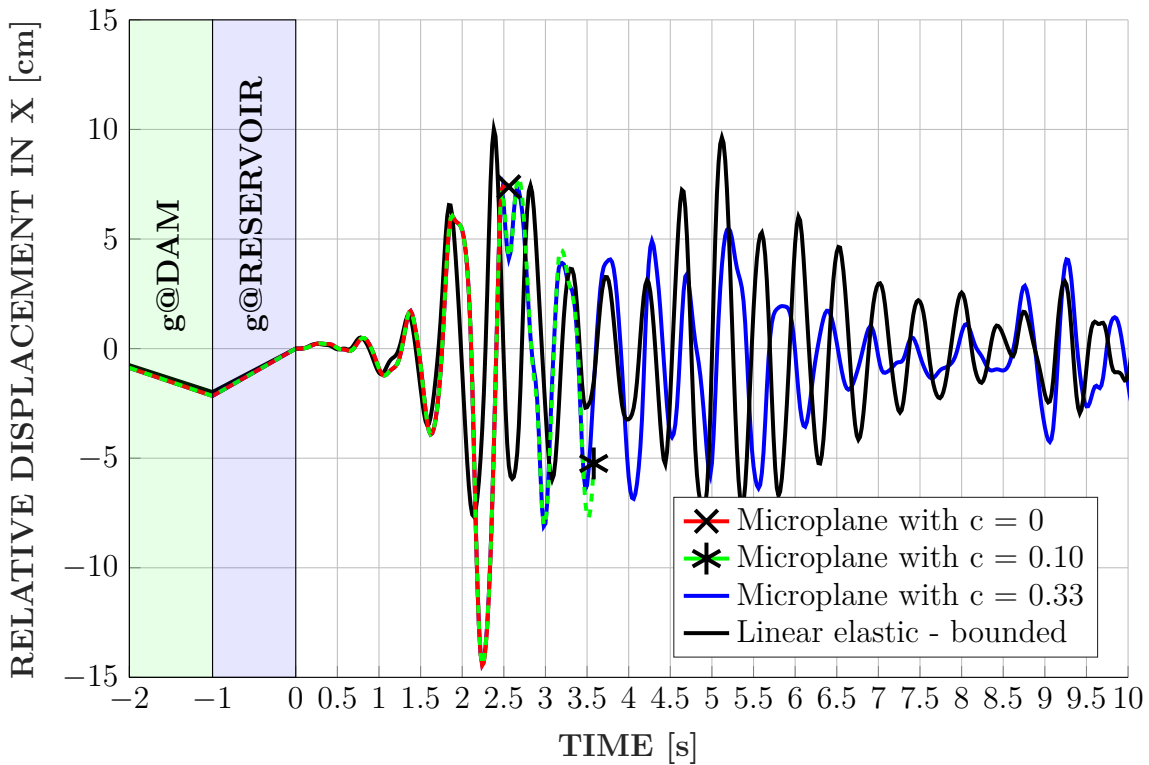
Fig. 5.7: Influence of non-local range to resulting crest displacement relative to u/s heel side during excitation (El Centro NS)

(a) c=0.00   **(b)** c=0.10   **(c)** c=0.33
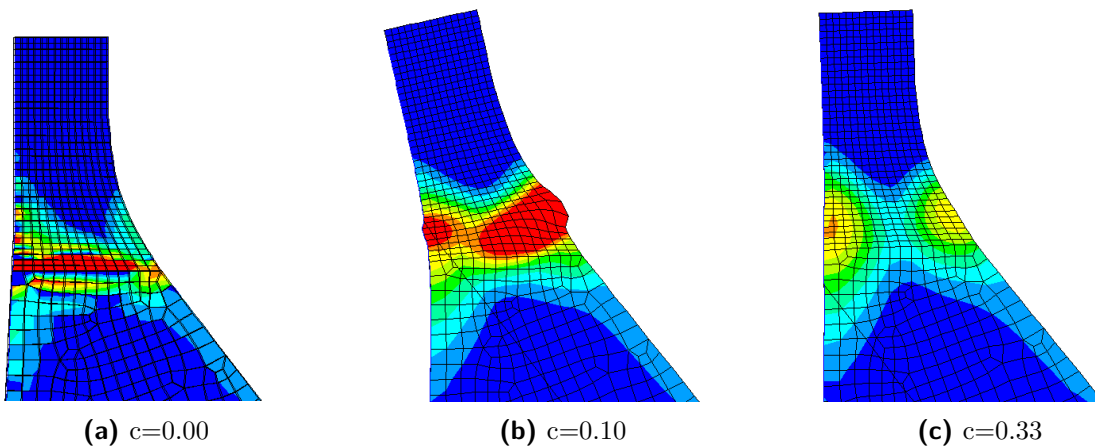
Fig. 5.8: Final damage pattern at weak point of the dam for various non-local ranges

The additional performed analyses with a bounded contact type in the base joint lead to the following changes in relative displacement and acceleration at the crest.
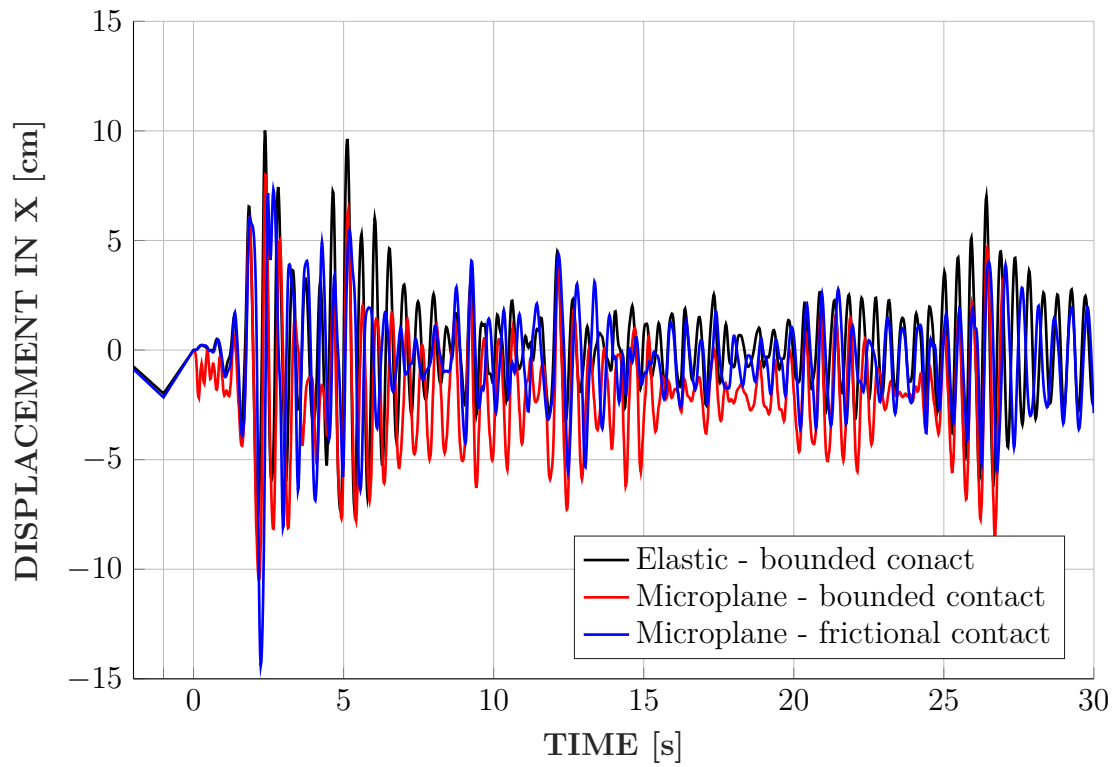
Fig. 5.9: Influence of the contact type to resulting crest displacements relative to u/s heel side during excitation (El Centro NS)
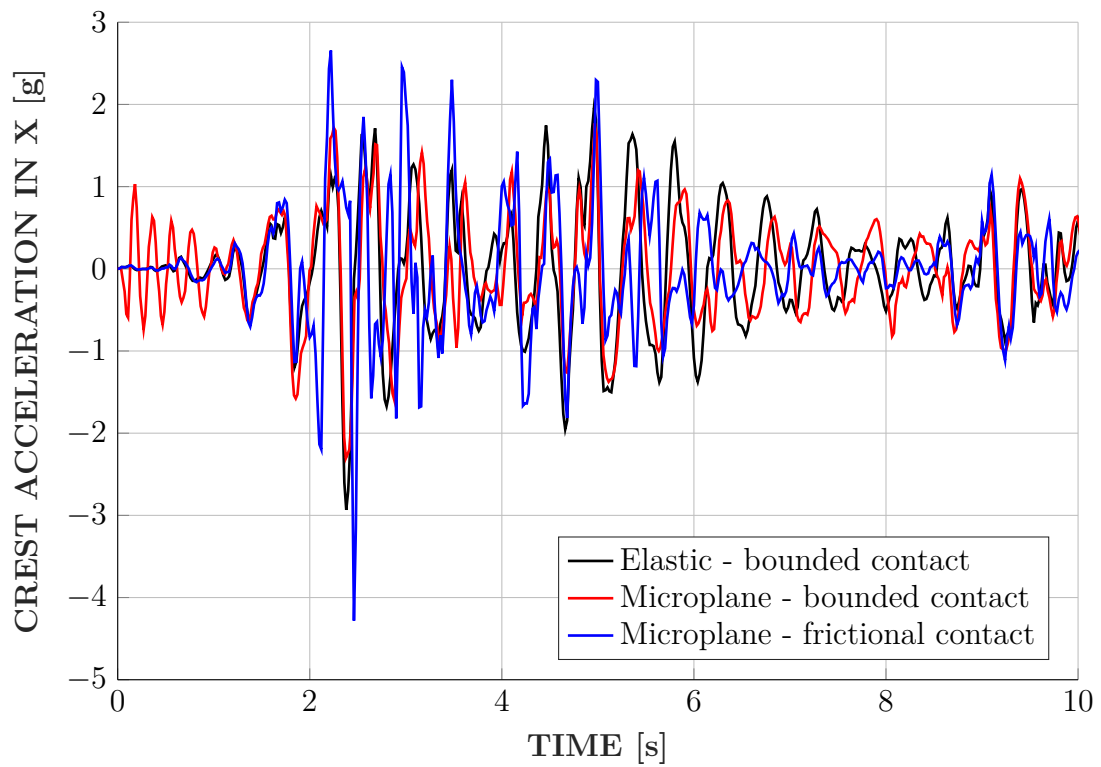
Fig. 5.10: Influence of the contact type to resulting crest acceleration relative to u/s dam heel during excitation (El Centro NS)

5.5 Non-Linear Analysis: Verification of Microplane Model

This section is about a possible verification of the calibration processes described in the chapters before. As a reference serves the seismic analyses done on the Pine Flat dam for the *ICOLD* Benchmark Workshop 2018 in Milan [38]. Aim was to compare the results for case E, considering the Endurance Time Acceleration Function (ETAF) obtained by the workshop with the ones obtained by the calibration attempts. As a drawback, the final report of this conference wasn't published to the day this thesis was submitted. Therefore, it was only possible to check some results taken from a summery published earlier.

For the procedure itself, the two microplane models given by *Ansys Mechanical* - coupled damage-plasticity (CDP) and elastic - are calibrated to represent the desired concrete properties. The elastic model was calibrated according to the procedure described in chapter 4.3.2. The size of the cube on which the fracture energy was determined was given by the edge length of the mesh. The CDP-model was calibrated in two ways: First, the three-point bending test from chapter 4.3.3 was used. Second, the calibration was only done on a single element 4.3.2. There the size of the calibration element was given by the width of the fracture process zone.

Using fracture energy as a calibration input for a non-local model (as the CDP) is challenging. This is, because the softening behaviour of the given model is described depending on plastic strains. Therefore, in order to obtain an energy, a length scale is required. For models without a non-local regularization, this scale is simply the edge length of the elements themselves. Using a non-local regularization leads to a redistribution of the plastic strains onto a limited range. This range also depends on the lasting strain distribution itself - i.e. for a uniformly distributed strain field like at the tested cube, this regularization doesn't cause any changes of the final strain state.

Material Parameters

Table 5.3 lists parameters describing the linear behaviour of the Pine dam.

Material	Parameter		Unit
Dam body			
Density	ϱ_c	2483	kg/m^3
Young's modulus	$E_{c,dyn}$	22.41	GPa
Poisson ratio	ν_c	0.2	
Foundation			
Density	ϱ_f	$1 \cdot 10^{-10}$	kg/m^3
Young's modulus	$E_{f,dyn}$	22.41	GPa
Poisson ratio	ν_f	0.2	
Reservoir			
Density	ϱ_w	1000	kg/m^3
Sonic celerity	c_{sonic}	1439	m/s
Damping			
Mass proportional damping	α_{mass}	0.750	
Stiffness proportional damping	$\beta_{stiffness}$	0.0005	

Tab. 5.3: Material parameters for dam body and massless foundation, as well as input parameters for reservoir (fluid elements) - Pine dam model according to the Benchmark workshop

A total of five different calibrations were tested. An explanation can be taken from table 5.4. All of them are calibrated to represent the desired fracture energy for 250 N/m. For the regularized model, the compressive damage parameter is obtained from the recommended relation of $\beta_t = 1.5 \cdot \beta_c$ (see [31]).

ID	Model	$l_{elem}[m]$	$\beta_t[-]$	$\beta_c[-]$	Calibration Method
ELAsgl35	elastic	0.35	-	-	Single element
CDPtri70	regularized	0.70	4910	3273	Three point-bending test
CDPtri35	regularized	0.35	4910	3273	Three point-bending test
CDPsgl35	regularized	0.35	2590	1727	Single element
CDPsgl35(DC)	regularized	0.35	2590	1727	Single element(only displacement-convergence criterion)

Tab. 5.4: Calibration attempts for the Benchmark example with a given fracture energy of 250 N/m

Table 5.5 lists parameters of the non-linear material model remaining unaltered for the calibration attempts.

Material	Parameter		Unit
Elastic Microplane			
Uni-axial tensile strength	f_{ut}	2	MPa
Uni-axial compressive strength	f_{uc}	28	MPa
Strength ratio	k	14	
Scaling factor	f	1.56	
Yield function parameter	k_0	0.795	
Yield function parameter	k_1	0.795	
Yield function parameter	k_2	0.095	
Tensional strain limit	η	$8.92 \cdot 10^{-5}$	
Damage residual value	α	0.9	%
Damage evolution parameter	β	9200	
Coupled Microplane			
Uni-axial tensile strength	f_{ut}	2	MPa
Uni-axial compressive strength	f_{uc}	28	MPa
Bi-axial compressive strength	f_{bc}	32.2	MPa
Compressive cap parameter	σ_V^C	-18.7	MPa
Tensile damage threshold	γ_{t0}	0	
Compressive damage threshold	γ_{c0}	0.0001	
Tensile cap parameter	R_T	1	
Compressive cap parameter	R	2	
Hardening parameter	D	1000	
Non-local range	c	0.1	m^2
Non-local averaging parameter	m	2.5	

Tab. 5.5: Parameters for elastic and coupled damage-plasticity microplane models

Mesh
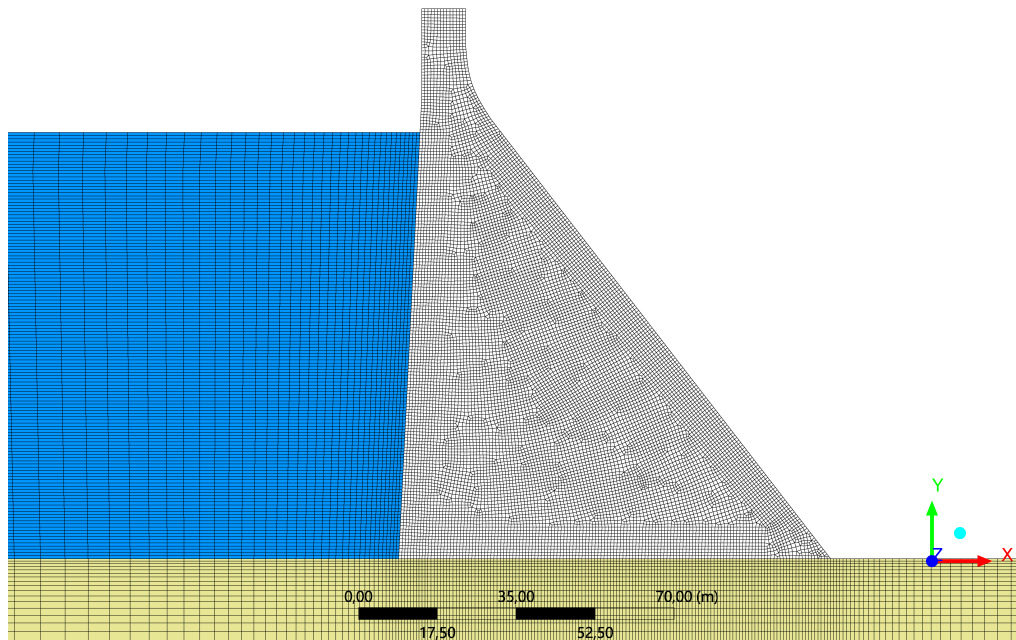
Fig. 5.11: Pine Flat Dam mesh for analysis with ETAF

Two different mesh size were used. One with a mean edge size at the dam body of 0.70 m and the other with a mean mesh size of 0.35 m. The coarse mesh consists of $28,532$ elements with $71,768$ nodes. The fine mesh consists of $74,413$ elements with $194,959$ nodes. For both types, the foundation and dam body are modelled by quadratic elements. The reservoir consists of linear elements.

Both meshes were modelled so that the elements at the dam body's boundaries are oriented normally to the edge over a certain depth (see figure 5.12).
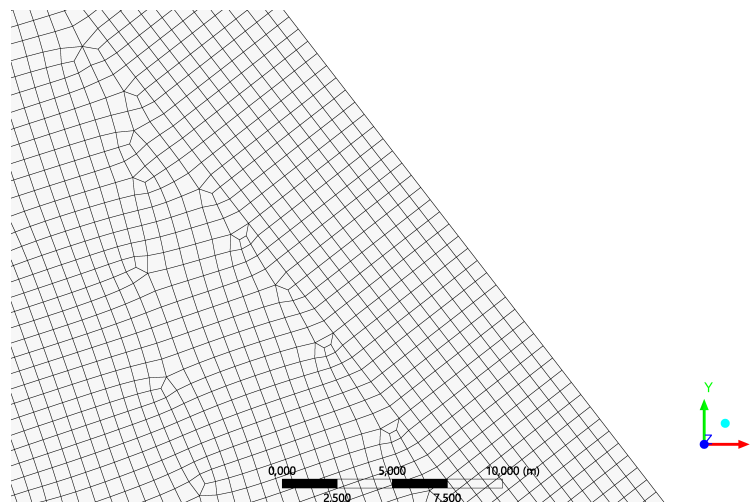
Fig. 5.12: Element orientation close to boundaries

Computation time for the simulation of the first 6 secs with the ETAF was for the coarse mesh 3:44:15 h (7 cores @ 3.40GHz) with a total allocated memory of 9,280 MB. The fine mesh required 15:50:04 h (13 cores @ 3.40GHz) computational time with a maximum allocated

memory of 20,767 MB. Furthermore, the amount of data written/read from the hard drive was 4,951/6,620 GB for the coarse mesh and 24,520/32,524 GB for the fine mesh. The produced output files were in sizes between 15 and 60 GB depending on the variables requested and the output rate. Usually, the output rate was equal to the temporal resolution of the input acceleration. For analysis done on the fine mesh, the output rate was 10 times this resolution. This was necessary in order to reduce the size of the result files to a reasonable amount.

Results

In order to compare the obtained results from the performed analysis with the ones from the Benchmark Workshop, the so-called ETA curves were computed. First, the engineering demand parameters (EDP) were obtained from transient analysis. Second, the cumulative absolute value was calculated (see figure 5.13).
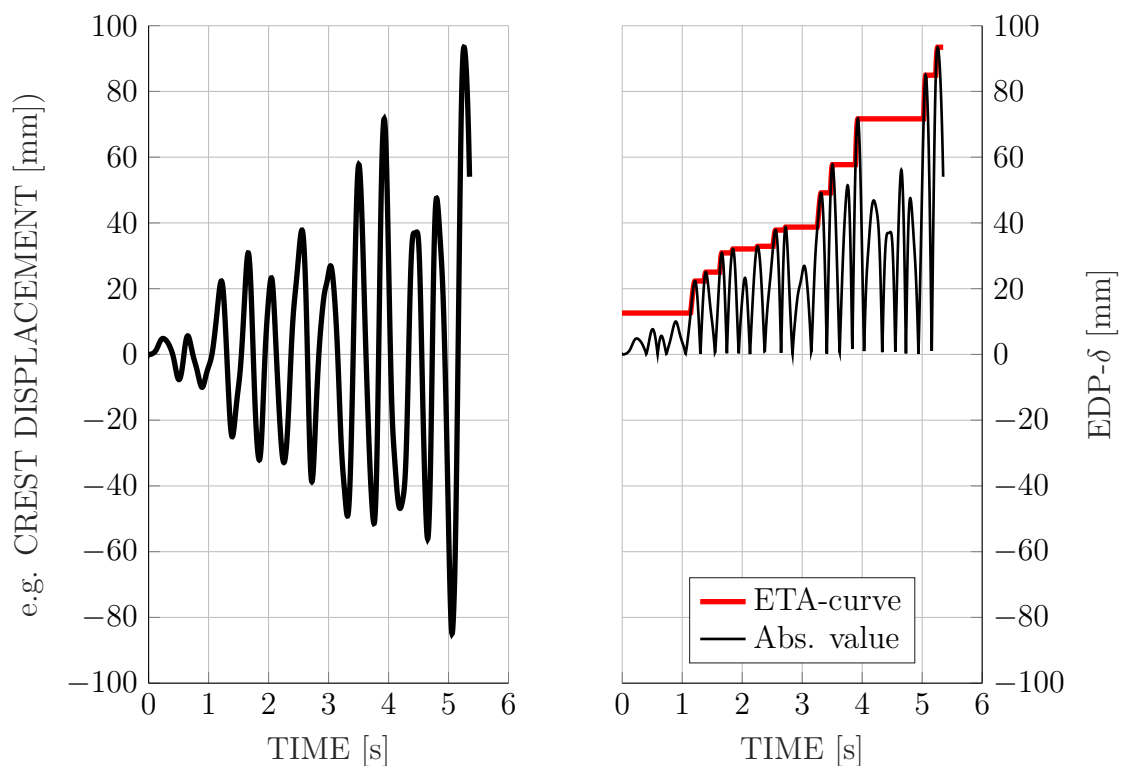
Fig. 5.13: Procedure to obtain endurance time analysis (ETA) curve: EDP from transient analysis *(left)* and its cumulative absolute value *(right)*

In this case the desired EDPs were: Displacement at the dam's heel at point A, displacement at the crest point C and the dynamic pressure at point A (see figure 5.2).

Furthermore, the ratio over time between damaged length and total base length as well as damaged area to total dam cross section area were calculated.

Cumulative displacement in point A shows no significant difference between the two calibration attempts for the regularized model and the elastic model. But all achieved values are smaller (maximum of 7 mm) than the ones obtained from the Benchmark workshop which are between 20 and 400 mm after 6 seconds of run time. This may be caused by the singularity at point A.
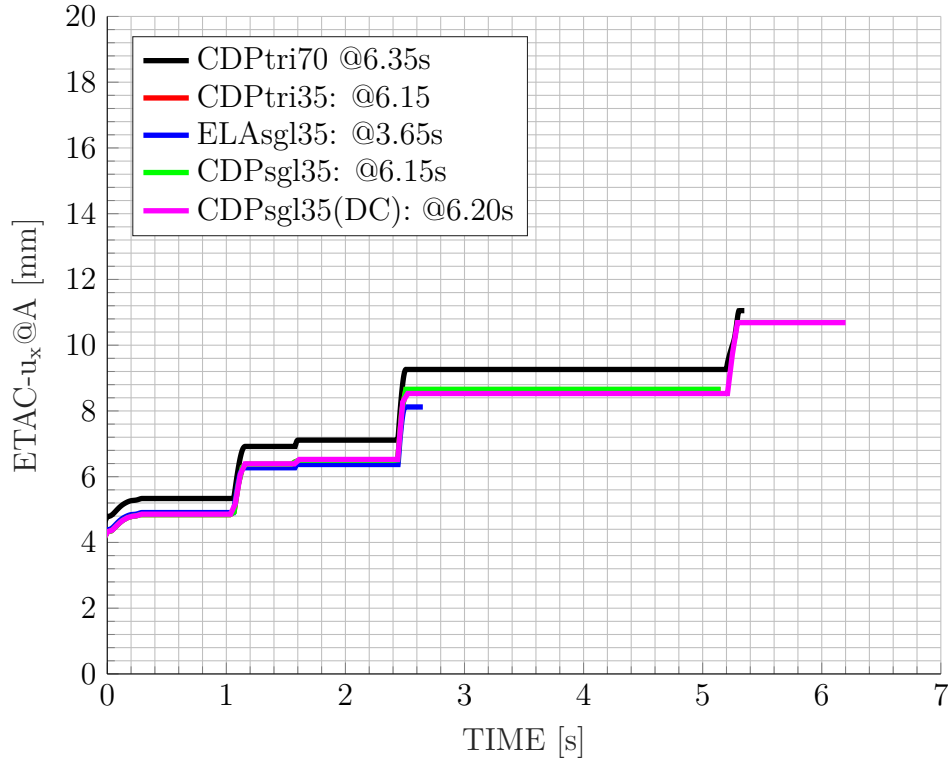
(a) Cumulative displacement at A
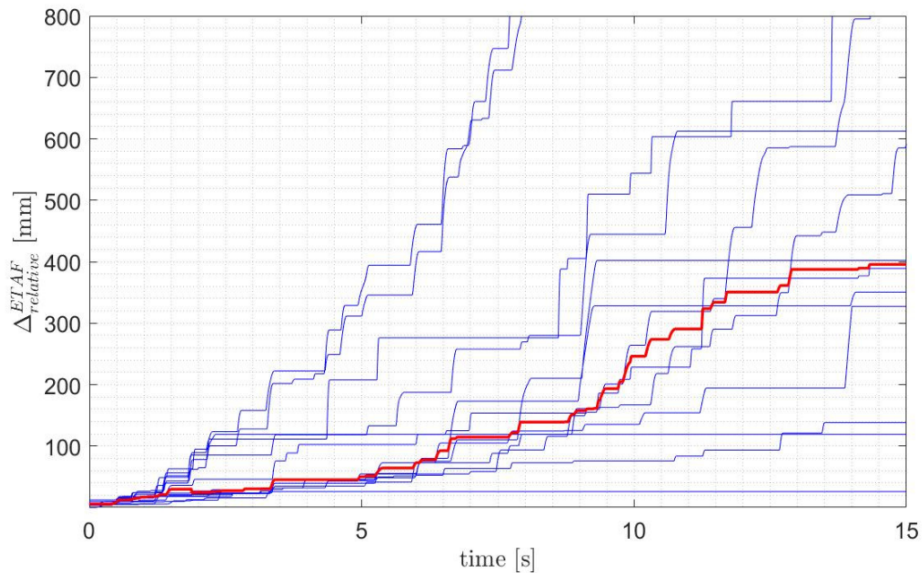
(b) References from Benchmark Workshop

Fig. 5.14: Comparison between resulting cumulative displacement at point A obtained from **(a)** performed analysis and **(b)** results obtained by Benchmark workshop

Cumulative displacement in point C shows no significant difference between the two calibration attempts for the regularized model and the elastic model. Achieved values up to 160 mm are in range of the ones obtained from the Benchmark workshop which are between 10 and 450 mm.
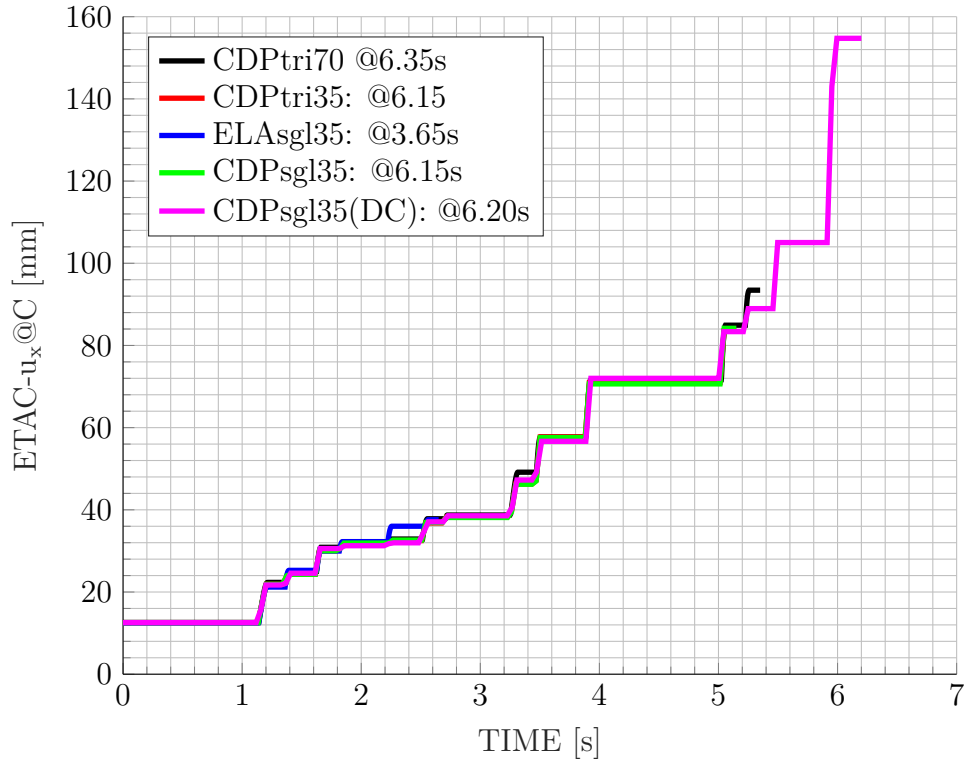
(a) Cumulative displacement at C
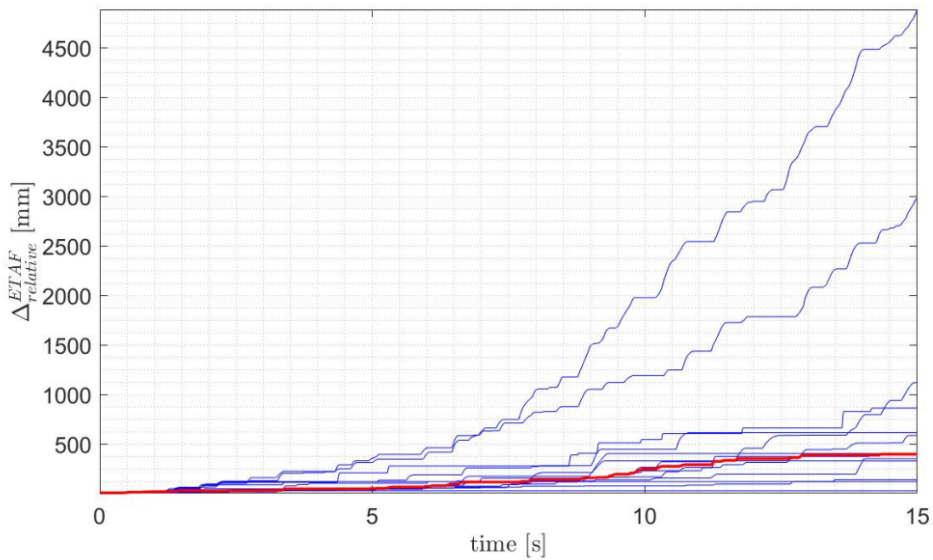
(b) References from Benchmark Workshop

Fig. 5.15: Comparison between resulting cumulative displacement at point A obtained from **(a)** performed analysis and **(b)** results obtained by Benchmark workshop

Cumulative dynamic pressure shows no significant difference between the two calibration attempts for the regularized model. Achieved values up to 0.38 MPa are in range of the ones obtained from the Benchmark workshop which are between 0.2 and 1.8 MPa.
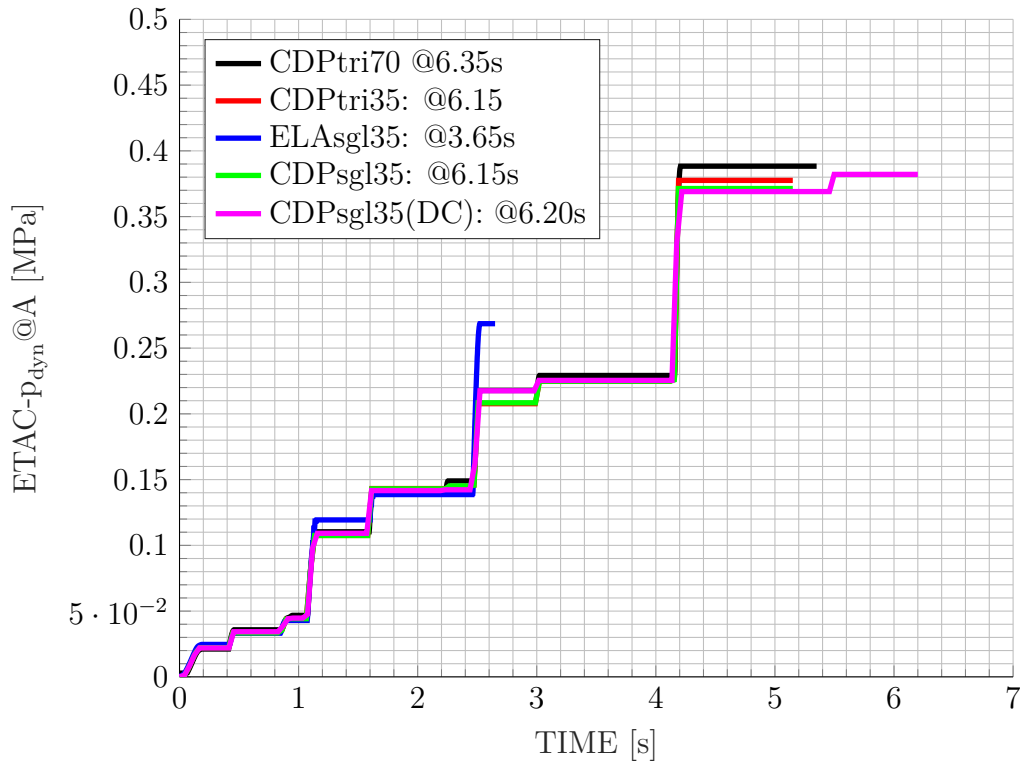
(a) Cumulative dynamic pressure at A
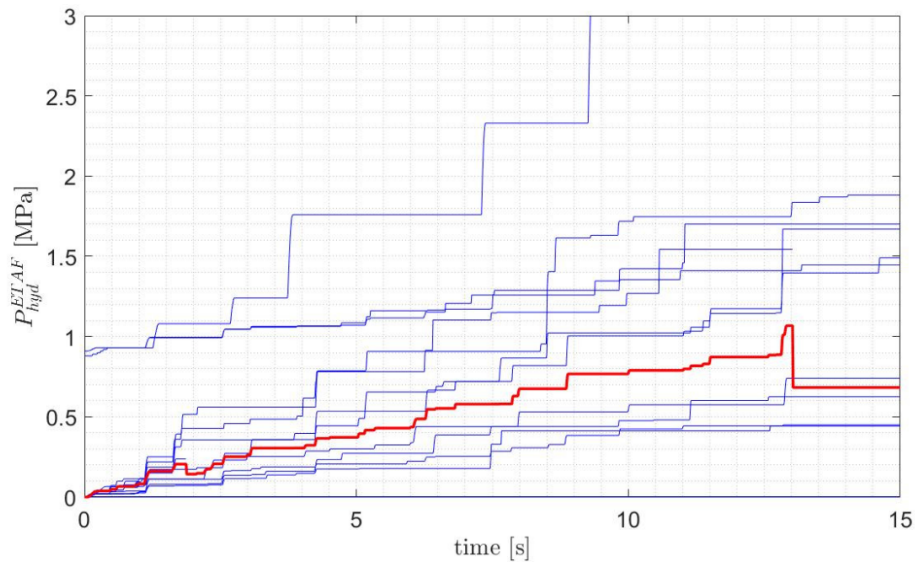
(b) References from Benchmark Workshop

Fig. 5.16: Comparison between resulting cumulative dynamic pressure at point A obtained from **(a)** performed analysis and **(b)** results obtained by Benchmark workshop

#16 (t = 3 s)   #24 (t = 14 s)   #28 (t = 8,5 s)   #33 (t = 6,5 s)
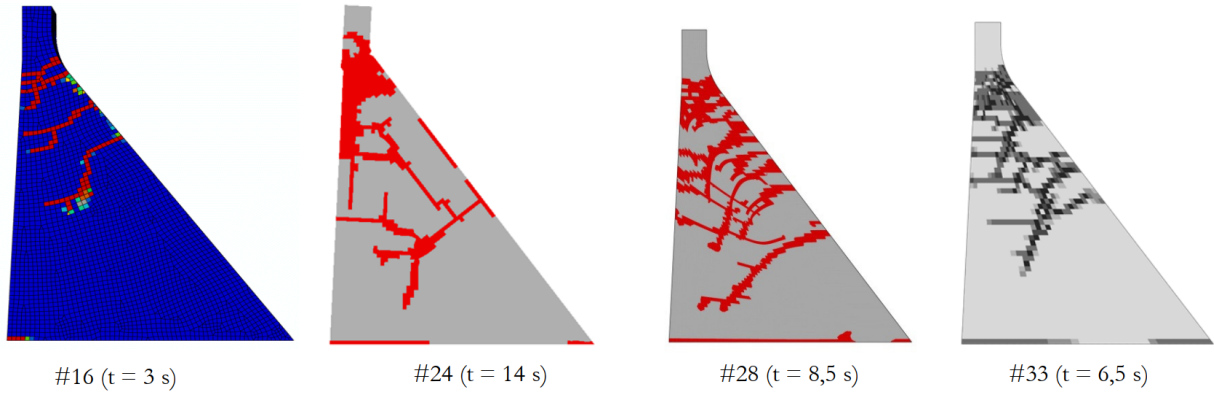
Fig. 5.17: Damage patterns of analyses done at the Benchmark Workshop for models which do not reach the end of the ETAF

Damage patterns which are presented in the pre-report of the workshop (see figure 5.17) couldn't be reproduced. Furthermore, the damage development over time is calculated from the ratio between elements with damage and number of total elements. It shows no significant difference between the two calibration attempts for the regularized model, neither for smaller element sizes or results by using displacement convergence only. The elastic microplane model delivers much faster damage development. It can be stated that the critical moment for convergence loss lies about 10 % damaged length of the base joint. Displacement convergence only can last for almost 18 % damaged length (see figure 5.18).
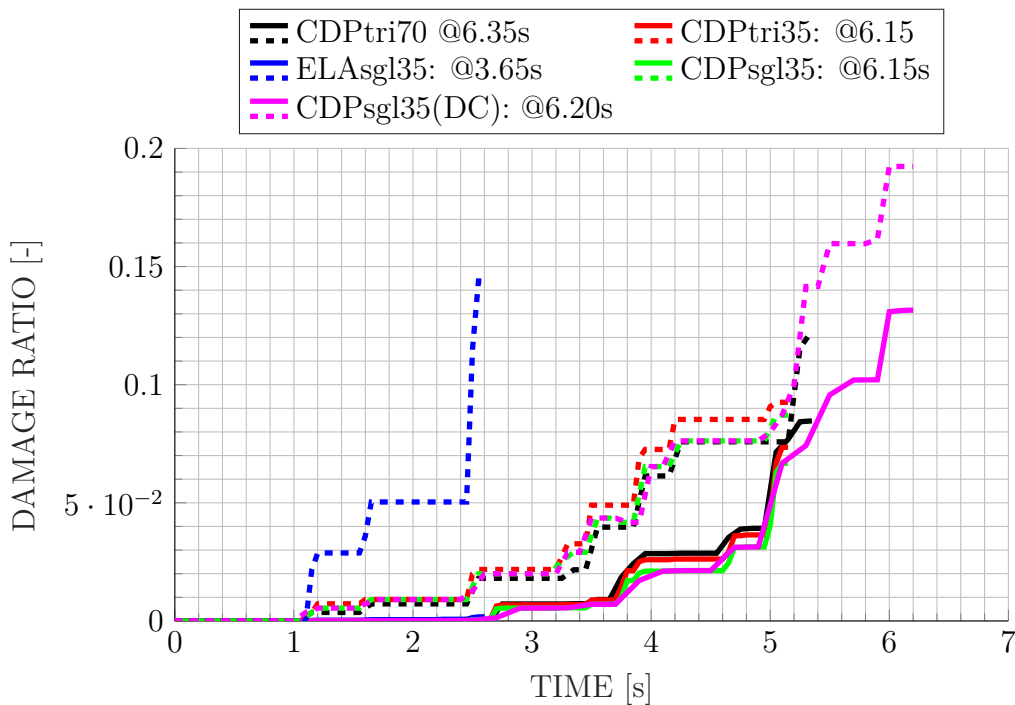
Fig. 5.18: Damage ratio during analysis with ETAF until model failure for different material models, dam body areal damage (solid lines) and damage along base joint (dashed lines)

Figure 5.19 shows a comparison between the regularized and the elastic microplane model. The first was calibrated using an artificial three point bending test and the second was calibrated on a single element to have the desired fracture energy. The damage distribution and the

duration time until convergence loss shows that these two attempts lead to critical different results.

(a)   **(b)**
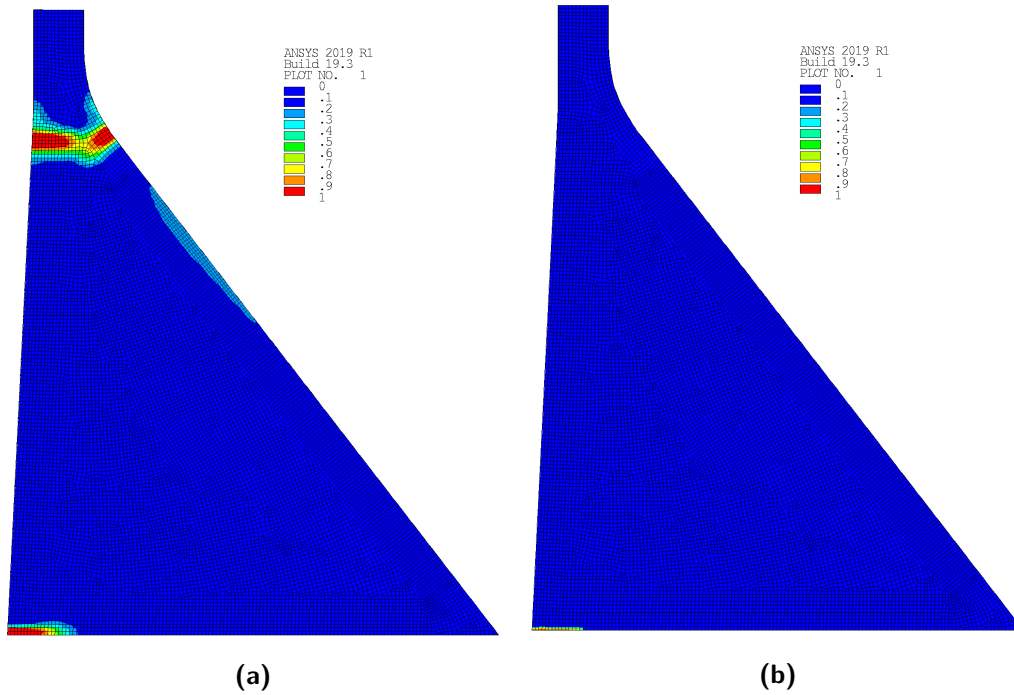
Fig. 5.19: Final tensile damage distribution: **(a)** regularized model, calibrated on 3-point-bending test ($T_{fail} = 6.35s$) and **(b)** elastic model calibrated on a single element ($T_{fail} = 3.65s$)

Figure 5.20 shows the tensile damage distribution at time of convergence failure for two calibration attempts for the regularized microplane model using different convergence criteria.

(a)   **(b)**
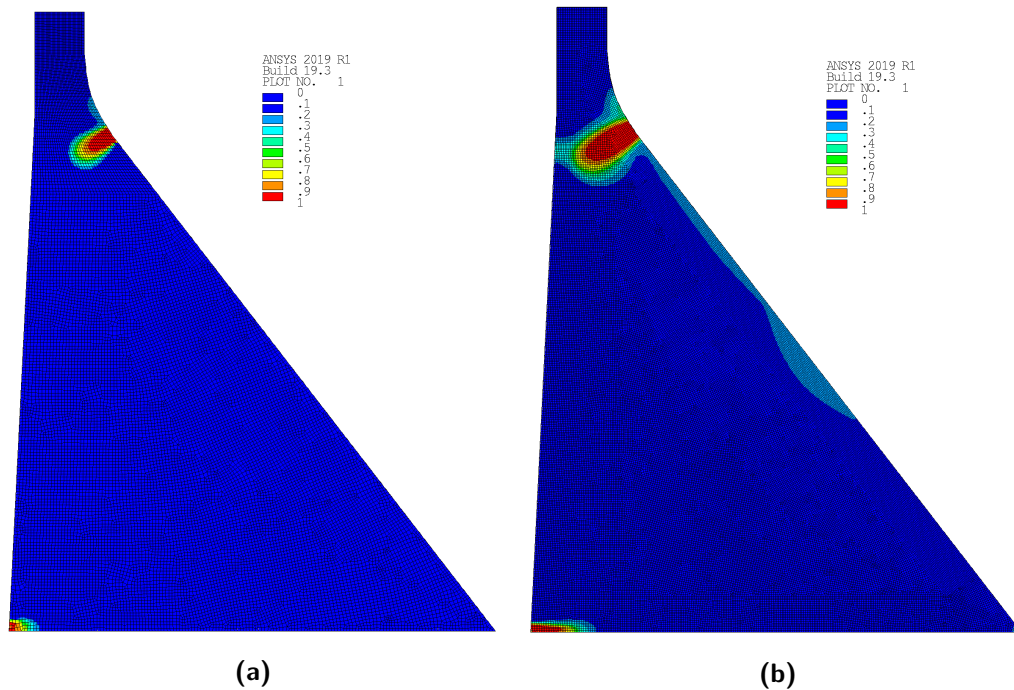
Fig. 5.20: Final tensile damage distribution for regularized model calibrated on a single element with **(a)** force ($T_{fail} = 6.35s$) and **(b)** displacement convergence ($T_{fail} = 7.20s$)

5.6 Numerical Problems

Here are shown numerical or material model based problems which couldn't be overcome during this thesis.

Figure 5.21 shows the maximum main principle stress over time for the given seismic excitation. It can be seen that the maximum stress exceeds the parametric defined tensile strength of 2 MPa by up to 20% along the downstream side of the dam. At the upstream side of the base joint, the values are exceeded even up to 50% and at the joint dip up to a multiple. This may be explained from the singularity caused by the sharp edge between dam body and foundation. The same effect was already explored by modelling the Brazilian test.
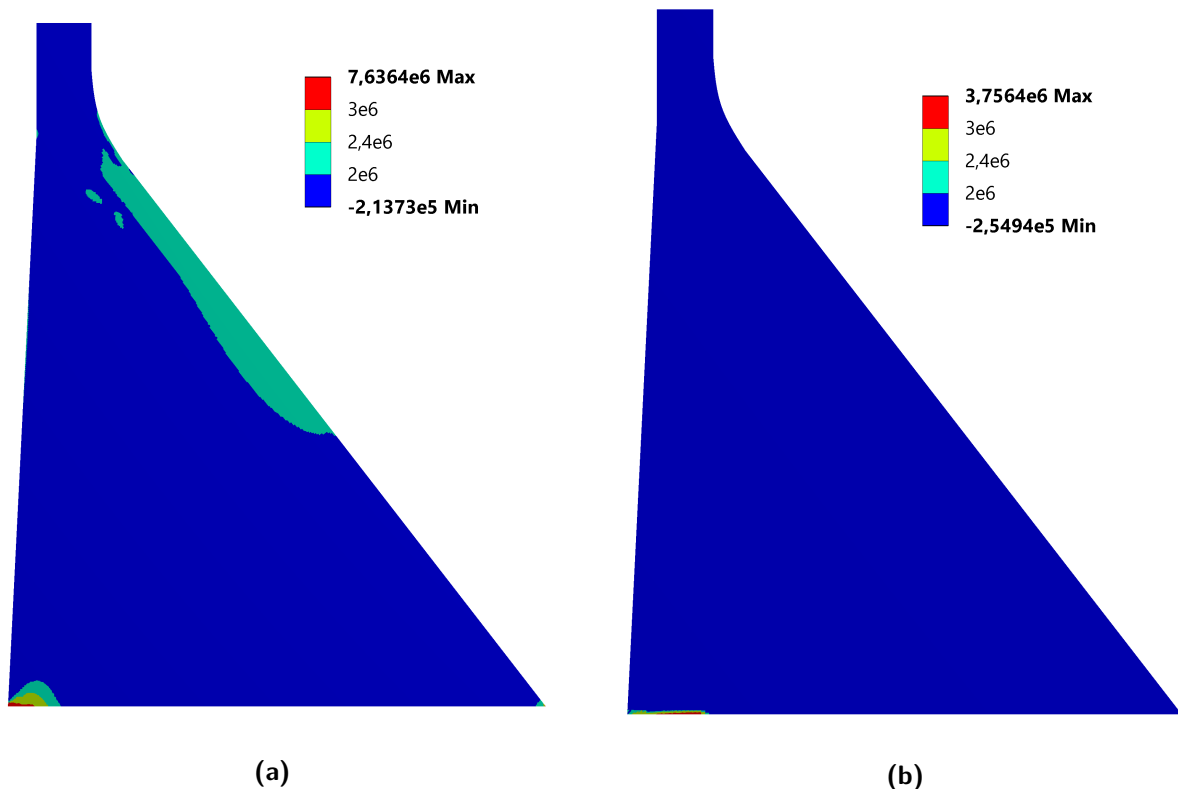
Fig. 5.21: Distribution of the maximum first principle stress over time for **(a)** regularized model fitted to the three point bending test and **(b)** elastic model fitted to a single element

The same behaviour was observed by usage of the elastic microplane model without regularization (see figure 5.22). Although, there the overall maximum remained much lower.

Another phenomenon encountered was the volume increase of highly damaged elements, which leads to unreasonable deformation displays (see figure 5.23a). Furthermore, numerical scattering was observed (see figure 5.23b). This may be caused due the regularization in combination with very small time step close to $1e-7$ seconds.

(a)   **(b)**
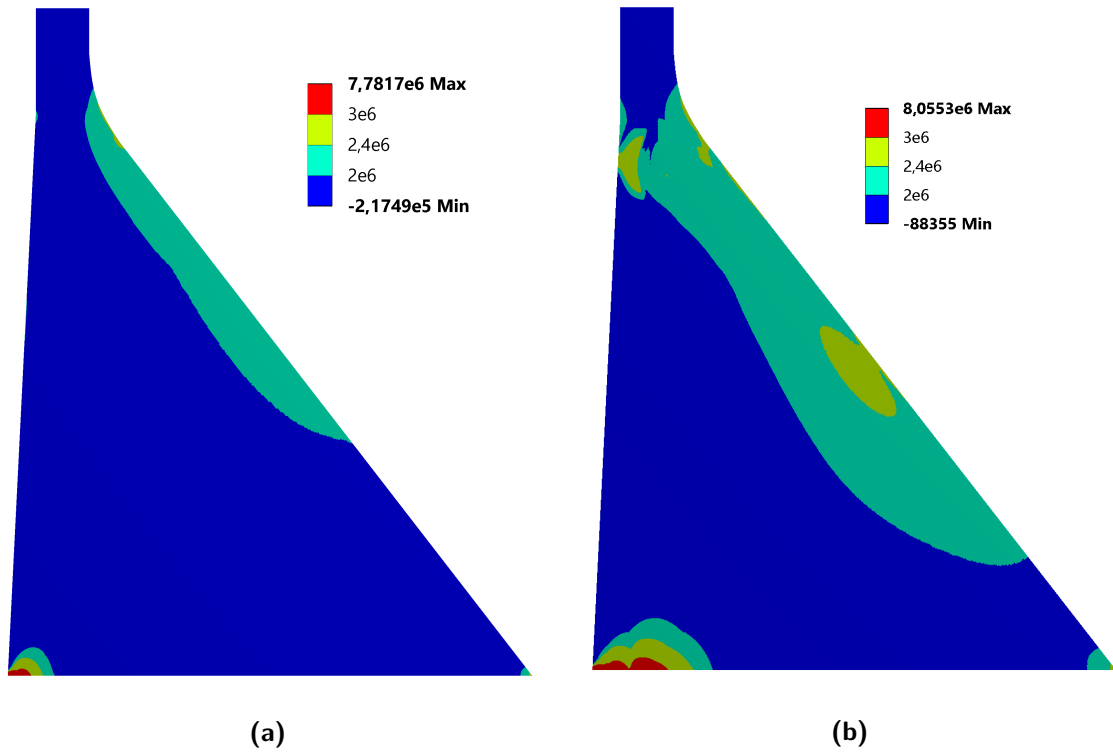
Fig. 5.22: Distribution of the maximum first principle stress over time for the regularized model calibrated on one element using **(a)** force convergence (failed at 6.35s) and **(b)** displacement convergence (failed at 7.20s)

(a)   **(b)**
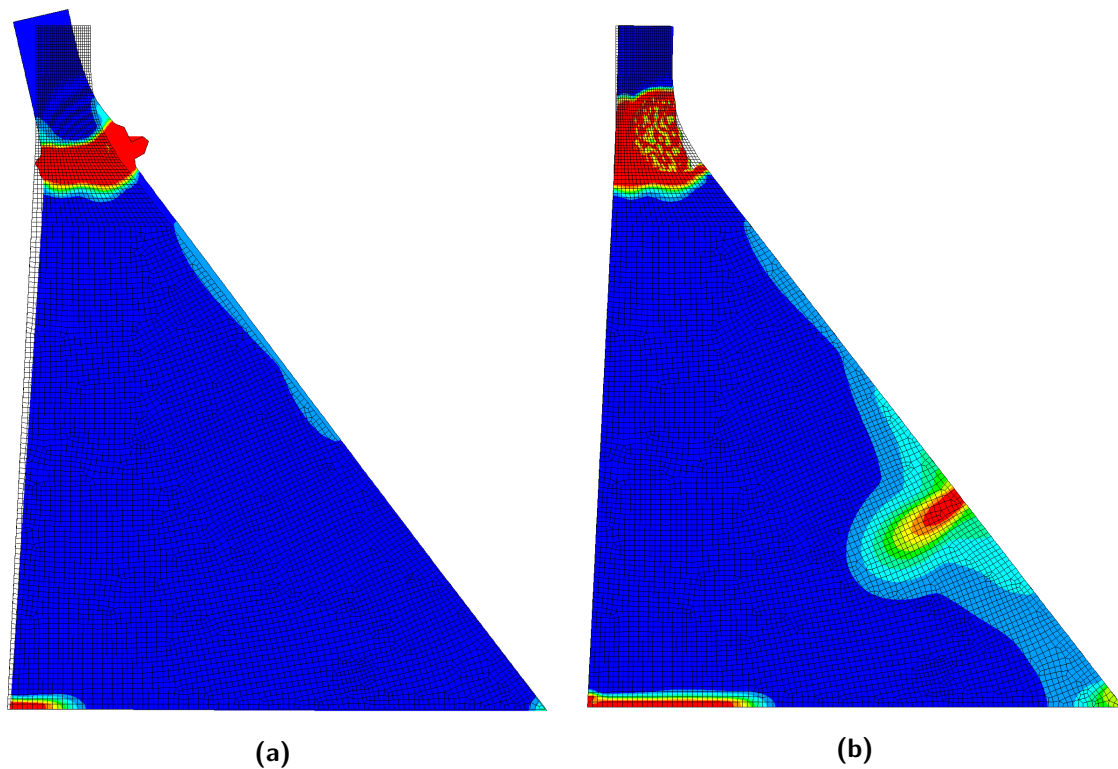
Fig. 5.23: Numerical errors encountered during analyses **(a)** volume increase in plastic zones **(b)** numerical scattering may caused to failure in non-local interaction

5.7 Rigid Block Analysis: Partial Stability
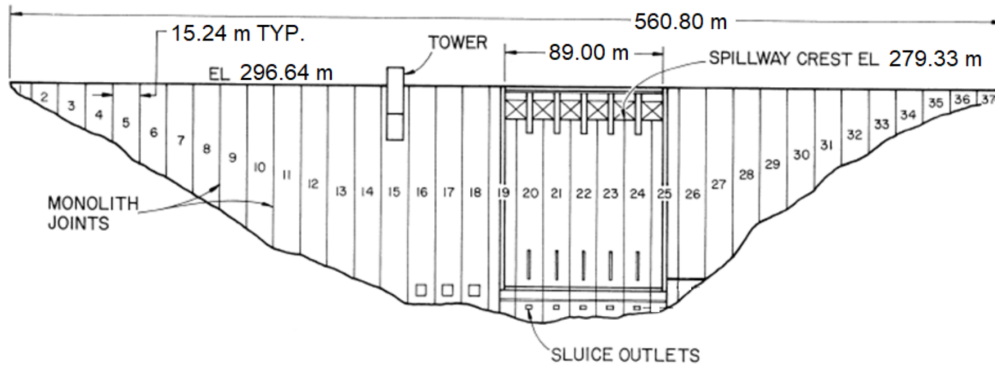
Fig. 5.24: Block geometry of the Pine Flat Dam [38]

A rigid block analysis was performed on two blocks forming from elongation of the crack trajectories obtained by the non-linear analysis (see figure 5.25). The following assumptions were made:

(1) Blocks are sliding on an infinite plane surface
(2) Friction angle of the joint is 45°
(3) No cohesive forces are acting
(4) No water is present in the cracks during seismic excitation
(5) No frictional forces are transferred on vertical faces of the block: Block joints are open
(6) Uniform stress distribution along sliding plane
(7) Static water force does not change over time: block sliding into the reservoir is neglected
(8) Hydrodynamic pressures modelled with added mass approach according to Westergaard, only horizontal acceleration considered
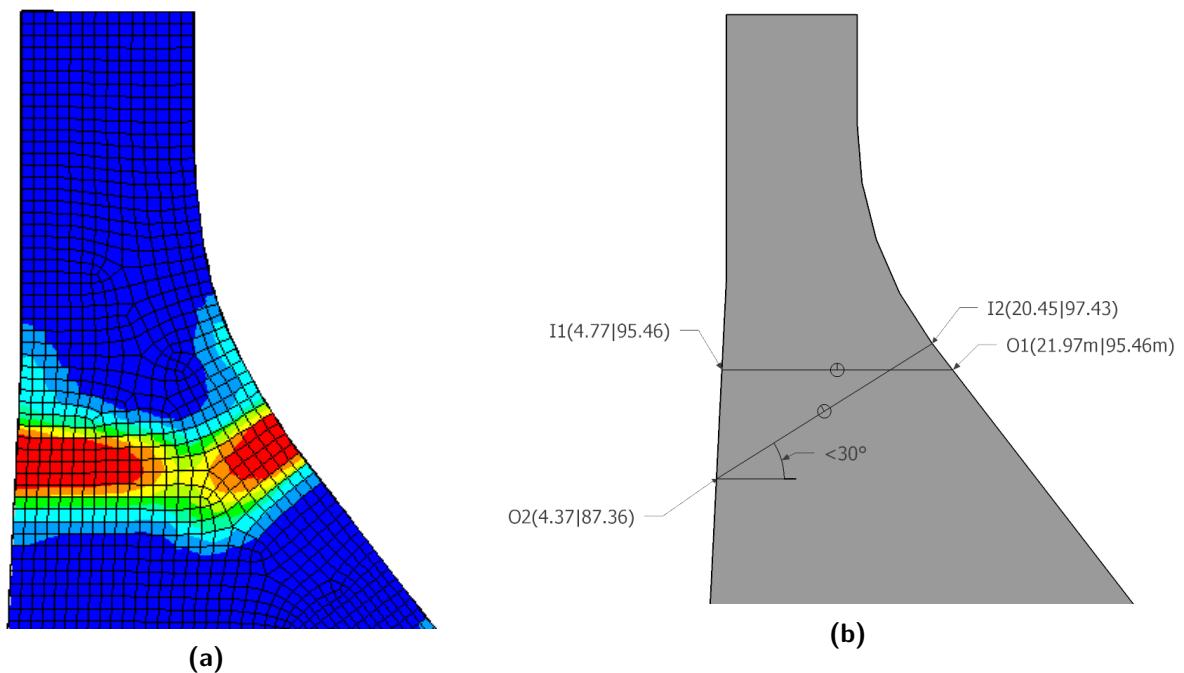
Fig. 5.25: **(a)** resulting damage from non-linear analysis and **(b)** identified crack trajectories

This seismic deformation analysis follows the most common approach in practice developed by *Newmark* for a rigid block sliding on a plane [48].

5.7.1 Newmark Block A - Horizontal Sliding Plane
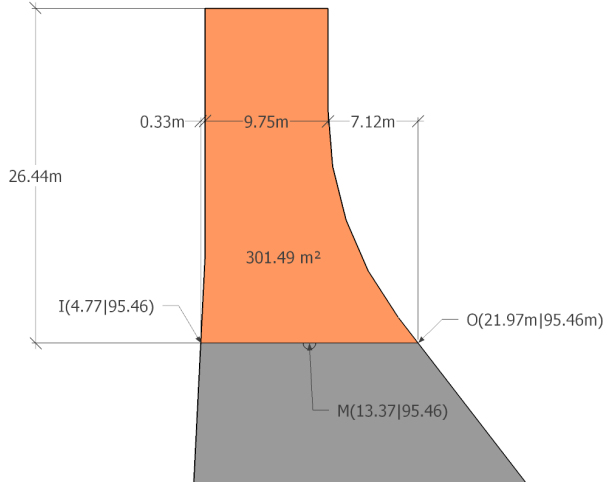
(a) Block sliding along horizontal crack line
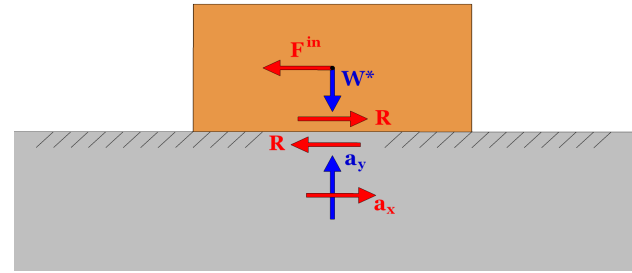
(b) Simplified block model A (horizontal crack) on infinite sliding plane

The equation of equilibrium for the block displayed in figure 5.26b is:

$$F^{in} = R \tag{5.3}$$

Where

$$R = W^* \cdot \tan(\varphi) \quad W^* = m \cdot (g + a_y) \quad F^{in} = m \cdot a_x$$

Because the block only starts moving if this equilibrium limit is exceeded, the yield acceleration can then be formulated as:

$$a^{yield} = (g + a_y) \cdot \tan(\varphi) \tag{5.4}$$

The effective acceleration a^{eff} (see figure 5.27), which actually moves the block has to be greater than the obtained yield acceleration. As the sliding plane is horizontal, the movement can happen in downstream and upstream direction.

Figure 5.28 shows the horizontal displacement according to *Newmark* in the downstream and upstream direction, as well as the sum of these two. However, the installed waterstops in the block joints can usually bear a displacement of about half a meter. The calculated final displacement up to four meters clearly exceeds this limit. Therefore, the sealing of the block joint is not sustained and water may enter the opened joint in case of a refilling of the reservoir. This may cause a failure of the separated block although a danger of tipping is not given as shown in section 5.7.3.
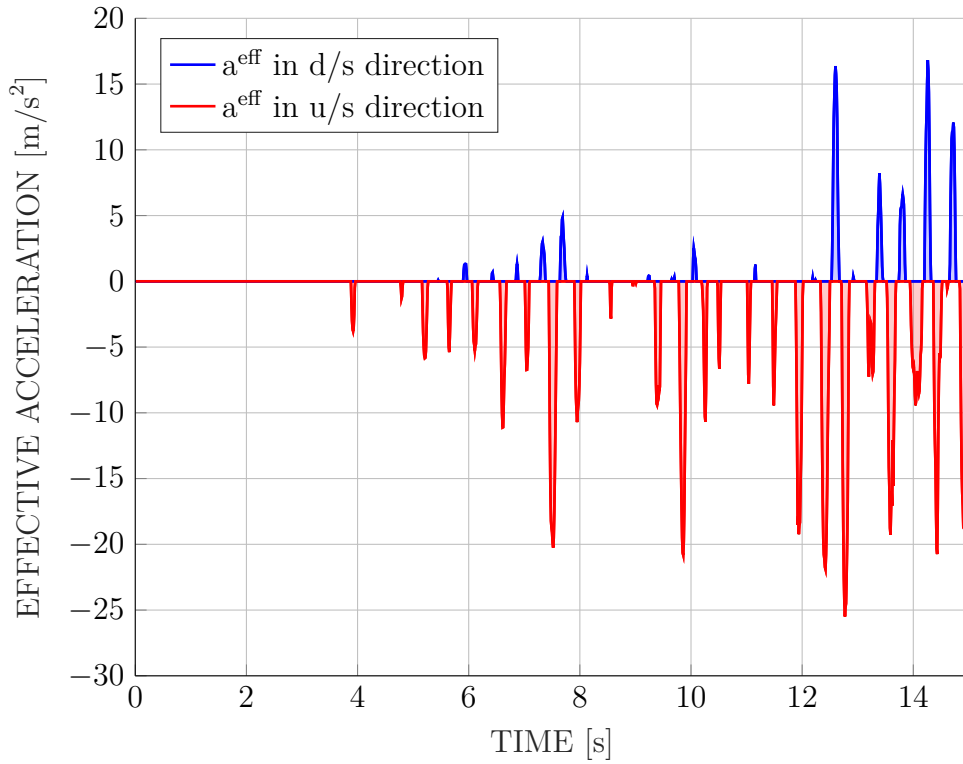
Fig. 5.27: Effective acceleration on block over time for horizontal block sliding
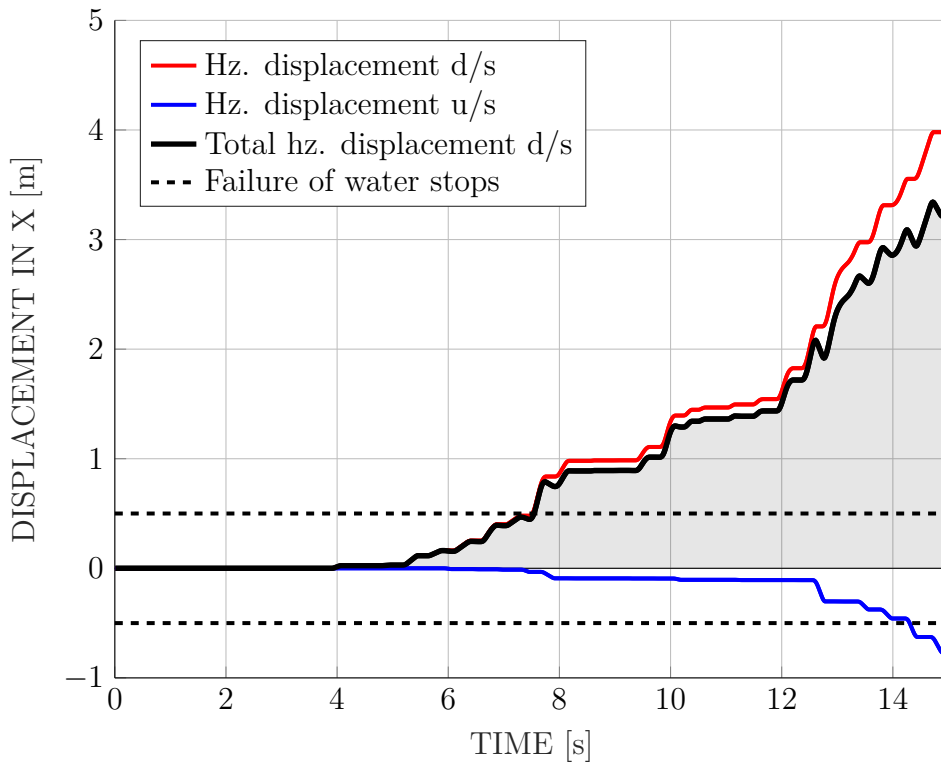
Fig. 5.28: Displacement according to Newmark method over time for horizontal block sliding

5.7.2 Newmark Block B - Inclined Sliding Plane

(b) Simplified block model B (on inclined crack) on infinite sliding plane
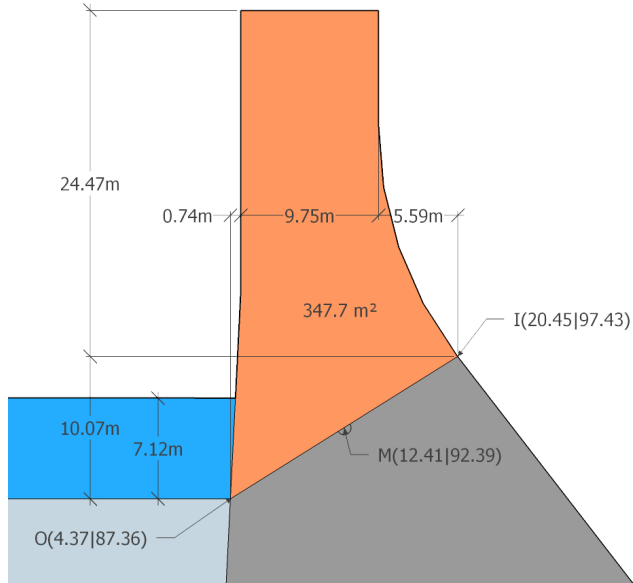
(a) Block sliding along inclined crack line (30 degrees)

The equation of equilibrium for the block with the length $l = 15.24m$ displayed in figure 5.29b is:

$$F^{in} \cdot \cos(\alpha) + W^* \cdot \sin(\alpha) - F_w^{stat} - F_w^{dyn} = R \tag{5.5}$$

Where

$$R = \left[W^* \cdot \cos(\alpha) - F^{in} \cdot \sin(\alpha) \right] \cdot \tan(\varphi)$$

$$W^* = m \cdot (g + a_y) \qquad F^{in} = m \cdot a_x$$

$$F_w^{stat} = \frac{1}{2} \cdot \rho_w \cdot g \cdot l \cdot h^2 \cdot \cos(\alpha)$$

$$F_w^{dyn} = a_x \cdot \frac{7}{12} \cdot \rho_w \cdot l \cdot \sqrt{H \cdot h^3} \cdot \cos(\alpha)$$

The total added mass is calculated according to *Westergaard* for a water depth h and a water level of H measured from the heel of the dam. This added mass is then multiplied by the horizontal acceleration a_x. The part of the resulting force which is parallel to the crack trajectory is named F_w^{dyn}.

The yield acceleration (see figure 5.27) for the block with an inclined sliding plane results to:

$$a^{yield} = \frac{F_w^{stat} - W^* \cdot (\sin(\alpha) - \cos(\alpha) \cdot \tan(\varphi))}{m \cdot (\cos(\alpha) - \sin(\alpha) \cdot \tan(\varphi)) - \frac{7}{12} \cdot \rho_w \cdot l \cdot \sqrt{H \cdot h^3} \cdot \cos(\alpha)} \tag{5.6}$$

Figure 5.28 shows the horizontal displacement according to *Newmark* in the upstream direction. The calculated final displacement is roughly 4.5 meter. However, because the installed waterstops in the block joints can only bear a displacement of about half a meter, the

sealing of the block joint is not sustained. Therefore, water may enter the opened joint in case of a refilling of the reservoir. This may cause a failure of the separated block although a danger of tipping and sliding is not given as shown in section 5.7.3.
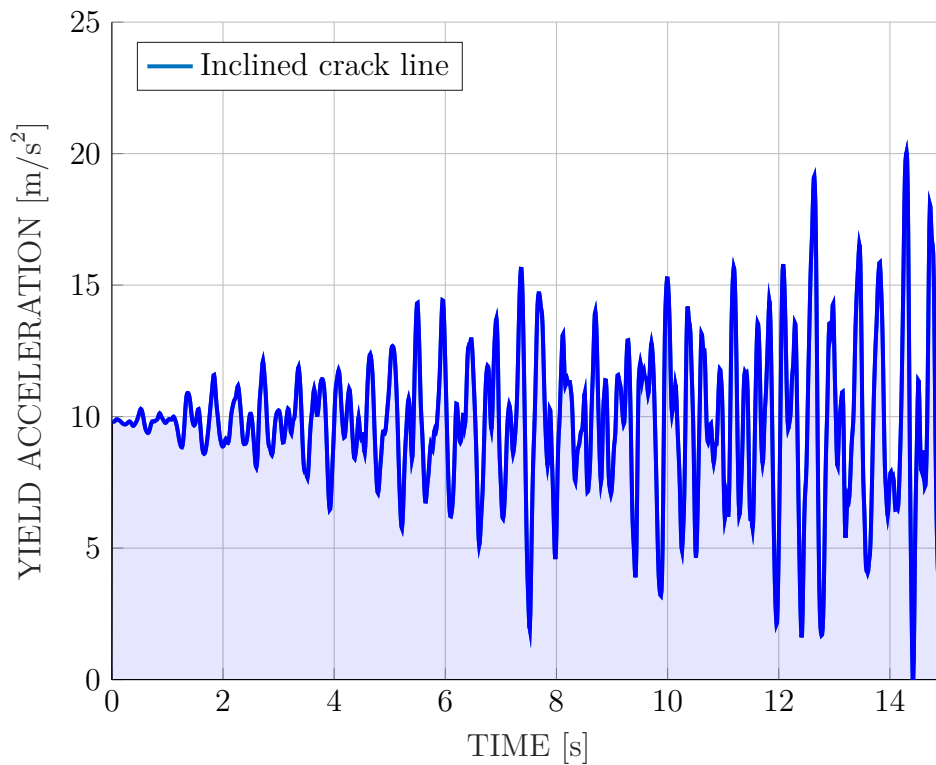
Fig. 5.30: Yield acceleration over time for inclined block sliding
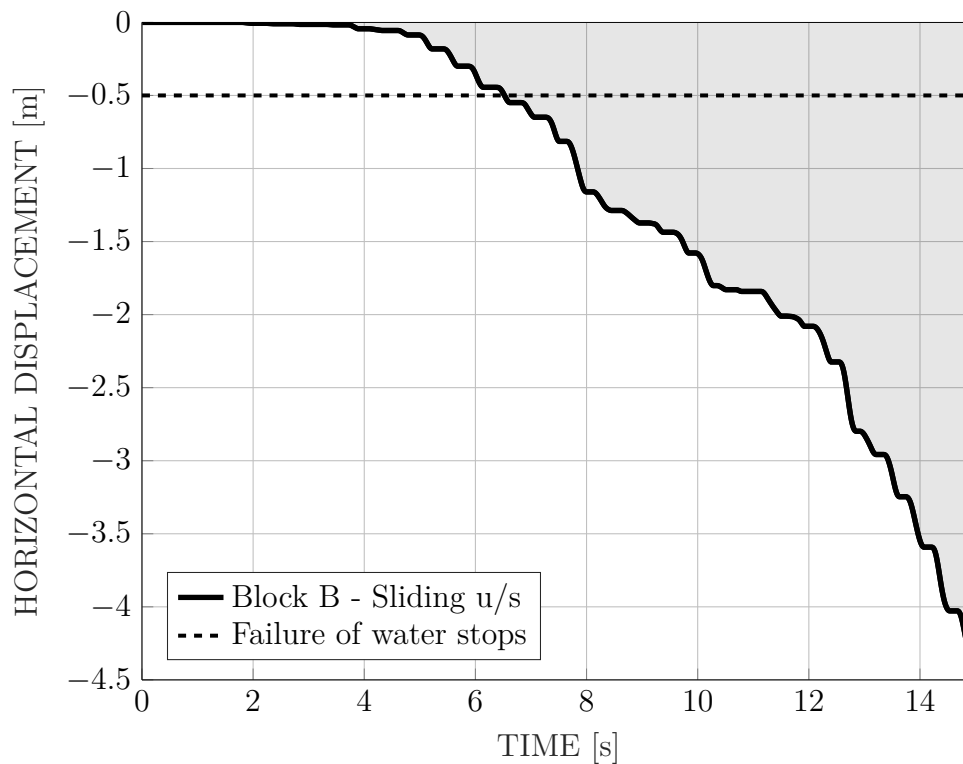
Fig. 5.31: Displacement according to Newmark method over time for inclined block sliding

5.7.3 Factor of Safety

A remaining factors of safety after excitation can be calculated regarding sliding stability and hazard of tipping. It should be stated that these obtained values are purely *theoretical*: If the block moves more than the waterstop's bearable distance (usually up to half a meter), the block has to be already considered as failed because without proper sealing uncontrolled water release may occur.

For both blocks, centre of gravity were computed by approximating their area by triangular defined by three vectors **a**, **b** and **c**. The area of these triangles was computed by:

$$A = \frac{1}{2} |\, (\mathbf{b} - \mathbf{a}) \times (\mathbf{c} - \mathbf{a}) \,| \tag{5.7}$$

The centre of gravity of each was then obtained by:

$$\mathbf{x} = \frac{1}{3} \left(\mathbf{a} + \mathbf{b} + \mathbf{c} \right) \tag{5.8}$$

Each block's centre of gravity is then calculated by:

$$\mathbf{C} = \frac{\Sigma \, A \cdot \mathbf{x}}{\Sigma A} \tag{5.9}$$

The results are listed in table 5.6. The origin of the used coordinate system is the upstream heel of the dam.

	X [m]	**Y [m]**
Block A	11.42	107.21
Block B	10.81	105.43

Tab. 5.6: Geometric centre of gravity of the two investigate blocks

Then, the factor of safety against tipping was calculated as the ratio of the horizontal distance from the tipping point to the block's centre of gravity and the final horizontal displacement obtained from the Newmark method (see figure 5.32):

$$FoS = \frac{X_c}{X_c - d} \tag{5.10}$$
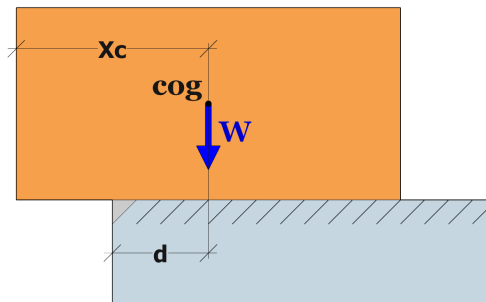
Fig. 5.32: Factor of safety against tipping

The factor of safety against sliding was computed by the equilibrium of static forces. The FoS was evaluated for a steady water level in the reservoir as follows:

$$FoS = \frac{W \cdot \cos(\alpha) \cdot \tan(\varphi)}{W \cdot \sin(\alpha) - F^{stat}} \tag{5.11}$$

For the case after a possible lowering of the water table in the reservoir:

$$FoS = \frac{\cos(\alpha) \cdot \tan(\varphi)}{\sin(\alpha)} \qquad (5.12)$$

Results are summarized in table 5.7.

Factor of Safety

Block A - tipping	1.83
Block B - tipping	1.46
Block B - sliding, steady reservoir level	1.84
Block B - sliding, lowered reservoir level	1.30

Tab. 5.7: Factor of safety for blocks A and B

6 Conclusion and Summary

Modelling the behaviour of large structures, e.g. dams, remains a challenging task. This includes the selection of suitable model assumption for the damping factor of foundation and dam as well as material or base joint properties. Also, the application of boundary conditions desires high attention especially in terms of absorption and reflection abilities. Furthermore, the final results and their computational time depend on the creation of an appropriate mesh.

The main contributor to dealing with these tasks is the *International Commission on Large Dams* (ICOLD). Their regularly held benchmark workshops [3, 49] and publications e.g. *ICOLD Bulletins* [50] represent the state of the art of dam analysis and related topics. Today, non-linear modelling becomes a necessity if structural failure cannot be excluded in linear analyses. This may be the case for unusual and extreme loading cases, e.g. extraordinary earthquakes. The enduring effort to improve reliable concepts hand in hand with the ongoing increase of computational power leads to new possibilities of modelling these structures. However, the selection of representative parameters for the involved material models of concrete, water and rock must be done with care.

Lifelong monitoring of existing dams delivers lots of data for the calibration of seismic properties and linear material behaviour. This data can then be used for the determination of dynamic material properties, e.g. dynamic stiffness or dynamic Poisson ratio, as shown in [51]. In contrary, calibration data for material models is still rare if they are supposed to simulate non-linear behaviour, e.g. strain-softening. Also, the validation of the used model requires data of non-linear behaviour of the whole dam structure. This data - usually - can only be recorded if the structure is close to its failure. However, it is necessary to reconsider dynamic material properties due to high strain rates, especially for seismic excitation.

Regarding the modelling of the cracking behaviour, the used material model should be selected according to the given task. Linear or Plastic Fracture Mechanics and Crack Band Models can be used if the stability of a single, existing crack should be monitored. Plasticity models and Extended Finite Element Method are most suitable if the overall performance of a structure with multiple fracture zones is of interest. These two methods are also adapted for the formation of new cracks. Commercial software like *Ansys Mechanical* supports all these kinds of models. It is up to the investigating engineer to select the most suited method.

Material models with non-local regularization are capable of replicate the material behaviour caused by the concrete specific Fracture Process Zone. A very fine mesh and therefore higher computational power is required if the width of this zone is very small compared to the size of the entire structure. Furthermore, the selection of the parameter defining the range of this zone is crucial. Although various ways to its determination exist, not all of them are practical or economical applicable on dam concretes due to the large required specimen sizes. However, it should be kept in mind that the influence of this parameter on the material model behaviour is significant.

To summarize the results of the performed analyses, the tested model - in its current form - is only conditional qualified to predict crack forming in large scale structures. It has

advantages over tensorial damage models like mesh independence, multiple shear planes and easy convergence behaviour. Yet, the lack of validation on large structures and its failure to model crack initiation at singularity points cannot be ignored. Therefore, a practical application of the investigated model cannot be ensured.

For the future, more material tests on dam concrete with its large grain sizes is needed to be performed. These shall provide a solid data base for the calibration of non-linear concrete material models used to simulate large scale structures. Furthermore, this thesis should serve as an inducement to improve non-linear material models in order to overcome existing difficulties in relation with the modelling of large, unreinforced concrete structures.

Finally, the pros and cons of the coupled damage-plasticity model provided by *Ansys Mechanical* on their application on large scale structures undergoing seismic loading encountered during this thesis, are summarized as follows.

$\oplus$ *Reduced mesh dependency:* with active non-local regularization orientation and size variations of mesh elements do not influence the overall behaviour as harsh as for tensorial damage models.

$\oplus$ *Damage healing:* this is essential for simulation of seismic loading. Due to the separation of tensile and compressive damage, the forming and re-closing of cracks can be modelled. For simple damage models, damage occurring during tension also affects compressive response in the same manner.

$\oplus$ *Enhanced convergence:* the non-local regularization leads to redistribution of plastic strains which prevent localized strain peaks from causing convergence problems.

$\oplus$ *Representation of FPZ:* a fracture process zone rather then a single crack is modelled, which represents better the cracking behaviour of aggregate materials like concrete.

$\oplus$ *Additional represented effects:* multiple damage planes leads to the capability of representing e.g. the vertex effect described in chapter 4.2.3.

$\oplus$ *Physical parameters:* most of the parameters used in this model have a direct physical meaning like strength or stiffness, others also describe independent physical behaviour like damage development or thresholds.

$\oplus$ *Full stress degradation:* exponential damage development enable possibility to model almost zero stress by high strains, no residual value is needed.

$\oplus$ *Hysteresis loop:* modelling of a full hysteresis loop is possible.

$\ominus$ *Computational effort:* due to the microplane model itself, more state variables need to be calculated and stored as in ordinary damage models, this requires a higher amount of physical memory during the solving process as well as to store the results, furthermore this leads to a larger computational time.

$\ominus$ *Fine mesh size vs large geometry:* depending on the chosen non-local range, the required mesh size tends to be very small compared to the afflicted geometry, therefore an enormous amount of elements are needed to model the dam properly, this leads to larger computational time and required memory.

$\ominus$ *Singularity:* the non-local regularization has shown to be in-consisted by dealing with sharp edges where forces are submitted, e.g. Brazilian test or base joint of the dam model. Such geometries should definitely be avoided in order to obtain reasonable results.

⊖ *Dynamic stiffening:* the influence of the loading speed and loading duration on the material responses, e.g. stiffness, can only be represented in terms of an alternated dynamic modulus E_{dyn} but not in terms of a rate dependent material law.

⊖ *Calibration:* small scale experimental data of non-linear material behaviour is rarely available for dam concrete using grain sizes larger than the ordinary concrete.

⊖ *Validation:* the lack of data of dam structures on their behaviour during a seismic event, e.g. detailed material data, tensile tests, introduced crack patterns due the shaking, makes a validation of the material model when used at a large scale difficult.

⊖ *Accessibility:* microplane material laws and their results are accessible only through scripting commands (at least for *Ansys Mechanical*).

List of Figures

List of Tables

Bibliography

[1] J. Salamo and D.W. Harri. *Evaluation of Nonlinear Material Models in Concrete Dam Finite Element Analysis*. U.S. Bureau of Reclamation, 2014.

[2] J. Enzell and M. Tollsten. *Thermal cracking of a concrete arch dam due to seasonal temperature variations*. 2017.

[3] R. Malm, M. Hassanzadeh, and R. Hellgren. *Proceedings of the 14th ICOLD International Benchmark Workshop on Numerical Analysis of Dams*. 2018.

[4] Eugen Brühwiler. "Bruchmechanik von Staumauerbeton". PhD thesis. Lausanne: Ecole Polytechnique Federale De Lausanne, 1988.

[5] S.P. Shah, S.E. Swartz, and C. Ouyang. *Fracture Mechanics of Concrete: Applications of Fracture Mechanics to Concrete, Rock and Other Quasi-Brittle Materials*. Northwestern University, Sept. 1, 1995. ISBN: 978-0-471-30311-4.

[6] Ran Zhu. *Scale and Aggregate Size Effects on Concrete Fracture : Experimental Investigation and Discrete Element Modelling*. Comue Universite Bretagne Loire, Dec. 20, 2018.

[7] K. Kirane, Z.P. Bažant, and G. Zi. "Fracture and Size Effect on Strength of Plain Concrete Disks under Biaxial Flexure Analyzed by Microplane Model M7". In: *Journal of Engineering Mechanics* 140.3 (Mar. 2014), pp. 604–613. ISSN: 0733-9399, 1943-7889.

[8] Bernhard Günter Trunk. "Einfluss der Bauteilgrösse auf die Bruchenergie von Beton". PhD thesis. ETH Zurich, 1999.

[9] C. Le Bellego et al. "Calibration of nonlocal damage model from size effect tests". In: *European Journal of MechanicsA/Solids 22* (2003).

[10] Z.P. Bažant and J. Planas. *Fracture and size effect in concrete and other quasibrittle materials*. Boca Raton, Florida 33431: CRC, 1998. 337 pp. ISBN: 0-8493-8284-X.

[11] Arne Hillerborg. *A model for Fracture Mechanics*. 1978.

[12] Z.P. Bažant and G. Pijaudier-Cabot. "Measurement of Characteristic Length of Nonlocal Continuum". In: *Journal of Engineering Mechanics* 115.4 (Apr. 1989), pp. 755–767. ISSN: 0733-9399, 1943-7889.

[13] M. Kozłowski, M. Kadela, and A. Kukiełka. "Fracture Energy of Foamed Concrete Based on Three-Point Bending Test on Notched Beams". In: *Procedia Engineering* 108 (2015), pp. 349–354. ISSN: 18777058.

[14] Per-Erik Petersson. *Crack Growth and Development of Fracture Zones in Plain Concrete and Similar Materials*. 1981. ISBN: 0349-4985.

[15] Herbert N. Linsbauer. *Damage Potential of an Upstream-Side Crack in a Gravity Dam Subjected to an Impact Loading in the Reservoir*. 2009.

[16] H. N. Linsbauer et al. "Simulation of Cracking in Large Arch Dam: Part I". In: *Journal of Structural Engineering* 115.7 (July 1989), pp. 1599–1615. ISSN: 0733-9445, 1943-541X.

[17] James.R. Rice. "A Path Independent Integral and the Approximate Analysis of Strain Concentration by Notches and Cracks". In: *Journal of Applied Mechanics* 35 (1968), pp. 379–386.

[18] Z.P. Bažant and B.H. Oh. "Crack band theory for fracture of concrete". In: *Matériaux et Constructions* 16.3 (May 1983), pp. 155–177. ISSN: 0025-5432, 1871-6873.

[19] Eleni Chatzi. *Introduction to the Extended Finite Element Method*. 2013.

[20] R. Ahmed et al. *A gradient-regularized coupled damage-plasticity model for concrete-like materials*. 2019.

[21] Z.P. Bažant and H. Oh. Byung. *Microplane Model for Fracture Analysis of Concrete Structures*. 1983.

[22] G. I. Taylor, M. A., and F.R.S. *Plastic Strain in Metals*. 1938.

[23] Zdeněk P. Bažant. "Microplane model for strain controlled inelastic behaviour". In: *Mechanics of Engineering Materials* 43 (1984), pp. 45–59.

[24] Z.P. Bažant and P.G. Gambarova. "Crack Shear in Concrete: Crack Band Microplane Model". In: *Journal of Structural Engineering* 110.9 (Sept. 1984), pp. 2015–2035. ISSN: 0733-9445, 1943-541X.

[25] I. Carol, Z.P. Bažant, and P.C. Prat. *New explicit Microplane Model for Concrete: Theoretical Aspects and Numerical Implementaion*. 1992.

[26] Z.P. Bažant et al. "Microplane Model for Concrete: II: Data Delocalization and Verification". In: *Journal of Engineering Mechanics* 122.3 (Mar. 1996), pp. 255–262. ISSN: 0733-9399, 1943-7889.

[27] Z.P. Bažant, Y. Xiang, and P.C. Prat. "Microplane Model for Concrete. I: Stress-Strain Boundaries and Finite Strain". In: *Journal of Engineering Mechanics* 122.3 (Mar. 1996), pp. 245–254. ISSN: 0733-9399, 1943-7889.

[28] Z.P. Bažant et al. "Microplane Model M4 for Concrete. I: Formulation with Work-Conjugate Deviatoric Stress". In: *Journal of Engineering Mechanics* 126.9 (Sept. 2000), pp. 944–953. ISSN: 0733-9399, 1943-7889.

[29] F.C. Caner and Z.P. Bažant. "Microplane Model M4 for Concrete. II: Algorithm and Calibration". In: *Journal of Engineering Mechanics* 126.9 (Sept. 2000), pp. 954–961. ISSN: 0733-9399, 1943-7889.

[30] F.C. Caner and Z.P. Bažant. "Microplane Model M7 for Plain Concrete. I: Formulation". In: *Journal of Engineering Mechanics* 139.12 (Dec. 2013), pp. 1714–1723. ISSN: 0733-9399, 1943-7889.

[31] I. Zreid and M. Kaliske. "A gradient enhanced plasticity–damage microplane model for concrete". In: *Computational Mechanics* 62.5 (Nov. 2018), pp. 1239–1257. ISSN: 0178-7675, 1432-0924.

[32] F.C. Caner, Z.P. Bažant, and J. Červenka. "Vertex Effect in Strain-Softening Concrete at Rotating Principal Axes". In: *Journal of Engineering Mechanics* 128.1 (Jan. 2002), pp. 24–33. ISSN: 0733-9399, 1943-7889.

[33] Z.P. Bažant and B.H. Oh. "Microplane Model for Progressive Fracture of Concrete and Rock". In: *Journal of Engineering Mechanics* 111.4 (Apr. 1985), pp. 559–582. ISSN: 0733-9399, 1943-7889.

[34] Imadeddin Zreid and Michael Kaliske. "An implicit gradient formulation for microplane Drucker-Prager plasticity". In: *International Journal of Plasticity* 83 (Aug. 2016), pp. 252–272. ISSN: 07496419. DOI: 10.1016/j.ijplas.2016.04.013.

[35] Z.P. Bažant and B.H. Oh. *Efficient Numerical Integration on the Surface of a Sphere.* 1986.

[36] R.R. Craig and Kurdila. *Fundamentals of structural dynamics.* 2nd ed. Hoboken, N.J: John Wiley, 2006. 728 pp. ISBN: 978-0-471-43044-5.

[37] Anil K. Chopra. *Dynamics of structures: theory and applications to earthquake engineering.* 4th ed. Upper Saddle River, N.J: Prentice Hall, 2012. 944 pp. ISBN: 978-0-13-285803-8.

[38] J. Salamon et al. *ICOLD Benchmark Workshop: Theme A - Formulation Seismic Analysis of Pine Flat Concrete Dam.* 2019.

[39] American Society of Civil Engineers, ed. *Minimum design loads for buildings and other structures.* ASCE standard. Reston, Va: American Society of Civil Engineers : Structural Engineering Institute, 2010. 608 pp. ISBN: 978-0-7844-1085-1.

[40] M. A. Hariri-Ardebili, H. Mirzabozorg, and R. Kianoush. "Comparative study of endurance time and time history methods in seismic analysis of high arch dams". In: *International Journal of Civil Engineering* 12.2 (2014), p. 18.

[41] Henri P. Gavin. "Numerical Integration in Structural Dynamics". In: *Department of Civil & Environmental EngineeringDuke University* (2018).

[42] Richard Malm. *Guideline for FE Analyses of Concrete Dams.* Energiforsk, 2016.

[43] F Barlat and J Lian. *Mechanical APDL Element Reference.* 2011.

[44] Inc ANSYS, ed. *ANSYS 9.0 Contact Technology Guide.* 2004.

[45] G. Anzaldo Munoz. *ANSYS 13.0 Introduction to contact.* Apr. 2009.

[46] D. Xenos et al. "Calibration of nonlocal models for tensile fracture in quasi-brittle heterogeneous materials." In: *Journal of the Mechanics and Physics of Solids 82* (2015).

[47] U.S. Bureau of Reclamation. *Raise Pine Flat Dam - Upper San Juaquin River Basin Storage Investigation.* 2003.

[48] N.M. Newmark. "Effects of Earthquakes on Dams and Embankments". In: 15.2 (1965), pp. 139–160.

[49] G. Mazzà et al. "ICOLD Benchmark Workshops to compare models for seismic analyses". English. In: 2019, pp. 69–74.

[50] Xhoni Smart. *Selecting seismic parameters for large dams - Guidelines (revision of Bulletin 72).* International Commission on Large Dams (ICOLD), 2016.

[51] E.J. Staudacher and G. Zenz. "Determination of material parameters using numerical models and field measurement data". English. In: (2019), pp. 135–144.

[52] International Federation for Structural Concrete, ed. *Model Code 2010.* Bulletin 65. Lausanne: International Federation for Structural Concrete, 2012. 311 pp. ISBN: 978-2-88394-105-2.